Constraining the nuclear equation of state from nuclear physics and neutron star observations

Einschränkungen für die Zustandsgleichung von Kernmaterie durch Kernphysik und Neutronensternbeobachtungen

Zur Erlangung des Grades eines Doktors der Naturwissenschaften (Dr. rer. nat.)
genehmigte Dissertation von Svenja Kim Greif aus Groß-Gerau
Tag der Einreichung: 16.07.2019, Tag der Prüfung: 28.10.2019
Darmstadt — D 17

1. Gutachten: Prof. Ph.D. Achim Schwenk
2. Gutachten: Prof. Ph.D. Anna L. Watts

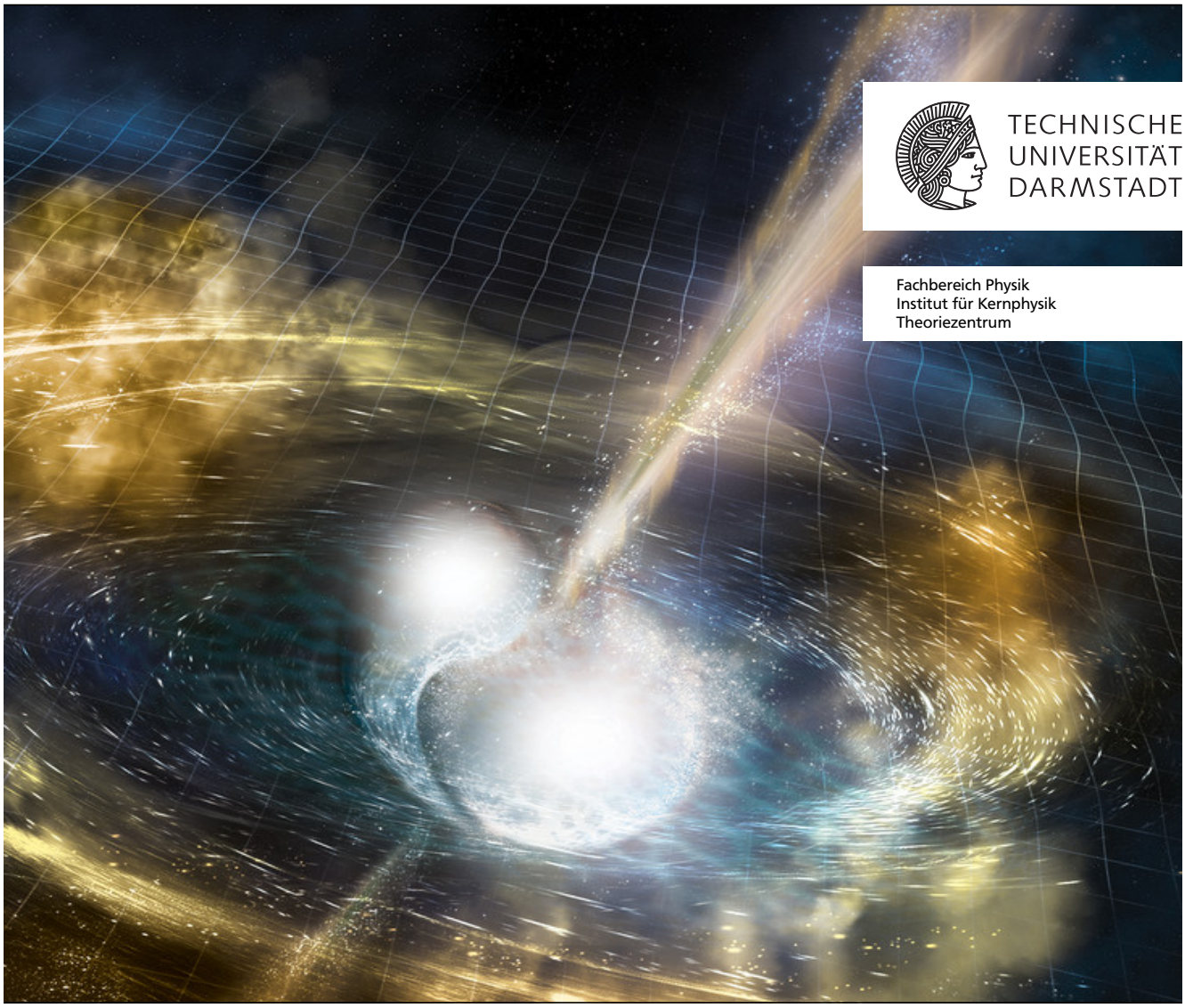

Constraining the nuclear equation of state from nuclear physics and neutron star observations
Einschränkungen für die Zustandsgleichung von Kernmaterie durch Kernphysik und Neutronenstern-beobachtungen

Genehmigte Dissertation von Svenja Kim Greif aus Groß-Gerau

1. Gutachten: Prof. Ph.D. Achim Schwenk
2. Gutachten: Prof. Ph.D. Anna L. Watts

Tag der Einreichung: 16.07.2019
Tag der Prüfung: 28.10.2019

Darmstadt — D 17

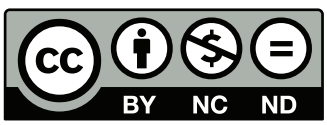

In memory of my best friend and companion, Niccy.

Abstract

Neutron stars are born when massive stars run out of their nuclear fuel and undergo gravitational collapse. Neutron stars belong to the most compact objects in the observable Universe. Macroscopic properties of neutron stars like their masses and radii are sensitive to the microscopic properties of the nuclear equation of state of dense matter. The equation of state is determined by the strong interaction among the constituents. The underlying theory is quantum chromodynamics that is, however, highly non-perturbative in the physics regime relevant for neutron stars. Moreover, neutron stars provide an interplay between nuclear physics and astrophysics. Astrophysical observations like the detection of $2\,M_\odot$ neutron stars have a major impact on the equation of state. Radii are, however, inherently difficult to measure due to systematic uncertainties. Other observables like the moment of inertia or the tidal deformability present promising alternatives. The double neutron star system PSR J0737 − 3039 constitutes an outstanding system as it provides the prospect of a moment of inertia measurement for the first time. A new era stated with the pioneering observation of gravitational waves from a binary neutron star merger. The analysis of the gravitational wave signal of GW170817 provides a range for the tidal deformability of typical neutron stars. Moreover, the current NICER mission will provide simultaneous mass-radius measurements.

In this thesis, we use state-of-the-art chiral effective field theory interactions to describe the equation of state at nuclear densities. In the high-density regime beyond nuclear saturation density, we use different extrapolation approaches. First, we utilize the established ansatz of piecewise polytropic equations of state which provides a direct parametrization. However, piecewise polytropic equations of state possess unphysical behavior such as discontinuities in the speed of sound. Second, we use a physically motivated parametrization of the speed of sound inside the neutron star from which we derive the equation of state. Both methods allow us to probe the equation of state over a large range of densities. We further impose general constraints on the equation of state such as the requirement of causality at all densities and the support of at least $2\,M_\odot$ neutron stars. From the equations of state compatible with the constraints, we determine diverse neutron star observables. We begin with non-rotating neutron stars and focus on their masses and radii. We study correlations among properties of the equation of state at nuclear densities and observables of typical neutron stars. Moreover, we explore the impact of hypothetical, simultaneous measurements of masses and radii of neutron stars on the equation of state. Applying both simple compatibility cuts and the framework of Bayesian statistics, we investigate the sensitivity of the inference on the chosen parametrization of the equation of state. We extend then our considerations to slowly rotating neutron stars and study the moment of inertia. Assuming hypothetical moment of inertia measurements, we determine constraints for the radius of neutron stars and thus the equation of state. In addition, we extend our considerations of isolated neutron stars to binary neutron star systems. In particular, we treat the tidal field of the companion as a small perturbation. This allows us to determine the tidal deformability. By applying higher orders in the metric perturbation, we calculate the quadrupole moment of neutron stars. Although the structure of neutron stars is sensitive to the equation of state, relations between the moment of inertia, the tidal deformability, and the quadrupole moment are remarkably insensitive. We investigate the properties of neutron stars in binary systems and ultimately confront the results of our models with the gravitational wave constraints from a binary neutron star merger.

Cover picture: Artistic interpretation the first observed binary neutron star merger. The gravitational wave signal was named GW170817 referring to the date of observation, August 17, 2017 [5]. Courtesy of National Science Foundation, LIGO, Sonoma State University, Aurore Simonnet. Figure taken from Ref. [2].

Zusammenfassung

Neutronensterne werden geboren, wenn massive Sterne keinen Kernbrennstoff mehr haben und aufgrund der Eigengravitation kollabieren. Sie gehören zu den massivsten Objekten im beobachtbaren Universum. Makroskopische Eigenschaften von Neutronensternen wie deren Massen und Radien sind sensitiv auf die mikroskopischen Eigenschaften der nuklearen Zustandsgleichung. Die Zustandsgleichung ist bestimmt durch die starke Wechselwirkung zwischen ihren Komponenten. Die zugrundeliegende Theorie ist die Quantenchromodynamik, welche stark nicht-perturbativ in dem für Neutronensterne relevanten physikalischen Bereich ist. Darüber hinaus bieten Neutronensterne ein Wechselspiel zwischen Kernphysik und Astrophysik. Astrophysikalische Beobachtungen wie die Detektion von $2\,M_\odot$–Neutronensternen haben einen großen Einfluss auf die Zustandsgleichung. Radien sind jedoch aufgrund systematischer Unsicherheiten von Natur aus schwierig zu messen. Andere Eigenschaften wie das Trägheitsmoment oder die Deformierbarkeit aufgrund von Gezeitenkräften stellen vielversprechende Alternativen dar. Das Doppel-Neutronenstern System PSR J0737 − 3039 stellt ein herausragendes System dar, da es die Perspektive einer erstmaligen Trägheismomentmessung bietet. Eine neue Ära begann mit der bahnbrechenden Beobachtung von Gravitationswellen aus der Kollision zweier Neutronensterne. Die Analyse des Gravitationswellensignals von GW170817 liefert einen Bereich für die Deformierbarkeit durch Gezeitenkräfte typischer Neutronensterne. Darüber hinaus wird die aktuelle NICER Mission gleichzeitige Masse–Radius Messungen ermöglichen.

In dieser Arbeit verwenden wir modernste Wechselwirkungen der chiralen effektiven Feldtheorie, um die Zustandsgleichung bei Kerndichten zu beschreiben. Im Bereich hoher Dichten jenseits der Kernsaturierungsdichte verwenden wir verschiedene Extrapolationsansätze. Zum einen verwenden wir den etablierten Ansatz von stückweise polytropen Zustandsgleichungen, welcher eine direkte Parametrisierung ermöglicht. Allerdings weisen stückweise polytrope Zustandsgleichungen ein unphysikalisches Verhalten wie beispielsweise Unstetigkeit der Schallgeschwindigkeit auf. Zum anderen verwenden wir eine physikalisch motivierte Parametrisierung der Schallgeschwindigkeit im Inneren des Neutronensterns, aus der wir die Zustandsgleichung ableiten. Beide Methoden ermöglichen es, die Zustandsgleichung über einen großen Bereich von Dichten zu untersuchen. Wir legen der Zustandsgleichung weiterhin allgemeine Einschränkungen wie beispielsweise die Forderung nach Kausalität bei allen Dichten und die Reproduktion von $2\,M_\odot$ Neutronensternen auf. Von den Zustandsgleichungen, die mit den Einschränkungen kompatibel sind, bestimmen wir verschiedene Observablen von Neutronensternen. Wir beginnen mit nicht rotierenden Neutronensternen und konzentrieren uns auf deren Massen und Radien. Wir untersuchen Korrelationen zwischen den Eigenschaften der Zustandsgleichung bei nuklearen Dichten und Eigenschaften typischer Neutronensterne. Darüber hinaus untersuchen wir die Auswirkungen hypothetischer, simultaner Messungen von Massen und Radien von Neutronensternen auf die Zustandsgleichung. Mit einfachen Kompatibilitätsanalysen und der Bayesschen Statistik untersuchen wir die Sensitivität der Inferenz auf die gewählte Zustandsgleichung. Dann erweitern wir unsere Überlegungen auf langsam rotierende Neutronensterne und untersuchen das Trägheitsmoment. Unter der Annahme hypothetischer Trägheitsmomentmessungen ermitteln wir Einschränkungen für den Radius von Neutronensternen und damit für die Zustandsgleichung. Darüber hinaus weiten wir unsere Überlegungen zu isolierten Neutronensterne auf Neutronensterne in Doppelsternsystemen aus. Im Speziellen betrachten wir das Gezeitenfeld des Begleitsterns als kleine Störung. Auf diese Weise können wir die Deformierbarkeit aufgrund der Gezeitenkräfte bestimmen. Indem wir höhere Ordnungen in der Störung der Metrik betrachten, berechnen wir das Quadrupolmoment von Neutronensternen. Obwohl die Struktur von Neutronensternen sensitiv auf die Zustandsgleichung ist, sind Relationen zwischen dem Trägheitsmoment, der Deformierbarkeit aufgrund von Gezeitenkräften und das Quadrupolmoment bemerkenswert unsensitiv. Wir untersuchen die

Eigenschaften von Neutronensternen in Doppelsternsystemen und konfrontieren schließlich die Ergebnisse unserer Modelle mit den Einschränkungen durch die Eigenschaften der Gravitationswellen, welche von der Kollision zweier Neutronensterne beobachtet wurden.

Contents

1 Motivation and introduction

Neutron stars are unique laboratories to study matter under extreme conditions. With masses comparable to the mass of the Sun but radii $\sim 10^5$ times smaller than the solar radius, neutron stars exhibit extremely large densities on the order of $10^{14} - 10^{15}\,\mathrm{g\,cm^{-3}}$ and are thus very compact objects [14, 123, 140]. Neutron stars are supported against the gravitational collapse by the pressure generated by degenerated neutrons and repulsive strong interactions [243, 277]. Other than that further compact astrophysical objects exist: white dwarfs and black holes. White dwarfs have a mass comparable to neutron stars but their radii are almost three orders of magnitude larger [243]. Consequently, white dwarfs are much less dense than neutron stars. In contrast to white dwarfs and neutron stars, black holes can only be observed indirectly through their interaction with the matter surrounding them[1] [33, 243].

Neutron stars represent an interdisciplinary research field since diverse disciplines of physics and astrophysics are involved in studying their properties [33]: General relativity (GR), quantum chromodynamics (QCD), nuclear physics, hadronic physics, particle physics, neutrino physics, plasma physics, solid-state physics, and superfluid hydrodynamics. Moreover, neutron stars cover a broad range of magnitudes, ranging from the femtometer scale $10^{-15}\,\mathrm{m}$ relevant for the interactions of the matter inside the neutron star up to $10^5\,\mathrm{m}$ in the case of the wavelength of the gravitational waves (GW) emitted in binary neutron star mergers and rotating neutron stars.

The matter inside a neutron star is under extreme conditions: strong gravitational fields, strong magnetic fields, high densities, and isospin asymmetry. A large variety of neutron star properties depend on the nuclear equation of state (EOS). The EOS that describes matter inside a neutron star is not fully understood so far. Especially the density regime within the core of neutron stars is still an open problem. The interplay of theoretical considerations and observations of neutron stars results in constraints for various properties of neutron stars and therefore for the EOS itself.

The topic of neutron stars and the EOS is broad and extensive. Excellent books that cover the fundamentals of this diverse research topic can be found in Refs. [112, 123, 200, 243] and various reviews can be found in Refs. [29, 30, 140, 172, 219].

For the remainder of the present chapter, we introduce the reader into the fascinating topic of neutron stars. We begin with summarizing general properties of neutron stars and give a brief historical synopsis of the hypothesis of the existence of neutron stars, the discovery of the first pulsar, and the pioneering measurement of gravitational waves from a binary neutron star merger. Subsequently, we sketch the formation process of neutron stars in core-collapse supernova explosions followed by a summary of the structure of these compact objects. We then provide the basic concepts of neutron star observations where we focus on the measurement of masses, radii, and moments of inertia as well as GW astronomy. Further, we provide an overview on the EOS and the connection between the low-density regime and neutron star gross properties.

1.1 Neutron stars as fascinating objects

Neutron stars are extreme astrophysical objects. The densities inside cover a broad range from about a few $\mathrm{g\,cm^{-3}}$ in the outer regions up to $10^{15}\,\mathrm{g\,cm^{-3}}$ in the neutron star core [29, 30, 123, 140, 172]. Thus, the density in the center of such a compact object exceeds the nuclear saturation density ρ_0

[1] Recently, the first picture taken of the shadow surrounding a supermassive black hole was demonstrated by the *Event Horizon Collaboration* [12].

($\rho_0 \sim 2.8 \times 10^{14}\,\mathrm{g\,cm^{-3}}$ or equivalently ~ 0.16 nucleons per fm^{-3}) by a multiple [29, 178]. Such extreme densities can be explored in heavy-ion collisions [78] or studied by neutron star observations (cf. Sec. 1.4). The structure of neutron stars is determined by the interactions between the constituents. Hence, neutron stars are unique laboratories for studying dense matter.

The mass of a neutron star is of the order of the solar mass $M_\odot$ ($M_\odot = 1.98848(9) \times 10^{30}\,\mathrm{kg}$) [30, 178, 277]. GR predicts a maximum mass for compact objects that is sensitive to the underlying EOS [180]. The knowledge of the maximum mass of neutron stars is a crucial ingredient in identifying compact objects as black holes when their mass exceeds the maximum neutron star mass [131, 243]. The value of the maximum mass is still an open question. The maximum mass predicted by theoretical studies is sensitive to the microphysical input. Hence, the ambiguity of the maximum mass is a direct consequence of the uncertainties of the EOS beyond nuclear saturation density [29]. Theoretical works and reviews that elucidate the maximum mass in more detail can be found in Refs. [17, 29, 50, 131, 202, 229]. The heaviest observed neutron star so far has a mass of $\sim 2\,M_\odot$ [16]. The mass of PSR J0740 + 6620 was determined by longterm observations and recently reported as $2.17^{+0.11}_{-0.10}\,M_\odot$ [69].

The radii of neutron stars are in the range of about $10-14\,\mathrm{km}$ [29, 172, 178, 219, 251]. The radius is sensitive mostly to properties of the EOS at around nuclear saturation density [180]. A typical neutron star contains about $10^{56} - 10^{57}$ baryons [29, 277]. Neutron stars can be fast rotators whereby the rotational frequencies vary from 0.1 Hz to kHz [195]. Such high frequencies are comparable with the rotational frequencies of a conventional kitchen blender. The fastest rotating neutron star observed so far is PSR J1748 − 2446ad with a frequency of 716 Hz [141]. The magnetic field strength can be in the order of $10^{12}\,\mathrm{G}$ or even larger [196]. The surface gravity is about 10^{11} times stronger than the surface gravity of Earth [29, 174]. Neutron stars are sources of GW like rotating neutron stars with deviations from spherical symmetry. Much stronger GW are emitted in binary systems, in particular neutron star merger [14, 243].

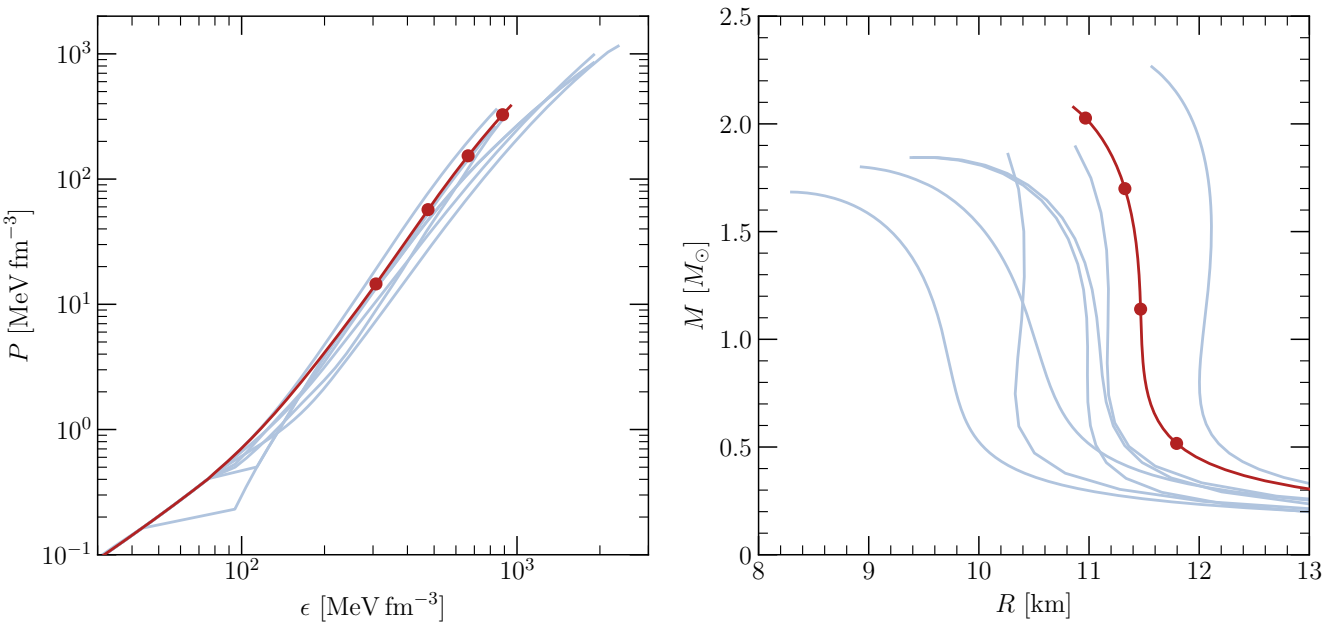

Figure 1.1.: *Left panel*: The pressure P as a function of the energy density ϵ with a double logarithmic scaling. The red dots mark energy density-pressure pairs which correspond to different densities. We present various EOS, i.e., AP1 − 4 and WFF1 − 4 where we highlight AP4 in red. *Right panel*: The neutron star mass M as a function of the radius R. The red dots correspond to mass-radius pairs with the central density highlighted in the left panel.

The gross properties of neutron stars are determined by the interactions of their constituents. The mass-radius relation serves hereby as an appropriate tool since this relation and the EOS are linked via hydrostatic equilibrium in a unique manner [185]. Constraining the EOS as well as the mass-radius relation is a challenge in physics [172, 282]. For large enough maximum masses, the radius for neutron stars in the mass region of about $1 - 1.5\,M_\odot$ is not very sensitive to the mass [178]. Thus, the radius of $1.4\,M_\odot$ neutron stars and the predicted maximum mass are important quantities [178]. In Fig. 1.1, the discussed interplay of the EOS and the mass-radius relation as well as the properties of the latter are depicted. Astrophysical observations permit the possibility to constrain the EOS [172].

1.2 A brief history of neutron stars

In 1932, Lev Landau[2] anticipated the existence of neutron stars [169]. In his work, Landau investigated the maximum mass of white dwarfs (independently from Chandrasekhar). Further, he wrote about the possible existence of even heavier stars than white dwarfs. He finished his work with the statement: "the density of matter becomes so great that atomic nuclei come in close contact, forming one gigantic nucleus" [169]. One month after Landau's paper, Chadwick's paper on the discovery of the neutron was published [65]. Baade and Zwicky proposed neutron stars as the final product of supernova explosions [20, 21, 22]. Further, the hypothesis that neutron stars consist mainly of neutrons was put forward [20].

The structure equations for describing neutron stars in the framework of GR were independently derived by Tolman [270] and Oppenheimer and Volkoff [205]. These works described the interior of neutron stars via an ideal Fermi gas. Oppenheimer and Volkoff deduced that neutron stars have a maximum mass as a consequence of GR. The first estimate for the maximum mass of a neutron star was found to be $M_{\mathrm{OV}} = 0.71\,M_\odot$ [205]. Here, we remark that the equations of hydrostatic equilibrium to describe the structure of compact stars were earlier found by Chandrasekhar and von Neumann while their work remained unpublished [123]. The upper limit M_{OV} found by Oppenheimer and Volkoff has long been outdated. More sophisticated models for the description of the constituents contained in neutron stars and the interactions predict larger masses and even heavier neutron stars were observed since then. Nonetheless, the EOS and also neutron star models were still subject of research and further progress was achieved by theoreticians, cf. Refs. [13, 59, 126, 235, 246].

Even though neutron stars were studied extensively by theoreticians, astronomers did not consider the possibility to observe neutron stars for about 30 years since neutron stars were considered to be too faint for the observation with telescopes due to their small size [29, 277]. At this point, it was not clear that pulsars are indeed rotating neutron stars [29, 277]. In 1964, the hypothesis was made that neutron stars may appear as fast rotators [150]. One year later, a remarkable intense radio source in the Crab nebulae was observed [144]. In 1968, Gold proposed that the strong magnetic fields and high rotational frequencies of pulsars can be associated with rotating neutron stars while the precise emission mechanism of radio signals is still an open question [114]. The first radio pulsar, PSR B1919+21 or PSR J1915+1606[3], was eventually detected on August 6, 1967 by Jocelyn Bell and Anthony Hewish [143]. The received signal was outstanding because of its strength and its periodic nature with a period of 1.337 s [143]. In 1974, Hewish and Ryle were awarded for this remarkable discovery with the Nobel prize. The decision of the Swedish Nobel prize committee not to consider Jocelyn Bell was criticized [292]. Subsequently, the object in the Crab nebulae was identified as a *pulsar* in 1969 [68]. This discovery finally made it possible to associate the remnant of a supernova explosion with the birth of a

[2] Further details on Lev Landaus role in the prediction of the existence of neutron stars can be found in Ref. [301] (cf. also Ref. [123]).

[3] The designation of pulsars follows a certain nomenclature: *PSR* stands for "pulsating source of radio emission". The prefix is then followed by either the letter *B* or *J* denoting "Besselian epoch" (epoch 1950) and "Julian epoch" (epoch 2000), respectively, that specify the epoch of discovery. Since the position changes with time, pulsars can have more than one name which is the case for the Hulse-Taylor pulsar for instance. The subsequent digits denote the right ascension and the last digits after the sign denote the degree of declination. In case of a double pulsar system, the pulsars are distinguished by *A* or *B* after the declination.

neutron star [140]. In 1974, the Hulse-Taylor pulsar B1913 + 16 was discovered [152]. This discovery was remarkable since the observed system turned out to be the first observation of a binary neutron star system. This discovery was awarded with the Nobel prize in 1993 [151, 259]. Moreover, the observed advance of the periastron and decay of the orbital period gave strong indications that GW exist [243]. In April 2003, the binary neutron star system PSR J0737 − 3039 was discovered. At the time of discovery, this system was the most relativistic binary system ever found and its particular characteristics make it an excellent laboratory for testing GR as well as alternative theories of gravity [56, 191].

On February 11 in 2016, the first detection of GW was announced which were measured on September 14, 2015 [4]. In the same year on December 26, another GW event was observed [3]. These observations started a new era on GW astronomy and several more signals were detected since then. On August 17 in 2017, GW from a binary neutron star merger were observed by the LIGO and Virgo GW detectors [5].

1.3 Formation and structure

Neutron stars are born at the end of the life of massive stars with masses of at least $8\,M_\odot$ [57, 178]. Lighter progenitors will end in white dwarfs [243]. Due to nuclear reactions, an iron core evolves in the center of a massive star that obtains more mass over the star's lifetime. The death of the star is inevitable when the mass of the iron core is no longer supported against gravitational collapse [228]. The final fate of a massive progenitor can either be a neutron star or a black hole [95, 274]. In the following, we give a brief discussion of the supernova process in which neutron stars are born. For a more thorough introduction and more details, we refer the reader to Refs. [42, 153, 156].

Inside the star, nuclear fusion reactions via hydrostatic burning take place [154]. The hydrostatic burning is divided into different burning stages which cause the interior of the star to be onion-like structured [154]. The different stages involve hydrogen, helium, carbon, oxygen, and silicon burning [154]. Silicon burning constitutes the final burning stage and subsequently no heavier elements can be produced [154]. In the center of the star there is an iron core surrounded by a silicon shell [154]. The mass of the core increases due to silicon burning at the interface of the core [154]. The iron core is stabilized against the gravitational collapse by the pressure of degenerated electrons [154]. When the core reaches the Chandrasekhar mass $M_{\mathrm{Ch}} \approx 1.44\,M_\odot$, the core is no longer stabilized and collapses [154]. The gravitational collapse of the core occurs within about 0.1 s [123]. The matter falls towards the core while the density increases. When the matter of the core becomes incompressible at nuclear densities, the infalling matter bounces off the stiff core [154, 156]. The bounce initiates a shock wave that travels within several hours outwards and blows away the outer layers of the star [42, 123]. The shock wave competes with the infalling matter and initially stalls. Eventually, the revival of the shock takes place [228]. When the shock reaches the surface, electromagnetic radiation of all wavelengths is emitted [123]. These catastrophic events are referred to as *core-collapse supernova explosion*. Neutrino emission constitutes the largest part of the released energy of about 10^{53} erg (10^{53} erg $= 10^{46}$ J) [123, 156]. Only a small part of the released energy is emitted via light [156].

After the bounce, a proto-neutron star is formed in the center of the collapsing star [154]. Proto-neutron stars have radii of about $20 - 30$ km [57]. Depending on the progenitor's mass, the proto-neutron star can either evolve to a neutron star or a black hole [154]. A proto-neutron star differs in several aspects from a neutron star: Proto-neutron stars are hotter, opaque to neutrinos, and larger than neutron stars, and have large electron fractions of about $Y_{\mathrm{e}} \sim 0.35$ [123, 172]. The lifetime of a proto-neutron star is about a minute [123]. The newly-born neutron star is low in neutrons and contains a large amount of degenerate electrons as well as neutrinos [154]. It has a temperature of $T \sim 10^{11}$ K and cools down by neutrino emission [29, 112, 228]. After a few days, the temperature cooled down to $T \sim 10^{10}$ K and after about a month the temperature amounts to $T \sim 10^{8}$ K [29, 112]. Within less than a million years, the neutron star has cooled down to temperatures about $T \sim 10^{6}$ K when it cools through photon emission [112]. However, the Fermi energy of nuclear matter at ρ_0 amounts roughly 30 MeV and increases with the density [200]. Hence, neutron stars can be described with an EOS at $T \approx 0$ [156].

A core-collapse supernova explosion is not the only process in which neutron stars are born. A white dwarf in a binary system with a star can gain mass via accretion. The gravitational collapse sets in when the Chandrasekhar mass M_{Ch} is exceeded [123]. However, the proportion of neutron stars formed via accretion-induced collapse is expected to be small compared to the total population [105]. More details on the formation of double neutron star systems can be found in Ref. [258].

Neutron stars consist mostly of neutrons with a small proton fraction of about 5%. The structure is, however, more complex and we provide an overview in the following. From the surface of the neutron star to its center, the pressure and the density increase. According to current studies, neutron stars are made up by several layers [123, 178, 255]. The main layers are the outer crust, the inner crust, the outer core, and the inner core that, however, feature a substructure themselves [123, 178]. Further, neutron stars are surrounded by an atmosphere [123, 178]. We show a schematic drawing of the neutron star structure in Fig. 1.2.

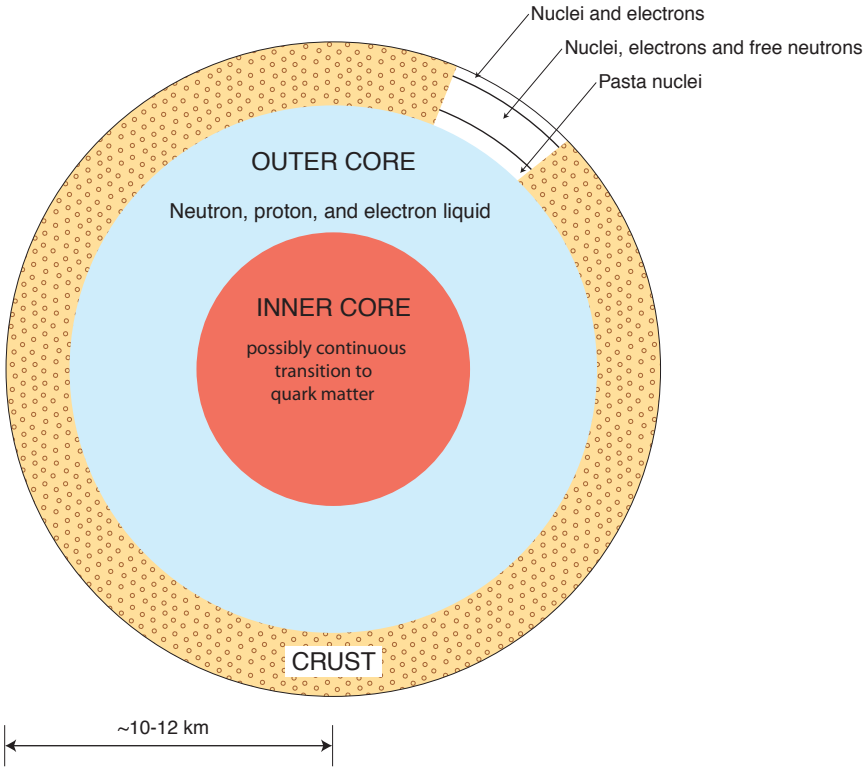

Figure 1.2.: Schematic illustration of the structure of a neutron star. From the surface to the center are shown the crust, the outer core, and the inner core. The distinct regions differ by the density of the matter and the occurring constituents. The shown sizes of the layers are not to scale. Figure taken from Ref. [28].

In the following, we discuss the internal structure of the distinct regions of the neutron star in more detail. The atmosphere is a thin layer of plasma surrounding the neutron star [123]. Hot neutron stars with an effective surface temperature of about 3×10^6 K exhibit an atmosphere thickness in the order of a few ten centimeters, while cold neutron stars with effective surface temperatures of about 3×10^5 K have an atmosphere thickness of about a few millimeters [123]. The atmosphere is supposed to consist of hydrogen, in the case of isolated or quiescent neutrons stars also helium or carbon might be abundant. In the case of accreting neutron stars, the composition of the atmosphere is more complex [44, 228, 233]. Compared to the total mass of the neutron star, the mass of the atmosphere is negligible [228]. However, the emission of thermal electromagnetic radiation from the atmosphere provides opportunities to study neutron star observables [123, 228]. The observed radiation provides information on the effective

surface temperature, the surface gravity, the chemical composition, as well as the strength and geometry of the surface magnetic field [123]. Hence, the investigation of the atmosphere provides a crucial ingredient for the measurement of masses and radii of neutron stars [123, 228]. More information on neutron star atmospheres can be found in Ref. [303] and references therein.

The thickness of the entire crust amounts about one tenth of the radius of a neutron star [228], where the outer crust is some hundred meters thick and the thickness of the inner crust is about one kilometer [123]. The crust manly consist of solid matter [123, 228, 243]. The outer crust is made up by a lattice of iron nuclei embedded in a sea of relativistic degenerate electrons [29, 58, 123, 196]. The matter of the neutron star's outer regions is therefore basically white dwarf matter [196]. The Fermi energy of the electrons increases with increasing density. Consequently, it is energetically more favorable to decrease the electron number. Hence, the nuclei undergo β-decay and the matter inside the neutron star becomes more neutron-rich [212, 228]. The neutron drip density at which neutrons begin to drip out of nuclei is about $\rho \approx 4.3 \times 10^{11}\,\mathrm{g\,cm^{-3}}$ [123, 228].

The inner crust covers a density range from the neutron drip density to about $\sim 0.5\,\rho_0$ [58, 123]. This part of the neutron star is made up by neutron-rich nuclei, surrounded by an electron gas and a superfluid neutron [123, 228]. For increasing density, the density of the neutrons surrounding the nuclei increases until the neutron densities inside and outside the nuclei equalize [212]. Nuclei dissolve and ultimately merge due to the high densities at the interface of the inner crust and the outer core [123, 228]. For increasing density inside the neutron star crust, not only the composition of the matter changes but also the shape of the nuclei. The geometry of the nuclei changes from spheres to cylinders to slabs to tubes and bubbles. These shapes remind of noodles such that this particular phase is referred to as *nuclear pasta* [66, 134, 206, 223, 281].

The core contains about 99% percent of the total mass of the neutron star [228]. Inside the core, the nuclei are completely dissolved into their constituents, i.e., protons and neutrons [58]. The outer core is several kilometers thick and the densities range to about ρ_0 [123]. The outer core consists manly of neutrons as well as a small percentage of protons and electrons which is due to charge neutrality and β-equilibrium [123, 228]. Moreover, muons might exist [123]. The occurring neutrons and protons are presumed to be in a superfluid phase [228]. The inner core is several kilometers thick and the densities in the center of the neutron star extend up to several times ρ_0 [123]. To date, the composition of the matter inside the core is still an open puzzle, current hypotheses consider hyperonization, pion condensation, kaon condensation, or quark matter [123].

1.4 Observation of neutron star properties

Most neutron stars are observed as pulsars [195]. The first radio pulsar was discovered in 1967 [143]. Forty years later, 2000 objects are known, but the entire population of active radio pulsars is obviously unknown [33, 195]. An online database of the known pulsars and their observed properties is provided by the Australia Telescope National Facility (ATNF), cf. Refs. [1, 195]. Pulsars are highly-magnetized, rotating neutron stars with observed spin periods ranging from 1.4 ms to 8.5 s [33, 140]. The misalignment of the angular momentum and the magnetic axis causes the emission of broadband radio waves [140, 196]. Moreover, the direction of the emitted radiation changes [123].

Pulsars are very accurate clocks, since pulsar periods are remarkably stable [174]. Nevertheless, the rotation of the neutron star slows down gradually [33]. The spin down rate $\dot{P}$ provides the possibility to access information on the magnetic field strength, the luminosity, and the age of the neutron star [174]. Therefore, the $P-\dot{P}$ diagram constitutes a useful tool to study properties of pulsars. In Fig. 1.3, we show the $P-\dot{P}$ diagram which is used to categorize pulsars into normal pulsars and millisecond pulsars. Normal pulsars are characterized by $P \sim 0.5\,\mathrm{s}$ and $\dot{P} \sim 10^{-15}\,\mathrm{s\,s^{-1}}$ and are located in the "island of points". Millisecond pulsars are located in the lower left corner of the $P-\dot{P}$ diagram and characterized by $P \sim 3\,\mathrm{ms}$ and $\dot{P} \sim 10^{-20}\,\mathrm{s\,s^{-1}}$ [33]. Pulsars in the age of $1-100\,\mathrm{Myr}$ are considered as being young. These pulsars have magnetic fields of about $B \sim 10^{12}\,\mathrm{G}$. During its lifetime, the pulsar's rotation slows

down. In terms of the $P-\dot{P}$ diagram, the pulsar evolves down to the lower right corner and ultimately enters the *graveyard*. Neutron stars in binary systems can leave the graveyard via mass accretion. Being $1-10\,\mathrm{Gyr}$ old, pulsars are considered as old. These pulsars exhibit magnetic fields strengths of about $B \sim 10^8\,\mathrm{G}$. A further group are magnetars which have magnetic field strengths in the order of $B \sim 10^{15}\,\mathrm{G}$ [174]. Pulsars can be isolated objects or appear in binary systems [123]. About 80% of the known millisecond pulsars are in a binary system whereas only 1% of the normal pulsars have a companion [33].

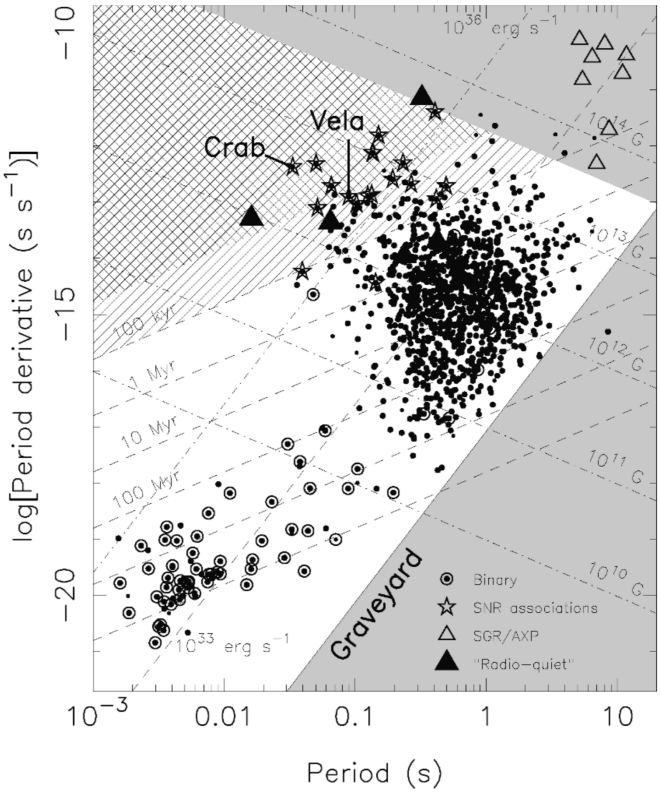

Figure 1.3.: $P-\dot{P}$ diagram. The pulsar's period P and its derivative $\dot{P}$ provide estimates of the age and the magnetic field trajectories of constant age are represented as dashed lines and trajectories of constant magnetic field as dash-dotted lines. Figure taken from Ref. [189].

The emitted signals are received periodically and a single signal originates from a single rotation of the neutron star [248]. The detected signal suffers deviations that encode information on properties of the neutron star, the interstellar medium between the neutron star and the detector, and the interaction with the companion in the case of a binary system [248]. Although individual pulses differ in shape and intensity, the sum over several hundred or even thousand pulses results in a stable shape at a given frequency [248]. The reproducibility of the averaged pulse profile enables high-precision measurements [248].

As we mentioned above, the maximum mass of neutron stars is a key property for constraining the EOS. A pioneering discovery was the precise mass measurement of PSR J0348 + 0432 with a mass of $2.01 \pm 0.04\,M_\odot$ [16][4] that ruled out several EOS which do not support such heavy neutron stars.

Pulsars provide a suitable testbed for GR and alternative theories of gravity [248, 293]. The Galaxy and the interstellar medium can be explored by studying pulsars. Diverse disciplines in physics can be

[4] In earlier works, PSR J0348+0432 and PSR J1614 − 2230 are mentioned as the heaviest neutron stars observed so far. The mass of PSR J1614 − 2230 was initially measured to be $1.97 \pm 0.04\,M_\odot$ [80] and was recently updated to be $1.928 \pm 0.017\,M_\odot$ [102].

probed especially with matter under extreme conditions. In summary, pulsars are unique systems that can be used as laboratories for physical and astrophysical phenomena.

1.4.1 Masses of neutron stars in binary systems

Binary systems can be characterized by five so-called Keplerian parameters derived from Kepler's laws [189]. The Kepler parameters are the orbital period P_b, the projection of the pulsar's semi-major axis on the line of sight $x = a_\mathrm{p} \sin i$ (where i is the inclination angle of the orbit), the eccentricity of the orbit e, and the longitude of the periastron ω [172, 277]. The mass of the pulsar M_p and the mass of its companion M_c are related by a mass function

$$f_\mathrm{p} = \left(\frac{2\pi}{P_\mathrm{b}}\right)^2 \frac{\left(a_\mathrm{p} \sin i\right)^3}{G} = \frac{(M_\mathrm{c} \sin i)^3}{M^2}, \tag{1.1}$$

where $M = M_\mathrm{p} + M_\mathrm{c}$ denotes the total mass of the binary system [172, 174]. The mass function given above can be derived by using Kepler's third law [277]. The determination of the inclination i is complicated [172]. However, it is possible to estimate the inclination if eclipses are observed such that the inclination can be assumed to be $\sin i \sim 1$ [174]. However, even if the inclination is obtained, the mass function f_p provides only a relation between the pulsar's mass and the companion's mass [172, 277]. The mass function f_c of the companion is only accessible in few systems [172].

Binary pulsars are compact systems and consequently relativistic effects are relevant [172]. The general relativistic effects alter the expected pulse times-of-arrival (TOA) and are thus detectable [33, 277]. The post-Keplerian (PK) parameters describe the changes of the expected TOA. The PK parameters are theory-independent, phenomenological corrections to the Kepler parameters [73, 74] (cf. also Refs. [33, 162, 161, 248]). GR and alternative theories of gravity predict the PK parameters as functions of the two *a priori* unknown masses [77, 248]. Hence, the measurement of any two PK parameters allows to determine the two objects in the binary system [248, 277]. Each additional measured PK parameter over-determines the system. The over-determinacy serves as self-consistency checks and thus as a test for the considered theory of gravity [248].

Among others, the PK parameters are the advance of the periastron $\dot{\omega}$, the combined effect of variations in the transverse Doppler shift and gravitational redshift around an elliptical orbit γ, the orbital decay due to the emission of quadrupole gravitational radiation $\dot{P}_\mathrm{b}$, and the range r and shape s parameters that characterize the Shapiro delay of the pulsar's signal as it propagates through the gravitational field of its companion [277]. In the case of GR, the PK parameters are given by

$$\dot{\omega} = 3\left(\frac{P_\mathrm{b}}{2\pi}\right)^{-\frac{5}{3}} (T_\odot M)^{\frac{2}{3}} (1-e^2)^{-1}, \tag{1.2}$$

$$\gamma = e\left(\frac{P_\mathrm{b}}{2\pi}\right)^{\frac{1}{3}} T_\odot^{\frac{2}{3}} M^{-\frac{4}{3}} M_2 (M_1 + 2M_2), \tag{1.3}$$

$$\dot{P}_\mathrm{b} = -\frac{192\pi}{5}\left(\frac{P_\mathrm{b}}{2\pi}\right)^{-\frac{5}{3}} \left(1 + \frac{73}{24}e^2 + \frac{37}{96}e^4\right)(1-e^2)^{-\frac{7}{2}} T_\odot^{\frac{5}{3}} M_1 M_2 M^{-\frac{1}{3}}, \tag{1.4}$$

$$r = T_\odot M_2, \tag{1.5}$$

$$s = x\left(\frac{P_\mathrm{b}}{2\pi}\right)^{-\frac{2}{3}} T_\odot^{-\frac{1}{3}} M^{\frac{2}{3}} M_2^{-1}, \tag{1.6}$$

with $s = \sin i$, $T_\odot = GM_\odot/c^3 \approx 4.925\,\mu s$, and $M = M_1 + M_2$ [74, 77, 248, 260]. The advance of the periastron $\dot{\omega}$ provides a measurement of the total mass M of the system and the decay of the orbital decay $\dot{P}_\mathrm{b}$ permits access to the chirp mass $\mathscr{M}$ that is given by [33, 293]

$$\mathscr{M} = \frac{(M_1 M_2)^{\frac{3}{5}}}{(M_1 + M_2)^{\frac{1}{5}}}. \tag{1.7}$$

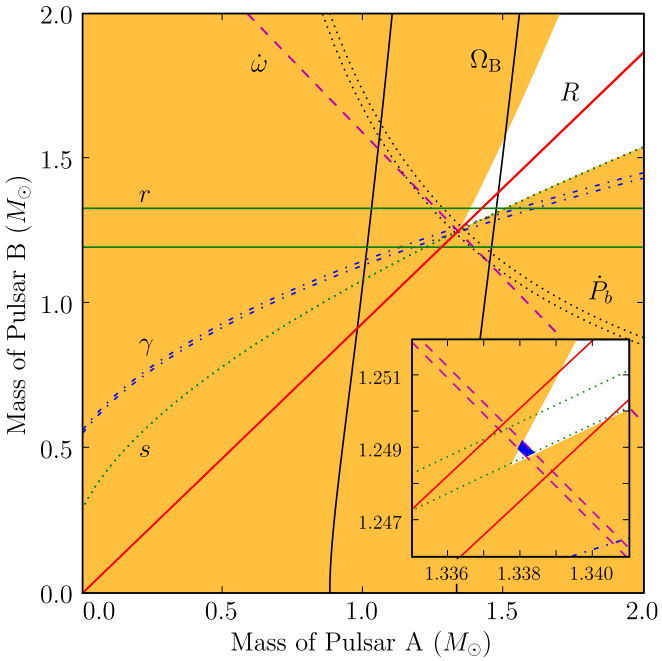

Figure 1.4.: Mass-mass diagram for the double pulsar system PSR J0737−3039. The inset shows a magnified clipping of the region where the functions from the PK parameters intersect. The shown PK parameters are based on GR. Figure taken from Ref. [51].

The observed PK parameters are usually depicted in a mass-mass diagram [33]. All functions for the PK parameters intersect in one point which thus yields the masses of the two objects. In practice, the functions intersect not in a single point but in an intersection area due to the uncertainties associated with the observed PK parameters. Since GR and also alternative theories of gravity predict different parameterizations of the PK parameters, the resulting shapes of the functions in the mass-mass diagrams can differ [33, 162]. This constitutes also a test for GR and alternative theories of gravity. The test is passed when all functions of the PK parameters intersect in one point within the uncertainties [293]. In Fig. 1.4, we show the mass-mass diagram for the double pulsar system PSR J0737−3039. We refer to this particular system in the context of a prospect moment of inertia measurement in Sec. 1.4.3.

Masses can be measured with an impressively high accuracy [172]. Examples for successful high-precision mass measurements are the Hulse-Taylor pulsar PSR 1913+16 with a mass $M = 1.4408 \pm 0.0003\,M_\odot$ [152], the millisecond pulsar PSR J1614−2230 with $M = 1.928 \pm 0.017\,M_\odot$ [80, 102], and the millisecond pulsar PSR J0348+0432 with $M = 2.01 \pm 0.04\,M_\odot$ [16]. In Fig. 1.5, available masses from neutron stars in binary systems are collected.

1.4.2 Neutron star radii

Compared with other astrophysical objects like massive stars, neutron stars are small with radii around 12 km. Moreover, neutron stars are far away which makes the measurement of their radii a difficult task. So far, direct measurements of neutron star radii are not accessible [277]. The existent radius estimates are not measured precisely so far and have not yet been performed for neutron stars of which the mass has been measured [172].

Thermal emissions can lead to simultaneous measurements of neutron star masses and radii [172, 174]. For this approach, the thermal emission of the neutron star is modeled as black body emission. By measuring the flux and taking the redshift into account, the radiation radius is obtained. This effective radius is connected to the mass and the radius of the neutron star [172, 277]. Since a neutron star is not a black body, the modulation of the thermal emission due to the atmosphere and the magnetic field have

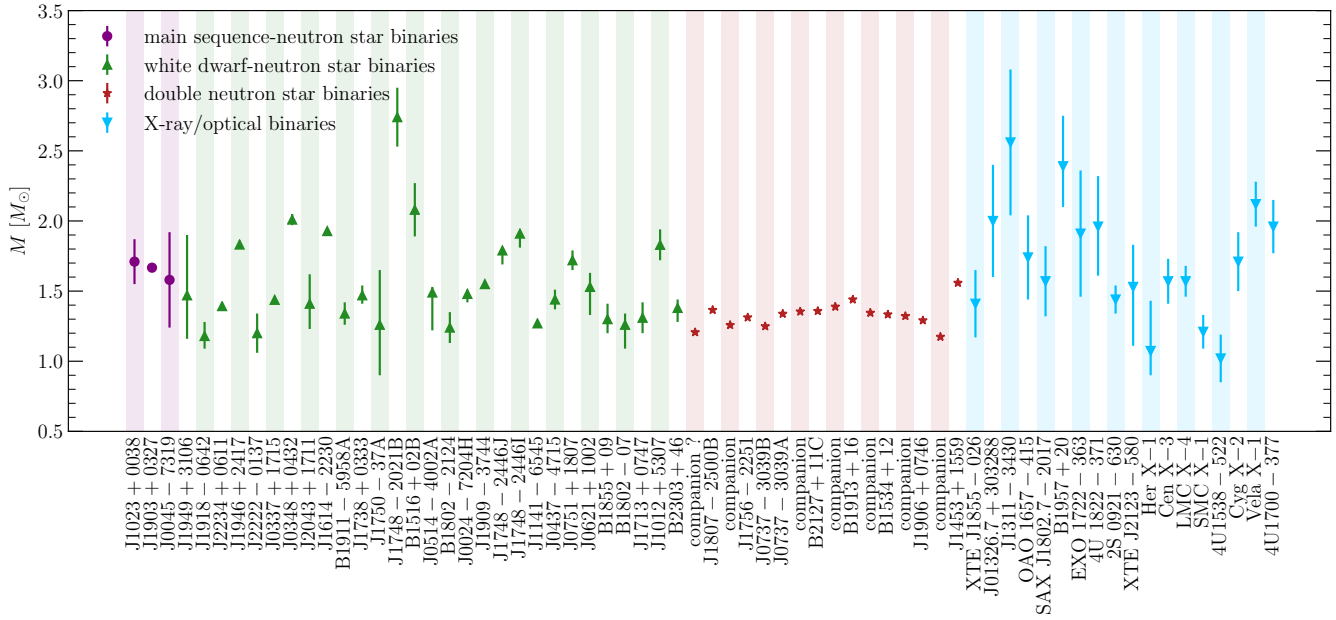

Figure 1.5.: Masses of observed neutron stars in binary systems with 1σ error bars. The different colors and symbols categorize the different binary systems, i.e., main sequence-neutron star binaries, white dwarf-neutron star binaries, double neutron star binaries, and X-ray/optical binaries. Figure adapted from from Refs. [171, 172, 179] and data taken from Ref. [171].

to be taken into account [172]. However, the radius obtained has uncertainties which arise from different origins. The distance to the observed neutron star is afflicted with uncertainties as well as the absorption behavior of X-rays of the interstellar medium and the strength of the magnetic field of the neutron star [172, 174, 277]. The isolated neutron star RX J1856 − 3754 constitutes an intensively studied source of which the mass and the radius were determined, i.e., $M = 1.86 \pm 0.23\,M_\odot$ and $R = 11.7 \pm 1.3\,\mathrm{km}$ [172, 217, 280].

NASA's NICER (Neutron star Interior Composition Explorer) mission has one goal to measure neutron star radii [18]. NICER is attached to the *International Space Station*. A number of selected targets are planned to be observed. The primary science goal of the NICER mission is the detection of thermal X-ray emission from millisecond pulsars [18, 108]. The X-ray emission originates from rotating hot spots on the neutron star's surface [108]. Hot spots are regions of larger temperature than the surrounding surface and are not necessarily located at the polar caps of the neutron star [228]. The intensity of the signal is modulated by various factors such as the position, size, and geometry of the hot spots as well as their motion [108, 228]. Moreover, the compactness $C = M/R$ influences the light-bending and allows consequently the detection of a far-side located hot spot [108]. Pulse profile modeling provides thus access to the compactness and the mass of the targets [198, 208]. In the end, the analysis of the results will provide uncertainty ranges in the mass-radius space that will put available EOS models to the test [108].

1.4.3 Prospect of a moment of inertia measurement

Damour and Schäfer [76] describe how the moment of inertia of neutron star can be measured in principle. High-precision timing-measurements of binary neutron stars are the most promising systems to study in this context [76]. In compact systems like binary neutron stars, spin-orbit coupling is in principle observable [76]. The spin-orbit coupling manifests in two effects on the binary system [25, 76]. First, the orientation of the orbit of the binary system is altered due to the precession of the orbital plane

about the direction of the angular momentum [25, 76]. The changes are proportional to the spins of the two objects whereas the spin of the companion is negligible in most systems [25, 162]. Second, the spin-orbit coupling leads to an extra contribution to the advance of the periastron $\dot{\omega}$ caused by relativistic effects [26, 76].

According to Refs. [76, 162], the spin-orbit coupling leads to an additional, small contribution to the second order of the post-Newtonian (pN) expansion. The total advance of the periastron can thus be written as

$$\dot{\omega} = \dot{\omega}_{1\mathrm{pN}} + \dot{\omega}_{2\mathrm{pN}} + \dot{\omega}_{\mathrm{SO}} \,,$$

where the spin-orbit contribution $\dot{\omega}_{\mathrm{SO}}$ is connected to the moment of inertia [162]. In order to determine the moment of inertia, the advance of the periastron $\dot{\omega}$ has to be measured and the spinless contributions $\dot{\omega}_{1\mathrm{pN}}$ and $\dot{\omega}_{2\mathrm{pN}}$ need to be identified. The advance of the periastron $\dot{\omega}$ is a PK parameter and thus high-precision measurements of $\dot{\omega}$ could not only yield the determination of the moment of inertia but also provide tests of theories of GR and alternative theories of gravity [76].

In the work of Ref. [36], observational data from the Crab nebula was used to constrain the moment of inertia of the Crab pulsar. Depending on the mass M_{neb} of the Crab nebula[5], the authors give different estimates for the lower bound of the moment of inertia I_{Crab} of the Crab pulsar, i.e., $I_{\mathrm{Crab}} > 1.61 \times 10^{45}\,\mathrm{g\,cm^2}$ for $M_{\mathrm{neb}} = 2\,M_\odot$ and $I_{\mathrm{Crab}} > 3.04 \times 10^{45}\,\mathrm{g\,cm^2}$ for $M_{\mathrm{neb}} = 4.6\,M_\odot$, respectively [36]. A subsequent work (see Ref. [37]) considered several improvements and gives as revisited estimates $I_{\mathrm{Crab}} > 1.93 \times 10^{45}\,\mathrm{g\,cm^2}$ for $M_{\mathrm{neb}} = 4.6\,M_\odot$ and $I_{\mathrm{Crab}} > 2.68 \times 10^{45}\,\mathrm{g\,cm^2}$ for $M_{\mathrm{neb}} = 6.4\,M_\odot$ [37]. In both studies, the authors concluded that the moment of inertia is sensitive to the EOS especially to the stiffness (cf. Sec. 1.5) [36, 37].

In 2003, a unique system was discovered: PSR J0737−3039 [56]. At first a pulsar with a period of 22.7 ms was identified which is named PSR J0737−3039A. The companion was later identified as a radio pulsar – PSR J0737−3039B – with a period of 2.7 s [191]. This system is outstanding since both neutron stars are radio pulsars [56, 191]. The discovery of PSR J0737−3039 was the first observation of a double neutron star system [56, 191]. In particular, it was stated that PSR J0737−3039A may provide a first measurement of the moment of inertia of a neutron star [191].

We start by providing some properties of PSR J0737−3039. More details on the measured parameters and especially the observational details can be found in Refs. [51, 56, 162, 161, 191]. The masses of both neutron stars were measured and are given by $M_{\mathrm{A}} = 1.3381(7)\,M_\odot$ and $M_{\mathrm{B}} = 1.2489(7)\,M_\odot$ [161]. The orbital period is with $P_{\mathrm{b}} = 147\,\mathrm{min}$ rather short [162]. The advance of the periastron amounts $\dot{\omega} = 16.88(10)^\circ\,\mathrm{yr}^{-1}$ [56]. Hence, the double pulsar exhibits a four times larger advance of the periastron than the Hulse-Taylor pulsar. Moreover, the double pulsar is 10 times closer to the Earth and the binary separation significantly less than in the case of the Hulse-Taylor pulsar [56]. The contribution of the spin-orbit coupling to $\dot{\omega}$ is in PSR J0737−3039 larger by about one order of magnitude than in PSR B1913+16 [191]. Consequently, the relativistic effects have a larger impact on the double pulsar than the Hulse-Taylor pulsar. This property will potentially enable the first measurement of the moment of inertia of a neutron star [76, 191]. The accuracy of measurements of relativistic effects in compact systems increases with the rotational frequency [162]. Consequently, relativistic effects can be measured with a higher precision for pulsar A since pulsar B has a much smaller rotational frequency. However, the observation of the binary system has to be performed for several years to achieve a high enough timing accuracy to determine the spin-orbit contribution $\dot{\omega}_{\mathrm{SO}}$ [162, 191]. Many authors discussed the possible accuracy of a future measurement of I_{A} and the consequences for the EOS. The consideration of hypothetical moment of inertia measurements with a 10% accuracy showed that such observations have the potential to rule out several EOS [35, 162, 182, 201].

[5] We refer the reader to Ref. [36] and references therein for details on the estimates of the mass M_{neb} of the Crab nebula.

1.4.4 Gravitational wave astronomy

In the years 1915 and 1916, Albert Einstein published his works on GR [85, 86]. In subsequent works, he predicted the existence of GW [87]. However, Einstein himself doubted that GW will ever be observed since their interaction with matter is very weak. More insights on Einstein's skepticism is summarized in Ref. [64]. First attempts to detect GW were made by Weber in the 1960s [283]. The first attempt to detect GW was based on a *resonant mass detector* built up by an aluminum cylinder connected to piezoelectric sensors. The concept of the detector was based on vibrations in the inside of the detector when it was hit by GW. The piezoelectric sensors then translate the vibrational signal into an electric signal [283]. Even though no experimental group was able to reproduce Webers findings, other scientists were motivated to explore the field of GW further [199, 243]. 100 years after Einstein's publication on GR – on September 14 2015 – the first GW from a binary black hole merger were observed [4]. This started a whole new era of GW astronomy and further black hole-black hole mergers were observed since then. On October 16 2017, the detection of the first binary neutron star merger was announced. The signal was observed on August 17 2017 and accordingly named GW170817 [5]. More on the history of GW can be found in Refs. [64, 199].

GW are small distortions of spacetime that are emitted by accelerated masses [58, 237]. GW can be studied by using a metric $g_{\mu\nu}$ that describes a flat spacetime $\eta_{\mu\nu}$ and considering a linearized perturbation $h_{\mu\nu}$, i.e.,

$$g_{\mu\nu} = \eta_{\mu\nu} + h_{\mu\nu}$$

with $|h_{\mu\nu}| \ll 1$ [33, 243]. For more details, we refer the reader to Refs. [58, 200, 243, 255]. Similar to electromagnetic waves, GW propagate with the speed of light [33, 58]. In contrast to electromagnetic waves that interact with electrically charged matter, GW interact with all kinds of matter. Moreover, GW are completely characterized by two different polarizations h_+ and $h_\times$ that differ by 45° [33, 58, 70, 243]. In Fig. 1.6, we show a schematic drawing of the two polarizations of GW.

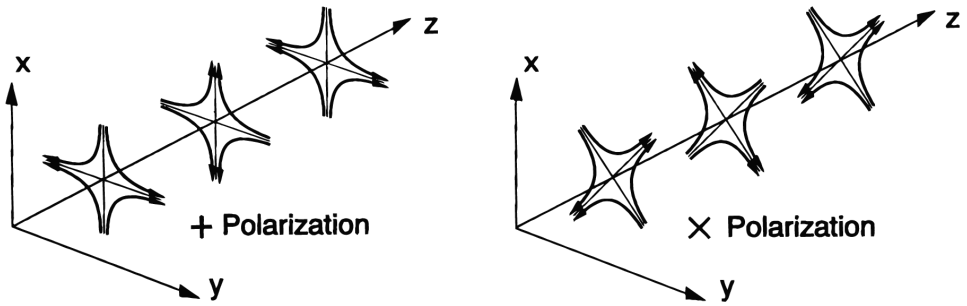

Figure 1.6.: Schematic representation of the propagation of GW with the two possible polarizations h_+ and $h_\times$. Figure taken from Ref. [9].

The weak interaction of GW with matter makes the detection of these waves a challenge [237]. Catastrophic events such as a merger of two compact objects like neutron stars and black holes are suitable systems to study GW [58, 70, 72, 238, 239]. A merger of two objects can be divided into three phases: inspiral, merger, and ringdown [58]. During the inspiral phase, the two objects move around each other in a spiral motion [70]. The objects get slowly closer to each other during a timespan of millions of years. When the distance between the neutron stars becomes small enough, tidal forces become relevant [228]. During the inspiral GW are emitted due to energy loss which manifests in the decrease of the orbital separation between the two objects. The GW frequency and amplitude increase with time [14]. The

amplitude is determined by the masses of the coalescing objects [14]. The coalescence of the neutron stars is the actual merger [228].

GW observations provide direct constraints for the EOS [70]. Ground-based GW detectors are organized as a network. Current detectors are LIGO (Laser Interferometer Gravitational-Wave Observatory, Hanford Site and Livingston, USA) [8, 9, 129], Virgo (Santo Stefano a Macerata, Italy) [11, 49], and GEO600 (Sarstedt, Germany) [295]. The KAGRA (Kamioka Gravitational Wave Detector, Gifu Prefecture, Japan) detector is in the commissioning phase and is expected to be online by the end of 2019 [19, 247]. The LIGO-India project is a planned third LIGO detector in India [275].

The underlying principle is a sophisticated laser interferometer with beam lines of several hundred meters or even kilometers length [58]. The perpendicularly arranged interferometer arms are realized by evacuated pipes. At the end of the arms, mirrors are installed. The laser beam entering the interferometer is split by a beam splitter. After repeated reflection within the arms, the beams are recombined. Eventually, the recombined beam hits a photodiode and the received intensity can be analyzed. The interferometer arm-lengths are modified when the interferometer is hit by GW. One of the interferometer arms is effectively shortened while the other arm is prolonged. This interaction ultimately changes the interference pattern and thus allows to study the GW signal [64, 199]. The network of GW detectors permit coincidence measurements and can provide access to the location of the source in the sky [237]. At this point it is worth to consider the weak interaction of GW with matter. For the example of the LIGO interferometer with 4 km arm lengths, the change of the arm lengths was $\sim 4 \times 10^{-16}$ cm for the first direct measurement of GW [199].

Before the objects coalescence, ground-based GW detectors are able to detect the last thousand orbits for which the frequencies range from about 10 Hz to 1000 Hz [70, 293]. GW detectors measure the intensity and phase of GW. The phase encodes information on the inspiraling objects [237]. GW signals are noisy [237]. In order to obtain observables from such signals, the signal of the inspiral is modeled which yields the so-called template. The template is then integrated against the observed signal. The maximal overlap of the observed waveform and the theoretically modeled template yield the best fit parameters [101, 228]. The fit parameters encode information on the observables of interest (cf. Ref. [101] and references therein for details). The actual modeling of the GW templates is subject of current research [39, 224].

The late inspiral phase is a formidable source of GW [237]. Nonetheless, the late inspiral phase poses inevitable challenges. The full general relativistic equations that are highly non-linear need to be solved. Further, relativistic hydrodynamics needs to be taken into account. Unknown observables like the spins alter the GW signal. Lastly, the frequency in the late inspiral phase tight before the actual merger lies outside the most sensitive frequency band of LIGO [101, 146]. In the early inspiral phase the objects are at large orbital separation, hence the objects can be treated as point particles [210]. The phase of the GW signal is then influenced by one parameter. This parameter is the tidal deformability λ that is the ratio of the induced quadrupole moment to the perturbing tidal field of the companion [101, 146]. The tidal deformability is sensitive to the internal properties of matter and permits thus to probe the EOS [218]. Moreover, previous studies indicate that the dimensionless tidal deformability $\bar{\lambda}$ might be more accurately measurable than the tidal deformability λ [167, 168] (cf. also Ref. [39]).

In the early phase of the inspiral, the frequency evolution is sensitive to the chirp mass $\mathscr{M}$ that is a particular combination of the component masses M_1 and M_2 [5, 237] (cf. Eq. (1.7)). Furthermore, the chirp mass $\mathscr{M}$ can be accessed by measuring the orbital period P_b and the orbital decay $\dot{P}_\mathrm{b}$ [237]. This ultimately provides information on the distance to the binary system [237]. The chirp mass $\mathscr{M}$ is best measurable with an accuracy of a few tenth of a percent [46, 70, 71, 100, 211, 215]. In later phases of the inspiral, effects of the gravitational interaction get larger and are related to the mass ratio

$$q = \frac{M_2}{M_1}\,, \tag{1.8}$$

where $M_1 \geq M_2$. Further influences are the spin-orbit and spin-spin coupling [70]. The GW phase is determined by the binary tidal deformability

$$\widetilde{\Lambda} = \frac{16}{13} \frac{(M_1 + 12M_2) M_1^4 \bar{\lambda}_1 + (M_2 + 12M_1) M_2^4 \bar{\lambda}_2}{(M_1 + M_2)^5}, \tag{1.9}$$

that depends on the individual masses as well as the individual tidal deformabilities $\bar{\lambda}_1$ and $\bar{\lambda}_2$ [101].

We have mentioned earlier that GW of a binary neutron star merger were observed [5]. In the first publication on the event GW170817 [5], source properties like the individual masses M_1 and M_2, the chirp mass $\mathscr{M}$, the mass ratio M_2/M_1, and the total mass M_{tot} were given among other observables. Further, estimations for the tidal deformability $\bar{\lambda}_{1.4\,M_\odot}$ for $1.4\,M_\odot$ neutron stars as well as the binary tidal deformability $\widetilde{\Lambda}$ were provided. In subsequent publications by the LIGO Scientific and Virgo collaborations [6, 7], the measured observables were corrected and we summarize the properties of GW170817 that we will use in our work in Table 1.1.

Table 1.1.: Properties of GW170817 provided by Refs. [6, 7].

parameter	
chirp mass $\mathscr{M}$	$1.186 \pm 0.001\,M_\odot$
primary mass M_1	$1.36 - 1.60\,M_\odot$
secondary mass M_2	$1.16 - 1.36\,M_\odot$
total mass M_{tot}	$2.73^{+0.04}_{-0.01}\,M_\odot$
mass ratio q	$0.73 - 1.00$
tidal deformability $\bar{\lambda}_{1.4\,M_\odot}$	190^{+390}_{-120}
binary tidal deformability $\widetilde{\Lambda}$	300^{+500}_{-190}

1.5 Nuclear matter and the nuclear equation of state

So far, we discussed neutron stars, their evolution, and how they can be observed. We also indicated that the EOS is a crucial ingredient for studying neutron stars, with important open problems, especially at high densities. In the present section, we provide more details on the EOS itself. Reviews on modern EOS and progress in the field can be found in Refs. [24, 120, 176, 177].

The EOS is a thermodynamic relation that depends on the interaction of the particles of which the considered matter consists [174]. For neutron stars the EOS of cold dense matter is required. Hereto, we introduce the baryon density

$$n = n_\text{n} + n_\text{p}, \tag{1.10}$$

with the densities of neutrons n_n and protons n_p. As discussed in Sec. 1.3, neutron stars consist mostly of neutrons and only a few percentage of protons and electrons. Thus, it is useful to introduce the proton fraction

$$x = \frac{n_\text{p}}{n}. \tag{1.11}$$

In the case of $x = 0.5$ the described matter is called *symmetric nuclear matter* and in the case of $x = 0$ it is *pure neutron matter*. Symmetric matter is a special case of matter since in that case neutrons and protons can be treated as a single species – the nucleon. The proton fraction is thus a parameter that

differentiates between neutron matter and symmetric matter. The energy difference between symmetric nuclear matter and pure neutron matter is described by the symmetry energy $S(n)$, which are defined as

$$S(n) = \frac{E}{A}(n, 0) - \frac{E}{A}(n, 0.5), \tag{1.12}$$

with the energy per baryon $E/A(n, x)$ of uniform nuclear matter with proton fraction x [173]. The energy per baryon of symmetric nuclear matter exhibits a minimum with respect to the density n at n_0 which is called *nuclear saturation*. In this context, saturation refers to the empirically found circumstance that the central density is approximately constant in heavy nuclei. This behavior of nuclear matter originates from the short range interaction and the strong repulsion at short distances of the nuclear force as well as the Pauli principle.

In the quadratic expansion, an expansion of $E/A(n, x)$ about $n = n_0$ and $x = 0.5$ yields

$$\frac{E}{A}(n, x) \approx \frac{E}{A}(n, 0.5) + (1-x)^2 S_2(n), \tag{1.13}$$

where we only consider terms up to the quadratic coefficient [83, 173, 174]. Given the case that contributions of higher orders are negligible, $S_2(n)$ can be identified with $S(n)$ and the expansion about n_0 yields

$$S(n) \approx S_v + \frac{L}{3}\left(\frac{n}{n_0} - 1\right) + \frac{K_{sym}}{18}\left(\frac{n}{n_0} - 1\right)^2, \tag{1.14}$$

where S_v denotes the volume symmetry energy, L is the slope parameter, and K denotes the *symmetry compressibility* and we have neglected higher order terms in density [173]. Nuclear experiments that determine masses of nuclei can constrain S_v and L [174]. In Fig. 1.7, we show experimental constraints on S_v and L complemented by theoretical constraints.

The symmetry compressibility K_{sym} is determined by the curvature of $E(n, x)$ at saturation density n_0. For increasing compressibility, the steepness of the EOS at high densities increases. Thus, EOS are categorized as *soft* or *stiff* EOS depending on whether the compressibility is small or large. Soft EOS predict smaller maximum neutron star masses compared to stiff EOS [112, 123].

The pressure of neutron star matter at saturation density can is given by L [253]. Hence, the parameters S_v and L have predictive power in terms of the radius of neutron stars [174]. For densities around nuclear saturation density and larger, neutron star matter consists mostly of neutrons [174, 181] (cf. Sec. 1.3). Hence, neutron star matter can be approximated by pure neutron matter [253]. Moreover, the pressure of pure neutron matter at densities below saturation density is correlated with the neutron skin thickness [54, 273]. Small neutron star radii are predicted for EOS models that also predict small neutron skin thicknesses [148].

Among others, experimental efforts to the EOS compromise measurements of nuclear masses and charge radii (cf. Refs. [157, 158, 159, 204]), giant dipole resonances and dipole polarizabilities (cf. Refs. [213, 256, 271]), and measurements of the neutron skin (cf. Refs. [149, 232]).

Lattimer and Prakash [176, 177] found that properties of the nuclear EOS predicted by realistic EOS models at about saturation density are correlated with neutron star observables. Specifically, the correlation found in Refs. [176, 177] relates the pressure at saturation density with the radius of neutron stars in the mass range of typical neutron stars.

A promising approach to the EOS is chiral EFT which provides a systematic expansion of the nuclear forces including an uncertainty estimation (cf. Ref. [193] and references therein), where the uncertainties originate in the many-body Hamiltonian and the applied many-body method [127, 155]. In general, the Hamiltonian of the many-body problem considers the contributions of the kinetic energy and the contributions of the two-nucleon, three-nucleon interactions, and so on. Available many-body

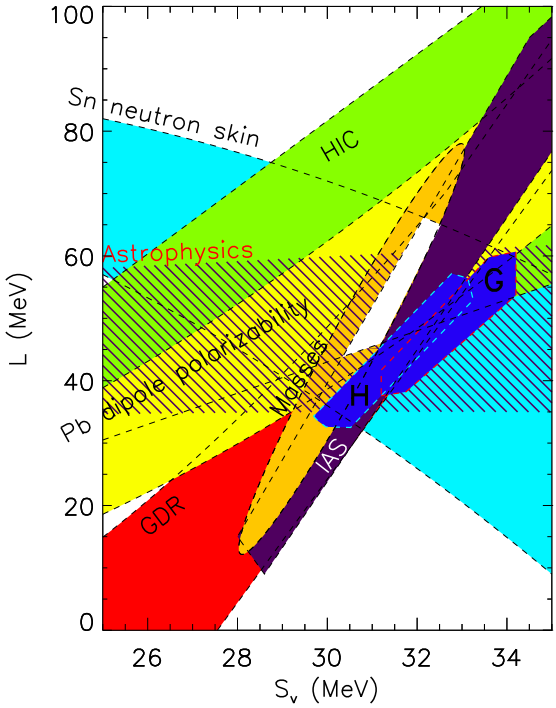

Figure 1.7.: Experimental constraints for L and S_v. The letters 'G' and 'H' represent the results from theoretical works of Gandolfi *et al.* [106] and Hebeler *et al.* [136], respectively. Figure taken from Ref. [181].

methods include many-body perturbation theory (MBPT, cf. Ref. [138] and also Refs. [136, 137]), quantum Monte Carlo (QMC) methods (cf. Refs. [106, 107, 110, 111, 192, 263]), coupled-cluster (CC, cf. Refs. [23, 124, 125]) method, and self-consistent Green's functions (SCGF, cf. Refs. [62, 63, 81, 231]) represent complementary frameworks. We provide a brief overview on MBPT in Sec. 2.2.1.1.

In summary, progress in experimental methods and setups yield further constraints for parameters of the EOS that ultimately yield constraints for the radius of neutron stars. On the other hand, astrophysical observations provide information on the tidal deformability and the prospect of moment of inertia measurements provide constraints for the radius of neutron stars. Moreover, the NICER mission will provide direct measurements of neutron star radii in the future.

The rest of the thesis is structured as follows: In Chap. 2, we particularly focus on the theoretical approaches to the EOS. We provide a short introduction to QCD – the underlying theory of strong interactions. In this regard, we also address the challenges that emerge in describing nuclear matter. Two distinct approaches – chiral effective field theory (EFT) and perturbative quantum chromodynamics (pQCD) – constitute suitable methods for accessing the EOS. While chiral EFT probes the low-density regime in neutron stars, pQCD provides information for densities much higher than in neutron stars. Ensuing, we provide relations among EOS properties required for the present work. We then present two models for the EOS which are used to extrapolate into the high-density regime. The piecewise polytropic EOS model constitutes an established direct parametrization of the EOS. However, this approach suffers from discontinuities of physical quantities such as the speed of sound. Hence, we discuss a speed of sound parametrization to construct the EOS. In Chap. 3, we discuss the theoretical framework for

calculating neutron star observables. We begin with a brief introduction to the basic concepts of GR and then discuss how the neutron star observables relevant for this work are calculated. Beginning with non-rotating neutron stars, we describe the approach to observables such as masses, radii, and binding energies. We then apply the Hartle-Thorne approximation to first order in the angular velocity of the neutron star such that we obtain access to the moment of inertia of slowly rotating neutron stars. By taking small external tidal perturbations into account, we access the tidal deformability of neutron stars. We then discuss the Hartle-Thorne approximation to second order which provides the quadrupole moment of neutron stars. Eventually, we address numerical issues with the presented structure equations that are given as functions of the radial coordinate. Hereto, we discuss a transformation of the independent variable such that all structure equations are parametrized in terms of the pseudo-enthalpy. In Chap. 4, we focus on non-rotating neutron stars. We explore the EOS and mass-radius space for both the piecewise polytropic EOS model and the speed of sound parametrization and provide a comparison of both models. Moreover, we examine the speed of sound and the binding energy of neutron stars. A special focus is put on correlations between EOS parameters and properties of typical neutron stars. We then discuss the inference of constraints for the EOS and the radius of neutron stars. Concerning this we apply simple compatibility cuts as a first step. Afterwards, we apply a more sophisticated approach by using Bayesian statistics [118]. In Chap. 5, we extend our considerations by investigating slowly rotating neutron stars, and examine the implications of moment of inertia measurements on the EOS. In Chap. 6, we explore properties of binary neutron star systems and tidal interactions. We investigate properties of neutron star mergers and include constraints from the pioneering observation of a binary neutron star merger in 2017. Our considerations include universal relations that are insensitive to details of the EOS. In Chap. 7, we summarize the present work and provide an outlook.

Throughout this thesis, we use natural units, i.e., $G = c = \hbar = 1$.

2 Theoretical description of the equation of state

The structure of neutron stars is determined by the hydrostatic equilibrium between the internal pressure and the gravitational force. The pressure in turn is given by the EOS. In the context of neutron stars, the EOS of strongly interacting matter up to densities exceeding several times nuclear saturation density and low temperatures is required. The density regime beyond nuclear saturation density is relevant for neutron stars and is, however, poorly understood so far [29, 60, 61]. The description of the interaction between the nucleons is the subject of current research. The current state of knowledge is that the nuclear force between nucleons is a residual force of the strong interaction between quarks which is described by QCD. However, QCD is highly non-perturbative at energies relevant for studying nuclear matter up to nuclear densities. Nonetheless, further approaches provide constraints for the density regimes below nuclear saturation density and asymptotically high densities provide information on the EOS. Chiral EFT constitutes an effective approach to nuclear forces at low energies exploiting symmetries and the symmetry-breaking pattern of QCD. Moreover, chiral EFT allows a systematic, model-independent access to nuclear forces. Nonetheless, the predictive power is limited by the restriction to low densities. On the other side of the spectrum of densities, perturbative QCD is applied to densities beyond $\sim 50\,\rho_0$. The density regime in between the chiral EFT regime and the perturbative QCD regime is therefore afflicted by significant uncertainties. We present two extrapolation methods for densities in between the extreme density regions. First, we discuss a piecewise polytropic EOS model as presented in Refs. [136, 137]. This approach allows to parametrize the EOS directly. Second, we discuss a parametrization of the speed of sound as introduced originally in Greif *et al.* [118] from which we infer the EOS.

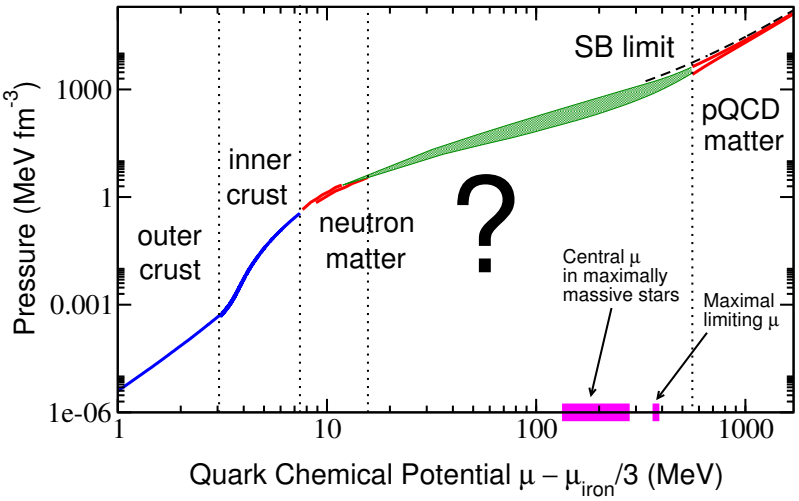

Figure 2.1.: Schematic representation of the EOS where the pressure is given as a function of the quark chemical potential. The vertical bands indicate the distinct regions inside a neutron star. The region marked with the question mark represents the regime of the EOS where polytropes as an extrapolation method were used (cf. Ref. [164]). Figure taken from Ref. [104].

In Fig. 2.1, we show a schematic representation of the EOS. Different density regimes are indicated, i.e., subnuclear densities (blue), nuclear densities (red), intermediate densities (green), and high densities (red), which we discuss in the following.

2.1 Equation of state of the outer and inner crust

In Sec. 1.3, we discussed the structure of neutron stars where we also put a focus on the crust of neutron stars. For densities below the neutron drip density, the EOS is well understood. First attempts to determine the ground-state properties of nuclear matter at densities below $\rho \approx 4.3 \times 10^{11}\,\mathrm{g\,cm^{-3}}$ were done by Salpeter [236]. In a following work, Baym *et al.* [31] made further improvements on the crust EOS. The revisions include improvements of the empirical mass formula. Modifications of the composition were considered by the implementation of effects of the lattice of nuclei [29, 31, 243]. The Baym-Pethick-Sutherland (BPS) EOS [31] describes the density regime of the outer crust of neutron stars. A pedagogical review of the mathematical implementation of the BPS EOS for the crust can be found in Ref. [243].

The density regime of the inner crust was explored by Negele and Vautherin [203]. The underlying idea was a separation of the matter into unit cells whereas Negele and Vautherin considered spherically symmetric cells [123, 203]. Charge neutrality was obtained by taking into account an equal number of protons and electrons for each cell. The energy per particle inside a cell was then minimized [203]. An extensive review of the physics of neutron star crusts can be found in Ref. [66].

2.2 Quantum chromodynamics

QCD is a relativistic quantum field theory and the underlying theory of strong interactions and as such part of the Standard Model of particle physics [193, 291]. QCD describes the interactions between quarks and gluons which are the fundamental degrees of freedom of the theory and the building blocks of hadrons which in turn are the relevant degrees of freedom of nuclear matter up to nuclear densities [93, 291]. Quarks are the fermionic matter fields and six species are known – the so-called *flavors*. The flavors are grouped into the light quarks *up*, *down*, and *strange* and the heavy quarks *charm*, *bottom*, and *top*. In Table 2.1, we provide the masses m, the electric charges q, and the isospins I_z of the quark flavors.

Table 2.1.: Masses m, electric charges q, and isospins I_z of the six known quark flavors. The flavors are distinguished into the light flavors (up, down, and strange) and the heavy flavors (charm, bottom, and top). Note that isospin is only associated with up and down flavors. Data taken from Ref. [257].

flavor	$m\,[\mathrm{MeV}]$	$q\,[e]$	I_z
up	$2.2^{+0.5}_{-0.4}$	$+\frac{2}{3}$	$+\frac{1}{2}$
down	$4.7^{+0.5}_{-0.3}$	$-\frac{1}{3}$	$-\frac{1}{2}$
strange	95^{+9}_{-3}	$-\frac{1}{3}$	–
charm	1275^{+25}_{-35}	$+\frac{2}{3}$	–
bottom	4180^{+40}_{-30}	$-\frac{1}{3}$	–
top	~ 170000	$+\frac{2}{3}$	–

The interaction is mediated via massless gauge bosons called gluons [93]. Every quark and every gluon has a corresponding antiparticle. Besides the electric charge, quarks carry also a strong charge

called color, i.e., red, green, or blue, whereas gluons carry both a color and an anticolor charge. The names of the color charges refer to additive color mixing. So far, only colorless systems were observed [93].

The coupling constant α_S depends on the energy scale [43, 145], i.e., $\alpha_S(Q^2)$. This property is called *asymptotic freedom*. In Fig. 2.2, we show a summary results from various experiments probing the strong coupling strength α_S. Perturbation theory provides reliable predictions for the observable of interest when the coupling strength is small enough [43].

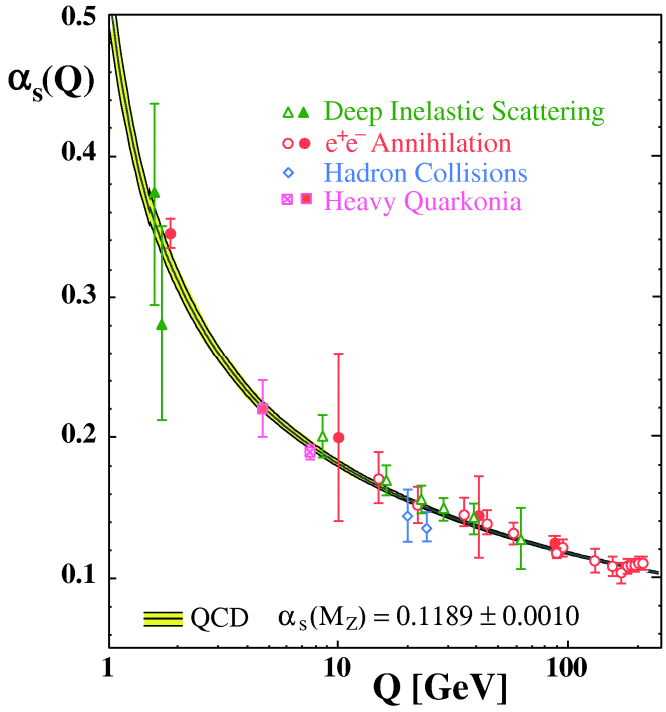

Figure 2.2.: The coupling strength α_S as a function of the energy scale Q. The data points represent results from different experimental approaches that probed the coupling strength. See Ref. [43] and references therein for more details. Figure taken from Ref. [43].

In the case of color-charged objects, the interaction is weak at short distances or equivalently at high-momentum transfer. This property of QCD is referred to as *asymptotic freedom* and quarks are weakly interacting [119, 193, 216]. Hence, α_S goes to zero for increasing energy which permits a perturbative treatment [254]. At large distances ($\gtrsim 1\,\text{fm}$) or equivalently low energies, the interaction is strong. Hence, QCD is in this energy regime highly non-perturbative [193].

Symmetries are an important concept in physics. In the context of QCD, chiral symmetry plays an important role. The light quarks are equal except for their masses in terms of the strong interaction [93]. The masses of the quarks are free parameters in QCD. Masses of typical hadrons are of the order of 1 GeV while the masses of the two lightest quarks – up and down quark – are of the order of only a few MeV (cf. Table 2.1). Hence, QCD can be studied in the limit of massless light quarks as a good approximation by neglecting the mass term of the two-flavor Lagrangian. It can be shown that the Lagrangian is invariant under separate unitary global transformations of the right- and left-handed quark fields [93]. Under this approximation the left- and right-handed quarks are completely decoupled [89, 93]. This symmetry is referred to as chiral symmetry. Chiral symmetry is, however, spontaneously broken, i.e., it is a symmetry of the Lagrangian but not of the ground state as realized, e.g., by a Mexican-hat shaped potential [93]. This can be seen from the fact that no parity doublets of hadrons exist [93]. If chiral symmetry was exact, for each hadron an identical hadron with identical quantum numbers except for the parity would exist

[93]. Goldstone's theorem (cf. Refs. [115, 116]) states that every generator of a spontaneously broken symmetry yields a massless excitation of the vacuum. Such excitations are called *Goldstone bosons*. In the case of the spontaneous breakdown of the chiral symmetry of QCD, the Goldstone bosons are identified with the pions [93]. Quarks are albeit not massless and the mass term of the Lagrangian causes that the symmetry is also explicitly broken [93]. Consequently, pions are not massless – pions are pseudo Goldstone bosons which explains their non-vanishing but compared to all other hadrons very small mass [284].

2.2.1 Chiral effective field theory constraints at low energies

The binding of nucleons into nuclei is caused by the nuclear force which is a residual force from the strong interaction comparable with the van der Waals force between molecules [93, 193]. However, the coupling constant α_S is of the order 1 in the case of the energy scales of nuclear physics [93]. Hence, nuclear forces are not directly accessible from QCD so far. Chiral EFT represents an effective approach to the nuclear force [193].

Chiral EFT is a systematic approach to study nuclear forces at low energies. We now provide a brief introduction to chiral EFT. A throughout discussion is out of the scope of this thesis, comprehensive introductions are provided by Refs. [89, 90, 92, 93, 127, 193, 194].

For setting up an EFT, the degrees of freedom for the relevant energy regime have to be identified. This leads to the identification of soft and hard scales. Within the relevant low-energy regime, the emerging symmetries need to be known. Moreover, the breaking-pattern, if existent, must be known. From this knowledge, the most general Lagrangian can be written down that is consistent with the symmetries and symmetry breaking pattern of the underlying theory. The effective Lagrangian is then expanded in low momenta. From the expansion the Feynman diagrams are then calculated [193].

In the seminal works [287, 288, 289] by Weinberg, chiral EFT was pioneered in the early 1990's (see also Ref. [286]). The degrees of freedom in chiral EFT are nucleons and pions. Pions constitute the Goldstone bosons of the broken chiral symmetry. Due to the low-energy scale of nuclear physics, quarks and gluons are not resolved. All heavier particles are integrated out [286]. The intermediate and long-range interaction is mediated via pion-exchange whereas the short range interaction is mediated by contact interactions [120]. Hence, a breakdown scale Λ_b for chiral EFT emerges which is given by heavier mesons such as the ρ-mesons, i.e., $\Lambda_b \sim 500\,\mathrm{MeV}$ [94].

The starting point of an EFT is to replace the Lagrangian $\mathscr{L}$ of the fundamental theory by an effective Lagrangian $\mathscr{L}_{\mathrm{eff}}$. In the case of QCD, the effective Lagrangian is the most general Lagrangian consistent with the relevant symmetries and the (broken) chiral symmetry of QCD [286]. The effective Lagrangian can be written as

$$\mathscr{L}_{\mathrm{eff}} = \mathscr{L}_{\pi\pi} + \mathscr{L}_{\pi\mathrm{N}} + \mathscr{L}_{\mathrm{NN}} + \dots , \tag{2.1}$$

where $\mathscr{L}_{\pi\pi}$ describes the dynamics among pions, $\mathscr{L}_{\pi\mathrm{N}}$ describes the interactions between pions and nucleons, $\mathscr{L}_{\mathrm{NN}}$ deals with the nucleon-nucleon contact interaction [193]. The effective Lagrangian consists of an infinite number of terms which exhibit an increasing number of derivatives and nucleon fields [287]. The terms can then be organized by using the expansion parameter Q that is defined by

$$Q = \max\left(\frac{q}{\Lambda_b}, \frac{m_\pi}{\Lambda_b}\right), \tag{2.2}$$

where q refers to the typical momentum of nucleons and $m_\pi \approx 140\,\mathrm{MeV}$ denotes the pion mass [91]. In chiral EFT, the pion mass and the breakdown scale represent the soft scale and the hard scale, respectively. The order of the diagrams is determined by a power-counting, where the Weinberg power-counting (cf. Refs. [287, 288]) is commonly used in chiral EFT. The orders are then sorted by Q^ν with

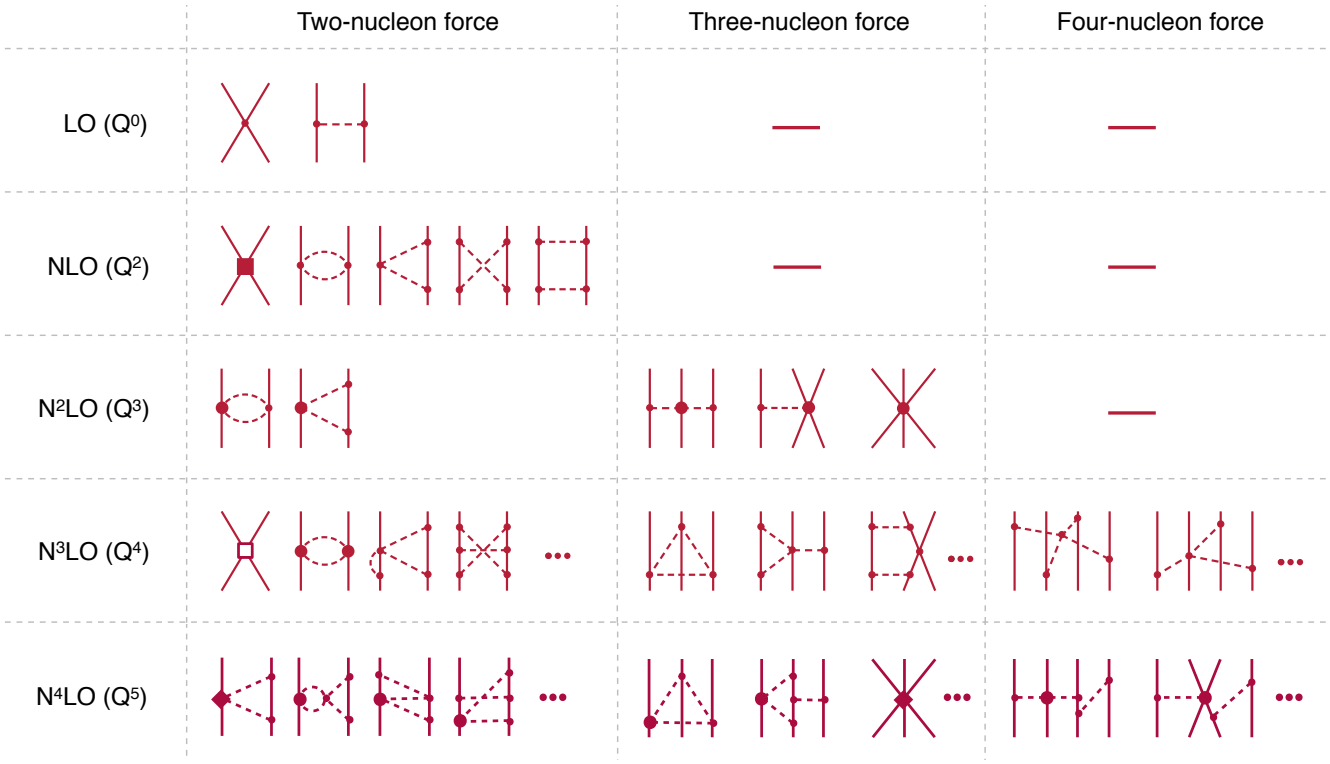

Figure 2.3.: Diagrammatic representation of the chiral forces. In the shown Feynman diagrams, the solid lines represent nucleons and the dashed lines represent pions. From top to bottom, the order ν of the chiral expansion increases, whereas LO refers to *leading order*, NLO refers to *next-to-leading order*, and so on. From left to right, the number of involved nucleons increases. Figure taken from Ref. [91].

the increasing integer ν, where $\nu = 1$ is forbidden [193]. The different orders are referred to as leading order (LO, $\nu = 0$), next-to-leading order (NLO, $\nu = 2$), next-to-next-to-leading order (N^2LO, $\nu = 3$), and so on. In Fig. 2.3, we show the hierarchy and the systematic ordering of the nuclear forces as determined by chiral EFT including the power-counting up to N^4LO. The predictive power of chiral EFT can be systematically improved by including higher orders [89].

The expansion involves unknown coupling constants which are referred to as *low-energy constants* (LEC) [93]. The LEC contain the information about the short-distance interaction and thus the high-energy regime that is not resolved within chiral EFT [93]. The LEC are usually fitted to nuclear observables [193].

2.2.1.1 From nuclear forces to the equation of state

In the context of neutron stars, the EOS of neutron-rich matter is required. Chiral EFT provides systematic access to the nuclear forces discussed above. The potentials represent the microscopic input to the many-body Schrödinger equation. The solution of the many-body problem, however, is not straight forward and many-body methods have to be applied. Various many-body methods are available, including MBPT, SCGF, CC, and QMC. In the following, we provide the basic ideas of MBPT, for more details also on the other methods, we refer the reader to Refs. [23, 62, 63, 81, 106, 107, 110, 111, 124, 125, 136, 137, 138, 192, 231, 263].

Starting point of all ab-initio methods is the general form of the Hamiltonian, i.e.,

$$H = T + V = T + V_{\mathrm{NN}} + V_{\mathrm{3N}} + V_{\mathrm{4N}} + \dots , \tag{2.3}$$

where T denotes the contribution of the kinetic energy and V denotes the contribution of the interaction, while V_{NN} is the two-nucleon interaction, V_{3N} the three-nucleon interactions, and V_{4N} the four-nucleon interactions. In MBPT, the interaction of the nucleons is treated as a perturbation. Thus, the contribution from the kinetic energy represents the lowest order term to the energy [261]. The ground state of the unperturbed system T is obtained by considering the free system of which the solutions are known, i.e., $T\,|\Phi_n^{(0)}\rangle = E_n^{(0)}\,|\Phi_n^{(0)}\rangle$ with the energy levels $E_n^{(0)}$ and eigenstates $|\Phi_n^{(0)}\rangle$. In the case of infinite matter the single particle states occupy all plane-wave states up to a given Fermi momentum k_{F}, which is related to the density of the system via

$$\rho = g\,\frac{k_{\mathrm{F}}^3}{6\pi^2}\,,$$

where g is the spin-isospin degeneracy. The corrections $E^{(1)}$ at first order in the interaction are then obtained by calculating the expectation value

$$E^{(1)} = \sum_{\alpha} \langle\alpha|\,V\,|\alpha\rangle \tag{2.4}$$

$$= \sum_{\alpha_{\mathrm{NN}}} \langle\alpha_{\mathrm{NN}}|\,V_{\mathrm{NN}}\,|\alpha_{\mathrm{NN}}\rangle + \sum_{\alpha_{\mathrm{3N}}} \langle\alpha_{\mathrm{3N}}|\,V_{\mathrm{3N}}\,|\alpha_{\mathrm{3N}}\rangle + \sum_{\alpha_{\mathrm{4N}}} \langle\alpha_{\mathrm{4N}}|\,V_{\mathrm{4N}}\,|\alpha_{\mathrm{4N}}\rangle \tag{2.5}$$

$$= E_{\mathrm{NN}}^{(1)} + E_{\mathrm{3N}}^{(1)} + E_{\mathrm{4N}}^{(1)}\,, \tag{2.6}$$

where $|\alpha\rangle$ denote all occupied NN, 3N, and 4N states of the free system. The contributions $E_{\mathrm{NN}}^{(1)}$, $E_{\mathrm{3N}}^{(1)}$, and $E_{\mathrm{4N}}^{(1)}$ are the first-order corrections for the energy. For higher-order corrections and more details on perturbation theory, we refer the reader to Ref. [99].

Presently, it is possible to systematically compute all contributions from NN and 3N interactions up to third order, while NN are up to fourth order (cf. Ref. [82]).

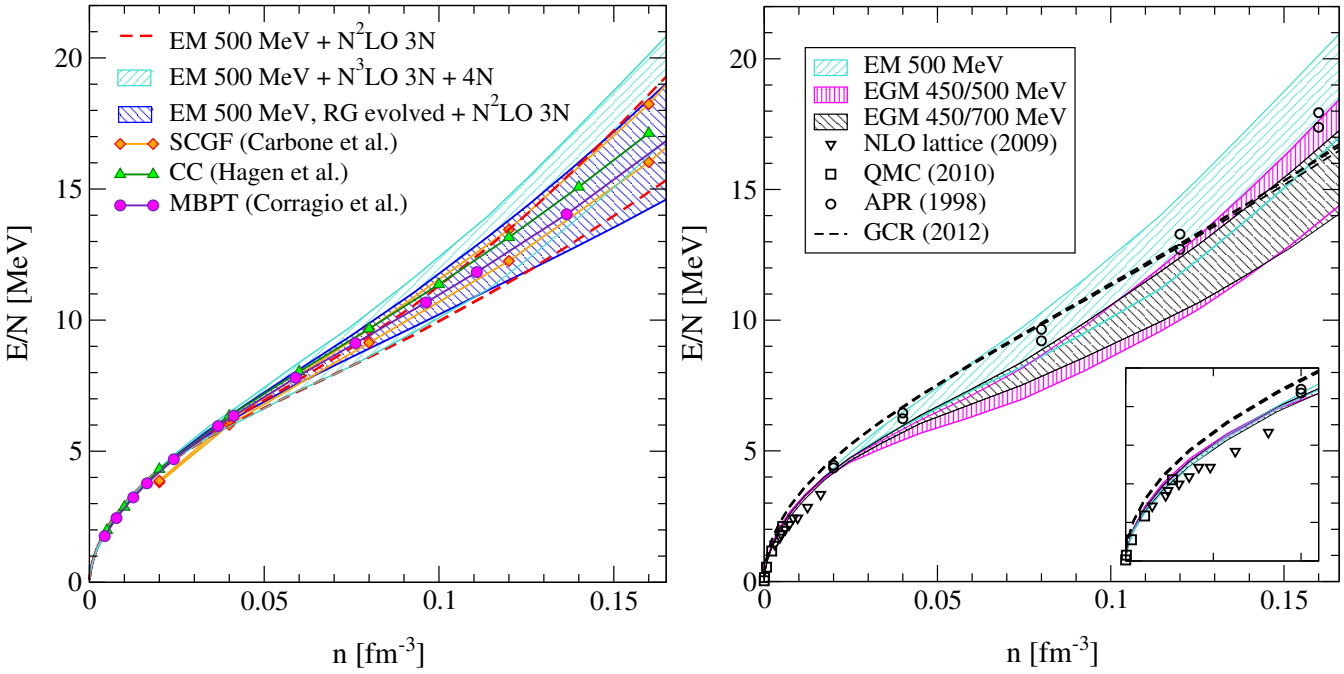

Figure 2.4.: Energy per particle E/N as a function of the particle density n based on chiral EFT and various many-body methods. *Left panel*: Chiral EFT interactions with the 500 MeV N^{3}LO potential at the NN level [88]. *Right panel*: Complete N^{3}LO calculation [163, 264]. Figure taken from Ref. [135] (cf. also Ref. [137]).

In Fig. 2.4, the energy per particle as a function of the particle density is shown based on various many-body methods. In the left panel of Fig. 2.4, the results are based on chiral EFT interactions with the 500 MeV N^3LO potential at the NN level [88] and the results shown in the right panel of Fig. 2.4 are based on the first complete N^3LO calculation [163, 264]. For details, we refer the reader to Ref. [135] and references therein. The presented results in the left panel of the figure show that the results for the energy per particle up to nuclear saturation density are consistent for various many-body methods. The results shown in the right panel of the figure show that the obtained energy per particle agrees for different interactions.

2.2.2 Nuclear equation of state at intermediate densities

So far, we provided an overview of the nuclear EOS up to densities of about nuclear saturation density. In this density regime, chiral EFT starts to break down and is no longer applicable. The strong coupling constant α_S is still too large for applying perturbation methods in the strong coupling. As a consequence, other methods have to be considered. Available extrapolation methods are the direct parametrization of the EOS by using a piecewise polytropic expansion or the indirect parametrization by using a model for the speed of sound inside neutron stars that can be constrained by neutron star observations. Such extrapolation methods play a key role in this thesis such that we dedicate the last section of the present chapter for a thorough discussion.

2.2.3 Perturbative quantum chromodynamics constraints at high densities

In Sec. 2.2, we gave a brief introduction of QCD. In the subsequent section, we discussed chiral EFT as a suitable tool for studying the EOS at nuclear densities. In the present section, we focus on the high-energy regime where the asymptotic freedom of QCD permits perturbative approaches to the EOS. We now give a brief introduction to pQCD and how this approach can be used to study neutron star cores and thus the EOS of nuclear matter. A comprehensive discussion of the field can be found in Ref. [160]. However, the expansion of the EOS towards densities relevant in neutron stars requires the consideration of high orders in the coupling constant [279].

The work of Kurkela *et al.* [165] extended previously achieved efforts in pQCD. Such calculations consider vanishing quark masses and were improved by including a non-vanishing strange quark mass (cf. Refs. [164, 165] and also references therein). Kurkela *et al.* [164] showed that further improved constraints for the EOS of neutron star matter can be achieved by including constraints of pQCD. Hereto, the authors used results from chiral EFT at low densities (cf. Ref. [264]) and imposed them on the EOS to approach the pQCD results in the limit of high densities. The initially found pQCD results from Refs. [165, 166] are given in a compact form via fitted functions in Ref. [103]. The fitted pressure P_{QCD} as a function of the baryon chemical potential μ_b is given by

$$P_{\mathrm{QCD}}(\mu_\mathrm{b}) = P_{\mathrm{SB}}(\mu_\mathrm{b})\left(c_1 - \frac{d_1 X^{-\nu_1}}{(\mu_\mathrm{b}/\mathrm{GeV}) - d_2 X^{-\nu_2}}\right) \tag{2.7}$$

with the pressure of massless, non-interacting quarks [103]

$$P_{\mathrm{SB}}(\mu_\mathrm{b}) = \frac{3}{4\pi^2}\left(\frac{\mu_\mathrm{b}}{3}\right)^4 . \tag{2.8}$$

In the expression given above, c_1, d_1, d_2, ν_1, and ν_2 denote fit parameters and $X \equiv 3\bar{\Lambda}/\mu_\mathrm{b}$ is a dimensionless parameter. The quantity $\bar{\Lambda} = (2/3)\,\mu_\mathrm{b}$ is the renormalization scale [103]. In Ref. [103], the fit parameters are determined in the regime $\mu_\mathrm{b} < 2\,\mathrm{GeV}$, $P(\mu_\mathrm{b}) > 0$, and $X \in [1,4]$ and read

$$c_1 = 0.9008\,, \quad d_1 = 0.5034\,, \quad d_2 = 1.452\,, \quad \nu_1 = 0.3553\,, \quad \nu_2 = 0.9101\,.$$

In the context of the nuclear EOS and pQCD, the speed of sound of the matter inside a neutron star is subject of current research. The matter inside a neutron star fulfills the causality constraint which means that the speed of sound is required to be smaller than the speed of light. However, the speed of sound is a property of the EOS and has in turn an impact on the structure of the neutron star. A review article by Canuto [60] reveals the ambiguity of the limit of the speed of sound at high densities. By considering an ultra-relativistic non-interacting gas of fermions, the pressure P asymptotically approaches $\epsilon/3$ for large densities and the speed of sound approaches therefore $c/\sqrt{3}$ [123, 285]. Results from pQCD support this limit while further suggesting that the speed of sound approaches $c/\sqrt{3}$ from below [103, 165]. This can be seen from Eq. (2.7).

2.3 Extrapolation methods for the equation of state

In the present section, we provide a thorough discussion of two extrapolation methods of the EOS beyond nuclear densities. First, we review useful relations for the EOS. We then discuss the polytropic EOS and extend our considerations to a piecewise polytropic EOS model as presented in Ref. [137]. Subsequently, we present an indirect parametrization of the EOS using a speed of sound model as introduced in our paper, Ref. [118].

2.3.1 Properties of the nuclear matter equation of state

So far, we discussed in this chapter the fundamental theory of strongly interacting matter and different approaches to deal with nuclear forces. In this thesis, we use two extrapolation methods to explore the density regime beyond nuclear densities of the EOS in a systematic manner. Hereto, we require several thermodynamic relations that we shall present in this section.

A relation between the pressure P and the particle density n is given by the first law of thermodynamics under the assumption of $T = 0$ and reads [58, 122]

$$P(n) = n^2 \frac{\mathrm{d}}{\mathrm{d}n}\left(\frac{\epsilon}{n}\right) \tag{2.9}$$

for a given energy density ϵ. This allows us to express the EOS as a one-parameter EOS $\epsilon(P)$ which is sufficient to study cold neutron stars [130, 186]. Further, we note that the condition $\epsilon(P) \geq 0$ has to be fulfilled and the EOS has to be a monotonically increasing function, i.e., $\mathrm{d}\epsilon/\mathrm{d}P \geq 0$ such that the EOS is thermodynamically stable [186].

For a given EOS, the adiabatic index is defined as [123, 186]

$$\Gamma = \frac{\epsilon + P}{P}\frac{\mathrm{d}P}{\mathrm{d}\epsilon}\,. \tag{2.10}$$

The condition $\Gamma > 0$ must be fulfilled to ensure thermodynamic stability [186]. Monotonicity of Γ does not need to be fulfilled [186]. Moreover, the adiabatic index is a measure for the stiffness of an EOS [123]; an EOS exhibits softening for small Γ and stiffening for large Γ.

For some applications it is useful to parametrize the EOS as a function of the pseudo-enthalpy h [186], which is given by [123, 185]

$$h(P) = \int_0^P \frac{\mathrm{d}P'}{\epsilon(P') + P'} \tag{2.11}$$

and is a dimensionless quantity. In the context of neutron stars, the pseudo-enthalpy decreases monotonically from the center of the neutron star to the surface where h ultimately vanishes [123]. The

expression given above allows us to rewrite the EOS in terms of the pseudo-enthalpy, i.e., $P(h)$ and $\epsilon(h)$. The particle density expressed as a function of the pseudo-enthalpy is given by [123]

$$n = \frac{\epsilon + P}{\mathrm{e}^h m_\mathrm{b}} \,. \tag{2.12}$$

The speed of sound of the nuclear EOS is a crucial ingredient in exploring the uncertain density regime beyond nuclear saturation density. The speed of sound c_s as a function of the energy density ϵ is given by [170, 285]

$$\frac{\mathrm{d}P}{\mathrm{d}\epsilon} = c_\mathrm{s}^2 \,. \tag{2.13}$$

Fundamental constraints like the requirement of *causality* are usually imposed which means that the speed of sound has to be lower than the speed of light [123]. However, past works investigated whether superluminal EOS violate the causality constraint, cf. Refs. [47, 48, 234]. In Sec. 2.2.3, we discussed the speed of sound for asymptotically high densities. The knowledge of the EOS at low densities and the conformal limit provided by pQCD allow in principle various interpolation methods for the density region in between. This statement refers in particular to the question whether the limit of $c/\sqrt{3}$ can be exceeded or not. However, the work of Bedaque and Steiner [34] showed that the conformal limit has to be exceeded at densities relevant for neutron stars to fulfill the maximum mass constraint of reproducing $2\,M_\odot$ neutron stars.

2.3.2 Piecewise polytropic expansion

In the following, we explore the EOS at densities larger than nuclear densities and discuss an extrapolation method for the EOS to this density regime. The approach of using polytropes or piecewise polytropic expansions has been established, cf. Refs. [38, 136, 137, 207, 244, 250, 251, 278, 304]. In the following, we summarize the method of piecewise polytropic expansion presented by Read *et al.* [225]. A polytropic EOS as a function of the mass density $\rho = mn$ is given by

$$P(\rho) = K\rho^\Gamma \,, \tag{2.14}$$

with the adiabatic index Γ and a constant K. The adiabatic index Γ adjusts the stiffness of the EOS (cf. Sec. 2.3.1). The EOS is then determined by using the first law of thermodynamics for $T = 0$, i.e.,

$$\mathrm{d}\frac{\epsilon}{\rho} = -P\,\mathrm{d}\frac{1}{\rho} \,, \tag{2.15}$$

where we insert Eq. (2.14) and solve the integral [225]. We obtain

$$\epsilon(\rho) = (1+a)\,\rho + \frac{1}{\Gamma - 1} K\rho^\Gamma \,, \tag{2.16}$$

with the constant a which is determined by taking into account that ϵ/ρ gets equal to 1 for vanishing ρ [225].

We extend now our considerations to piecewise polytropic EOS and assume that the EOS is known for densities below a fiducial density ρ_0. The density space is divided into distinct intervals

$$\rho_0 < \rho_1 < \rho_2 < \dots \,,$$

whereby each polytropic segment i has an individual K_i and Γ_i [225]. The mass density interval is then set by

$$\rho_{i-1} \leq \rho \leq \rho_{i+1} \,.$$

Furthermore, the cases $\Gamma_i \neq 1$ and $\Gamma_i = 1$ must be considered separately from each other. Similar to the polytropic EOS, we solve Eq. (2.15) by inserting Eq. (2.14) under the consideration of Γ_i. For $\Gamma_i \neq 1$ the energy density is given by

$$\epsilon(\rho) = (1 + a_i)\rho + \frac{K_i}{\Gamma_i - 1}\rho^{\Gamma_i} \tag{2.17}$$

with the constants

$$a_i = \frac{\epsilon(\rho_{i-1})}{\rho_{i-1}} - 1 - \frac{K_i}{\Gamma_i - 1}\rho_{i-1}^{\Gamma_i - 1} \,, \tag{2.18}$$

$$K_i = \frac{P(\rho_{i-1})}{\rho_{i-1}^{\Gamma_i}} \,, \tag{2.19}$$

where we used that the energy density and the pressure have to be continuous. For $\Gamma_i = 1$, the energy density is given by

$$\epsilon(\rho) = (1 + a_i)\rho + K_i \rho \ln \rho \tag{2.20}$$

with the constants

$$a_i = \frac{\epsilon(\rho_{i-1})}{\rho_{i-1}} - 1 - K_i \ln \rho_{i-1} \,, \tag{2.21}$$

$$K_i = \frac{P(\rho_{i-1})}{\rho_{i-1}} \,. \tag{2.22}$$

With the approach described above, the EOS can be determined in the form $P(\epsilon)$ as well as in terms of the pseudo-enthalpy h by applying Eq. (2.11).

The method discussed above was used in the works by Hebeler *et al.* [136, 137]. In this thesis, we reproduce results from Ref. [137] and extend the presented framework by additionally considering slowly rotating neutron stars and tidal interactions in binary systems. We therefore summarize this approach in the following. According to Refs. [136, 137], the EOS is assumed to be known up to a fiducial density ρ_1. Furthermore, the density regime below ρ_1 is divided into two parts. For densities up to $\rho_{\text{crust}} = 0.5\,\rho_0$ the BPS crust EOS [31, 203] is used. According to Ref. [137], the choice of ρ_{crust} is robust which can be seen in Fig. 2.5 which shows that the resulting EOS for the BPS crust and the chiral EFT band are in good agreement. In the density region between ρ_{crust} and $\rho_1 = 1.1\,\rho_0$, results from chiral EFT interactions are applied [136, 137]. At this point, we emphasize that the data for the chiral EFT band provided in Ref. [137] only describes the envelope of the uncertainty band. Hence, the band is described by two distinct EOS to which we refer as the lower and upper limit of the chiral EFT band for the remainder of this work. In the context of the EOS, lower and upper limit refer to $P(\rho)$ and $P(\epsilon)$, respectively. For densities beyond ρ_1, the EOS is extrapolated by using the piecewise polytropic expansion as described above. In Ref. [136] a piecewise polytropic expansion with two segments was used and the obtained results were extended by a third segment in Ref. [137]. The extended approach showed no sizable changes in the spread of neutron star radii such that no significant changes are expected for additional polytropic segments [137].

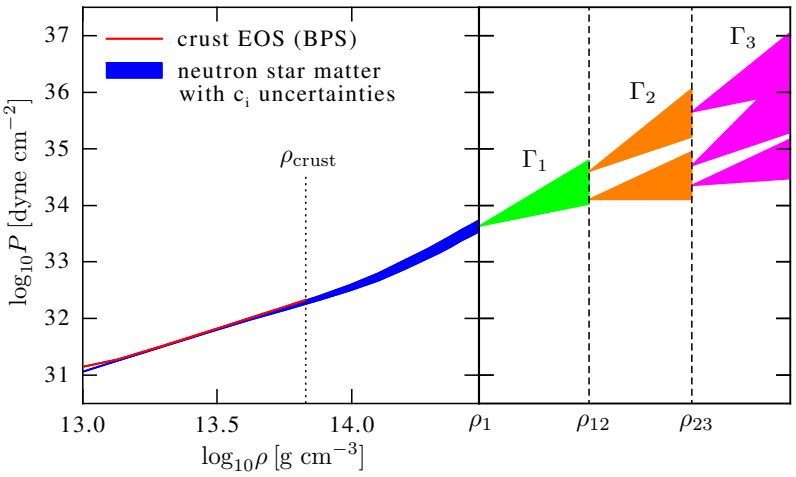

Figure 2.5.: Pressure P as a function of the energy density ϵ. The schematic representation of the EOS model shows the BPS crust EOS [31, 203] as a red line and the chiral EFT uncertainty band (cf. Ref. [136]) as a blue band. Further, the transition density ρ_{crust} that marks the transition from the crust EOS to the chiral EFT band is shown. The density ρ_1 indicates then the transition to the piecewise polytropic expansion. The triangular forms indicate the spread in the adiabatic indices Γ_1, Γ_2, and Γ_3. Not shown explicitly is that the transition densities ρ_{12} and ρ_{23} are also varied in the discussed approach. Figure taken from Ref. [137].

The three density regions are $1.5\,\rho_0 \leq \rho < \rho_{12}$, $\rho_{12} \leq \rho < \rho_{23}$, and $\rho_{23} \leq \rho < \rho_{\text{max}}$, with the transition densities ρ_{12} and ρ_{23} and the maximum considered density $\rho_{\text{max}} \approx 8.3\,\rho_0$ [137]. We further adapt the ranges for the adiabatic indices from Ref. [137], i.e., $1.0 \leq \Gamma_1 \leq 4.5$, $0 \leq \Gamma_2 \leq 8.0$, and $0.5 \leq \Gamma_3 \leq 8.0$. The chiral EFT band predicts at ρ_1 a range of about $2.25 - 2.50$ for the adiabatic index Γ which is the reason for the rather restrictive the range of Γ_1 in comparison with Γ_2 and Γ_3 [137]. The presented parameter space allows phase transitions when $\Gamma_2 = 0$ at intermediate densities. For the third polytropic segment no phase transitions are allowed [137].

A schematic presentation of the approach is shown in Fig. 2.5. In the density region below ρ_1, the BPS crust EOS as well as the chiral EFT band are shown. Further, the transition density ρ_{crust} is shown that marks the transition between the BPS crust EOS to the chiral EFT band. For densities beyond ρ_1 the piecewise polytropic expansion is indicated by triangles which are separated by the transition densities ρ_{12} and ρ_{23}. This can be understood by considering that polytropes are power functions and Fig. 2.5 shows both axes on a logarithmic scale.

The EOS that are built using the approach discussed above have to fulfill two further constraints to be physically reasonable. On the one hand, every EOS has to be causal over the whole density regime inside the neutron star. On the other hand, the predicted maximum mass must be at least $1.97\,M_\odot$ [137]. This mass constraint refers to the lower limit of the 1σ error of the heaviest observed neutron star PSR J0348 + 0432 [16].

2.3.3 Parametrization of the equation of state using a speed of sound model

In this thesis, we consider an additional approach to the EOS beyond nuclear densities. The construction of the piecewise polytropic EOS exhibits discontinuities in the speed of sound. This can be illustrated by the definition of the speed of sound given in Eq. (2.13) and the expressions for the polytropic expansion as presented in Sec. 2.3.2. Another parametrization of the speed of sound in order to obtain the EOS was recently done by Tews *et al.* [262].

We summarize in the following the approach originally introduced in our paper, Ref. [118]. The idea is to parametrize the speed of sound as a function of the energy density and deduce the EOS from this parametrization. As for the piecewise polytropic EOS model (cf. Sec. 2.3.2), we assume that the EOS is known for densities below a fiducial density $\rho_1 = 1.1\,\rho_0$. Following the approach presented in Sec. 2.3.2, the EOS coincides with the BPS crust EOS [31, 203] and the chiral EFT band [136, 137] for densities up to ρ_1.

We include a logistic function to fulfill the pQCD limit for high densities. Additionally, we include a Gaussian which allows the speed of sound to exceed $c/\sqrt{3}$ at intermediate densities. The complete parameterization is then given by

$$c_s^2(\bar{\epsilon}) = a_1 \mathrm{e}^{-\frac{1}{2}\frac{(\bar{\epsilon}-a_2)^2}{a_3^2}} + a_6 + \frac{\frac{1}{3}-a_6}{1+\mathrm{e}^{-a_5(\bar{\epsilon}-a_4)}}\,, \tag{2.23}$$

where $\bar{\epsilon} = \epsilon/(m_\mathrm{N}\cdot n_0)$ is a dimensionless energy density and $m_\mathrm{N} = 939.565\,\mathrm{MeV}$ denotes the nucleon mass. The parameters a_1, a_2, a_3, a_4, and a_5 are free parameters of the model and we present the parameter space in Table 2.2. We tested the limits of the parameters to ensure that the EOS model covers a sufficiently large spectrum in the EOS space [118]. The parameter a_6 is fixed by matching to the chiral EFT band from Ref. [137] using a χ^2 fit. The energy density and the speed of sound of the chiral EFT band at ρ_1 are required for the matching, i.e.,

$$\begin{aligned}
&\text{lower limit}: \quad \epsilon(\rho_1) = 167.8\,\mathrm{MeV\,fm^{-3}}\,, \qquad c_s^2(\rho_1)/c^2 = 0.034\,,\\
&\text{upper limit}: \quad \epsilon(\rho_1) = 168.5\,\mathrm{MeV\,fm^{-3}}\,, \qquad c_s^2(\rho_1)/c^2 = 0.055\,.
\end{aligned}$$

The matching ensures a continuous transition from the speed of sound given by the chiral EFT band to the speed of sound given by the parametrization.

Table 2.2.: Parameters for the speed of sound model given in Eq. (2.23) according to our paper, Ref. [118]. The parameter a_6 is not listed as this is not a free parameter. It is fixed by matching the the speed of sound extrapolation continuously to the speed of sound given by the chiral EFT band. For details see the text.

parameter	range
a_1	$0.1-1.5$
a_2	$1.5-12$
a_3/a_2	$0.05-2$
a_4	$1.5-37$
a_5	$0.1-1$

We impose further constraints on the resulting EOS from the model introduced above. Every EOS has to predict a maximum neutron star mass of at least $1.97\,M_\odot$ which is the lower limit of the 1σ error bar in the case of PSR J0348 + 0432 [16]. EOS that violate the mass constraint are discarded. Furthermore, causality has to be fulfilled for each EOS over the whole density regime in the interior of neutron stars. For asymptotically high densities, we impose that c_s^2 must converge to 1/3 from below.

Following Ref. [118], we allow phase transitions by setting $c_s^2 = 0$ whenever a considered parameter set results in negative c_s^2 values for a certain energy density range. For densities $n \leq 1.5\,n_0$ we assume that the bulk properties of matter can be described as a normal Fermi liquid. In Landau Fermi liquid theory (FLT) [32], the speed of sound is given by

$$c_{s,\mathrm{FLT}}^2(n) = \frac{1+F_0}{m_\mathrm{N}^*/m_\mathrm{N}}\frac{1}{3m_\mathrm{N}^2}\left(3\pi^2 n\right)^{\frac{2}{3}}\,, \tag{2.24}$$

where F_0 denotes the spin-independent and isotropic ($l = 0$) Landau parameter characterizing particle interactions. In FLT, nucleons are described in terms of effective degrees of freedom, so-called quasi-particles, with effective mass m_N^*. The dimensionless Landau parameter F_0 is expected to be attractive, and calculations for neutron matter suggest $F_0 \approx -0.5(2)$ as well as $m_N^*/m_N \approx 0.9(2)$ at saturation density [240, 241]. Moreover, both $1 + F_0$ and m_N^*/m_N are expected to be of order one. Given the above considerations, it is very conservative to assume

$$\frac{1+F_0}{m_N^*/m_N} \leq 3$$

up to $1.5\,n_0$. This implies

$$c^2_{s,\,\mathrm{FLT}}(n) = \frac{1}{m_N^2}\left(3\pi^2 n\right)^{\frac{2}{3}} . \tag{2.25}$$

We use Eq. (2.25) to determine a forbidden area for the speed of sound in the density regime up to $n = 1.5\,n_0$.

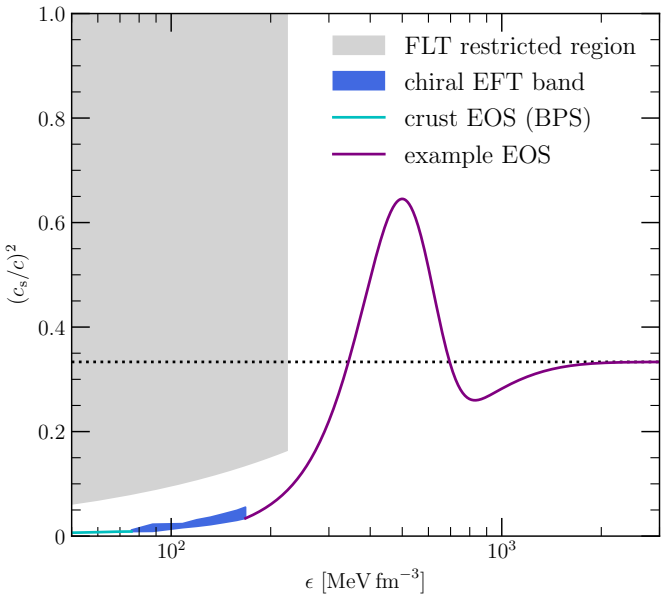

Figure 2.6.: The squared speed of sound c_s^2 as a function of the energy density ϵ. The black dotted horizontal line indicates the asymptotic limit from pQCD. The gray box shows the constraint from FLT for densities up to $1.5\,\rho_0$. We present an exemplary EOS that is matched to the lower limit of the chiral EFT band. The figure has been modified from Ref. [118].

In Fig. 2.6, we show an example EOS for one chosen set of parameters for an illustrative purpose. This figure features also the restricted area determined by the FLT constraint given in Eq. (2.25).

In contrast to our work, Tews *et al.* [262] consider two transition densities, i.e., $\rho_1 = 1.1\,\rho_0$ and $\rho_1 = 2\,\rho_0$. Moreover, the authors consider two fit parameters for the matching of the extrapolation to the low-density EOS. These two parameters are determined by fitting the speed of sound and its derivative. The speed of sound parametrization in Ref. [262] considers also a Gaussian to exceed the conformal limit of $c/\sqrt{3}$ at intermediate densities but the authors consider additionally a skewness parameter for the Gaussian.

3 Theoretical description of neutron stars

The present chapter provides the mathematical framework to calculate neutron star observables. Hereto, we provide a brief introduction to GR which constitutes an appropriate framework for studying neutron stars. Further, we provide an in-depth discussion of the calculation of neutron star observables. We begin with the consideration of spherical symmetric, non-rotating stars which provides access to the masses and radii of neutron stars. We extend this approach by determining the binding energy. However, neutron stars are actually rotating objects such that spherical symmetry is inherently broken. We therefore consider slowly rotating neutron stars using the Hartle-Thorne approximation. Hereto, we consider an expansion in the angular velocity to first order such that slow rotation is treated as a small perturbation of the non-rotating neutron star [130]. This allows us to calculate the moment of inertia. Within the scope of the slow-rotation approximation, the moment of inertia affects the speed of rotation for a fixed angular momentum as well as the rotational energy [131, 297]. We then extend our approach by considering binary systems which allow us to calculate the tidal deformability[1]. This observable measures how easily a neutron star can be deformed due to the tidal forces induced by a companion [147, 167, 300]. Further, we use a truncation at second order which opens the access to study the quadrupole moment of neutron stars within the Hartle-Thorne approximation. The quadrupole moment determines to what extend the neutron star is deformed by the existence of a companion [297].

Lastly, we present a numerical framework to determine the neutron star observables we discuss in this chapter. Hereto, we parametrize the EOS as a function of the pseudo-enthalpy and transform all necessary differential equations in terms of this dimensionless quantity.

3.1 General relativity

In this thesis, we assume GR is a suitable theory of gravity for the description of neutron stars. In the present section, we provide a brief introduction into GR and how this theory is applied in studying neutron stars. A throughout discussion of GR is beyond the scope of this thesis but we sketch the ideas and concepts that are required. Details can be found in Refs. [112, 113, 200, 243, 255, 285].

GR was postulated by Albert Einstein in 1915 [85, 86] as an extension to special relativity that was postulated as well by Einstein ten years earlier in 1905 [84]. A brief synopsis of the history of GR and Einstein's path to establishing this theory can be read in Ref. [200].

Besides GR, alternative theories of gravity are studied. However, GR passed all experimental tests with flying colors so far. Will [293] provides a throughout review on tests of GR and also an overview on alternative theories of gravity, see also references therein. The first three tests were suggested by Einstein himself, namely the gravitational redshift of light, the light deflection by massive bodies, and the perihelion precession of Mercury, and probe the weak-field regime [113]. Among the most precise tests are the investigation of the weak-field gravity conditions in the solar system [41, 294].

GR is a geometric theory of gravity [58, 243]. Consequently, the movement of a particle is not caused by gravitational forces but by the curvature of spacetime [58, 123]. The curvature of spacetime is dictated by the presence of masses [123]. The spacetime can be described with three spacial coordinates and one time coordinate [243]. The distance between two events is determined by

$$\mathrm{d}s^2 = g_{\mu\nu}\,\mathrm{d}x^\mu \mathrm{d}x^\nu\,, \tag{3.1}$$

[1] Some authors refer to this observable as *tidal polarizability*.

where x^μ denote the coordinates in spacetime and $g_{\mu\nu}$ the components of the metric tensor [113, 243]. The connection between the geometry of spacetime and the interaction with masses and energy is expressed by Einstein's field equations

$$G_{\mu\nu} = 8\pi\, T_{\mu\nu}\,, \tag{3.2}$$

where $G_{\mu\nu}$ denotes the Einstein tensor and $T_{\mu\nu}$ the energy-momentum tensor. The expression above depicts a very compact representation of Einstein's field equations [58]. The quantities $G_{\mu\nu}$ and $T_{\mu\nu}$ are functions of the metric $g_{\mu\nu}$ as well as its first and second derivatives. Using symmetry arguments, one can show that Eq. (3.2) is a system of ten coupled, non-linear differential equations [58]. The energy-momentum tensor is a symmetric tensor with a vanishing divergence and expresses consequently the conservation of energy and momentum [112, 113]. The energy-momentum tensor has to be deduced by a theory of matter while in practical applications a perfect fluid is frequently assumed, i.e,

$$T_{\mu\nu} = (\epsilon + P)\, u_\mu u_\nu + P g_{\mu\nu}\,, \tag{3.3}$$

where u_μ is the four velocity [112, 113, 255]. The idealization of the matter inside a neutron star as a perfect fluid is justified by the fact that shear stresses as well as the energy transport inside the neutron star are negligible [200]. We refer the reader to Ref. [112] for a thorough discussion of a general form of the energy-momentum tensor.

Einstein's field equations are then solved with a suitable ansatz for the metric which eventually yields a solution for the metric. Solving Einstein's field equations is a difficult task: First, the involved differential equations are non-linear as already noted above. Second, spacetime and matter are mutually influential [113]. Analytical solutions are only known for a few problems [123]. The discipline of *numerical relativity* deals with the numerical solution of the field equations which is a computationally expensive challenge [123].

In the present work, we use suitable ansätze for the metric where we consider in particular non-rotating neutron stars, slowly rotating neutron stars, and small perturbing tidal fields which are discussed in the subsequent sections.

3.2 Non-rotating neutron stars

We start our discussion by considering non-rotating, spherical symmetric stars. In this work, we neglect the effects of magnetic fields which are argued to be solely small corrections [219]. The geometry of the spacetime in that case is well described by the Schwarzschild metric

$$\mathrm{d}s^2 = -\mathrm{e}^{\nu}\,\mathrm{d}t^2 + \mathrm{e}^{\lambda}\,\mathrm{d}r^2 + r^2\,\mathrm{d}\vartheta^2 + r^2\sin^2\vartheta\,\mathrm{d}\varphi^2\,, \tag{3.4}$$

where ν and λ are metric functions depending on the radial coordinate r solely, ϑ and φ denote the polar and azimuthal angles, respectively. The metric functions ν and λ vanish in the case of flat spacetime [123]. The independent works of Tolman [270] and Oppenheimer and Volkoff [205] are based on solving Einstein's field equations (3.2) and considering a spherical symmetric, non-rotating star by using the Schwarzschild metric given in Eq. (3.4). This yields the Tolman-Oppenheimer-Volkoff[2] (TOV) equations which are given by [205, 270]

$$\frac{\mathrm{d}P}{\mathrm{d}r} = -(\epsilon + P)\frac{m + 4\pi r^3 P}{r^2}\left(1 - \frac{2m}{r}\right)^{-1}\,, \tag{3.5a}$$

$$\frac{\mathrm{d}m}{\mathrm{d}r} = 4\pi r^2 \epsilon\,. \tag{3.5b}$$

[2] The literature refers often to the Oppenheimer-Volkoff equations, abbreviated as OV equations.

where r denotes the radial coordinate and m the gravitational mass within a sphere of radius r (cf. Refs. [140, 156, 200]). We note here that Eq. (3.5a) expresses the hydrostatic equilibrium [112]. Moreover, Eq. (3.5a) indicates that a maximum mass M_{max} of a neutron star[3] exists [113, 123]. Oppenheimer and Volkoff used the EOS of a free Fermi gas at $T = 0$ and solved Eqns. (3.5a) and (3.5b). In their work, the authors found that the maximum mass of neutron stars is $M_{\mathrm{OV}} \approx 0.71\,M_{\odot}$[4] [205]. We refer the reader to Chap. 1 where we provide details and references on the progress of the maximum mass from a theoretical as well as an observational point of view.

To get a closed system of equations, the EOS $\epsilon(P)$ must be known. The TOV equations are solved by choosing a central pressure $P_{\mathrm{c}} = P(r = 0)$ and integrating from the center to the surface of the star. The surface is defined by the radial coordinate R at which the pressure vanishes, i.e., $P(r = R) = 0$. Thus, R represents the radius of the neutron star. The mass is then defined by $M \equiv m(r = R)$. The other initial condition is given by $m(r = 0) = 0$. Inside the star, the conditions $P(r) > 0$ and $\mathrm{d}P/\mathrm{d}r < 0$ hold [123]. In summary, we note that the masses M and radii R are parametrized by the central pressure P_{c}.

The metric function ν is determined by solving the differential equation

$$\frac{\mathrm{d}\nu}{\mathrm{d}r} = \frac{2\left(m + 4\pi r^3 P\right)}{r^2}\left(1 - \frac{2m}{r}\right)^{-1} \tag{3.6}$$

with the boundary condition

$$\nu(R) = \ln\left(1 - \frac{2M}{R}\right). \tag{3.7}$$

The boundary condition for ν is derived from setting $P(R) = \epsilon(R) = 0$ in Eq. (3.6) and matching the interior solution and the exterior solution at the surface of the star. We note here that the solution of ν is not required for solving the TOV Eqns. (3.5a) and (3.5b), but ν is required for the calculation of quadrupole moments of neutron stars (cf. Sec. 3.5). Moreover, an expression for the metric function λ is required, which is given by

$$\mathrm{e}^{\lambda} = \left(1 - \frac{2m}{r}\right)^{-1}. \tag{3.8}$$

Furthermore, stellar models can be tested for stability for a sequence of central pressures P_{c}. A stellar model is only stable when the condition

$$\frac{\mathrm{d}M}{\mathrm{d}P_{\mathrm{c}}} > 0$$

is fulfilled, whereas the opposite condition

$$\frac{\mathrm{d}M}{\mathrm{d}P_{\mathrm{c}}} < 0$$

always indicates instability [123, 243].

[3] The actual value of M_{max} depends on the matter in the interior of the star and thus on the EOS [113]. A more detailed discussion on arguments for the existence of a maximum neutron star mass can be found in Ref. [123] and references therein.

[4] De facto, Oppenheimer and Volkoff wrote: "It seems likely that our limit of $\sim 0.7\,M_{\odot}$ is near the truth." in their publication [205].

Further, the binding energy of neutron stars can be accessed within the framework of non-rotating neutron stars. We start by determining the number of baryons contained inside a neutron star. The baryon number A is given by

$$A = 4\pi \int_0^R \mathrm{d}r\, r^2 n \cdot \left(1 - \frac{2m}{r}\right)^{-\frac{1}{2}} , \tag{3.9}$$

with the particle density n [112, 113, 123, 133]. The expression given above can be rewritten as

$$\frac{\mathrm{d}A}{\mathrm{d}r} = 4\pi r^2 n \cdot \left(1 - \frac{2m}{r}\right)^{-\frac{1}{2}} , \tag{3.10}$$

with the initial condition $A(r = 0) = 0$ [123]. Hence, the baryon number A is determined simultaneously with the mass M and the radius R of the neutron star.

The binding energy of a neutron star can be interpreted as the energy that is necessary to build such an object from a fixed number of baryons [113, 177]. The binding energy BE is defined by [113]

$$\mathrm{BE} = A m_\mathrm{b} - M , \tag{3.11}$$

where m_b denotes the baryon mass.

3.3 Slowly rotating neutron stars

Up to this point, we discussed static, spherical symmetric neutron stars. Nevertheless, actual neutron stars are indeed rotating objects. Rotation with an angular velocity Ω gives rise to deformations of a neutron star such that spherical symmetry is broken but axial symmetry is still valid. Thus, a full description requires the consideration of stellar deformations, support of heavier configurations, additional changes in the spacetime, and the general relativistic effect of frame-dragging (Lense-Thirring effect, cf. Refs. [53, 266]) [277].

A perturbative approach to determine the structure of rotating neutron stars is the Hartle-Thorne approximation [130, 133]. In this approach, an expansion of the metric in the angular velocity Ω is performed [130, 133]. Numerous works have discussed the Hartle-Throne approximation, cf. Refs. [27, 58, 123, 276]. We briefly address the applicability of the slow-rotation approximation to existing neutron stars. Rotation is considered as slow when the centrifugal forces are small in comparison with the gravitational forces [123, 130] that can be expressed via

$$\frac{R^3\Omega^2}{GM} \ll 1 . \tag{3.12}$$

This condition holds even for the fastest spinning known neutron star PSR J1748 − 2446ad that has a spin period of 1.396 ms [141]. By assuming a typical neutron star with $M = 1.4\,M_\odot$ and $R = 10\,\mathrm{km}$, one finds $R^3\Omega^2/GM \approx 0.11$ [123]. In this thesis, we focus especially on PSR J0737 − 3039A which is the fastest rotating known pulsar in a double neutron star binary system with a period of about 22.70 ms [56]. The authors of Ref. [276] claim that the slow-rotation approximation is well applicable for rotational frequencies less than 300 Hz which is the case for 96% of the known pulsars – thus also for PSR J0737 − 3039A. Other works substantiate that the slow-rotation approximation is applicable for most neutron stars, cf. Refs. [40, 219, 298].

Moreover, we only consider uniform rotation [130]. This can be justified by the fact that differential rotation dampens within a few days [139]. The Schwarzschild metric given in Eq. (3.4) exhibits no

off-diagonal elements which are inherently necessary to describe rotating systems. The metric for static, axial symmetric stars is then given by [130, 132]

$$\mathrm{d}s^2 = -H^2\mathrm{d}t^2 + Q^2\mathrm{d}r^2 + r^2K^2\left[\mathrm{d}\vartheta^2 + \sin^2\vartheta\,(\mathrm{d}\varphi - L\mathrm{d}t)^2\right], \tag{3.13}$$

with the r-dependent functions H, Q, K, and L [130]. The quantity L is an angular velocity that is connected to the moment of inertia [130]. Rotating massive objects drag spacetime along with their rotation. As a consequence, a free falling observer attains an angular velocity that is identified with L [130]. Up to first order in Ω, L is given by

$$L(r,\vartheta) = \omega(r,\vartheta) + \mathcal{O}\left(\Omega^3\right). \tag{3.14}$$

The metric given in Eq. (3.13) can now be simplified using the expression above. The result is then inserted into Einstein's field equations given in Eq. (3.2) which can then be solved. As we noted above, we are interested in the angular velocity acquired by a free falling observer towards the star [130], i.e.,

$$\bar{\omega} = \Omega - \omega, \tag{3.15}$$

that is referred to the rotational drag. Following Refs. [130, 133], the TOV Eqns. (3.5a) and (3.5b) have to be supplemented by a differential equation for the rotational drag $\bar{\omega}$. In the work of Hartle [130] it was shown that $\bar{\omega}$ is a function of the radial coordinate solely. The differential equation for $\bar{\omega}$ is given by

$$\frac{1}{r^4}\frac{\mathrm{d}}{\mathrm{d}r}\left(r^4 j\frac{\mathrm{d}\bar{\omega}}{\mathrm{d}r}\right) + \frac{4}{r}\frac{\mathrm{d}j}{\mathrm{d}r}\bar{\omega} = 0, \tag{3.16}$$

where the auxiliary function j is defined by

$$j = \mathrm{e}^{-\frac{1}{2}(\nu+\lambda)}. \tag{3.17}$$

The boundary value of j is deduced by considering the exterior solutions for the metric functions ν and λ that are given by

$$\mathrm{e}^{\nu} = \mathrm{e}^{-\lambda} = 1 - \frac{2M}{r}, \qquad r > R. \tag{3.18}$$

We evaluate Eq. (3.17) at the surface of the neutron star with the expressions given above and find the boundary condition $j(R) = 1$ [130]. The initial conditions for Eq. (3.16) are obtained by implying regularity at the center of the star [123], which yields

$$\bar{\omega}(0) = \bar{\omega}_\mathrm{c} \quad \text{and} \quad \left.\frac{\mathrm{d}\bar{\omega}}{\mathrm{d}r}\right|_{r=0} = 0, \tag{3.19}$$

where the value of $\bar{\omega}_\mathrm{c}$ can be chosen arbitrarily [130, 133], but sufficiently small to fulfill the requirement of slow rotation (cf. Eq. (3.12)) [123].

In general, the moment of inertia of a spheric symmetric star is given by [131]

$$I = \left.\frac{\partial J}{\partial \Omega}\right|_{\Omega=0}, \tag{3.20}$$

with the angular momentum J and the angular velocity Ω. We consider the Hartle-Thorne approximation up to first order in Ω and hence we obtain

$$J = I\Omega + \mathcal{O}\left(\Omega^3\right) \tag{3.21}$$

for the angular momentum [131]. The exterior solution given in Eq. (3.16) is then solved and the constants of integration are identified with the angular velocity Ω and the angular momentum J. The rotational drag is then given by [130, 133, 200]

$$\bar{\omega}(r) = \Omega - \frac{2J}{r^3}\,, \tag{3.22}$$

with the angular momentum [133]

$$J = \frac{1}{6}R^4\left(\frac{\mathrm{d}\bar{\omega}}{\mathrm{d}r}\right)_{r=R}\,. \tag{3.23}$$

Eventually, the angular velocity of the star is determined by [133]

$$\Omega = \bar{\omega}(R) + \frac{2J}{R^3}\,, \tag{3.24}$$

and the moment of inertia reads

$$I = \frac{J}{\Omega}\,. \tag{3.25}$$

At this point, we refer the reader to Refs. [130, 133] where the authors provide more information on how corrections to the radius can be considered in order to determine the deformation of a slowly rotating star.

3.4 Tidal perturbations

Up to this point, we solely considered isolated neutron stars. We now extend the presented framework by investigating neutron stars in an external tidal field induced by a companion. Hereto, we consider a spherical symmetric neutron star with mass M. The companion generates an external quadrupole field $\mathscr{E}_{ij}$. The external quadrupole field in turn alters the shape of the neutron star and a quadrupole field Q_{ij} emerges as a consequence. The deformation of the star has an effect on the g_{tt} component of the metric tensor, i.e.,

$$\frac{1-g_{tt}}{2} = -\frac{M}{r} - \frac{3Q_{ij}}{2r^3}\left(n^i n^j - \frac{1}{3}\delta^{ij}\right) + \mathcal{O}\left(\frac{1}{r^3}\right) + \frac{1}{2}\mathscr{E}_{ij}x^i x^j + \mathcal{O}\left(r^3\right)\,, \tag{3.26}$$

where $n^i = x^i/r$ [267]. The expression above thus yields access to the fields $\mathscr{E}_{ij}$ and Q_{ij}. In this work, we follow the work of Refs. [101, 146] such that we consider Eq. (3.26) to linear order in $\mathscr{E}_{ij}$ and assume the source to be at far distance. Consequently, the quadrupole field is given by

$$Q_{ij} = -\lambda\mathscr{E}_{ij}\,, \tag{3.27}$$

where we introduced the tidal deformability λ[5]. The tidal deformability is related to the tidal Love number by

$$k_2 = \frac{3}{2}\lambda R^{-5}\,, \tag{3.28}$$

[5] The reader should not confuse the tidal deformability λ with the metric function λ.

that was introduced by Love [190]. We note here that the tidal deformability and consequently the Love number provide a measure of the deformation of a neutron star [300].

Following the approach of Ref. [146], we restrict our considerations to static, linear perturbations to the metric of a spherical symmetric star $g^{(0)}_{\alpha\beta}$ such that the full metric $g_{\alpha\beta}$ is given by [268]

$$g_{\alpha\beta} = g^{(0)}_{\alpha\beta} + h_{\alpha\beta}\,,$$

with the linearized perturbation $h_{\alpha\beta}$ of the metric [146]. An ansatz for the metric perturbation is given by [227, 268]

$$h_{\alpha\beta} = \mathrm{diag}\left[-e^{\nu}H_0,\, e^{\lambda}H_2,\, r^2K,\, r^2\sin^2\vartheta K\right] Y_{2m}(\vartheta,\varphi)\,, \tag{3.29}$$

where the functions H_0, H_2, and K depend on r solely since we restrict our considerations to static perturbations [146, 228]. Further, the perturbation of the energy-stress tensor (cf. Eq. (3.3)) is given by [146, 268]

$$\delta T_0{}^0 = -\delta\rho = -\left(\frac{\mathrm{d}P}{\mathrm{d}\rho}\right)^{-1}\delta\rho\,, \tag{3.30}$$

$$\delta T_i{}^i = \delta\rho\,. \tag{3.31}$$

The perturbation of the metric and the perturbation of the energy-stress tensor are then inserted into the linearized Einstein field equations

$$\delta G_\alpha{}^\beta = 8\pi\,\delta T_\alpha{}^\beta\,. \tag{3.32}$$

According to Ref. [146], the metric functions H_0 and H_2 are related by $-H_2 = H_0 \equiv H$ and further the functions K' and H can be related using Einstein's field equations. As a result, the following differential equation is obtained [146]:

$$\begin{aligned} 0 =& \frac{\mathrm{d}^2H}{\mathrm{d}r^2} + \left[\frac{2}{r} + \frac{2m + 4\pi r^3(P+\epsilon)}{r(r-2m)}\right]\frac{\mathrm{d}H}{\mathrm{d}r} \\ &+ \left\{4\pi r\left[5\epsilon + 9P + \frac{(\epsilon+P)^2}{P\Gamma}\right] - \frac{6}{r} - \frac{4\left(m+4\pi r^3P\right)^2}{r^2(r-2m)}\right\}\frac{H}{r-2m}\,. \end{aligned} \tag{3.33}$$

We now consider the exterior region $r > R$ where the expression above is given by

$$0 = \frac{\mathrm{d}^2H}{\mathrm{d}r^2} + \left(\frac{2}{r} - \frac{2M}{r(2M-r)}\right)\frac{\mathrm{d}H}{\mathrm{d}r} - \left(\frac{6}{r(r-2M)} + \frac{4M^2}{r^2(2M-r)^2}\right)H\,. \tag{3.34}$$

Following Refs. [146, 268], the differential equation for the exterior region can be reformulated as an associated Legendre differential equation with $l = m = 2$:

$$\left(x^2-1\right)\frac{\mathrm{d}^2H}{\mathrm{d}r^2} + 2x\frac{\mathrm{d}H}{\mathrm{d}r} - \left(6 + \frac{4}{x^2-1}\right)H = 0\,, \tag{3.35}$$

where we introduced

$$x = \frac{r}{M} - 1\,.$$

Solutions of differential equations as given in Eq. (3.34) can be written in the general form

$$H = c_1 {Q_2}^2(x) + c_2 {P_2}^2(x)\,, \tag{3.36}$$

with the coefficients c_1 and c_2. Moreover, ${P_2}^2(x)$ and ${Q_2}^2(x)$ denote the associated Legendre polynomial and associated Legendre function of the second kind, respectively (cf. Ref. [10]), and are given by[6]

$${P_2}^2(x) = 3\left(x^2-1\right), \tag{3.37}$$

$${Q_2}^2(x) = \frac{3}{2}\left(x^2-1\right)\ln\left(\frac{x+1}{x-1}\right) - \frac{3x^3-5x}{x^2-1}\,. \tag{3.38}$$

Eventually, the exterior solution of Eq. (3.34) reads

$$\begin{aligned} H =& c_1\left(\frac{r}{M}\right)^2\left(1-\frac{2M}{r}\right)\left[-\frac{M(M-r)(2M^2+6Mr-3r^2)}{r^2(2M-r)^2}+\frac{3}{2}\ln\left(\frac{r}{r-2M}\right)\right] \\ &+ 3c_2\left(\frac{r}{M}\right)^2\left(1-\frac{2M}{r}\right). \end{aligned} \tag{3.39}$$

In order to determine the coefficients c_1 and c_2, we investigate the asymptotic behavior for large r and find

$$H = \frac{8}{5}\left(\frac{M}{r}\right)^3 c_1 + \mathcal{O}\left(\frac{M}{r}\right)^4 + 3\left(\frac{r}{M}\right)^2 c_2 + \mathcal{O}\left(\frac{r}{M}\right). \tag{3.40}$$

In conjunction with the exterior solution of the metric function ν (cf. Eq. (3.18)), we now have the asymptotic behavior of the metric element g_{tt} given in Eq. (3.29) at hand. We match the asymptotic solution to the expansion of the g_{tt} component in Eq. (3.26). Eventually, we determine the coefficients c_1 and c_2 and find

$$c_1 = \frac{15}{8}\frac{\lambda\mathcal{E}}{M^3}\,, \qquad c_2 = \frac{M^2\mathcal{E}}{3}\,, \tag{3.41}$$

where we used Eq. (3.27). Past studies (cf. Refs. [75, 146, 188, 218, 302]) showed that the tidal deformability does not depend on the function H itself but solely on the expression

$$y = \frac{r}{H}\frac{\mathrm{d}H}{\mathrm{d}r}\,. \tag{3.42}$$

As a consequence, Eq. (3.33) can be rewritten as a first-order differential equation for y that is given by

$$\frac{\mathrm{d}y}{\mathrm{d}r} = -\frac{y^2}{r} - \frac{r+4\pi r^3(P-\epsilon)}{r(r-2m)}y + \frac{4\left(m+4\pi r^3 P\right)^2}{r(r-2m)^2} + \frac{6}{r-2m} - \frac{4\pi r^2}{r-2m}\left[5\epsilon+9P+\frac{(\epsilon+P)^2}{P\Gamma}\right], \tag{3.43}$$

with the initial condition $y(0)=2$ [188].

Ultimately, we determine an expression for the tidal deformability by inserting Eq. (3.39) and its derivative with respect to r into Eq. (3.42). The expression obtained in this way shall then be evaluated at the radius R of the neutron star and we define $Y = y(R)$ [188]. The quantity Y is a measure for

[6] We note that the expressions for ${P_l}^m(x)$ and ${Q_l}^m(x)$ used differ from the mathematical definition because the regular definition holds only for $|x|<1$. However, in the presented case the condition $x>1$ holds which explains the changes in the arguments of the logarithms (cf. Ref. [10] for more details on ${P_l}^m(x)$ and ${Q_l}^m(x)$ in general).

the relativistic quadrupole gravitational potential which is induced by the tidal deformation [188]. The dimensionless tidal deformability $\bar{\lambda}$ is then determined via [188]

$$\bar{\lambda}(C,Y) = \frac{16}{15\Xi}(1-2C)^2\left[2+2C(Y-1)-Y\right], \tag{3.44}$$

where the parameter Ξ is given by

$$\begin{aligned}\Xi(C,Y) =& 4C^3\left[13-11Y+C(3Y-2)+2C^2(1+Y)\right] \\ &+3(1-2C)^2\left[2-Y+2C(Y-1)\right]\ln(1-2C) \\ &+2C\left[6-3Y+3C(5Y-8)\right].\end{aligned} \tag{3.45}$$

Above, we gave an expression for the dimensionless tidal deformability $\bar{\lambda}$ instead of the tidal deformability λ whereat the two quantities are related by

$$\bar{\lambda} = \frac{\lambda}{M^5}. \tag{3.46}$$

Previous research (cf. Refs. [167, 168]) supports the hypothesis that the dimensionless tidal deformability $\bar{\lambda}$ might be measurable more accurately than the tidal deformability λ.

3.5 Quadrupole deformation

In the present section, we discuss how the quadrupole moment of neutron stars is calculated. We follow the approach described in Refs. [130, 133]. Hence, we use the Hartle-Thorne approximation up to second order in Ω at which the shape of the neutron star is altered and thus lead to a non-vanishing quadrupole moment. The metric in Eq. (3.13) then reads

$$\begin{aligned}\mathrm{d}s^2 =& -\mathrm{e}^{\nu}(1+2h)\,\mathrm{d}t^2 + \mathrm{e}^{\lambda}\left[1+\frac{2m}{r-2M}\right]\mathrm{d}r^2 \\ &+r^2(1+2k)\left[\mathrm{d}\vartheta^2+\sin^2\vartheta\,(\mathrm{d}\varphi-\omega\,\mathrm{d}t)^2\right]+\mathcal{O}\left(\Omega^3\right).\end{aligned} \tag{3.47}$$

Only the metric functions h and k given in Eq. (3.47) are related to the quadrupole moment Q; hence we neglect the metric function m[7] in our discussion. The work of Regge and Wheeler [227] demonstrates that an expansion of the metric in spherical harmonics is possible:

$$h(r,\vartheta) = h_0(r) + h_2(r)\,P_2(\vartheta) + \dots, \tag{3.48a}$$

$$k(r,\vartheta) = k_0(r) + k_2(r)\,P_2(\vartheta) + \dots, \tag{3.48b}$$

where the indices denote the l values of the spherical harmonics. For the calculation of the quadrupole moment only the $l=2$ expressions are relevant [130]. Solving Einstein's field equations given in Eq. (3.2) with the ansatz for the metric given in Eq. (3.47) and considering the expansion in spherical harmonics in Eqns. (3.48a) and (3.48b) yields differential equations for h_2 and k_2. According to Hartle [130], it is convenient to introduce $v_2 = h_2 + k_2$ for numerical reasons, such that the final system of differential equations is given by

$$\begin{aligned}\frac{\mathrm{d}h_2}{\mathrm{d}r} =& \left\{-\frac{\mathrm{d}\nu}{\mathrm{d}r}+\frac{r}{r-2m}\left(\frac{\mathrm{d}\nu}{\mathrm{d}r}\right)^{-1}\left[8\pi(\epsilon+P)-\frac{4m}{r^3}\right]\right\}h_2 - \frac{4v_2}{r(r-2m)}\left(\frac{\mathrm{d}\nu}{\mathrm{d}r}\right)^{-1} \\ &+\frac{1}{6}\left[\frac{1}{2}\frac{\mathrm{d}\nu}{\mathrm{d}r}r-\frac{1}{r-2m}\left(\frac{\mathrm{d}\nu}{\mathrm{d}r}\right)^{-1}\right]r^3j^2\left(\frac{\mathrm{d}\bar{\omega}}{\mathrm{d}r}\right)^2-\frac{1}{3}\left[\frac{1}{2}\frac{\mathrm{d}\nu}{\mathrm{d}r}r+\frac{1}{r-2m}\left(\frac{\mathrm{d}\nu}{\mathrm{d}r}\right)^{-1}\right]r^2\frac{\mathrm{d}j^2}{\mathrm{d}r}\bar{\omega}^2,\end{aligned} \tag{3.49a}$$

$$\frac{\mathrm{d}v_2}{\mathrm{d}r} = -\frac{\mathrm{d}\nu}{\mathrm{d}r}h_2+\left(\frac{1}{r}+\frac{1}{2}\frac{\mathrm{d}\nu}{\mathrm{d}r}\right)\left[-\frac{1}{3}r^3\frac{\mathrm{d}j^2}{\mathrm{d}r}\bar{\omega}^2+\frac{1}{6}j^2r^4\left(\frac{\mathrm{d}\bar{\omega}}{\mathrm{d}r}\right)^2\right], \tag{3.49b}$$

[7] We followed here the notation of Hartle [130]. The reader should not confuse here the metric function m with the mass profile m. As stated in the text, the metric function m is not required in this work, hence there is no need to carefully distinguish between the metric function and the mass profile.

with the boundary conditions

$$v_2 = h_2 = 0 \qquad \text{at} \qquad r = 0 \qquad \text{and} \qquad r = \infty\,.$$

The interior solutions for h_2 and v_2 can be written as a sum of a particular and a homogeneous solution [130], i.e.,

$$h_2^{\text{int}} = h_2^{(\text{P})} + A \cdot h_2^{(\text{H})}, \tag{3.50a}$$
$$v_2^{\text{int}} = v_2^{(\text{P})} + A \cdot v_2^{(\text{H})}, \tag{3.50b}$$

with a constant A. We denote the particular and homogeneous solution with the superscripts (P) and (H), respectively. The particular solutions are obtained by integrating the full system of differential equations given in Eqns. (3.49a) and (3.49b) while the homogeneous solution are then given by solving the homogeneous part, i.e.,

$$\frac{\mathrm{d}h_2^{(\text{H})}}{\mathrm{d}r} = \left\{-\frac{\mathrm{d}\nu}{\mathrm{d}r} + \frac{r}{r-2m}\left(\frac{\mathrm{d}\nu}{\mathrm{d}r}\right)^{-1}\left[8\pi(\epsilon+P) - \frac{4m}{r^3}\right]\right\} h_2^{(\text{H})} - \frac{4v_2^{(\text{H})}}{r(r-2m)}\left(\frac{\mathrm{d}\nu}{\mathrm{d}r}\right)^{-1}, \tag{3.51a}$$
$$\frac{\mathrm{d}v_2^{(\text{H})}}{\mathrm{d}r} = -\frac{\mathrm{d}\nu}{\mathrm{d}r} h_2^{(\text{H})}. \tag{3.51b}$$

The initial conditions near $r = 0$ for the particular integrals are given by

$$h_2^{(\text{P})} \to a r^2, \tag{3.52a}$$
$$v_2^{(\text{P})} \to b r^4, \tag{3.52b}$$

where the constants a and b are related via

$$b + \frac{2\pi}{3}(\epsilon_\text{c} + 3P_\text{c})\, a = \frac{2\pi}{3}(\epsilon_\text{c} + P_\text{c})(j_\text{c}\bar{\omega}_\text{c})^2\,, \tag{3.53}$$

with $\epsilon_\text{c} \equiv \epsilon(0)$, $P_\text{c} \equiv P(0)$, $j_\text{c} \equiv j(0)$, and $\bar{\omega}_\text{c} \equiv \bar{\omega}(0)$ being the central values [130]. The initial conditions near $r = 0$ for the homogeneous part read

$$h_2^{(\text{H})} \to B r^2, \tag{3.54a}$$
$$v_2^{(\text{H})} \to -\frac{2\pi}{3}(\epsilon_\text{c} + 3P_\text{c})\, B r^4, \tag{3.54b}$$

with a further constant B. The constants a and B are chosen arbitrarily. Solving the particular and homogeneous differential equations and inserting the results in Eqns. (3.50a) and (3.50b) yield the interior solutions depending on the constant A. In order to obtain the exterior solutions for h_2 and v_2, we use the exterior solutions for ν, λ, and $\bar{\omega}$ as given in Eqns. (3.18) and (3.22) and insert the exterior solutions into Eqns. (3.49a) and (3.49b), accordingly [130]. The differential equations obtained in this way for $r > R$ read

$$\frac{\mathrm{d}h_2}{\mathrm{d}r} = -\frac{2v_2}{M} - \frac{2(r-M)h_2}{r(r-2M)} - \frac{3J^2}{M}\frac{r^2 - 2Mr - 2M^2}{r^5(r-2M)}, \tag{3.55}$$
$$\frac{\mathrm{d}v_2}{\mathrm{d}r} = -\frac{2Mh_2}{r(r-2M)} + \frac{6J^2}{r^5}\frac{r-M}{r-2M}. \tag{3.56}$$

Similar to the solutions of the differential equations for the interior region, we solve the differential equations for the exterior region by determining a particular and a homogeneous solution [130]. The

solutions for the differential equations for $h_2^{\rm ext}$ and $v_2^{\rm ext}$ in the exterior region can be determined analytically [130]. Eventually, the exterior solutions are given by

$$h_2^{\rm ext} = J^2\left(\frac{1}{Mr^3}+\frac{1}{r^4}\right)+KQ_2{}^2\left(\frac{r}{M}-1\right), \tag{3.57a}$$

$$v_2^{\rm ext} = -\frac{J^2}{r^4}+K\frac{2M}{[r\,(r-2M)]^{1/2}}Q_2{}^1\left(\frac{r}{M}-1\right), \tag{3.57b}$$

where K is a constant and the associated Legendre function of the second kind $Q_2{}^1(x)$ is given by [130] (cf. Sec. 3.4 for the expression of $Q_2{}^2(x)$)

$$Q_2{}^1(x) = \left(x^2-1\right)^{1/2}\left[\frac{3x^2-2}{x^2-1}-\frac{3}{2}x\ln\left(\frac{x+1}{x-1}\right)\right]. \tag{3.58}$$

In Eqns. (3.57a) and (3.57b), the constant K is related to the quadrupole moment Q and determined by matching the interior and exterior solutions of h_2 and v_2 at the surface of the star, i.e.,

$$h_2^{\rm int}(R) = h_2^{\rm ext}(R), \tag{3.59a}$$

$$v_2^{\rm int}(R) = v_2^{\rm ext}(R). \tag{3.59b}$$

We obtain $h_2^{\rm int}(R)$ and $v_2^{\rm int}(R)$ from the interior solutions by solving the particular integrals in Eqns. (3.49a) and (3.49b) as well as the homogeneous integrals in Eqns. (3.51a) and (3.51b). Hence, the left-hand side of the system above depends on $h_2^{\rm (P)}$, $h_2^{\rm (H)}$, $v_2^{\rm (P)}$, and $v_2^{\rm (H)}$ as well as the constant A – cf. Eqns. (3.50a) and (3.50b). We insert the expressions given in Eqns. (3.57a) and (3.57b) into the right-hand side of the expression above. Eventually, the system of equations

$$h_2^{\rm (P)}(R)+A\cdot h_2^{\rm (H)}(R) = J^2\left(\frac{1}{MR^3}+\frac{1}{R^4}\right)+KQ_2{}^2\left(\frac{R}{M}-1\right), \tag{3.60a}$$

$$v_2^{\rm (P)}(R)+A\cdot v_2^{\rm (H)}(R) = -\frac{J^2}{R^4}+K\frac{2M}{[R\,(R-2M)]^{1/2}}Q_2{}^1\left(\frac{R}{M}-1\right) \tag{3.60b}$$

has to be solved for K and ultimately yields

$$\begin{aligned} K = &\left[-J^2\left(\frac{1}{Mr^3}+\frac{1}{r^4}\right)+h_2^{\rm (P)}(R)-\frac{h_2^{\rm (C)}(R)}{v_2^{\rm (C)}(R)}\left(\frac{J^2}{r^4}+v_2^{\rm (P)}(R)\right)\right] \\ &\times\left[Q_2{}^2\left(\frac{r}{M}-1\right)-\frac{h_2^{\rm (C)}(R)}{v_2^{\rm (C)}(R)}\frac{2M}{[r\,(r-2M)]^{1/2}}Q_2{}^1\left(\frac{r}{M}-1\right)\right]^{-1}. \end{aligned} \tag{3.61}$$

The constant A is then not required to determine the quadrupole moment of neutron stars. Eventually, the quadrupole moment is given by [130, 133][8]

$$Q = \frac{8}{5}KM^3+\frac{J^2}{M}. \tag{3.62}$$

[8] The quadrupole moment in Ref. [130] is misprinted, the follow-up work in Ref. [133] provides the corrected equation.

3.6 Numerical method

In this section, we present the numerical method we use to calculate the neutron star observables. We start our discussion by focussing on the TOV equations given in Eqns. (3.5a) and (3.5b) that result in solutions for the pressure profile $P(r)$ and mass profile $m(r)$. The coupled differential equations are typically treated as an initial value problem and solved by integrating from the center of the star at $r = 0$ to the surface at $r = R$ where the pressure vanishes. The initial values are specified by $m(0) = 0$ and a chosen value for the pressure $P(0) = P_c$ [185].

Using this approach, neutron star properties like radii and masses can be determined. Nevertheless, the described approach exhibits problems [185, 187]. First, the domain of integration is not known initially since the radius is defined by the vanishing pressure. Second, the definition of the surface, i.e., $P(R) = 0$, is numerically difficult to solve since $\mathrm{d}P/\mathrm{d}r$ vanishes at the surface [187]. Furthermore, Eqns. (3.5a) and (3.5b) feature a singularity at the center of the star.

We follow the work of Ref. [185] and re-write the EOS $P(\epsilon)$ such that the pressure P as well as the energy density ϵ are given as functions of the pseudo-enthalpy h that we introduced in Chap. 2 (cf. Eq. (2.11)). As a consequence, we also transform the differential equations required for determining the neutron star structure. Using the chain rule of derivation and Eqs. (2.11) and (3.5a) yield

$$\frac{\mathrm{d}h}{\mathrm{d}r} = \frac{\mathrm{d}h}{\mathrm{d}P} \cdot \frac{\mathrm{d}P}{\mathrm{d}r} = -\frac{m + 4\pi r^3 P}{r\,(r - 2m)}\,. \tag{3.63}$$

It was proven by Hartle that the condition $2m(r)/r < 1$ is always fulfilled [131]. Using this condition and Eq. (3.63), it can be shown that $\mathrm{d}h/\mathrm{d}r \leq 0$ holds [185]. Consequently, h is a monotonically decreasing function of r. This justifies the transformation from r being the independent variable to h [185]. Making r and m the dependent variables and h the independent variable changes the TOV Eqns. (3.5a) and (3.5b) to

$$\frac{\mathrm{d}r}{\mathrm{d}h} = -\frac{r\,(r - 2m)}{m + 4\pi r^3 P}\,, \tag{3.64a}$$

$$\frac{\mathrm{d}m}{\mathrm{d}h} = 4\pi r^2 \epsilon \cdot \frac{\mathrm{d}r}{\mathrm{d}h}\,. \tag{3.64b}$$

The transformed TOV equations are then integrated from the initial conditions $r(h_c) = 0$ and $m(h_c) = 0$ to the surface of the star, where $h = 0$. The radius and the mass are then determined by $R = r(0)$ and $M = m(0)$. Thus, the domain of integration is initially fixed which solves one of the problems noted above [185, 187]. Further, the derivative $\mathrm{d}r/\mathrm{d}h$ does not vanish at the surface of the star which therefore solves the problem associated which the condition $P(R) = 0$ to determine the surface of the star [187]. The singularity in the center of the star remains [185], thus the integration has to be started near the center. This is performed by using a power series expansion [187]:

$$r(h) = r_1 (h_c - h)^{1/2} + r_3 (h_c - h)^{3/2} + \mathcal{O}(h_c - h)^{5/2}\,, \tag{3.65}$$

$$m(h) = m_3 (h_c - h)^{3/2} + m_5 (h_c - h)^{5/2} + \mathcal{O}(h_c - h)^{7/2}\,. \tag{3.66}$$

The coefficients in the two equations above are given by

$$r_1 = \left[\frac{3}{2\pi(\epsilon_c + 3P_c)}\right]^{\frac{1}{2}}\,, \tag{3.67}$$

$$r_3 = -\frac{r_1}{4(\epsilon_c + 3P_c)}\left[\epsilon_c - 3P_c - \frac{3(\epsilon_c + P_c)^2}{5P_c\Gamma_c}\right]\,, \tag{3.68}$$

$$m_3 = \frac{4\pi}{3}\epsilon_c r_1^3\,, \tag{3.69}$$

$$m_5 = 4\pi r_1^3\left[\frac{r_3\epsilon_c}{r_1} - \frac{(\epsilon_c + P_c)^2}{5P_c\Gamma_c}\right]\,, \tag{3.70}$$

where $\epsilon_c \equiv \epsilon(h_c)$, $P_c \equiv P(h_c)$, and $\Gamma_c \equiv \Gamma(h_c)$ denote the central energy density, central pressure, and central adiabatic index, respectively [185, 187].

The transformation for the baryon number A is straightforward. We use again the chain rule of derivation and additionally Eq. (2.12) with the result that the expression for the baryon number reads

$$\frac{\mathrm{d}A}{\mathrm{d}h} = 4\pi r^2 \frac{\epsilon + P}{\mathrm{e}^h \cdot m_b} \left(1 - \frac{2m}{r}\right)^{-\frac{1}{2}} \cdot \frac{\mathrm{d}r}{\mathrm{d}h} \,. \tag{3.71}$$

In the case of the moment of inertia of neutron stars, we transform the second order differential equation for $\bar{\omega}$ into a linear system of two differential equations by substituting

$$\frac{\mathrm{d}\bar{\omega}}{\mathrm{d}r} = \alpha \,, \tag{3.72}$$

which yields

$$\frac{\mathrm{d}\alpha}{\mathrm{d}r} = -\frac{4\alpha}{r} - \frac{1}{j}\frac{\mathrm{d}j}{\mathrm{d}r}\left(\alpha + \frac{4}{r}\bar{\omega}\right) . \tag{3.73}$$

Although the function j is depending on ν, one can show that the factor

$$\frac{1}{j}\frac{\mathrm{d}j}{\mathrm{d}r}$$

in the expression above is independent on ν and can be rewritten as

$$\frac{1}{j}\frac{\mathrm{d}j}{\mathrm{d}r} = -\frac{4\pi r^3 (P+\epsilon)}{r(r-2m)} \,. \tag{3.74}$$

See Appendix A for details. Hence, the differential equation for the metric function ν is not required for the calculation of moments of inertia. By substituting the factor, we find

$$\frac{\mathrm{d}\alpha}{\mathrm{d}r} = -\frac{4\alpha}{r} + \frac{4\pi r^3 (P+\epsilon)}{r(r-2m)}\left(\alpha + \frac{4}{r}\bar{\omega}\right) . \tag{3.75}$$

The transformation of the differential equations given in Eqns. (3.72) and (3.75) as functions of h is straightforward by using the chain rule. We show the results at the end of this section where we summarize all transformed differential equations. As stated above, the differential equations exhibit singularities at the center of the neutron star. Therefore, we expand the central value of $\bar{\omega}_c$ around $r = 0$ and obtain [298]

$$\bar{\omega}(r) = \bar{\omega}_c + \frac{8\pi}{5}(\epsilon_c + P_c)\,\bar{\omega}_c r^2 \,. \tag{3.76}$$

This does also apply for Eq. (3.43) that is required for the calculation of the tidal deformability. Referring to our discussion of the initial conditions for the transformed TOV equations and following Ref. [188], we perform an expansion to determine the initial condition for $y(r)$ near the center of the star and find

$$y(r) = 2 + y_2(h_c - h) + \mathcal{O}(h_c - h)^2 \,, \tag{3.77}$$

where the coefficient y_2 is given by

$$y_2 = -\frac{6}{7(\epsilon_c + 3P_c)}\left[\frac{\epsilon_c}{3} + 11P_c + \frac{(\epsilon_c + P_c)^2}{P_c \Gamma_c}\right] . \tag{3.78}$$

In the case of the differential equations for h_2 and v_2 further substitutions can be made. By comparing Eqns. (3.6) and (3.63) one finds

$$\frac{\mathrm{d}\nu}{\mathrm{d}r} = -2\frac{\mathrm{d}h}{\mathrm{d}r}\,. \tag{3.79}$$

The expression above is then used in conjunction with the chain rule to transform the differential equations for h_2 and v_2. Moreover, both differential equations depend on the function $j(r)$, which can be rewritten as a function of h as follows:

$$j(h) = \left(\frac{1-\frac{2m}{r}}{1-\frac{2M}{R}}\right)^{\frac{1}{2}} \cdot \mathrm{e}^{h}\,. \tag{3.80}$$

We refer to Appendix A where we show details on the derivation of the expression given above. This expression, however, depends on the mass M and the radius R of the neutron star. Consequently, the TOV equations as given in Eqns. (3.64a) and (3.64b) have to be solved in advance.

Applying this approach to all required differential equations, we eventually have the following system of differential equations:

$$\frac{\mathrm{d}r}{\mathrm{d}h} = -\frac{r\,(r-2m)}{m+4\pi r^3 P}\,, \tag{3.81a}$$

$$\frac{\mathrm{d}m}{\mathrm{d}h} = 4\pi r^2 \epsilon \cdot \frac{\mathrm{d}r}{\mathrm{d}h}\,, \tag{3.81b}$$

$$\frac{\mathrm{d}A}{\mathrm{d}h} = 4\pi r^2 \frac{\epsilon+P}{\mathrm{e}^h \cdot m_b}\left(1-\frac{2m}{r}\right)^{-\frac{1}{2}} \cdot \frac{\mathrm{d}r}{\mathrm{d}h}\,, \tag{3.81c}$$

$$\frac{\mathrm{d}\bar{\omega}}{\mathrm{d}h} = \alpha \cdot \frac{\mathrm{d}r}{\mathrm{d}h}\,, \tag{3.81d}$$

$$\frac{\mathrm{d}\alpha}{\mathrm{d}h} = \left[-\frac{4\alpha}{r} + \frac{4\pi r^3(P+\epsilon)}{r(r-2m)}\left(\alpha + \frac{4}{r}\bar{\omega}\right)\right] \cdot \frac{\mathrm{d}r}{\mathrm{d}h}\,, \tag{3.81e}$$

$$\begin{aligned}\frac{\mathrm{d}y}{\mathrm{d}h} = {} & \frac{(r-2m)(y+1)y}{m+4\pi r^3 P} + y + \frac{(m-4\pi r^3\epsilon)y}{m+4\pi r^3 P} \\ & + \frac{4\pi r^3(5\epsilon+9P)-6r}{m+4\pi r^3 P} + \frac{4\pi r^3(\epsilon+P)^2}{P\Gamma(m+4\pi r^3 P)} - \frac{4(m+4\pi r^3 P)}{r-2m}\,,\end{aligned} \tag{3.81f}$$

$$\begin{aligned}\frac{\mathrm{d}h_2}{\mathrm{d}h} = {} & \left\{2 - \frac{1}{2}\frac{r}{r-2m}\left(\frac{\mathrm{d}r}{\mathrm{d}h}\right)^2\left[8\pi(\epsilon+P) - \frac{4m}{r^3}\right]\right\} h_2 + \frac{2v_2}{r(r-2m)}\left(\frac{\mathrm{d}r}{\mathrm{d}h}\right)^2 \\ & + \frac{1}{6}\left[-r + \frac{1}{2}\frac{1}{r-2m}\left(\frac{\mathrm{d}r}{\mathrm{d}h}\right)^2\right] r^3 j^2 \left(\frac{\mathrm{d}\bar{\omega}}{\mathrm{d}h}\left(\frac{\mathrm{d}r}{\mathrm{d}h}\right)^{-1}\right)^2 \\ & + \frac{2}{3}\left[-r - \frac{1}{2}\frac{1}{r-2m}\left(\frac{\mathrm{d}r}{\mathrm{d}h}\right)^2\right] r^2 j^2 \frac{4\pi r^3(P+\epsilon)}{r(r-2m)}\bar{\omega}^2\,,\end{aligned} \tag{3.81g}$$

$$\frac{\mathrm{d}v_2}{\mathrm{d}h} = 2h_2 + \left(\frac{1}{r} - \left(\frac{\mathrm{d}r}{\mathrm{d}h}\right)^{-1}\right)\left[\frac{2}{3}r^3 j^2 \frac{4\pi r^3(P+\epsilon)}{r(r-2m)}\bar{\omega}^2 + \frac{1}{6}j^2 r^4\left(\frac{\mathrm{d}\bar{\omega}}{\mathrm{d}h}\cdot\left(\frac{\mathrm{d}r}{\mathrm{d}h}\right)^{-1}\right)^2\right]\frac{\mathrm{d}r}{\mathrm{d}h}\,. \tag{3.81h}$$

Depending on how the EOS is available, the adiabatic index as a function of the pseudo-enthalpy $\Gamma(h)$ has to be determined using Eq. (2.10).

In Appendix B, we provide some numerical test cases to benchmark our implementation of the discussed framework.

4 Non-rotating neutron stars

In this chapter, we discuss the structure of non-rotating neutron stars. In Chap. 2, two EOS models were introduced, namely the piecewise polytropic EOS model and the speed of sound parametrization. We determine the EOS space and mass-radius space for both parametrizations and provide a comparison of the predicted properties of non-rotating neutron stars for both models. Moreover, we investigate properties of the speed of sound in the case of the piecewise polytropic EOS model. We review correlations between properties of the EOS at nuclear densities and neutron star observables. It was shown [175, 177, 252] that the quantity $RP^{-1/4}$ is approximately constant for a typical neutron star in the density regime from saturation density to twice saturation density where R is the radius of a neutron star and P is the pressure. We investigate this correlations for the presented EOS models. Finally, we explore the impact of future simultaneous mass-radius measurements on the EOS. Based on the primary science targets of the NICER mission, we assume different scenarios. We then utilize two different approaches to infer constraints for the nuclear EOS. First, we apply simple compatibility cuts and second, we use Bayesian statistics. In this context, we also investigate the impact of the parametrization of the EOS on the inference of EOS constraints.

Parts of the results presented in this chapter has been published in Greif *et al.* (2019) [118].

4.1 Exploring the equation of state and mass-radius space

We start with considering the piecewise polytropic EOS model. The approach discussed in Chap. 2 is used to construct the EOS within the parameter space given in Sec. 2.3.2. Following Ref. [137], we discretize the parameter space such that we vary the transition densities ρ_{12} and ρ_{23} in steps of $0.5\,\rho_0$. The adiabatic indices Γ_1, Γ_2, and Γ_3 are varied in steps of 0.5 each. Given the pressure P and the energy density ϵ, we use Eq. (2.11) to parametrize the EOS as a function of the pseudo-enthalpy h such that we obtain $P(h)$ and $\epsilon(h)$.

We study non-rotating neutron stars by using the framework presented in Sec. 3.2 in combination with the reformulation presented in Sec. 3.6 and construct a sequence of neutron stars parametrized by the central value of the pseudo-enthalpy h_c which ultimately results in $M(h_c)$ and $R(h_c)$. While solving the TOV equations, we verify that the causality constraint is fulfilled. When the maximum neutron star mass $M_{\rm max}$ for the considered EOS is approached, we check if this mass is as least as high as the imposed mass constraint. Consequently, we obtain the mass-radius relation for each EOS compatible with the imposed constraints. We find $\sim 10^5$ EOS that fulfill the constraints using the discussed approach. From the EOS that are in accordance with the constraints, we determine the envelopes in the EOS as well as mass-radius space. In the left panel of Fig. 4.1, we show the resulting uncertainty band for the piecewise polytropic EOS model. Inside this uncertainty band only EOS that fulfill the demanded constraints are present. Comparing the left panel of Fig. 4.1 with the results shown in Ref. [137], we encounter a slightly larger uncertainty band for low energy densities and pressures with respect to the polytropic expansion. The resulting mass-radius uncertainty band is shown in the right panel of Fig. 4.1. Based on this, we provide an uncertainty range for the radius of a $1.4\,M_\odot$ neutron star where we find $R_{1.4\,M_\odot} = 9.97 - 13.65\,\text{km}$ and the central densities for this mass are in the range of $\rho_{c,\,1.4\,M_\odot} = 1.7 - 4.4\,\rho_0$. The maximum central density is $\rho_{c,\,\rm max} \approx 8.3\,\rho_0$ agrees with the findings from Ref. [137]. Further, we determine the mass of the most massive neutron star which we find to be $M_{\rm max} = 2.92\,M_\odot$.

In Ref. [137], a set of representative EOS[1] was introduced. This set consists of three EOS, i.e., a *soft*, an *intermediate*, and a *stiff* one, that allow to probe the mass-radius envelope. The soft and intermediate EOS are both matched to the lower limit of the chiral EFT band. The parameters of the soft EOS are $\Gamma_1 = 1.5$, $\Gamma_2 = 6.0$, $\Gamma_3 = 3.0$, $\rho_{12} = 2.5\,\rho_0$, and $\rho_{23} = 4.0\,\rho_0$. The intermediate EOS is given by the parameters $\Gamma_1 = 4.0$, $\Gamma_2 = 3.0$, $\Gamma_3 = 2.5$, $\rho_{12} = 3.0\,\rho_0$, and $\rho_{23} = 4.5\,\rho_0$. The stiff EOS is matched to the upper limit of the chiral EFT band and its parameters are $\Gamma_1 = 4.5$, $\Gamma_2 = 5.5$, $\Gamma_3 = 3.0$, $\rho_{12} = 1.5\,\rho_0$, and $\rho_{23} = 2.0\,\rho_0$ [137]. We also show these representative EOS and the corresponding mass-radius relations in Fig. 4.1 and we adapt the same color coding and linestyle as used in Ref. [137], i.e., the soft EOS is shown as a dashed green line, the intermediate EOS as solid orange, and the stiff EOS is presented as a dash-dotted red line.

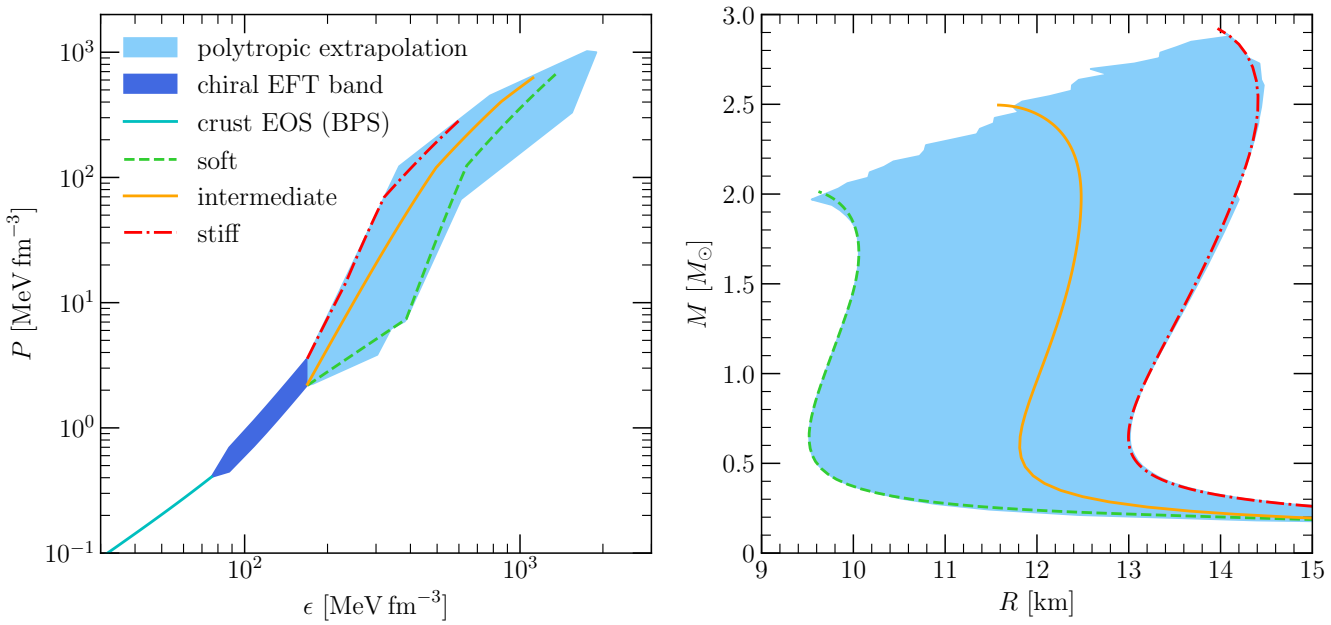

Figure 4.1.: *Left panel*: Pressure P as a function of the energy density ϵ. The light blue band results from the polytropic extrapolation used in Ref. [137] and summarized in this thesis. Note that the shown envelope is smoothed. The dark blue band depicts the chiral EFT uncertainty band from Hebeler *et al.* [137] (see also Ref. [136]). In addition, we show the results for the three representative EOS (soft, intermediate, and stiff). In contrast to Ref. [137], we found a bump with a less steep slope than the authors of Ref. [137]. Moreover, we show the BPS crust EOS [31, 203]. *Right panel*: Resulting mass-radius uncertainty band in light blue for the polytropic EOS model discussed in the text. The results for the chiral EFT band and the BPS crust EOS are for too large radii not shown here.

Next, we explore the EOS and mass-radius space for the speed of sound parametrization discussed in Sec. 2.3.3. Parts of the results discussed here were published in Ref. [118]. We apply the parameter space shown in Table 2.2 to Eq. (2.23) whereas the parameter a_6 is not determined at that point. The parameter space is discretized such that the parameters a_1, a_2, a_3, a_4, and a_5 have 14 steps. Furthermore, we choose a linear grid for the parameters a_1, a_3, and a_5 and a logarithmic grid for the parameters a_2 and a_4. We ensure that the chosen discretization is fine enough to cover a broad range both in EOS and mass-radius space. As discussed in Sec. 2.3.3, the parameter a_6 is fixed by matching to either the lower

[1] The authors of Ref. [137] provide numerical data for the BPS crust EOS, the lower and upper limit of the chiral EFT band, the representative EOS including the associated radii and masses.

or upper limit of the chiral EFT band[2]. From the matching, we obtain the speed of sound parametrized as a function of the energy density ϵ. We then obtain the pressure P by solving the integral given in Eq. (2.13). Eventually, the EOS is parametrized in terms of the pseudo-enthalpy h what yields $P(h)$ and $\epsilon(h)$ using Eq. (2.11). With the EOS at hand, we solve the TOV equations with the constraints listed in Sec. 2.3.3 and find $\sim 10^5$ EOS.

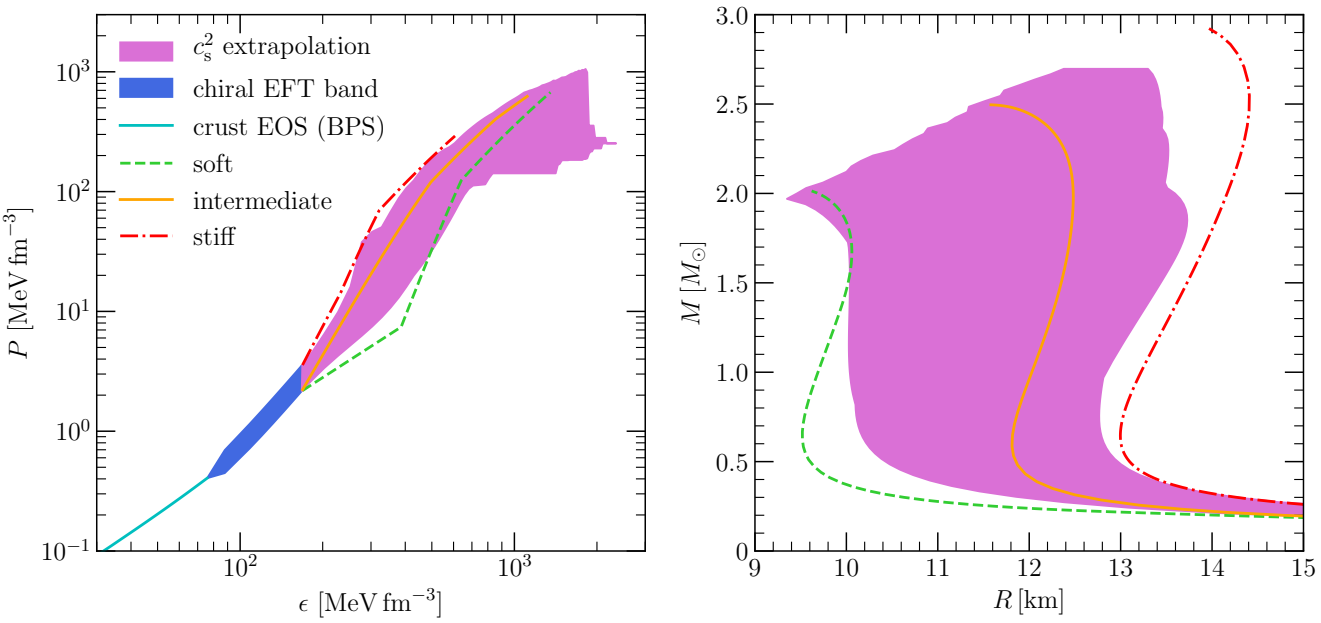

Figure 4.2.: *Left panel*: We show the EOS uncertainty band based on the speed of sound model discussed in the text. *Right panel*: We present the resulting mass-radius uncertainty range. For a comparison, we additionally show the results for the three representative EOS of the piecewise polytropic EOS model.

In Fig. 4.2, we present the resulting uncertainty band for the EOS based on the speed of sound model and the corresponding mass-radius uncertainty range. We also show the results for the three representative EOS of the piecewise polytropic EOS model to provide a qualitative comparison. The presented approach allows us to determine an uncertainty range for the radius of a $1.4\,M_\odot$ neutron star that we find to be $R_{1.4\,M_\odot} = 10.04 - 13.32\,\mathrm{km}$. The radius range for $1.4\,M_\odot$ neutron stars is smaller for the speed of sound model than in the case of the piecewise polytropic EOS model as presented above ($R_{1.4\,M_\odot} = 9.97 - 13.65\,\mathrm{km}$). For the central densities in $1.4\,M_\odot$ neutron stars, we find the range to be $\rho_{\mathrm{c},1.4\,M_\odot} = 1.8 - 4.6\,\rho_0$. The maximal central density $\rho_{\mathrm{c,max}}$ is about $11.0\,\rho_0$. The presented speed of sound parametrization predicts $M_{\mathrm{max}} = 2.72\,M_\odot$ as the maximum neutron star mass which is a somewhat smaller value than predicted by the piecewise polytropic EOS model.

In Fig. 4.3, we provide a qualitative comparison of the polytropic EOS model and the speed of sound parametrization. The piecewise polytropic EOS model covers a larger area in EOS space than the speed of sound parametrization which translates also in a larger covered area in mass-radius space. We identified two reasons for the deviations between the two discussed approaches to the EOS. First, the constraints for the EOS differ in the intermediate-density regime. In the case of the piecewise polytropic EOS model, the parameter space is limited by the values for the parameter Γ_1 (cf. Sec. 2.3.2 for details). Thus, the FLT constraint for the speed of sound parametrization is more restrictive. Due to the FLT constraint, stiff EOS and consequently mass-radius relations with larger radii are discarded. We conclude from this

[2] At this point, we note that it is possible to parametrize the EOS inside the chiral EFT band. Such a parametrization provides improvements in applications such as Bayesian inference (cf. Sec. 4.3.2.1). In collaboration with K. Hebeler, G. Raaijmakers, A. Schwenk, and A. Watts, a new parametrization of the EOS inside the chiral EFT band is in preparation.

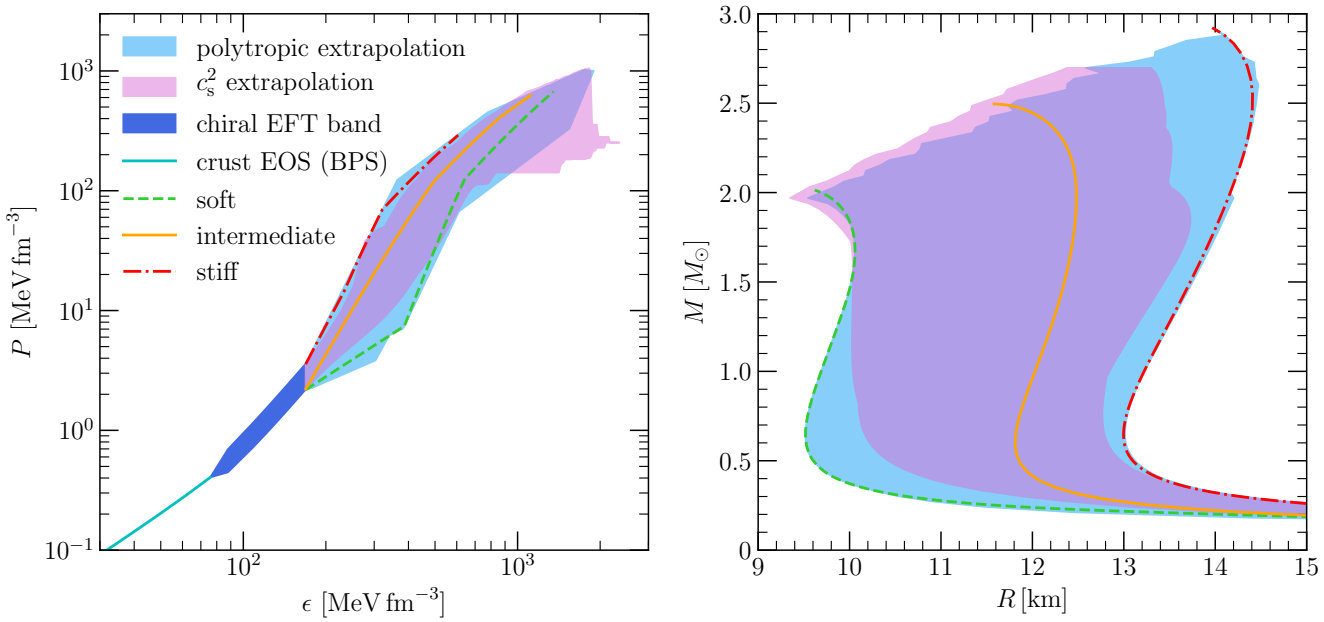

Figure 4.3.: Similar figure as Figs. 4.1 and 4.2. The left panel depicts the EOS space where we additionally show the BPS crust EOS and the chiral EFT band. The right panel features the mass-radius space. In both panels, we show the three representative EOS of the piecewise polytropic EOS model as introduced by Hebeler *et al.* [137]. We present a qualitative comparison between the piecewise polytropic EOS model and the speed of sound parametrization. The piecewise polytropic EOS model covers a larger area in EOS space as well as mass-radius space than the speed of sound parametrization. See the text for the discussion of the reasoning for the deviations between the two models. A similar figure is published in our paper, Ref. [118].

that the upper limit of the radius of typical neutron stars is sensitive to the intermediate-density regime of the EOS. Second, the piecewise polytropic EOS model allows phase transitions followed by a strong stiffening. The stiffening at high densities allows EOS that are soft at lower densities to fulfill the mass constraint. Even though phase transitions are also allowed for the speed of sound parametrization, the strong stiffening is prohibited by the construction of the model (cf. Sec. 2.3.3). Hence, small radii for light neutron stars are not reached in the case of the speed of sound parametrization.

In Chap. 2, we noted that the piecewise polytropic EOS model exhibits unphysical behavior in the speed of sound. In Fig. 4.4, we present the speed of sound c_s/c as a function of the energy density ϵ in the case of the piecewise polytropic EOS model. The results show the discontinuities in the speed of sound that result from the construction of the piecewise polytropic EOS model. In the work of Ref. [34], it was pointed out that the speed of sound in neutron stars has to exceed the value of $c/\sqrt{3}$. The representation of our results in Fig. 4.4 provides no information if every EOS inside the uncertainty band supports this statement. In the following, we investigate the properties of the speed of sound with special focus on thresholds that are exceeded. We choose four speed of sound thresholds $c_{s,1}^{\text{thold}}/c = 1/\sqrt{3}$, $c_{s,2}^{\text{thold}}/c = 0.65$, $c_{s,3}^{\text{thold}}/c = 0.75$, and $c_{s,4}^{\text{thold}}/c = 0.95$. We sample over all EOS inside the uncertainty band of the piecewise polytropic EOS model where we only consider densities larger than $\rho_1 = 1.1\,\rho_0$. For each $c_{s,i}^{\text{thold}}$, we determine $c_s(\rho)$ for increasing densities. For the lowest density $\rho_{c,\min}$ at which $c_s(\rho_{c,\min})$ exceeds $c_{s,i}^{\text{thold}}$, we determine the corresponding mass $M(\rho_{c,\min})$ and radius $R(\rho_{c,\min})$. We present our results in Fig. 4.5. Our results show that $c_{s,1}^{\text{thold}}$ has to be exceeded for densities relevant in neutron stars to fulfill the mass constraint. This result is in accordance with the findings presented in Ref. [34].

Additionally, we determine the maximum speed of sound value $c_{s,\max}$ for every EOS in the uncertainty band. From the collected data for $c_{s,\max}$, we determine the minimal value and find $\min\left(c_{s,\max}\right)/c \approx 0.66$

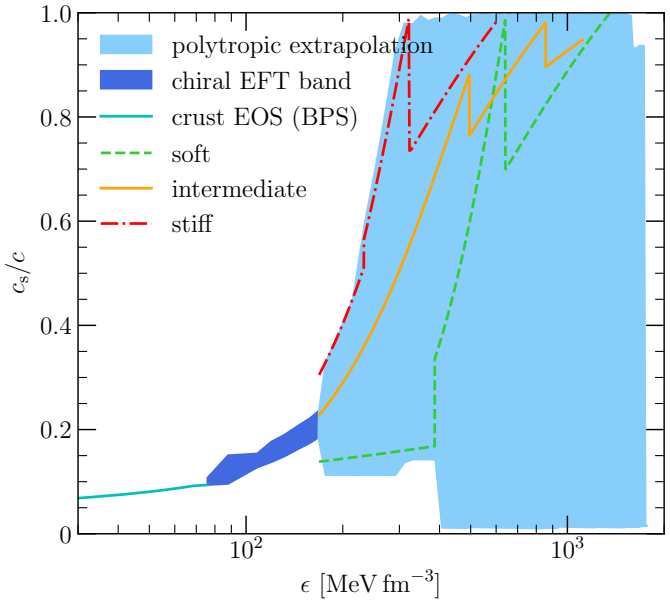

Figure 4.4.: Speed of sound c_s as a function of the energy density ϵ for the piecewise polytropic EOS model. We show the results for the chiral EFT uncertainty band as a dark blue band and in light blue we show the uncertainty band for the whole EOS band. Further, we provide the results for the three representative EOS which clearly show the discontinuity.

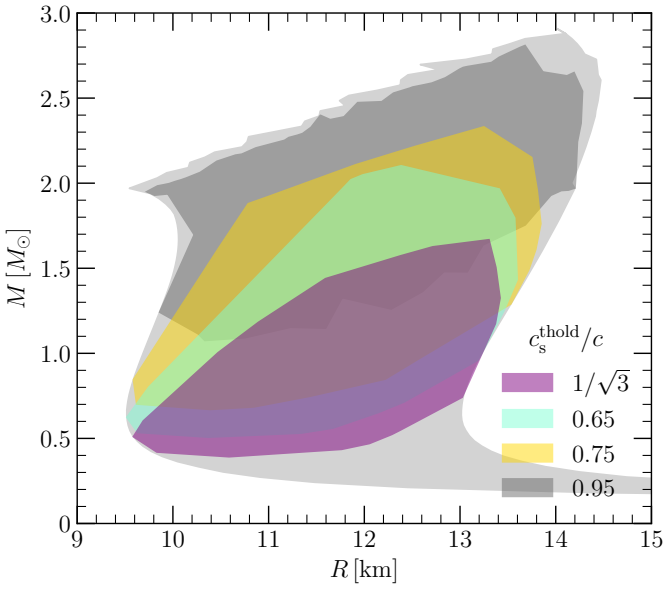

Figure 4.5.: Mass M as a function of radius R. The gray area depicts the entire region allowed by the general EOS construction. The highlighted areas represent M–R pairs that reach values for the speed of sound $c_{s,i}^{\mathrm{thold}}/c \leqslant 1/\sqrt{3}$ (purple), 0.65 (blue), 0.75 (orange), and 0.95 (dark gray).

which is larger than the conformal limit $c_{\mathrm{conf}}/c = 1/\sqrt{3}$. Thus, the findings discussed by Ref. [34] are supported by the piecewise polytropic EOS model. In the case of the speed of sound parametrization, the limit of $1/\sqrt{3}$ is exceeded by the construction of the model [118] (cf. Sec. 2.3.3).

4.2 Correlations among neutron star observables and the equation of state

In the following, we investigate correlations among neutron star observables and EOS parameters. The work of Lattimer and Prakash [177] showed that the radius of typical neutron stars is correlated with the pressure around nuclear saturation density of the underlying EOS. In Ref. [177], a correlation between masses of $M = 1.0\,M_\odot$ and $1.4\,M_\odot$ and the pressure at $n = 1.0\,n_0$, $1.5\,n_0$, and $2.0\,n_0$ was investigated. Taking into account several realistic EOS, the authors found the correlation to follow a power law

$$R_M \approx C(n, M)\,[P(n)]^{0.23-0.26}\,,$$

with the coefficient $C(n, M)$ [177]. According to the authors of the work presented in Ref. [177], the correlation given above is valid for a small range of exponents. A later work by Steiner *et al.* [253] justified that 0.25 is a reasonable choice for the exponent in the expression above, but adjustments can be performed. Accordingly, we consider the correlation given above in the form

$$R_M \approx C(n,\,M)\,[P(n)]^{\frac{1}{4}}\,, \tag{4.1}$$

in this work. A revision of the work presented in Ref. [177] was made by Lattimer and Lim [175] since the observation of $2\,M_\odot$ neutron stars ruled out several EOS that were considered in the initial work. The revised coefficients are given by

$$C(n_0, 1.4\,M_\odot) = 9.52 \pm 0.49\,\mathrm{km}\,,$$
$$C(2\,n_0, 1.4\,M_\odot) = 5.68 \pm 0.14\,\mathrm{km}\,,$$

in the case of $1.4\,M_\odot$ neutron stars [175]. The correlation for $1\,M_\odot$ neutron stars was not revised hence we consider the coefficients found by Lattimer and Prakash [177], i.e.,

$$C(n_0, 1\,M_\odot) = 9.53 \pm 0.32\,\mathrm{km}\,, \tag{4.2}$$
$$C(2\,n_0, 1\,M_\odot) = 5.82 \pm 0.21\,\mathrm{km}\,. \tag{4.3}$$

Such a correlation has the potential to deduce constraints for the EOS and neutron star properties. Experiments and theoretical studies that constrain the pressure around saturation density imply therefore constraints for the radius of neutron stars [174]. Future astrophysical observations might yield mass-radius measurements which can then be used to constrain the pressure around saturation density [174]. We refer the reader to Sec. 1.5 were we summarize low-density properties of the EOS that are influenced by the pressure in the vicinity of saturation density.

In the following, we investigate whether the correlation between the pressure P at low densities and the radius R of typical neutron stars recovers for the piecewise polytropic EOS model. We restrict our considerations to $n = 2.0\,n_0$ since the piecewise polytropic extrapolation starts at $\rho_1 = 1.1\,\rho_0$. We sample over all EOS inside the EOS uncertainty band and determine for each EOS $P(2\,n_0)$ and $R_{1\,M_\odot}$ as well as $R_{1.4\,M_\odot}$. In Fig. 4.6, we show our results for $M = 1\,M_\odot$ in the left panel and for $M = 1.4\,M_\odot$ in the right panel. From our results, we obtain the pressure and radius ranges predicted by the considered EOS model. For the pressure we find the range to be $P(2\,n_0) = 3.9 - 69.6\,\mathrm{MeV\,fm^{-3}}$. For the two neutron star masses we find the radius ranges $R_{1\,M_\odot} = 9.69 - 13.22\,\mathrm{km}$ and $R_{1.4\,M_\odot} = 9.97 - 13.63\,\mathrm{km}$. Further, we present the uncertainty bands discussed in Refs. [175, 177] in the corresponding panels. The presented results for the piecewise polytropic EOS model deviate from the approximative relation. At this point, we stress that the presentation of our results in Fig. 4.6 does not reflect how the results are actually distributed.

In Fig. 4.7, we present the same results as in Fig. 4.6 extended by a color coding for the speed of sound at twice saturation density. This representation of the data allows to explore the distribution of the data.

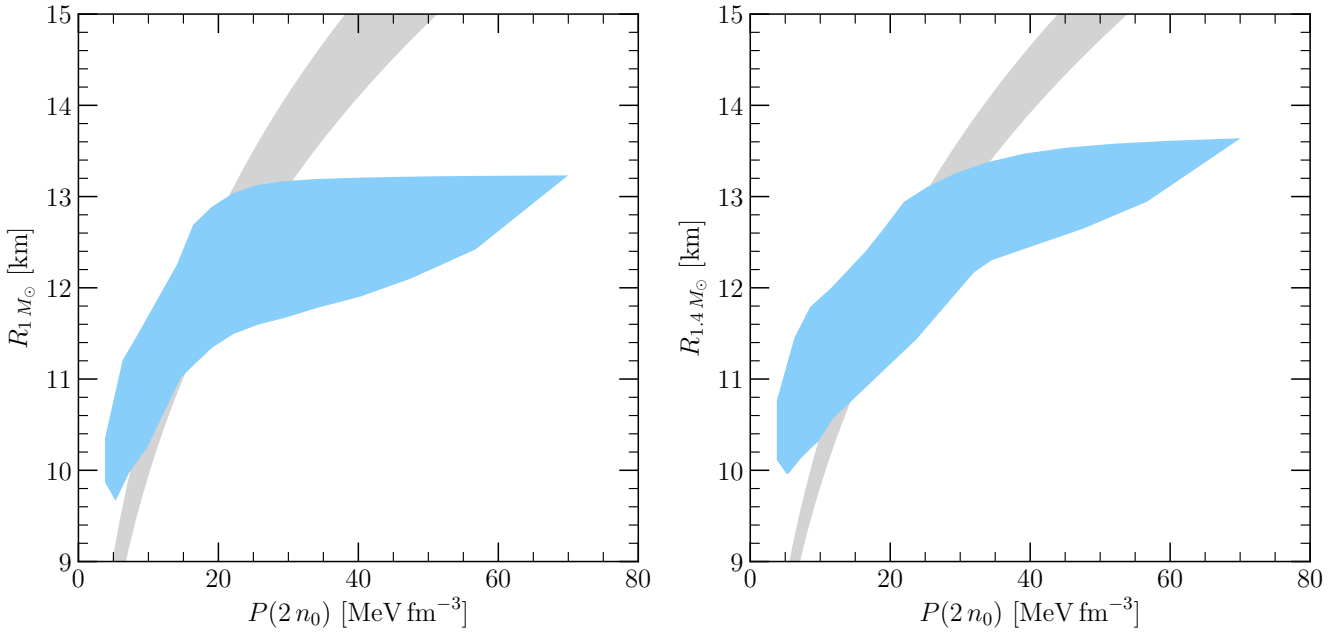

Figure 4.6.: *Left panel*: The radius $R_{1\,M_\odot}$ as a function of the pressure $P(2\,n_0)$. The gray band represents the correlation found by Lattimer and Prakash [177]. *Right panel*: The radius $R_{1.4\,M_\odot}$ as a function of the pressure $P(2\,n_0)$. The gray band represents the uncertainty band found by Lattimer and Lim [175]. In both panels our results for the piecewise polytropic EOS model are shown as the light blue areas. However, we note that the way in which we present our data does not reflect how the actual data points are distributed (cf. Fig. 4.7).

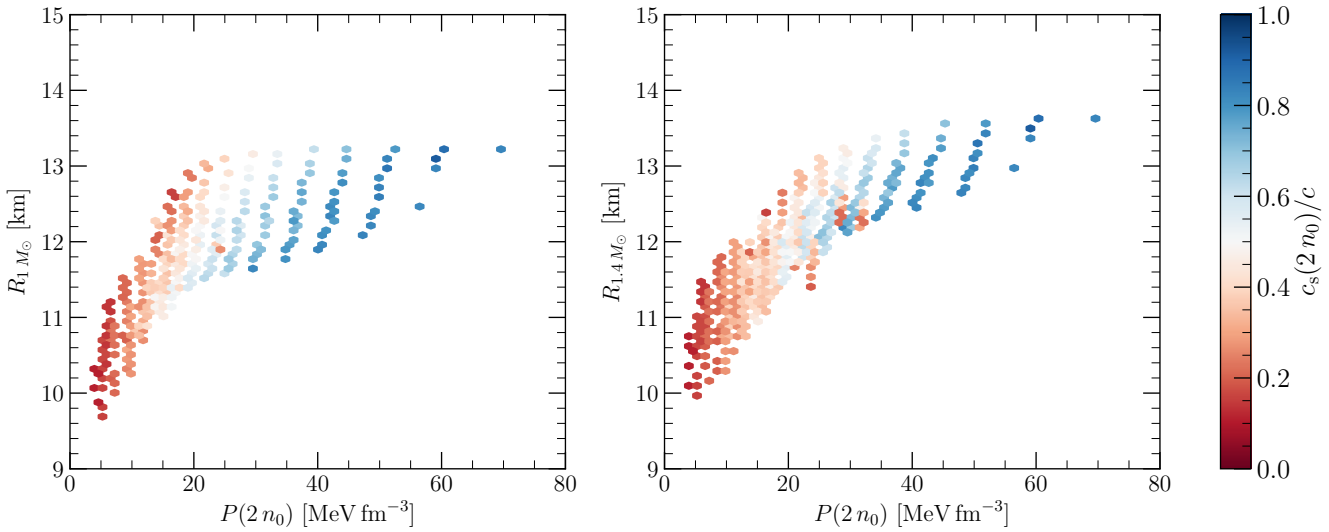

Figure 4.7.: Similar figure as Fig. 4.6. Additionally, we show the speed of sound at twice saturation density as a color coding in the case of the piecewise polytropic EOS model. The speed of sound $c_s(2\,n_0)$ increases for increasing pressure $P(2\,n_0)$ and the data points more dilute.

We observe that the qualitative properties in the case of $1\,M_\odot$ and $1.4\,M_\odot$ neutron stars are comparable and that the speed of sound at twice saturation density increases with simultaneously increasing pressure $P(2\,n_0)$ and radius $R_{1\,M_\odot}$ and $R_{1.4\,M_\odot}$, respectively.

We now investigate whether the discussed correlation is also fulfilled in the case of the speed of sound model parametrization. Our results for the radius of $1\,M_\odot$ and $1.4\,M_\odot$ neutron stars as a function of the pressure evaluated at twice saturation density are shown in Fig. 4.8. As for the piecewise polytropic EOS model we deduce the ranges for the pressure and the radii of the two considered neutron star masses. We find $P(2\,n_0) = 7.8 - 48.8\,\mathrm{MeV\,fm^{-3}}$ for the pressure range. For the radius ranges we find $R_{1\,M_\odot} = 10.04 - 12.84\,\mathrm{km}$ and $R_{1.4\,M_\odot} = 10.04 - 13.32\,\mathrm{km}$. The pressure and radius ranges in the case of the speed of sound parametrization are slightly smaller than in the case of the piecewise polytropic EOS model. Hence, the speed of sound parametrization yields a more narrow correlation than the piecewise polytropic EOS model. The smaller ranges are a consequence of the stronger constraints imposed at low densities in the speed of sound parametrization than for the piecewise polytropic EOS model. From our shown results, we find that the correlation indeed recovers for the speed of sound parametrization. The left panel of Fig. 4.8 shows additionally the uncertainty band from Ref. [177] and the right panel shows the uncertainty band of Ref. [175]. As for the piecewise polytropic EOS model, we observe deviations between the empirically determined relation and our results.

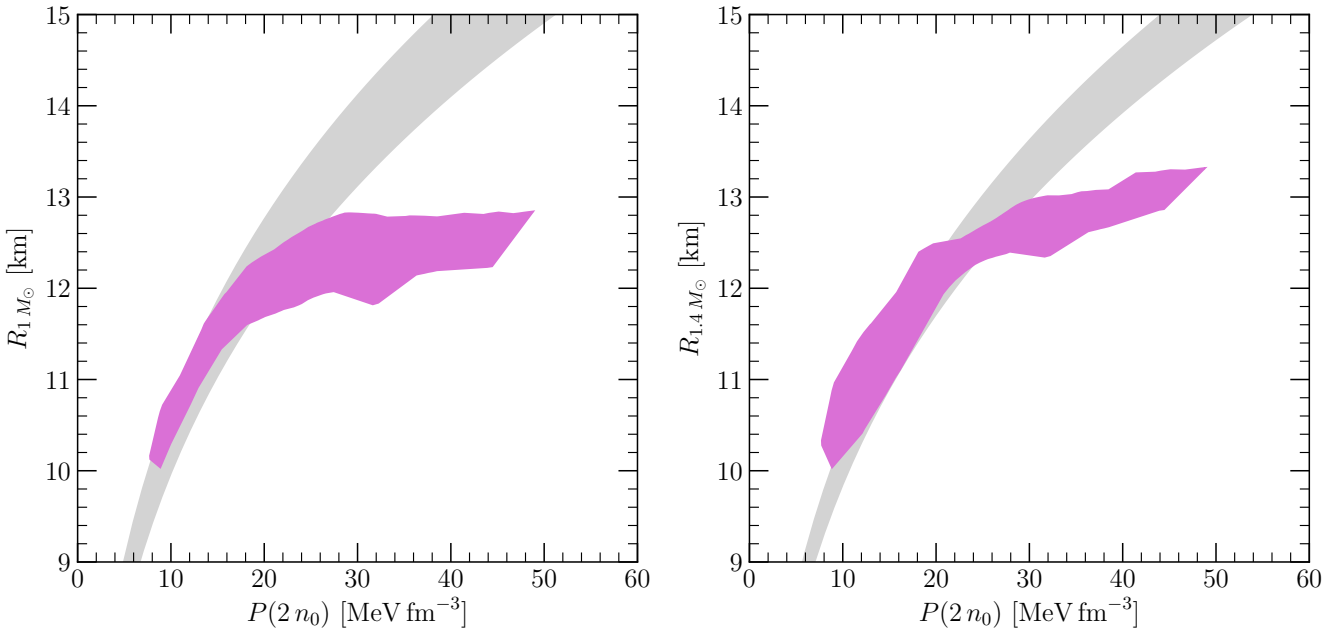

Figure 4.8.: Similar figure as Fig. 4.6. We present the results for the speed of sound parametrization in purple. Additionally, we show the uncertainty bands in gray from Ref. [177] in the left panel and from Ref. [175] in the right panel. See also Fig. 4.9 for a more detailed representation of the shown results.

In Fig. 4.9, we complement our results by additionally showing the speed of sound evaluated at twice saturation density. We observe similarities to the piecewise polytropic EOS model such as the increase in the speed of sound $c_s(2\,n_0)$ with increasing pressure $P(2\,n_0)$. However, for the largest pressures about $45\,\mathrm{MeV\,fm^{-3}}$ at twice saturation density, the corresponding speed of sound decreases.

Besides the mass and the radius of non-rotating neutron stars, we discussed in Chap. 3 an approach to calculate the binding energy. We determine the normalized binding energy BE/M and corresponding compactness parameter $C = M/R$ for a sequence of neutron stars for each EOS of the piecewise polytropic EOS model compatible with the constraints as discussed in Sec. 2.3.2. Subsequently, we determine the envelope of $\mathrm{BE}/M(C)$. In Fig. 4.10, we present the resulting uncertainty band for the neutron star binding energy BE/M as a function of the compactness C. We observe a tight correlation over an extended range of C. For $C \gtrsim 0.25$, the shown results exhibit a broadening of the spread in BE/M. For the

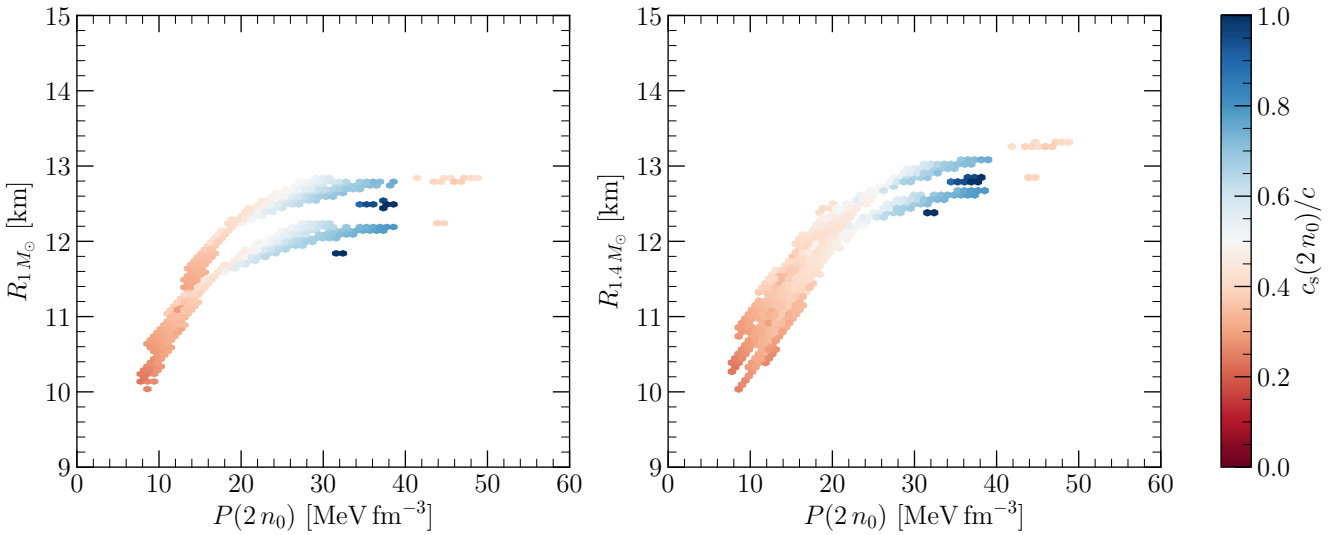

Figure 4.9.: Similar figure as Fig. 4.8. We show the results or the speed of sound parametrization. Additionally, we show a color coding for the speed of sound $c_s(2\,n_0)$ at twice saturation density. The speed of sound at twice saturation density increases with increasing pressure evaluated at the same density. However, the speed of sound decreases for the largest pressures at twice saturation density.

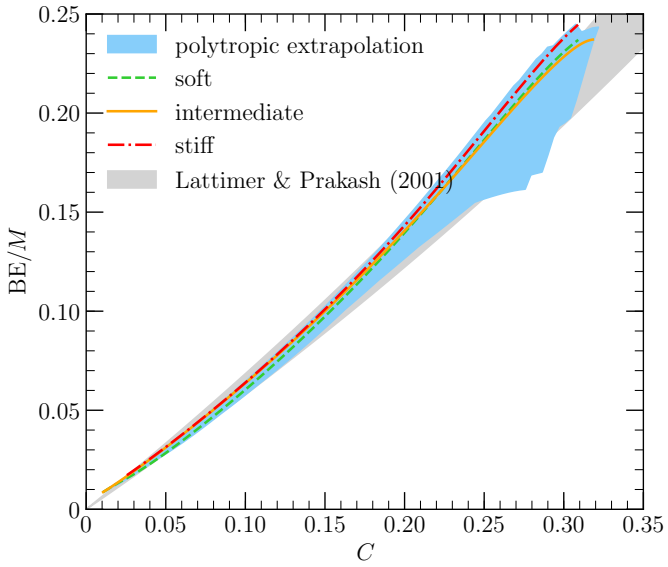

Figure 4.10.: The binding energy of a neutron star BE/M as a function of the compactness parameter C. The light blue band represents the results for the piecewise polytropic EOS model. Additionally, we show the results for the three representative EOS. The gray band depicts the resulting uncertainty band found by Lattimer and Prakash [177].

compactness parameter of typical neutron stars, we find a range of $C_{1.4\,M_\odot} = 0.15 - 0.21$ and we find the range of $\mathrm{BE}_{1.4\,M_\odot} = 0.14 - 0.20\,M_\odot$ for the binding energy of $M = 1.4\,M_\odot$ neutron stars.

In Ref. [177], Lattimer and Prakash investigated the relation between the dimensionless binding energy BE/M as a function of the compactness parameter C for several realistic EOS. An approximative relation is given by [177]

$$\frac{\mathrm{BE}}{M} = \frac{0.6C}{1-0.5C}, \tag{4.4}$$

which accounts for neutron stars with masses of at least $M = 1.65\,M_\odot$. In Fig. 4.10, we additionally show the uncertainty band introduced in Ref. [177] as a gray band. The uncertainty band of the piecewise polytropic EOS model is in good agreement with the results found by Lattimer and Prakash [177]. The authors of Ref. [175] utilized the approximative relation for the binding energy above to derive constraints for typical neutron stars. Hereto, experimental limits for the symmetry parameters S_v and L (cf. Sec. 1.5) were used to obtain estimates for the radius $R_{1.4\,M_\odot}$ of $M = 1.4\,M_\odot$ neutron stars. As a result, the authors obtained a range for the binding energy for $M = 1.4\,M_\odot$ neutron stars, i.e., $\mathrm{BE}_{1.4\,M_\odot} \approx 279^{+35}_{-25} \times 10^{51}$ erg which is equivalent to $\mathrm{BE}_{1.4\,M_\odot} \approx 0.14 - 0.18\,M_\odot$ [175]. Hence, our result ($\mathrm{BE}_{1.4\,M_\odot} \approx 0.14 - 0.20\,M_\odot$) is in good agreement with the findings of the literature presented in Ref. [175].

4.3 Inference of constraints for the radius and the equation of state

In the present section, we derive constraints for the radius of neutron stars and the nuclear EOS based on hypothetical neutron star observations. Hereto, we assume hypothetical mass-radius scenarios based on the primary science targets of the NICER mission. We utilize the unique relation between the EOS and the mass-radius relation.

In this section, we investigate the impact of mass-radius measurements on the EOS. Further, we investigate whether the choice of the parametrization impacts the inference of EOS constraints. In this work, we compare the established piecewise polytropic EOS model and the speed of sound parametrization. We use two approaches for the inference. First, we sample over all EOS inside the according uncertainty bands and keep the EOS and mass-radius relations that are consistent with the considered mass-radius measurements. Second, we use Bayesian inference to obtain EOS constraints resulting from mass-radius observations. The calculations using Bayesian inference where done by G. Raaijmakers and A. Watts using the protocol outlined in Ref. [230].

The following is based on the collaborative work that was done together with G. Raaijmakers, K. Hebeler, A. Schwenk, and A. Watts and originally published in Ref. [118].

4.3.1 Configurations of mass-radius posterior distributions

In order to compare different methods of constraining the EOS and the effect the parametrization has on these constraints, we explore multiple scenarios of mass-radius posterior distributions. All distributions are modeled as bivariate Gaussian distributions

$$\mathscr{P}(M,R|\mathscr{D},\mathscr{M},\mathscr{I}) = \frac{\sigma_M \sigma_R}{2} \exp\left[-\frac{(M-\mu_M)^2}{2\sigma_M^2} - \frac{(R-\mu_R)^2}{2\sigma_R^2}\right], \tag{4.5}$$

with the mean of the distribution centered on a specific underlying EOS. Note that realistic mass-radius posteriors expected from the waveform modeling technique used by NICER will have some degeneracy between mass and radius (cf. Ref. [198]). However, the differences that might result from different parametrizations of the EOS can be illustrated using simplified posteriors, without a mass-radius degeneracy.

For each scenario of different mass sources, we consider two different underlying EOS: a relatively soft, standard EOS with a radius around 11 km (labelled A); and a more extreme EOS covering a larger spread in radii (labelled B). We then define scenarios that may emerge as a result of the NICER observations.

For the first two scenarios we consider the two primary science targets of NICER [18]: the pulsar PSR J0437 − 4715 with a mass of $1.44 \pm 0.07\,M_\odot$ [226] and PSR J0030 + 0451, for which the mass is unknown. In Case 1 we assume that the mass of this pulsar is $2.0\,M_\odot$ and in Case 2 that it is $1.2\,M_\odot$. In Case 3 and 4 we add two more stars, so that we have four mass-radius posteriors. This is representative of the results eventually expected from NICER. The next two highest priority targets being studied by NICER are PSR J1231 + 1411 and PSR J2124 − 3358; for neither of these stars the mass is known. For Case 3 we assume that the three unknown masses lie relatively closely together: $1.4\,M_\odot$, $1.5\,M_\odot$, and $1.7\,M_\odot$. In Case 4 we take them to be more widely spread: $1.2\,M_\odot$, $1.7\,M_\odot$, and $2.0\,M_\odot$. This is obviously far from exhaustive, but lets us explore a range of representative scenarios.

We then add a random scatter to all masses and radii drawn from a Gaussian distribution centered on the EOS with a standard deviation of 3% of the chosen mass and radius values, except for the known neutron star mass. The uncertainties of the distributions, σ_M and σ_R, are randomly picked from a uniform distribution between $5 - 10\%$ of the central mass-radius values, except again when the mass is known. As each of these configurations is considered with two different underlying EOS, we have a total number of eight scenarios and provide numerical values of the considered mass-radius scenarios in Table 4.1. At this point, we note that the 1σ errors given in Table 4.1 need to be modified in order to obtain the semi-major and semi-minor axes of the ellipses of the assumed mass-radius measurements. From a χ^2 table we obtain a factor of 2.28 in the case of two degrees of freedom and a 68% credibility interval. Consequently, the lengths of the axes are determined by

$$\Delta_i = \sqrt{2.28 \cdot \sigma_i^2},$$

where i stands for M and R. In Fig. 4.11, we present an overview of the considered mass-radius scenarios in comparison with the unconstrained mass-radius uncertainty bands for the piecewise polytropic EOS model and the speed of sound parametrization.

Table 4.1.: Masses and radii of the considered hypothetical mass-radius measurements. The according uncertainties are chosen randomly to be between 5% and 10% except for the neutron star with the known mass of $1.44\,M_\odot$.

Case	$M\,[M_\odot]$	$R\,[\mathrm{km}]$	Case	$M\,[M_\odot]$	$R\,[\mathrm{km}]$
1A	1.44 ± 0.07	10.74 ± 0.61	1B	1.44 ± 0.07	12.30 ± 0.92
	2.01 ± 0.11	11.21 ± 0.75		2.10 ± 0.12	10.81 ± 0.74
2A	1.44 ± 0.07	11.58 ± 0.60	2B	1.44 ± 0.07	12.06 ± 0.64
	1.22 ± 0.08	10.89 ± 0.72		1.16 ± 0.07	13.08 ± 0.80
3A	1.44 ± 0.07	10.72 ± 0.83	3B	1.44 ± 0.07	12.42 ± 0.83
	1.67 ± 0.12	10.70 ± 0.85		1.68 ± 0.11	11.90 ± 0.79
	1.40 ± 0.08	10.86 ± 0.75		1.39 ± 0.10	12.08 ± 0.81
	1.53 ± 0.09	11.01 ± 0.80		1.41 ± 0.09	11.63 ± 0.61
4A	1.44 ± 0.07	11.21 ± 0.61	4B	1.44 ± 0.07	11.95 ± 0.76
	1.77 ± 0.10	11.18 ± 0.61		1.68 ± 0.13	11.81 ± 0.65
	1.16 ± 0.07	10.73 ± 0.72		1.25 ± 0.08	12.40 ± 0.69
	2.02 ± 0.12	10.66 ± 0.70		2.01 ± 0.15	12.11 ± 0.75

In the case of the sampling, we basically iterate over all allowed EOS of the two discussed EOS approaches for each mass-radius scenario. We then determine the mass-radius relations that are compatible with each mass-radius measurement of the considered scenario. In the end, we determine the envelopes of the resulting constrained areas in mass-radius space. This could be termed a simple compatibility cut. We note that in general these regions could be used as a very conservative estimate of the EOS that would have a finite probability when inference is performed. We present our results in Fig. 4.12. The results for the piecewise polytropic EOS model and the speed of sound parametrization are overall in good

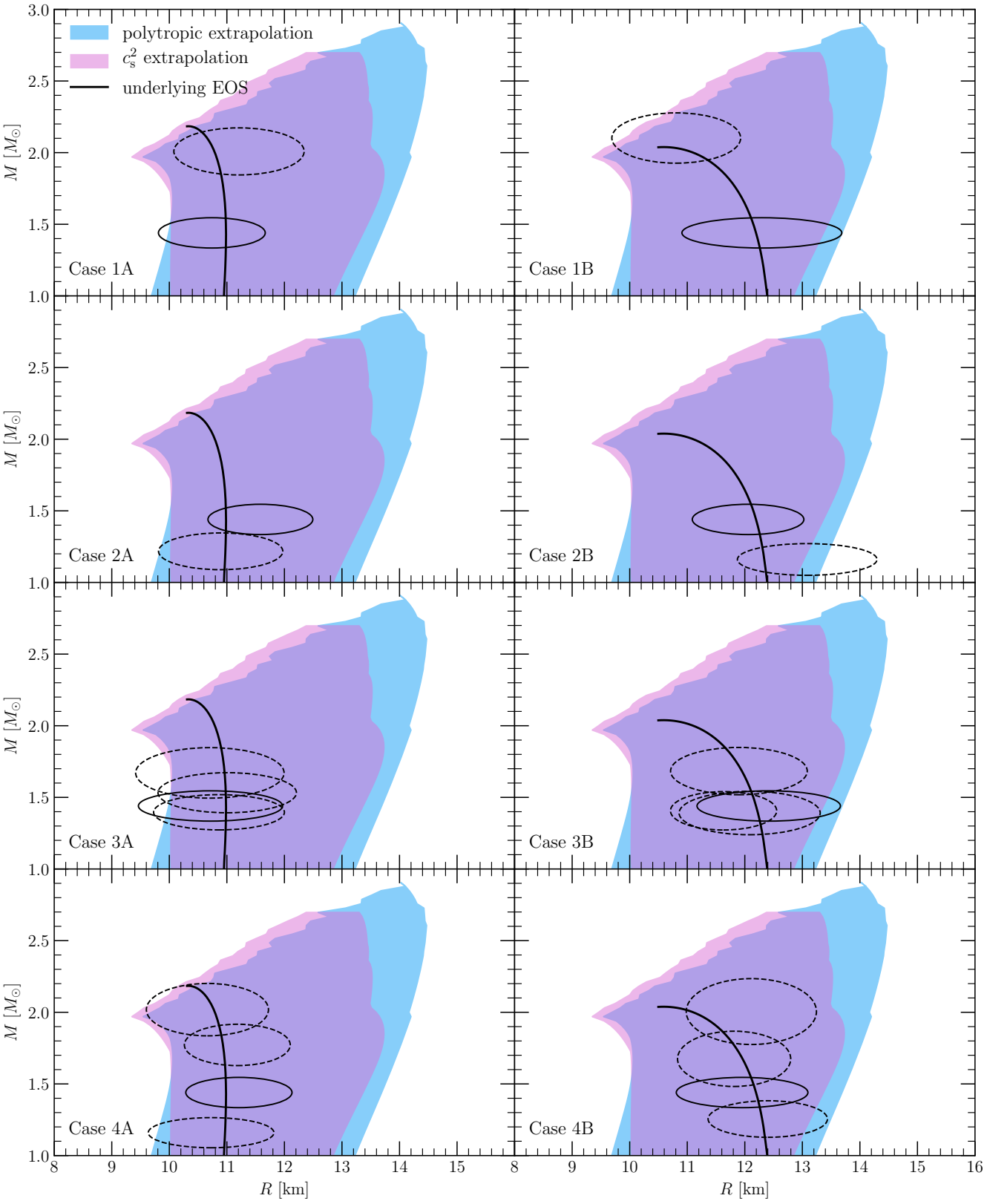

Figure 4.11.: Every panel shows the mass-radius relation of the underlying EOS whereas a soft EOS was assumed for the left panels and a stiff EOS for the right panels. The ellipses indicate the hypothetical mass-radius measurements (cf. Table 4.1) where solid outlines depict the cases of known neutron star mass of the source PSR J0437−4715 and dashed outlines depict the cases of unknown masses. A similar figure is published in our paper, Ref. [118].

agreement. By comparing the scenarios of the underlying soft EOS with the scenarios of the underlying stiff EOS, we observe that in the case of the stiff EOS the deviations between the models are larger than in the case of the soft EOS. We encounter the largest differences in 'Case 1B.' This case considers a light neutron star with a large radius and a heavy neutron star with a small radius. This particular combination is realized by EOS that exhibit a strong enough softening in the high-density regime. The piecewise polytropic EOS model allows more extreme changes for the EOS than the speed of sound model which explains the larger area covered by the polytropic model in 'Case 1B' as shown in Fig. 4.12. In each case, the mass-radius relation of the underlying EOS falls within the constrained mass-radius areas. Thus, the underlying EOS is recovered by the simple approach of applying compatibility cuts. Our results indicate that simultaneous mass-radius measurements can provide strong constraints on the EOS.

So far, we explored the impact of mass-radius measurements on the mass-radius space. We now investigate the impact of such measurements on the EOS. Hereto, we first determine the EOS that are consistent with the hypothetical mass-radius measurements for each case. Then, we determine the envelope of the remaining EOS and show our results in Fig. 4.13 for the piecewise polytropic EOS model and in Fig. 4.14 for the speed of sound parametrization. For both models, we observe a reduction in the EOS parameter space. Thus, the considered mass-radius scenarios yield constraints for the nuclear EOS. Depending on the actual scenario, either soft EOS or stiff EOS are ruled out by the hypothetical measurements. As the results for the mass-radius constraints indicate, the assumed underlying EOS is in all cases recovered.

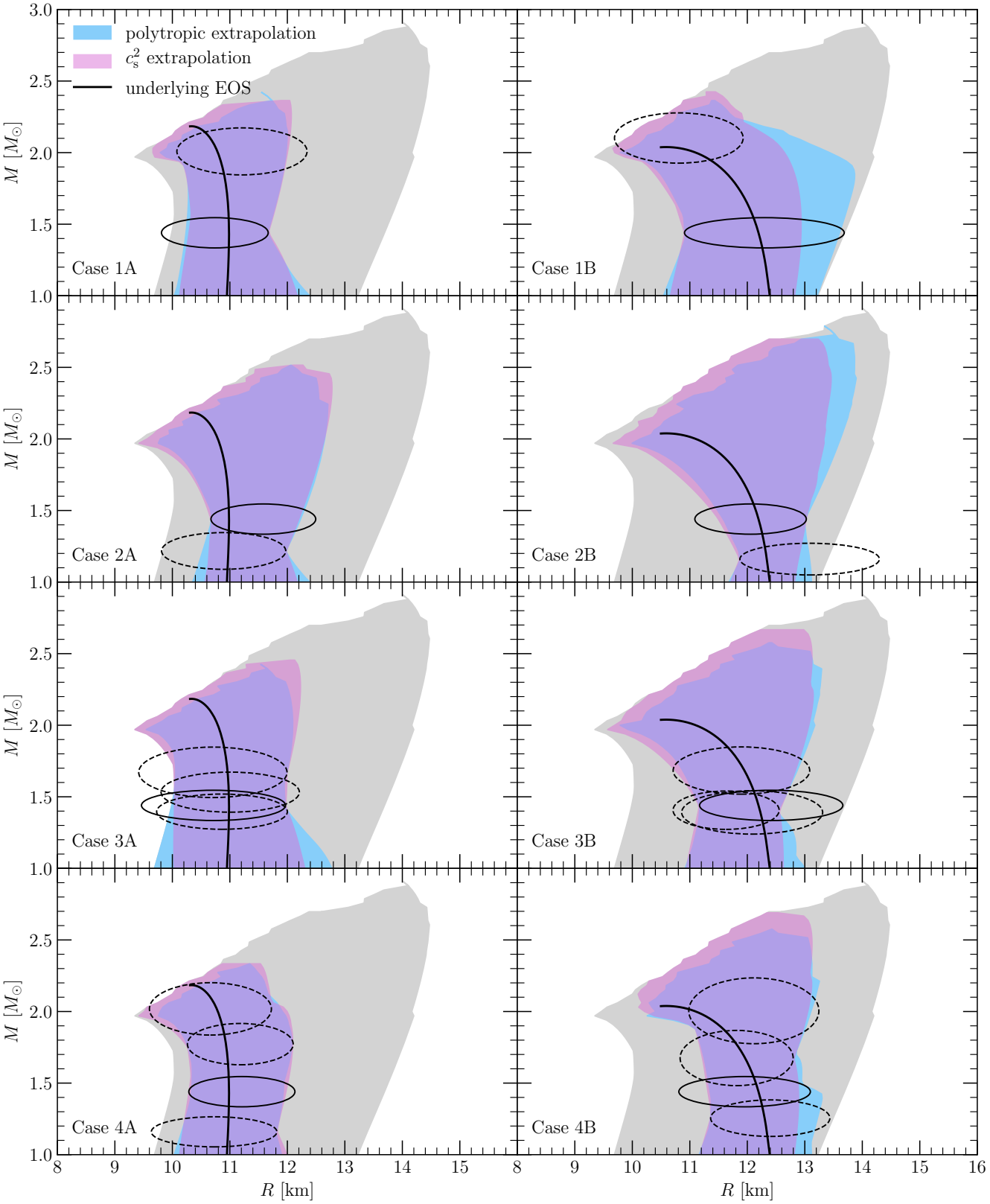

Figure 4.12.: Similar figure as Fig. 4.11. The light blue and purple areas represent the mass-radius regions of the piecewise polytropic EOS model and the speed of sound parametrization, respectively, that are consistent with the assumed mass-radius measurements indicated by the ellipses. The gray band indicates the unconstrained uncertainty bands of both models. A similar figure is shown in our paper, Ref. [118].

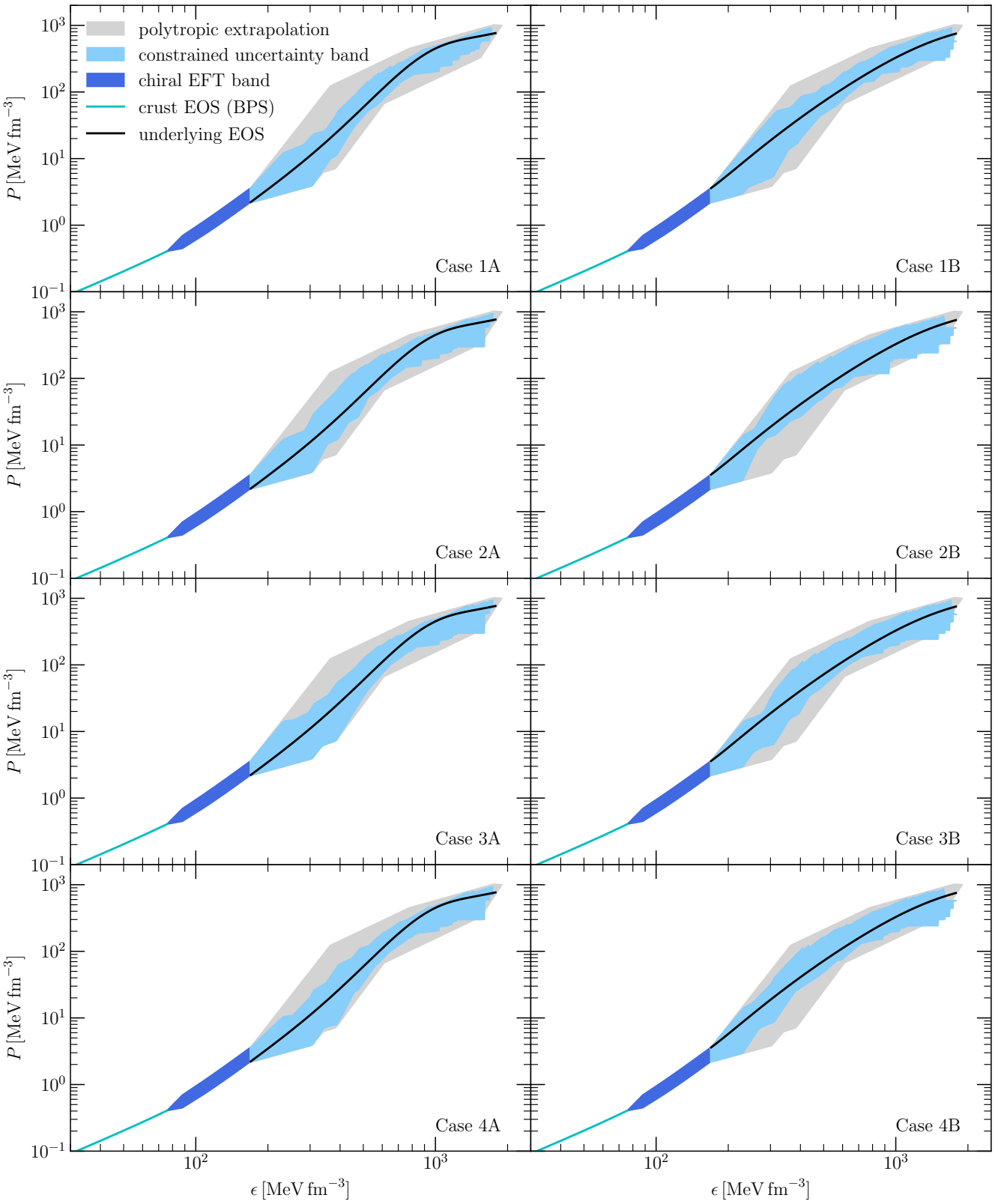

Figure 4.13.: In every panel, we show the pressure P as a function of the energy density ϵ. For comparison, we additionally show the BPS crust EOS, the chiral EFT band, and the uncertainty band from the piecewise polytropic EOS model. We present the constrained EOS band for the piecewise polytropic EOS model under the consideration of the mass-radius scenarios as listed in Table 4.1.

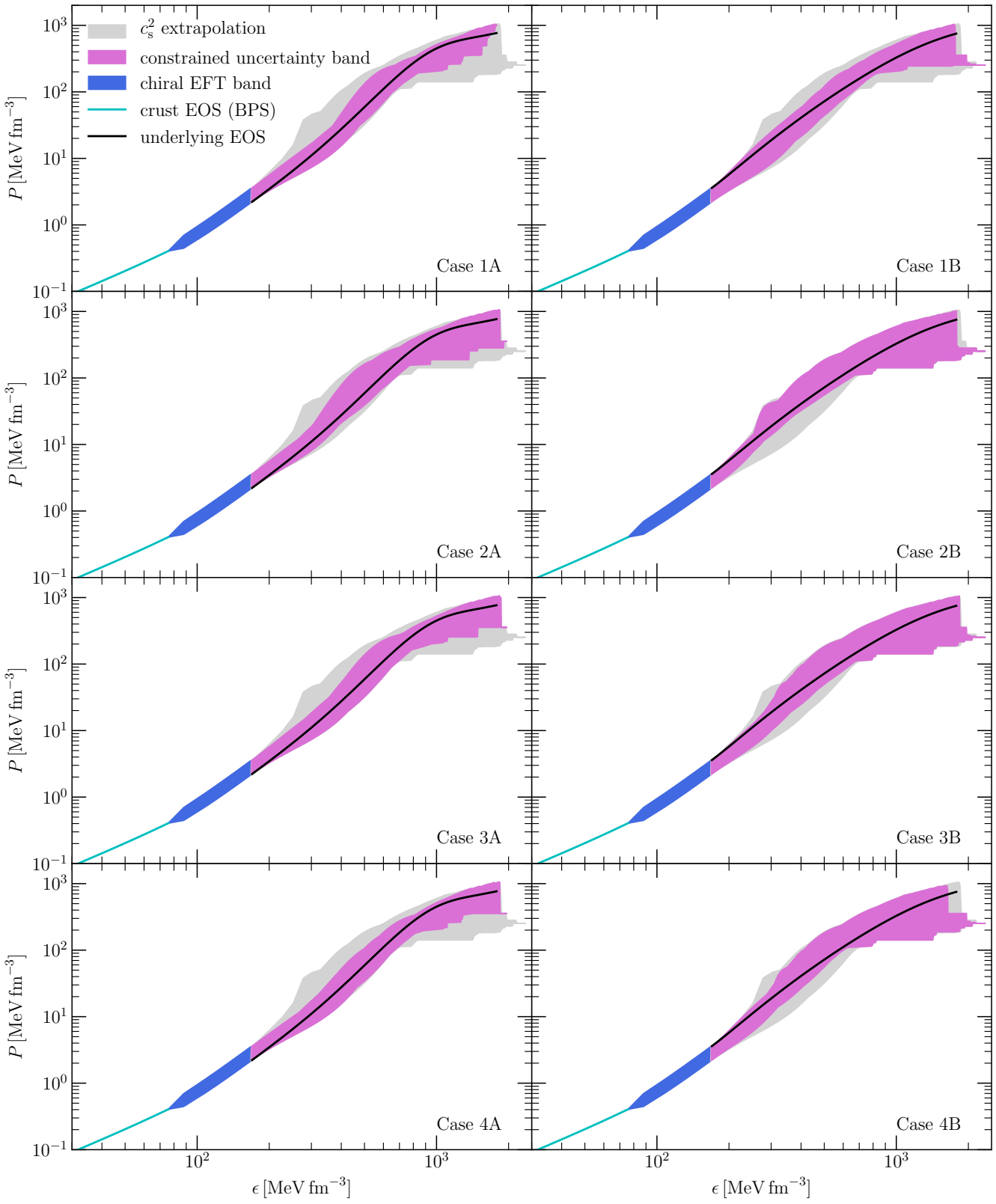

Figure 4.14.: Similar figure as Fig. 4.13. We show in light gray the unconstrained EOS uncertainty band of the speed of sound parametrization. The different panels show the envelopes obtained by considering the mass-radius scenarios presented in Table 4.1 and performing simple compatibility cuts.

4.3.2 Inferring equation of state constraints using Bayesian statistics

So far, we investigated the impact of mass-radius measurements on the EOS by considering simple compatibility cuts. We now discuss a more sophisticated approach to infer EOS parameters using Bayesian statistics. Other works that infer EOS parameters using Bayesian statistics can be found in Refs. [183, 209, 250].

We start with providing a short introduction into Bayesian statistics. A thorough introduction can be found in Ref. [272]. The basic idea of Bayesian statistics is to associate a probability with a hypothesis. This probability is then improved with the help of prior knowledge. In the framework of Bayesian statistics, this is summarized in Bayes theorem which is stated as

$$\mathscr{P}(A|B) = \frac{\mathscr{P}(B|A)\,\mathscr{P}(A)}{\mathscr{P}(B)}\,, \tag{4.6}$$

where A refers to a set of parameters and B to the given data. Further, $\mathscr{P}(A)$ denotes the *prior* distribution and $\mathscr{P}(B)$ denotes the likelihood of the observed data marginalized over all possible parameters. In the expression above, $\mathscr{P}(A|B)$ denotes the conditional probability of the event A occurring that B is true – this is the *posterior* probability distribution. Accordingly, $\mathscr{P}(B|A)$ is the conditional probability of B given that A occurs – this is the *likelihood* [237, 272].

Next, we describe the statistical framework for constraining the EOS using Bayesian inference, following the protocol outlined in Ref. [230]. Using Bayes' theorem, we can write the posterior distribution on the parameters of interest $\boldsymbol{\theta}$, in our case the EOS parameters and central densities (interior parameters), as being proportional to a prior distribution π times the likelihood $\mathscr{L}$,

$$\mathscr{P}(\boldsymbol{\theta}|\mathscr{D},\mathscr{M},\mathscr{I}) = \frac{\pi(\boldsymbol{\theta}|\mathscr{M},\mathscr{I})\,\mathscr{L}(\mathscr{D}|\boldsymbol{\theta},\mathscr{M})}{\mathscr{P}(\mathscr{D}|\mathscr{M},\mathscr{I})} \propto \pi(\boldsymbol{\theta}|\mathscr{M},\mathscr{I})\,\mathscr{L}(\mathscr{D}|\boldsymbol{\theta},\mathscr{M})\,. \tag{4.7}$$

where $\mathscr{D}$ denotes an observational dataset, $\mathscr{M}$ the model used, and $\mathscr{I}$ the Bayesian prior information, such as information from previously analyzed datasets. Because the EOS parameters and the central densities are deterministically related to the mass and radius of a neutron star through the relativistic stellar structure equations (the TOV equations in the non-rotating limit), the following must be true for the likelihood:

$$\mathscr{L}(\mathscr{D}|\boldsymbol{\theta},\mathscr{M}) \equiv \mathscr{L}(\mathscr{D}|\boldsymbol{M},\boldsymbol{R},\mathscr{M})\,. \tag{4.8}$$

Furthermore, for reasons of computational feasibility, we assume

$$\mathscr{L}(\mathscr{D}|\boldsymbol{M},\boldsymbol{R},\mathscr{M}) \propto \mathscr{P}(\boldsymbol{M},\boldsymbol{R}|\mathscr{D},\mathscr{M},\mathscr{I})\,. \tag{4.9}$$

This follows the approach outlined in Section 2.3.4 of Ref. [230], termed the *Interior Prior* paradigm (more robust than the alternative *Exterior Prior* method), but uses the approximative marginal likelihood function of the exterior parameters (mass and radius)[3], to calculate the marginal posterior function of interior (EOS) parameters. It is a computationally less intensive alternative to full direct inference of EOS parameters from the data. As outlined in Ref. [230], this assumption only holds when the prior on mass and radius, which is implicitly defined in the proportionality, is sufficiently non-informative[4]. A second assumption is that the datasets of different observed neutron stars are independent, which allows us to separate the likelihoods and rewrite Eq. (4.7), using Eqs. (4.8) and (4.9), as

$$\mathscr{P}(\boldsymbol{\theta} \mid \mathscr{D},\mathscr{M},\mathscr{I}) \propto \pi(\boldsymbol{\theta} \mid \mathscr{M},\mathscr{I}) \prod_{i=1}^{s} \mathscr{P}(M_i,R_i \mid \mathscr{D}_i,\mathscr{M},\mathscr{I})\,, \tag{4.10}$$

for s the number of observed stars. This method is numerically similar to the methods used in Refs. [209, 221, 250].

[3] Note that these are not actually computed in this work, but directly presented as bivariate Gaussian distributions.

[4] This is expected to be the case for the NICER analysis, even for sources like primary target PSR J0437 − 4715 where the well constrained mass arising from radio observations [226] is treated as a prior; this is because the original radio analysis used a non-informative prior in their computations.

4.3.2.1 Choice of priors

The choice of the prior in Eq. (4.10) can play an important role in the inference of EOS parameters [252] and as such has to be carefully considered. For the piecewise polytropic EOS model as well as for the speed of sound parametrization, we use a uniform, continuous prior for all parameters within the ranges described in Sec. 2.3.2. We impose the five requirements described in Sec. 2.3.3 for the speed of sound parametrization and adopt the requirements from Ref. [137] for the piecewise polytropic EOS model. The prior on the central energy density of the star is chosen as a uniform prior on $\log(\epsilon_c)$, with a lower bound of $\log(\epsilon_c/\mathrm{g\,cm^{-3}}) = 14.6$ and an upper bound that corresponds to the maximum central energy density reached in a neutron star for that given EOS.

To understand the significance of the prior, we sample its distribution for both models and transform it to the space of pressure and energy density as well as to mass and radius. The resulting prior probability distributions are shown in Fig. 4.15, where each histogram contains several times 10^5 samples. Comparing these distributions to the general bands highlighted in Fig. 4.3, one clearly sees much more structure in the distributions than one might naively expect from the bands. For the speed of sound parametrization the structures are qualitatively similar with the sound-speed based parametrization used in Ref. [262]. In the space of pressure and energy density, both models show a narrow region where the distribution is peaked, with the probability density at a given energy density quickly falling off when moving to higher and lower pressures. For both models these regions encompass reasonably stiff EOS, a consequence of enforcing that the EOS supports a $1.97\,M_\odot$ neutron star.

The distribution in mass-radius space shows similar structures, with the 68% credible regions enclosing remarkably narrow radius regions, e.g., for typical $1.4\,M_\odot$ neutron stars less than 1 km for the speed of sound parametrization. From Fig. 4.15 it is also evident that the piecewise polytropic EOS model is even more peaked towards larger radii, especially at masses above $\sim 1.5\,M_\odot$. The apparent bimodality of the 68% credible regions in both models is a consequence of matching the models to the lower and upper limit of the chiral EFT band at the transition density $n_1 = 1.1\,n_0$. The speed of sound parametrization further shows a significant peak just above $2\,M_\odot$. This is a result of the speed of sound decreasing for most EOS at densities around 2×10^{15} g/cm^3 or higher, causing their corresponding mass-radius curves to show only small changes in mass but large changes in radius. The fact that this occurs visibly just above $2\,M_\odot$ is because EOS that do not reach this mass are discarded.

We examine the bimodal features further by introducing a binning. To this end, we set up a two-dimensional grid in both EOS and mass-radius space. We sample then over all EOS compatible with the constraints and determine the distribution of the distinct EOS and mass-radius relations and show our results in Fig. 4.16. In the upper panels of Fig. 4.16, we present our results for the piecewise polytropic EOS model. We confirm that the matching to either the lower or upper limit of the chiral EFT band yields a bimodal structure in both EOS and mass-radius space. Moreover, the number of EOS with radii larger than $R \sim 12$ km is larger than for smaller radii. We further observe that particular mass-radius relations appear rather prominent. This results from the construction of the piecewise polytropic EOS model since subsets of the whole EOS band differ only in the third polytropic segment. Following the same approach, we determine the distribution in EOS space and mass-radius space in the case of the speed of sound parametrization. Our results are shown in the lower panels of Fig. 4.16. As for the piecewise polytropic EOS model, we observe a bimodal structure at low densities and light neutron stars. Moreover, the shown results of the mass-radius distribution are concentrated at large radii. In contrast to the results of the piecewise polytropic EOS model, the speed of sound parametrization exhibits a more smooth distribution of the EOS as well as mass-radius relations.

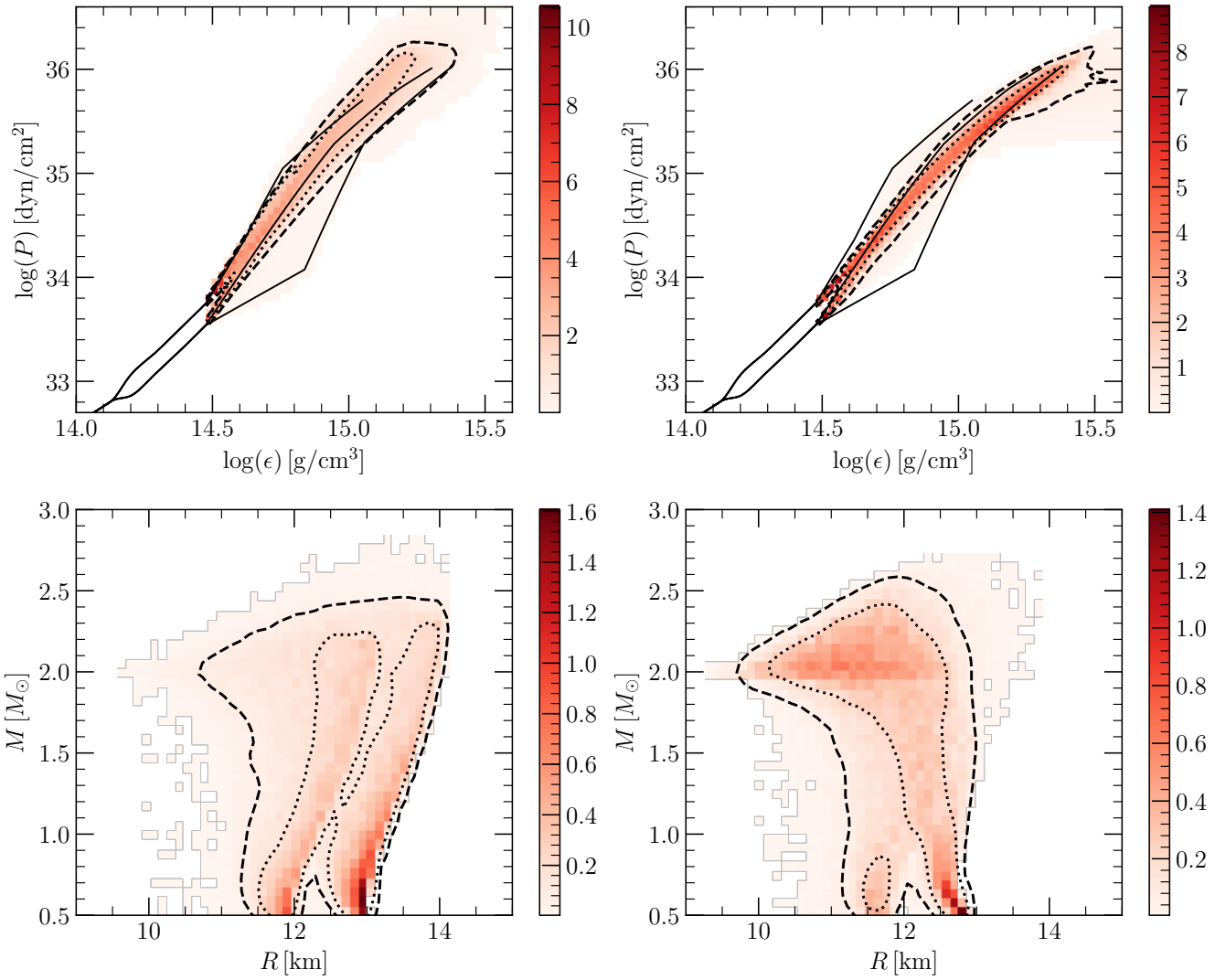

Figure 4.15.: *Top*: Prior probability distributions transformed to the space of pressure as a function of energy density for the piecewise polytropic EOS model (left panel) and speed of sound parametrization (right panel). The dotted and dashed lines indicate the 68% and 95% credible regions of the distributions, while the solid lines are the representative EOS from Ref. [137]. Both prior distributions exhibit a narrow region where most of the probability density is clustered, which falls off steeply towards higher and lower pressures. *Bottom*: Similar to the upper panels, but now the prior distributions are transformed to the space of mass and radius. We observe that the prior constraints from Secs. 2.3.2 and 2.3.3 result in a higher probability density towards larger radii for both parametrizations. The bimodal feature of the distributions are caused by the way the models have been matched to the lower and upper limit of the chiral EFT band. Figure taken from our paper, Ref. [118].

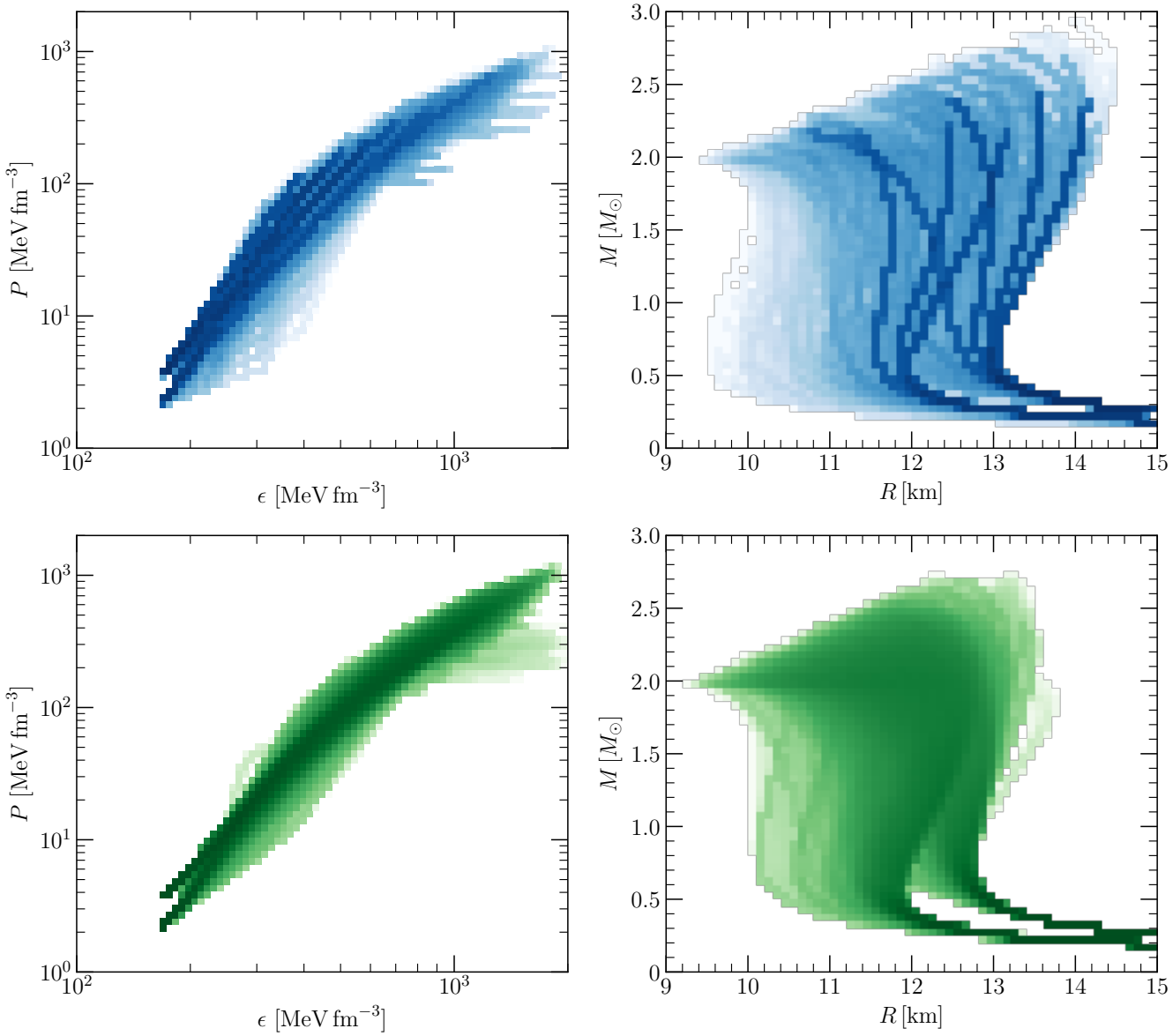

Figure 4.16.: The upper panels refer to the piecewise polytropic EOS model (blue) and the lower panels to the speed of sound parametrization (green). *Left panels*: Distribution of the EOS compatible with the constraints. The chiral EFT band is not shown. *Right panels*: Distribution of the resulting mass-radius relations. The darker the color appears, the more EOS and mass-radius relations are intersecting with the particular bin. Note that the color coding is scaled logarithmically by normalizing the number of EOS and mass-radius relations by taking the logarithm to the base 10.

4.3.3 Posterior distributions

To sample the posterior distribution in Eq. (4.10), we use the Python implementation of the Bayesian inference tool `MultiNest` [55, 96, 97, 98]. `MultiNest` makes use of a sampling technique called Nested Sampling [245], where a fixed number of parameter vectors is kept throughout the sampling (so-called live points), sorted by their likelihood values and drawn randomly from the prior distribution. The parameter vector with the smallest likelihood is replaced each time with a parameter vector with a

higher likelihood, thereby scanning over the full parameter space until the remaining parameter volume becomes small enough and the algorithm terminates.

This work is based on a collaborative research project with G. Raaijmakers and A. Watts. The inference of the posterior distributions is not part of the present thesis. We refer the reader for details to Ref. [118] where we further discuss Bayes factors for a quantitative comparison of the piecewise polytropic EOS model and the speed of sound parametrization.

4.3.3.1 Interior parameter space

For each scenario described in the previous section we obtain from `MultiNest` a set of equally-weighted posterior samples. The posterior distribution on the EOS parameters can then be estimated by binning these samples and applying a smoothing kernel density estimation[5]. Two examples (for Cases 1B and 4A) are given in Figs. 4.17 and 4.18 for the five EOS parameters in the speed of sound parametrization and the piecewise polytropic EOS model. In each subplot the distribution is marginalized over the parameters not shown. For the speed of sound parametrization we include the parameters describing the underlying EOS used to generate the mass-radius posteriors. These might not necessarily be the parameters that receive the most support from the likelihood after adding a random scatter, but they still represent an EOS that is consistent with the mass-radius posteriors.

We can translate this posterior distribution to the space of the EOS by discretizing ϵ_i onto a grid and calculating for each posterior sample the pressure $P = P(\epsilon_i)$. From these pressure values we create a set of one-dimensional histograms at an ϵ_i and subsequently calculate the 95% credible region. The individual credible regions at each ϵ_i are then joined together to obtain a band that represents the 95% credible region of the posterior distribution for the EOS. This is shown in Fig. 4.19. A striking feature of these bands is the narrowing at intermediate densities, which suggests that tight constraints on the physics of dense matter are possible[6]. In most cases the underlying EOS falls within these bands, but in some A scenarios the underlying EOS lies slightly outside for some energy densities. This is a consequence of the prior constraints, which lead to stiffer EOS receiving more prior support (see Fig. 4.15 and the discussion in Sec. 4.3.2.1), which is closer to the B scenarios. When the likelihood encompasses softer EOS, as in the A scenarios, the posterior distribution consequently peaks in the region that has finite support from both the prior and the likelihood, so that the posteriors get shifted to stiffer EOS. Moreover, the horizontal bars in each panel of Fig. 4.19 give the 95% confidence interval for the marginalized posterior distribution of the maximal central energy density reached in neutron stars. This shows the highest central densities that are relevant to neutron stars, which are well below the asymptotic pQCD regime.

In Fig. 4.20 we show the corresponding bands for the speed of sound as a function of the energy density for the speed of sound parametrization. The dark and light green bands correspond to the 95% and 68% credible regions, respectively. For the scenarios shown, the constraints from FLT at lower densities have no significant impact on the posterior distributions. The FLT constraints would become important if a large and heavy neutron star were to be included in the mass-radius posterior distributions (see Fig. 4.11). With increasing densities, the speed of sound increases monotonically well beyond $(c_s/c)^2 = 1/3$ up to energy densities exceeding 10^{15} g/cm^3 for all considered scenarios. Only close to the maximal central energy density (see horizontal bars in Fig. 4.19), when the maximal mass of the neutron star has been reached, does the speed of sound tend to decrease below this value again. This is

[5] In this case we have used a Gaussian kernel density estimation, which means that each bin is estimated as a Gaussian and weighted by its frequency. The full distribution is then a smooth summation of all the individual Gaussians. To determine the parameter k that controls the smoothing, we have used Scott's Rule [242], i.e., $k = n^{-1/(d+4)}$, where n is the number of datapoints and d the number of dimensions.

[6] As a check, we determined the predicted radii of a typical neutron star with a mass of $1.4\,M_\odot$ and the pressure at twice saturation density for each EOS inside the uncertainty band. We found that $R_{1.4\,M_\odot}$ is strongly correlated with $P(2\,n_0)$, which is consistent with the findings by Ref. [175].

due to the softening necessary to remain causal. This shows that the pQCD constraints used in the speed of sound parametrization (see Sec. 2.3.3) are important only for densities well beyond the regime that is relevant for typical neutron stars.

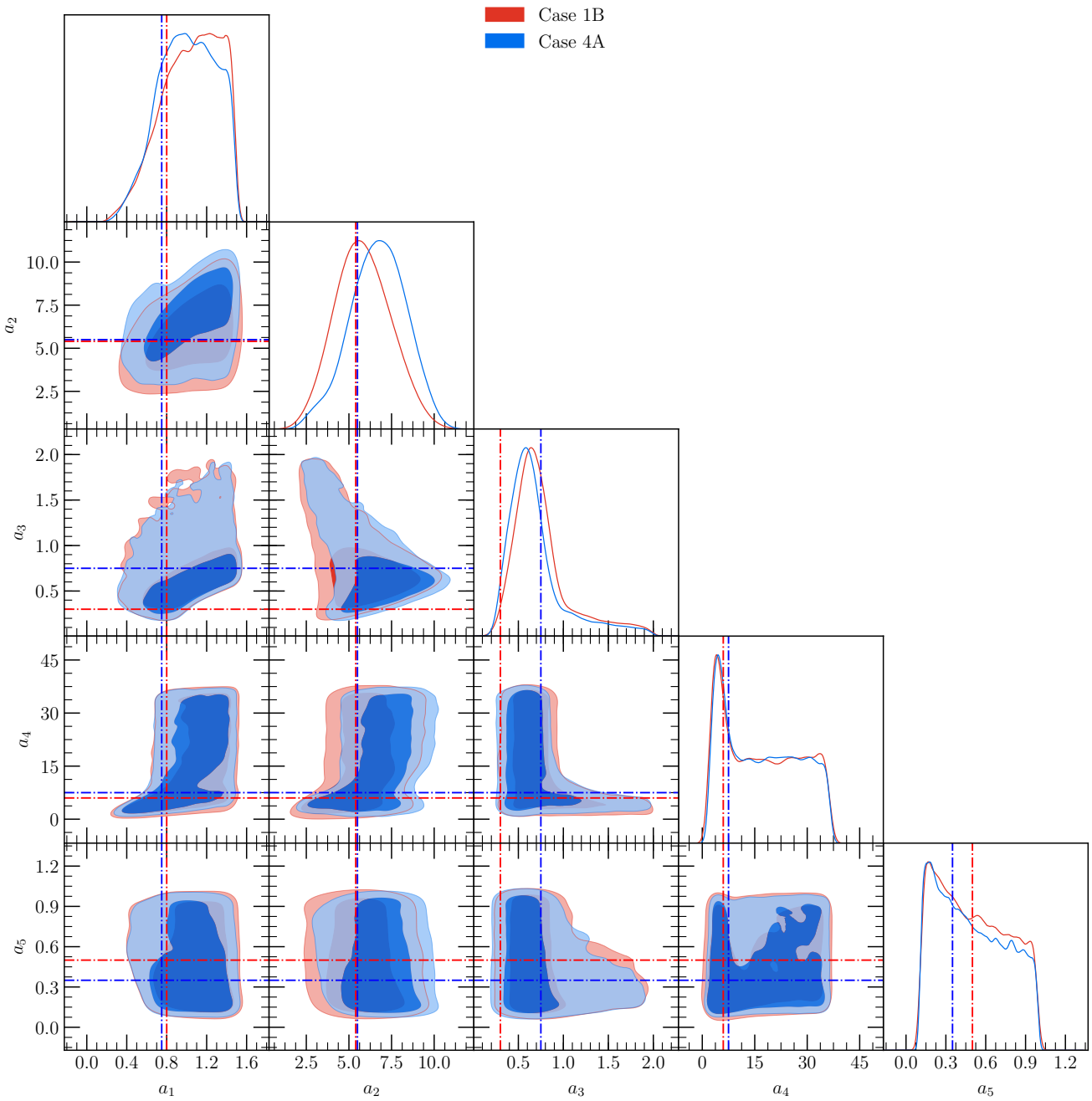

Figure 4.17.: Posterior distributions for the EOS parameters for the speed of sound parametrization for Cases 1B (red) and 4A (blue) (see Fig. 4.11 for both scenarios). The light and dark shaded regions indicate respectively the 68% and 95% credible regions of the two-dimensional marginalized posteriors. The line plots are the one-dimensional marginalized posteriors for each parameter. The dash-dotted blue and red lines give the parameters describing the underlying EOS used to generate the mass-radius posteriors (see Sec. 4.3.1). Figure adapted from Ref. [118].

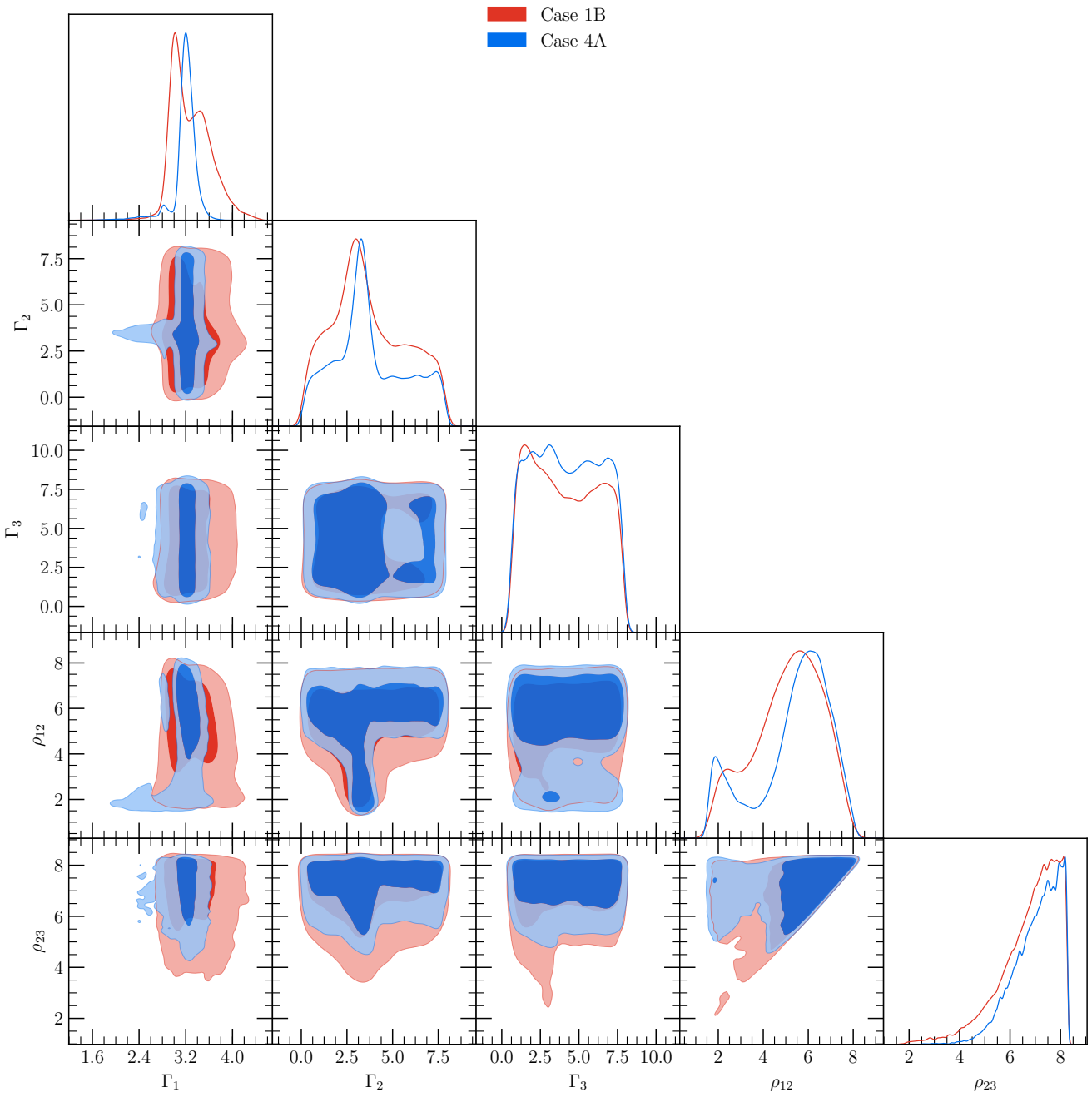

Figure 4.18.: Same as Fig. 4.17 but for the piecewise polytropic EOS model. Figure adapted from Ref. [118].

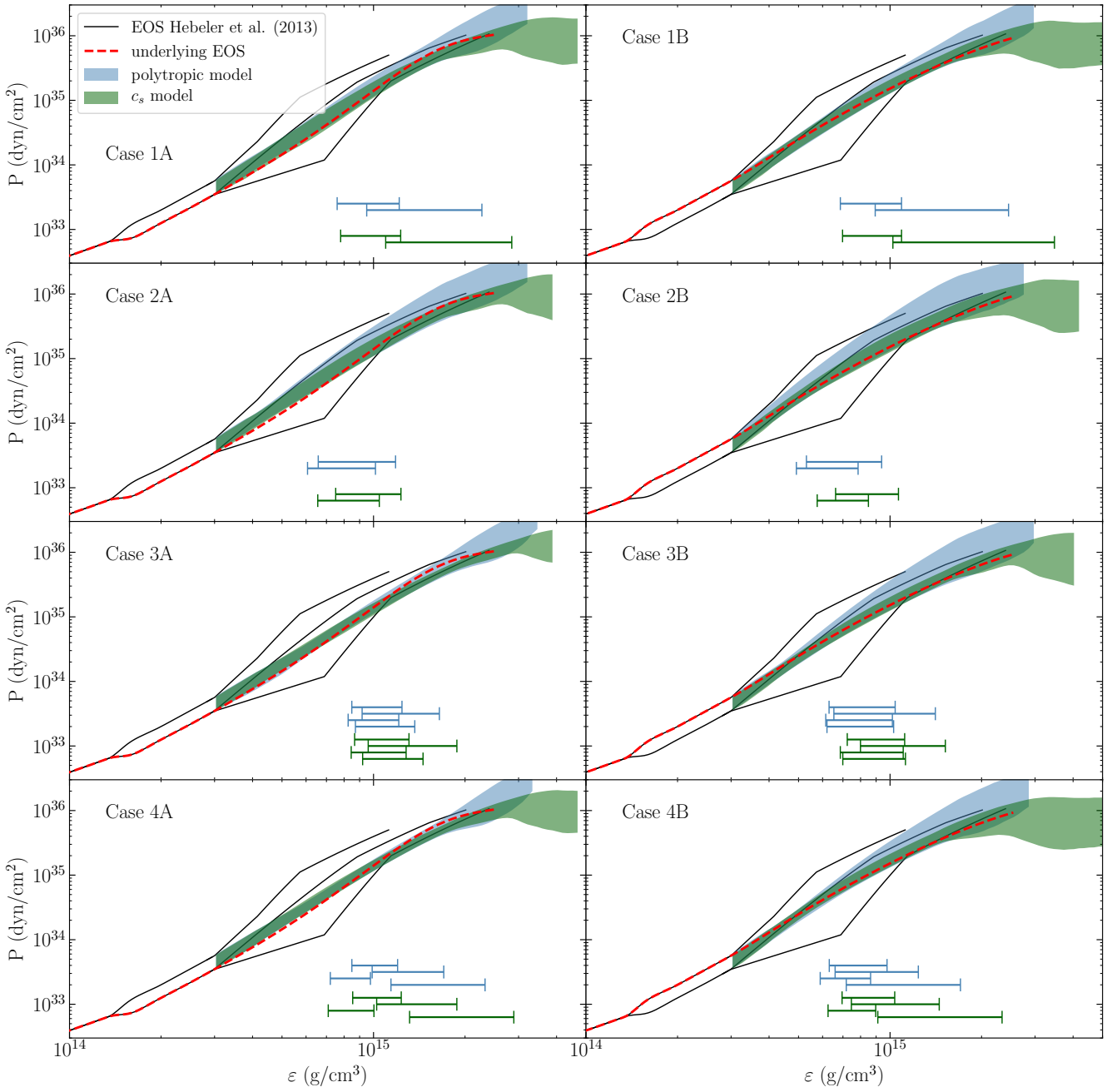

Figure 4.19.: 95% credible regions of the posterior distributions for the EOS for the speed of sound model (green) and the piecewise polytropic EOS model (blue). For comparison, the red dashed line represents the underlying EOS used to generate the mass-radius posteriors, while the black EOS are the three representative EOS from Ref. [137]. The narrow features of the green and blue regions are a result of the prior and the likelihood peaking in different regions of parameter space. Especially for Cases A, the posterior distribution follows closely the edge of the priors in Fig. 4.15, indicating that the posteriors are not completely likelihood-dominated. The green and blue horizontal bars in each panel give the 95% confidence interval for the marginalized posterior distribution of the maximal central energy density reached in neutron stars, for the speed of sound parametrization and the piecewise polytropic EOS model according to the color code. Figure taken from our paper, Ref. [118].

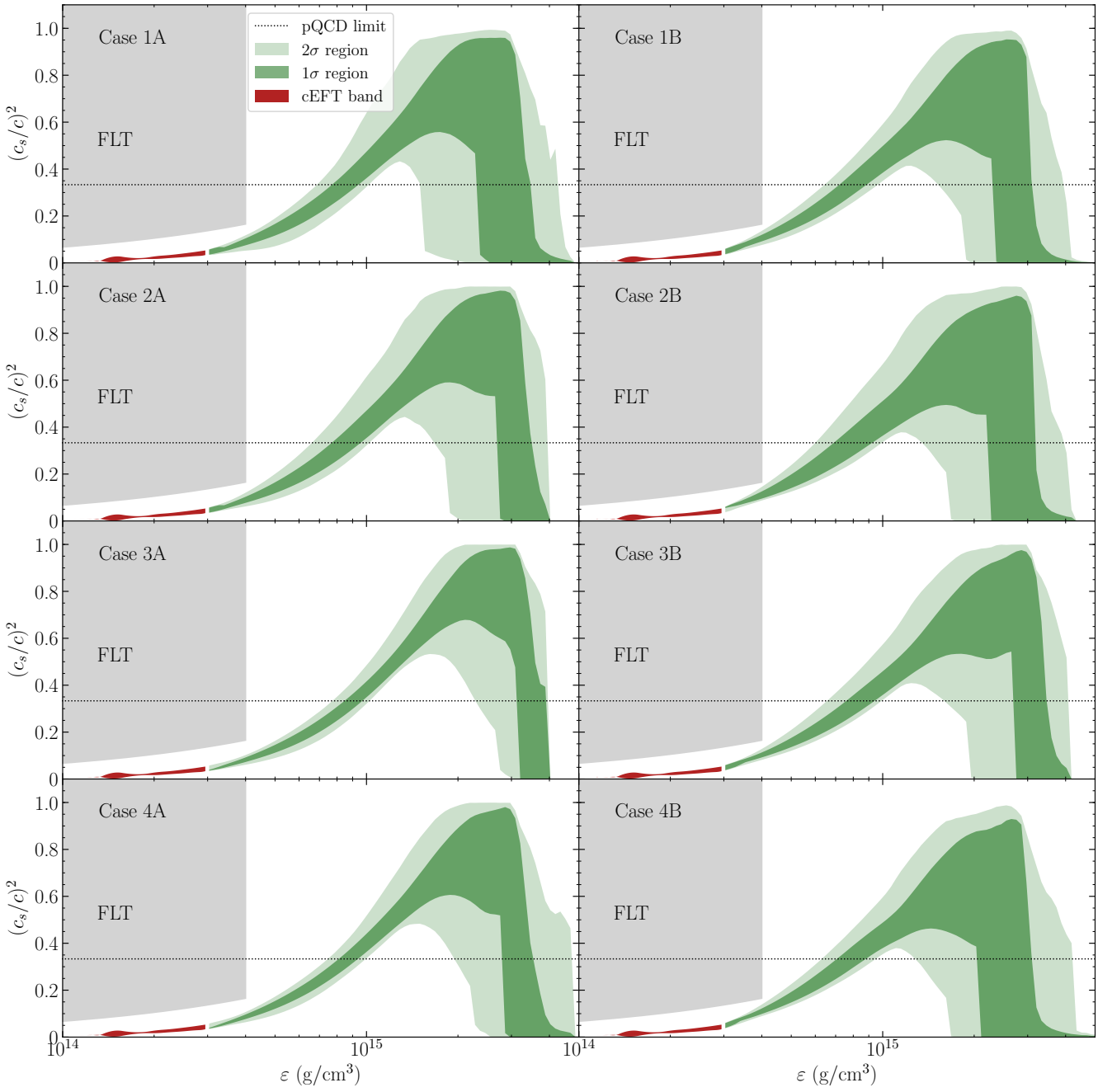

Figure 4.20.: Posterior distributions of the speed of sound in the speed of sound parametrization, where the dark and light green regions represent the joined 68% and 95% credible regions at discrete energy densities. The red area at lower densities gives the speed of sound of the chiral EFT band calculated by Ref. [136]. The dotted line indicates the value $1/\sqrt{3}$ of the speed of sound in the asymptotic pQCD limit, and the gray area is the excluded region by the Fermi liquid theory (FLT) constraints. Figure taken from our paper, Ref. [118].

4.3.3.2 Exterior parameter space

For the parameter space of neutron star masses and radii we show the posterior predictive distribution, which gives the probability of a new mass-radius point given the posterior distribution of the EOS parameters. To avoid redrawing samples from the posterior distributions, we use the posterior samples obtained in our analyses, marginalize over central densities, and draw a new central density from their prior distribution. Numerically this results in a set of mass-radius points for which we can calculate the 68% credible region by binning and performing kernel density estimation.

We show the credible regions for these posterior predictive distributions for all the scenarios considered in Fig. 4.21, for both the piecewise polytropic EOS model and speed of sound parametrization. In most cases both parametrizations result in similar bands in mass-radius space, however, there are also significant differences between the two parametrizations. In all cases where the likelihood is centered around lower-mass stars, the piecewise polytropic EOS model allows for a larger region at larger radii, especially in Cases 2B and 3B. This is a direct consequence of the form of the parametrization, as the piecewise polytropic EOS model includes EOS that produce mass-radius curves with almost constant radius up to high masses. The speed of sound model, however, does not permit these kinds of EOS due to the form of the Gaussian, which forces every EOS to soften again after the peak of the Gaussian to comply with the pQCD constraint. Note that the small bimodal feature for the piecewise polytropic EOS model at low masses in Cases 1B and 4B is a consequence of the way the polytropic extensions are matched to the upper and lower limit of the chiral EFT band.

For all posterior distributions for the A scenarios the 68% credible regions for both the piecewise polytropic EOS model and speed of sound parametrization seem centered towards larger radii than one might expect. This behavior again follows from the prior used on the EOS parameters. To better understand how the uniform prior on EOS parameters affects the posterior distribution, we show in Fig. 4.22 a one-dimensional cut for a $1.44\,M_\odot$ star of the probability distributions of the priors for both parametrizations and the likelihood given by the ellipse of the $1.44\,M_\odot$ star (PSR J0437 − 4715) of Fig. 4.15. Fig. 4.22 illustrates clearly that the posterior distribution is not completely likelihood-dominated, due to the prior pushing towards larger radii. As a result, there is only a small region of parameter space around 11.5 km where there is both finite support from the likelihood and the prior, leading to an unexpectedly peaked posterior for the radius and the narrow regions for the mass-radius bands in Fig. 4.22.

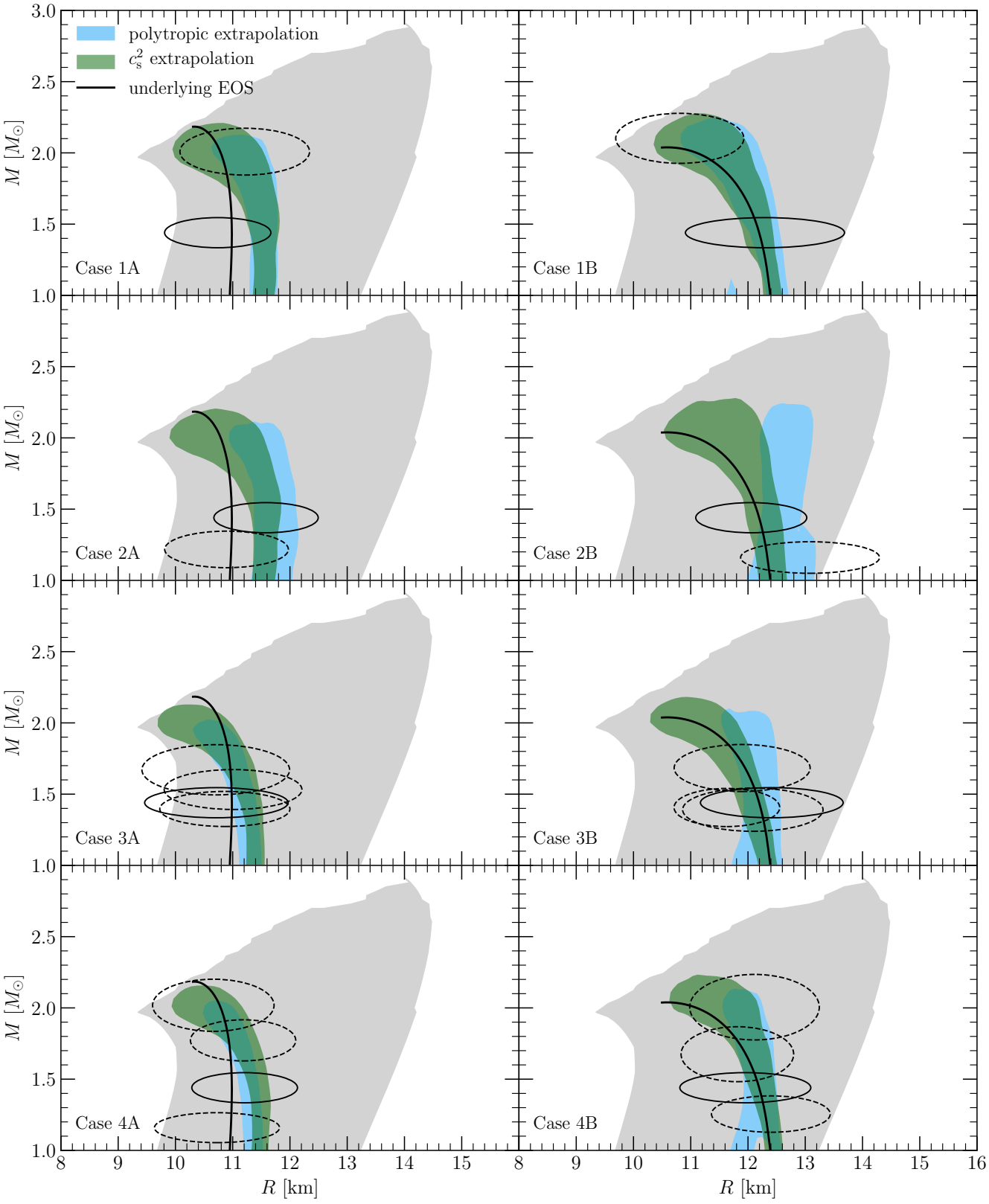

Figure 4.21.: 68% credible regions of the posterior distribution for the mass and radius for the piecewise polytropic EOS model (blue) and the speed of sound parametrization (green). The gray areas indicate the unconstrained mass-radius uncertainty region for both models. The elliptical contours of the input mass-radius posteriors for each scenario are shown as well for reference as shown in Fig. 4.11. A similar figure is published in our paper, Ref. [118].

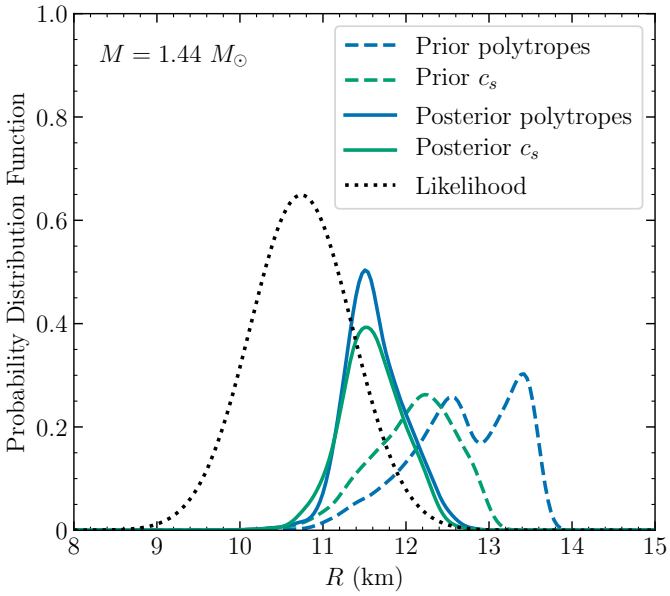

Figure 4.22.: One-dimensional cut for a $1.44\,M_\odot$ star of the probability distributions of the priors for both parametrizations and the likelihood given by the ellipse of the $1.44\,M_\odot$ star (PSR J0437 − 4715) of Fig. 4.15. In addition, we show the resulting posteriors for both parametrizations, both for Case 1A. Figure taken from our paper, Ref. [118].

5 Slowly rotating neutron stars

In the previous chapter, we focused on non-rotating neutron stars and studied related observables. We now extend the framework by considering slowly rotating neutron stars. In Chap. 3, we presented the approximative framework by Hartle and Thorne [130, 133] and discussed how the moment of inertia of neutron stars is calculated within this framework. Using the Hartle-Thorne approximation, we provide an overview on the moment of inertia for the piecewise polytropic EOS model. In the previous chapter, we explored a universal relation between the pressure around saturation density and the radius of a typical neutron star. Further universal relations emerge between the moment of inertia and the compactness parameter. With an uncertainty band for the universal relation at hand, we explore the properties of the EOS that describe the extremal limits of the uncertainty band. Furthermore, we investigate the sensitivity of the universal relation to the parametrization of the EOS. We then put a special focus on the double neutron star system PSR J0737 − 3039 which provides a promising prospect to a measurement of the moment of inertia for the first time. We investigate the impact of such a measurement on the radius of neutron stars as well as on the EOS. Moreover, we explore how further moment of inertia measurements of neutron stars with different masses constrain the EOS. Eventually, we investigate whether the choice of the EOS parametrization has an impact on the inference of radius and EOS constraints from hypothetical moment of inertia measurements.

5.1 Overview of the moment of inertia

In the present section, we study the moment of inertia in the case of the piecewise polytropic EOS model as presented in Sec. 2.3.2. We use the framework presented in Chap. 3 to calculate the moment of inertia and sample over the EOS parameter space under the consideration of the imposed constraints. Similarly to the mass-radius relation, we parametrize the moment of inertia as a sequence of the central pseudo-enthalpy h_c. For each EOS, we eventually determine the $I(M)$ as well as $I(R)$ relations. With the entity of $I(M)$ and $I(R)$ relations at hand, we determine both envelopes and present our results in Fig. 5.1. In the left panel of Fig. 5.1, we show the moment of inertia I as a function of the neutron star mass M. We additionally provide the results for the three representative EOS (cf. Sec. 4.1) in the left panel of Fig. 5.1. The results of the three representative EOS indicate that stiff EOS predict larger values for the moment of inertia than soft EOS. We now focus on the intermediate EOS of the three representative EOS to discuss a particular feature of the moment of inertia. For increasing central densities which is equivalent to increasing neutron star masses, the maximum moment of inertia is reached before the maximum mass is reached. The mass that is associated with the maximum moment of inertia is usually a few percent smaller than the maximum mass M_{max} [121, 123]. This can be illustrated by dimensional considerations and the properties of the MR relation shown in Fig. 4.1. The radius decreases for increasing neutron star masses. The decrease of the radius is stronger in the vicinity of the maximum mass. Simple dimensional considerations reveal that the moment of inertia scales linearly in the mass and quadratic in the radius. We find the maximum moment of inertia to be $289.1\,M_\odot\,\mathrm{km}^2$, where the maximal values are clearly correlated with the stiffness of the EOS. In addition, it is manifest that the three EOS which are representative with respect to the radius are also representative with respect to the moment of inertia and hence span the full moment-of-inertia range. From the results shown in Fig. 5.1 it is possible to deduce estimates for the moment of inertia for particular neutron star masses. For a typical neutron star with a mass of $M = 1.4\,M_\odot$, we find a moment of inertia range of $I_{1.4\,M_\odot} = 55.2-92.6\,M_\odot\,\mathrm{km}^2$. For the pulsar PSR J0737−3039A with $M = 1.338\,M_\odot$ we find the moment of inertia to be in the range $I = 51.5 - 86.0\,M_\odot\,\mathrm{km}^2$. Our predicted range is significantly smaller than

that of Ref. [220], where $I = 21.1 - 113.2\,M_\odot\,\mathrm{km}^2$, and similar to the range obtained by Ref. [117] with $I = 60.3 - 90.5\,M_\odot\,\mathrm{km}^2$.

In the right panel of Fig. 5.1, we show the moment of inertia as a function of the radius and also the according results for the three representative EOS. Later in this chapter, we discuss the impact of a moment of inertia measurement on the radius of neutron stars. To this end, we will revisit the results shown in the figure.

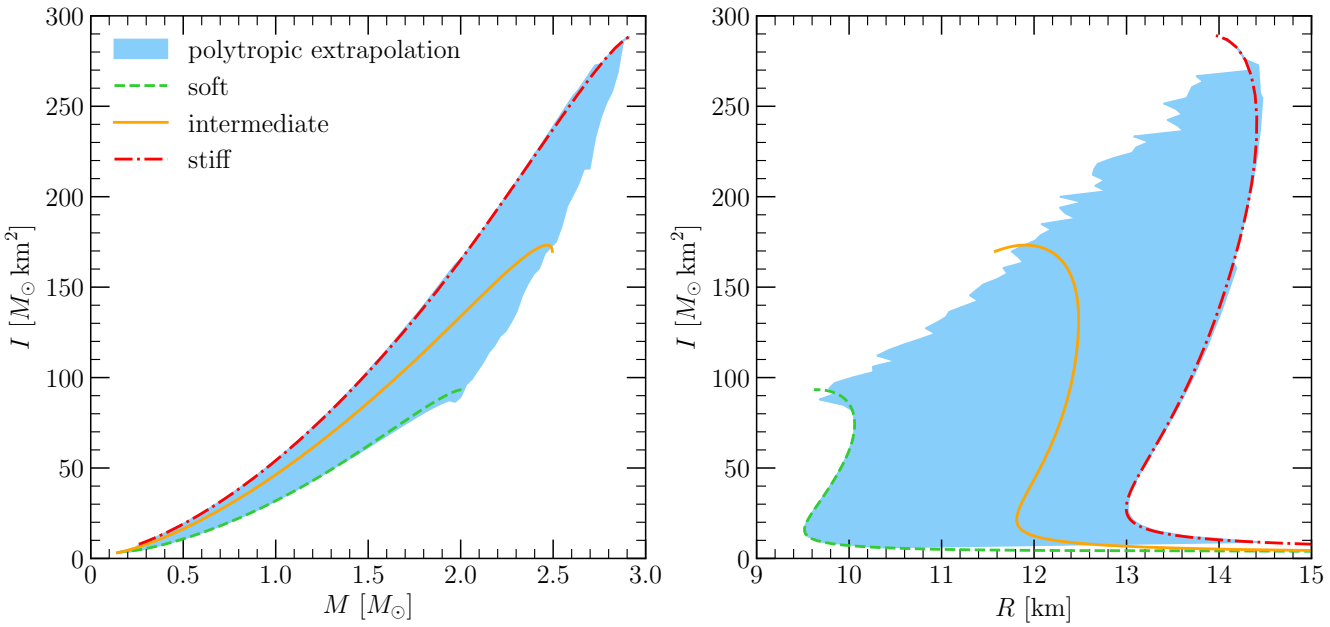

Figure 5.1.: *Left panel*: Moment of inertia I as a function of the mass M. Further, we present the results for the three representative EOS. The resulting relations indicate that soft EOS predict smaller moments of inertia and stiff EOS predict larger moments of inertia for equal mass neutron stars. *Right panel*: Moment of inertia I as a function of the radius R. Both panels show that the three representative EOS that are representative with respect to the radius of neutron stars are also representative with respect to the moment of inertia.

5.2 Moment of inertia and compactness

In the present section, we introduce a *universal relation*. We start by providing an introduction into the topic of universal relations among neutron star observables. Such relations describe the behavior of slowly rotating neutron stars with weak magnetic fields [52]. Universal relations emerge among several neutron star observables. The peculiarity of these relations lies in the fact that they are not sensitive to details of the EOS [300].

However, universal relations can be applied to observations to solve degeneracies among neutron star observables [52]. In the present section, we focus on a relation that connects the mass, the radius, and the moment of inertia. Simultaneous measurements of the mass and the moment of inertia of a neutron star will be possible in the future [76, 191, 290]. However, such measurements do not allow direct access to the radius of the neutron star. Ravenhall and Pethick [222] found that the normalized moment of inertia $I/(MR^2)$ is correlated with the compactness parameter $C = M/R$. Later works by Lattimer and Prakash [177], Bejger and Haensel [36], and Lattimer and Schutz [182] improved this relation. Moreover, in Ref. [182] was shown that such an empirical relation gives the possibility to deduce radius constraints based on simultaneous measurements of masses and moments of inertia. Steiner *et*

al. [252] and Breu and Rezzolla [52] incorporated additionally the $2\,M_\odot$ constraint such that further improvements were obtained.

Lattimer and Schutz [182] found an approximative relation which holds for $M/R > 0.07\,M_\odot\,\mathrm{km}^{-1}$ and is given by

$$I \approx (0.237 \pm 0.008)\,MR^2\left[1 + 4.2\cdot\frac{M}{R} + 90\cdot\left(\frac{M}{R}\right)^4\right]. \tag{5.1}$$

In a subsequent work by Steiner *et al.* [252], the approximative relation given above was revisited by including the observation of $2\,M_\odot$ neutron stars and the authors find

$$\frac{I}{MR^2} \approx 0.01 + (1.200 \pm 0.006)\cdot\left(\frac{M}{R}\right)^{\frac{1}{2}} - 0.1839\cdot\frac{M}{R} - (3.735 \pm 0.095)\cdot\left(\frac{M}{R}\right)^{\frac{3}{2}} + 5.278\cdot\left(\frac{M}{R}\right)^2 \tag{5.2}$$

Breu and Rezzolla [52] revisit the relation given in Eq. (5.1) and incorporate only EOS in their study that meet the $2\,M_\odot$ constraint. The revisited relation of Ref. [52] is given by

$$\frac{I}{MR^2} = 0.244 + 0.942\cdot\frac{M}{R} + 15.224\cdot\left(\frac{M}{R}\right)^4, \tag{5.3}$$

which is valid over the same range for the compactness parameter as the fit performed by Lattimer and Schutz given in Eq. (5.1).

In the left panel of Fig. 5.2 we present our results for the dimensionless moment of inertia compared to the correlation bands from Refs. [52, 182, 252]. Our results agree well with these for $M/R > 0.15\,M_\odot/\mathrm{km}$, whereas we find a deviation for smaller compactness parameters and also a somewhat larger band for $M/R > 0.2\,M_\odot/\mathrm{km}$. This shows that, e.g., predictions for neutron stars with small mass and large radii based on the former correlation bands are not compatible with the general EOS band. This is most likely due to low-density assumptions made that are incompatible with modern nuclear physics.

We now explore the discussed universal relation in the case of the speed of sound parametrization. This allows us further to compare the results for the piecewise polytropic EOS model and the speed of sound parametrization and thus to investigate sensitivities to the parametrization. We use the same framework to obtain the masses M, the radii R, and the moments of inertia I to ultimately calculate the normalized moment of inertia $I/(MR^2)$ and the compactness parameter C as discussed above. Further, we use the same approach to determine the envelope describing the resulting uncertainty band for the speed of sound parametrization. In the right panel of Fig. 5.2, we show our results for the speed of sound parametrization. Additionally, we show the fits discussed in Refs. [52, 182, 252]. We observe that our results for the dimensionless moment of inertia as a function of the compactness parameter are consistent with the uncertainty band provided by Lattimer and Schutz [182] as well as with the results of Steiner *et al.* [252]. Our uncertainty band coincides with the fit function found by Breu and Rezzolla [52] but the fit follows somewhat close to the lower limit of the uncertainty band from the speed of sound parametrization. Moreover, we show in the right panel of Fig. 5.2 the envelope of the corresponding results from the piecewise polytropic EOS model. We observe that both extrapolation methods yield similar results. Only minor deviations between the two envelopes exist for small and large compactness parameters, respectively. Hence, we conclude that the universal relation between the normalized moment of inertia $I/(MR^2)$ and the compactness parameter C is at least not sensitive to the considered EOS parametrizations in this work.

In Sec. 4.2, we reviewed a universal relation between the dimensionless binding energy BE/M and the compactness parameter $C = M/R$. The authors of Ref. [252] suggest to combine the universal relations of the binding energy and the moment of inertia. This results in a relation between BE/M and $I/(MR^2)$. We explore this particular combination of neutron star observables and present our resulting envelope in Fig. 5.3. The piecewise polytropic EOS model yields a rather narrow band.

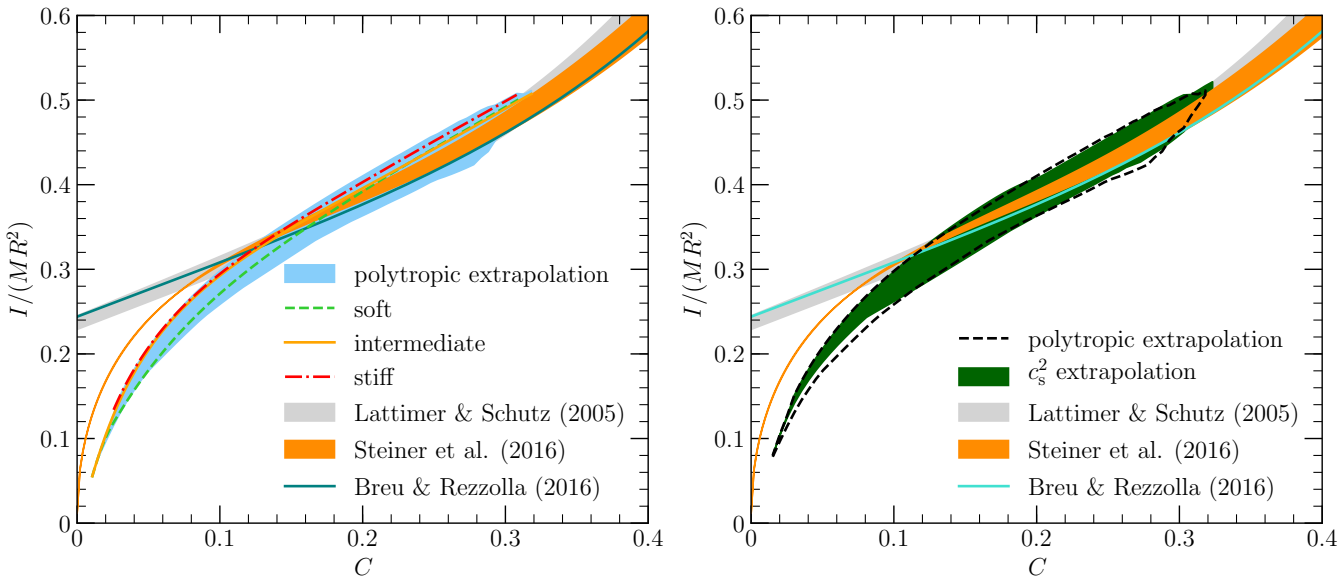

Figure 5.2.: *Left panel*: Dimensionless moment of inertia $I/(MR^2)$ as a function of the compactness parameter C. We also show the results in the case of the representative EOS discussed in the text. Our results show that the representative EOS are not representative with respect to this particular presentation of the moment of inertia. For comparison, we additionally present the uncertainty band from the approximative relation provided by Lattimer and Schutz [182] as a gray band as well as the revisited approximative relations explored by Steiner *et al.* [252] as an orange band and Breu and Rezzolla [52] as a dark turquoise solid line. We observe a good agreement of the results from the literature for $C > 0.1$. *Right panel*: We present the universal relation between the dimensionless moment of inertia $I/(MR^2)$ and the compactness parameter C in the case of the speed of sound parametrization as a purple area. Further, we present the results for the piecewise polytropic EOS model by a black dashed outline.

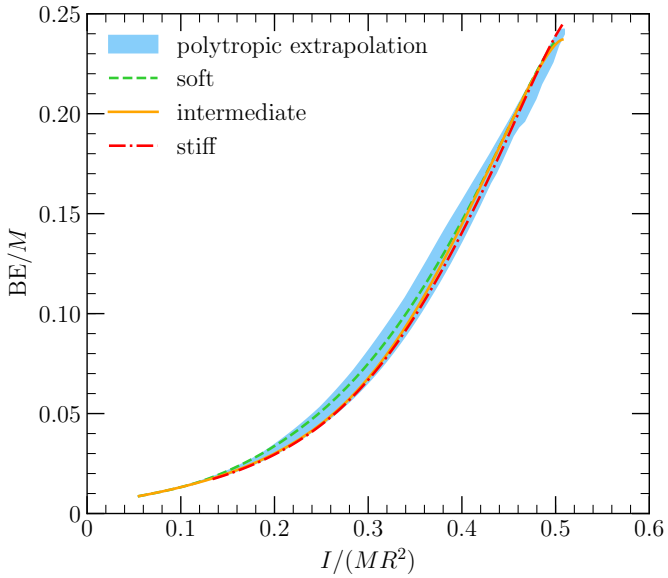

Figure 5.3.: Dimensionless binding energy BE/M as a function of the dimensionless moment of inertia $I/(MR^2)$ for the piecewise polytropic EOS model. We additionally show the results for the three representative EOS.

5.2.1 Extremal cases

Above, we discussed the $I/(MR^2)$–compactness parameter correlation for the piecewise polytropic EOS model. In addition, we show in the left panel of Fig. 5.2 the three representative EOS (soft, intermediate, stiff) of Ref. [137]. These are representative with respect to radius and moment of inertia for all masses (see Figs. 4.1 and 5.1), but as is clear from the figure do not capture the extremes of the dimensionless moment of inertia. In order to investigate band for the dimensionless moment of inertia in more detail, we determined the individual EOS that represent the limits of the band in the left panel of Fig. 5.2. To this end, we discretized M/R for $M/R \geqslant 0.1\,M_\odot\,\mathrm{km}^{-1}$ and determined the χ^2 of each EOS for the deviation of I/MR^2 from the lower (upper) band. The results for the individual EOS with the minimal χ^2 values are shown as red (blue) lines in Fig. 5.4.

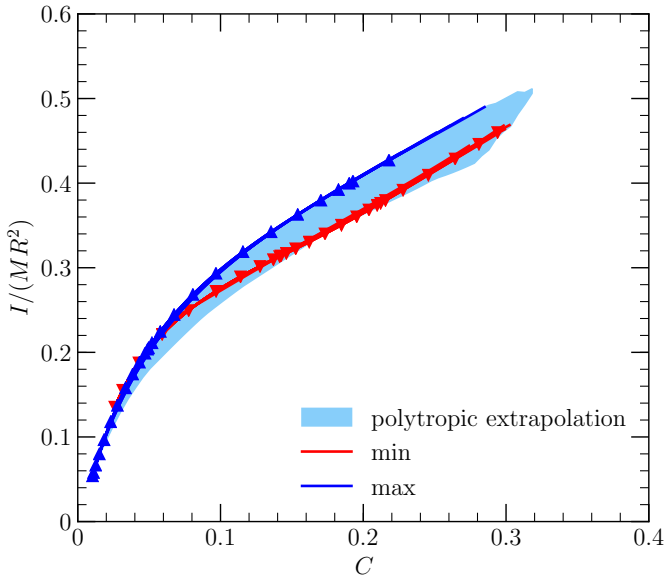

Figure 5.4.: Similar figure as Fig. 5.2. The red (blue) lines with down (up) triangle points are the individual EOS within the piecewise polytropic EOS model with minimal χ^2 of $I/(MR)^2$ with respect to the lower (upper) boundary (from fits for $C \geq 0.1$).

The corresponding EOS for these extreme cases are shown in Fig. 5.5. We observe that the EOS with a minimum χ^2 with respect to the lower boundary of the dimensionless moment of inertia I/MR^2 (red lines) tend to be rather stiff at nuclear densities and soft at high densities, whereas the EOS leading to large values of $I/(MR^2)$ tend to be soft at nuclear densities and stiff at high densities (blue lines). These trends are also reflected in the results for the mass, radius, and moment of inertia in Fig. 5.6, where these individual EOS are clearly extreme but nevertheless very interesting cases. The EOS with the low values for the dimensionless moment of inertia predict large radii at small masses (and moment of inertia) and small radii at larger masses (red lines), while the ones corresponding to large values for $I/(MR^2)$ show the opposite trend.

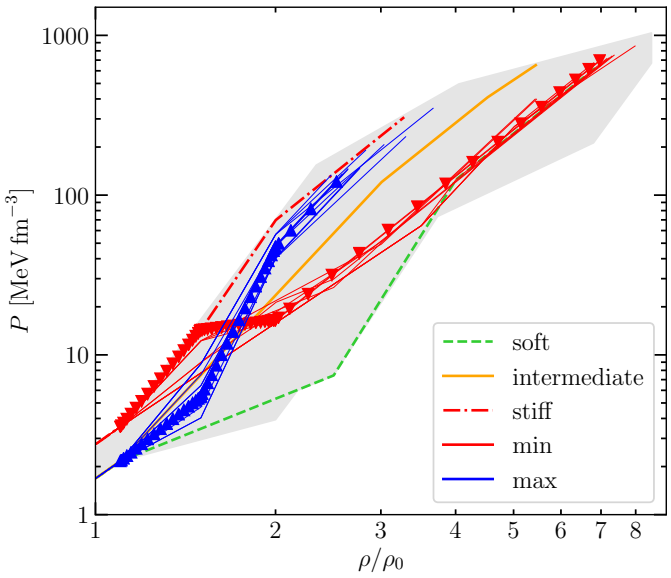

Figure 5.5.: Pressure P as a function of mass density ρ/ρ_0 in units of the saturation density. The gray region is the general EOS band based on the piecewise polytropic EOS model of Ref. [137]. The lines correspond to the individual EOS shown in Fig. 5.4, where the red and blue lines extremize the $I/(MR)^2$–compactness correlation.

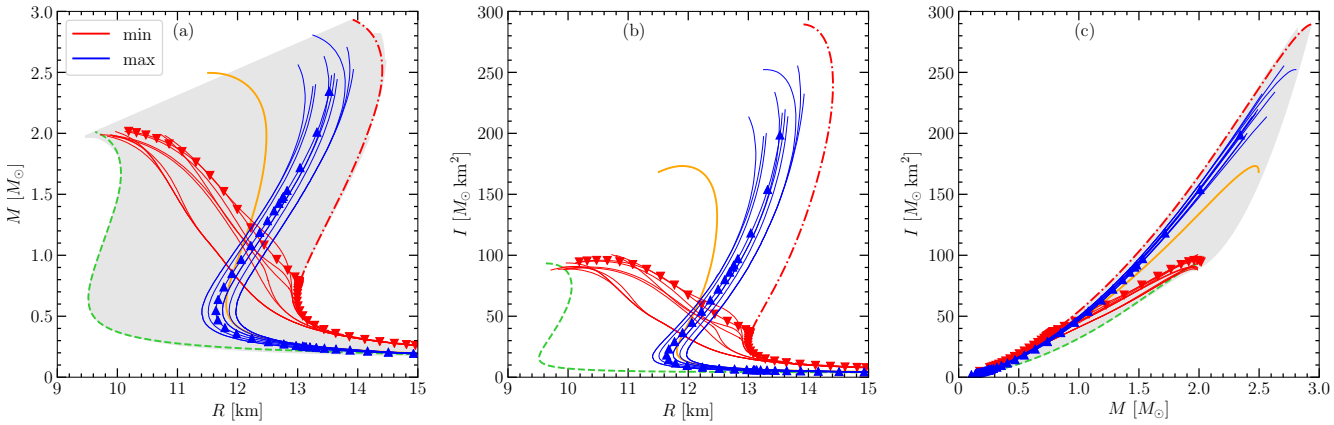

Figure 5.6.: Results for the mass M, radius R, and moment of inertia I of neutron stars based on the EOS constraints (bands) derived following Ref. [137] from microscopic calculations up to density $\rho_1 = 1.1\,\rho_0$, the mass constraint $M_{\rm obs} \geq 1.97\,M_\odot$, and causality constraints. The individual panels (a), (b), and (c) show the mass-radius, moment of inertia-radius and moment of inertia-mass results, respectively. The green (dashed) yellow (solid), and red (dot-dashed) lines correspond to the three representative EOS (soft, intermediate, and stiff, respectively) that allow to probe the full range of these uncertainty bands, see main text and Ref. [137] for details. We include the individual EOS shown in Fig. 5.4, where the red and blue lines extremize the $I/(MR^2)$–compactness correlation.

5.3 Improved constraints from moment of inertia measurements

Fits that describe universal relations as given in Eqns. (5.1), (5.2), and (5.3) were used in the literature to explore constraints for the radius of neutron stars by assuming a simultaneous measurement of the mass and the moment of inertia of a neutron star. In Refs. [52, 182], the fits were investigated for fixed moment of inertia values. Such considerations allow compatibility checks for masses and radii given a fixed moment of inertia. We apply this approach to the piecewise polytropic EOS model and choose four representative moment of inertia values, i.e., $I_1 = 50\,M_\odot\,\mathrm{km}^2$, $I_2 = 80\,M_\odot\,\mathrm{km}^2$, $I_3 = 120\,M_\odot\,\mathrm{km}^2$, and $I_4 = 180\,M_\odot\,\mathrm{km}^2$. We sample over all EOS inside the EOS uncertainty band and determine $R(I_i)$ and $M(I_i)$ for each fixed moment of inertia. In Fig. 5.7, we show the mass-radius uncertainty band in the case of the piecewise polytropic EOS model and highlight the mass-radius pairs that support the fixed moment of inertia values. The larger the assumed fixed moment of inertia values is, the larger are the compatible mass-radius pairs. This result substantiates the statement that stiff EOS predict larger moment of inertia values than softer EOS.

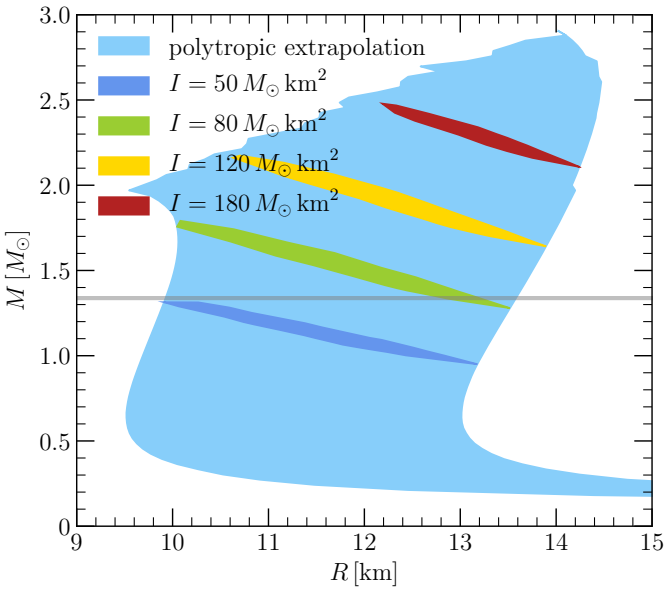

Figure 5.7.: Mass-radius uncertainty band for the piecewise polytropic EOS model as a light blue area. We show mass-radius pairs that are compatible with four representative values for the moment of inertia. Further, we show as a gray band the mass $M_\mathrm{A} = 1.3381 \pm 0.0007\,M_\odot$ of PSR J0737 − 3039A [161].

Next, we focus on the neutron star PSR J0737 − 3039A with mass $1.338\,M_\odot$, which is the target of a future moment of inertia measurement. In Fig. 5.8 we show the radius range for this neutron star based on the general EOS band, and in blue the correlation with as a function of the moment of inertia I. The range of I is given by the band shown in the left panel of Fig. 5.1 for the mass $M = 1.338\,M_\odot$, where we focus on the piecewise polytropic EOS model, as it provides the larger uncertainty range. It is again clear from Fig. 5.8 that the tightest radius constraints would result from values of I towards the extremes of the general EOS band.

Based on the framework discussed in Chap. 3, we now investigate to what extent information from moment of inertia measurements can improve these constraints. To this end, we assume that it is possible to measure simultaneously the neutron star mass (with negligible uncertainty) and the moment of inertia with central value I_c and relative uncertainty of $\Delta I = \pm 10\%$ and $\pm 20\%$, respectively. We consider three different masses, $M = 1.35\,M_\odot$, $2.0\,M_\odot$, and $2.4\,M_\odot$, and for each mass, three possible central values I_c, which approximately correspond to the moment of inertia given by the three representative EOS shown

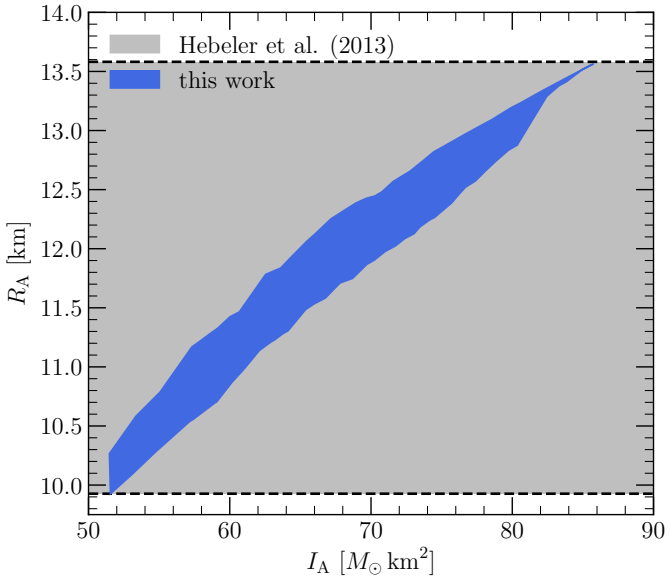

Figure 5.8.: The radius R_A as a function of the moment of inertia I_A for fixed neutron star mass $M = 1.3381\,M_\odot$. The gray band represents the radius range deduced from the consideration of non-rotating neutron stars based on Ref. [137]. We present our results as a dark blue area that is obtained by considering slowly rotating neutron stars.

in the left panel of Fig. 5.1. The values of I_c for these assumed measurements are listed in Table 5.1, where we also give the improved radius ranges resulting from such a simultaneous measurement. In addition, we show the allowed I–R areas in Fig. 5.9, where the three panels correspond to the soft, intermediate, and stiff EOS scenarios. For a $2.4\,M_\odot$ neutron star, the soft EOS is ruled out (see Fig. 4.1), and no soft I_c scenario exists in this case. We also note that the EOS can have a more intricate behavior in the general EOS band, e.g, going from soft to stiff and vice versa with higher slopes in the M–R diagram (see Fig. 5.6).

Table 5.1.: We present the three masses and the considered moment of inertia scenarios for exploring the impact on the radius of neutron stars in the case of the piecewise polytropic EOS model. The columns give the mass M (in units of $M_\odot$), the radius R (in units of km) inferred from the framework discussed in Ref. [137], the moment of inertia scenarios I_c (in units of ($M_\odot$ km^2)), and the constrained radius R (in units of km) under the assumption of two uncertainties for the moment of inertia measurement, i.e., 10% and 20%.

$M\,[M_\odot]$	R[km] (literature)	$I_c\,[M_\odot\,\mathrm{km}^2]$		R[km] $\Delta I_c = 10\%$	R[km] $\Delta I_c = 20\%$
1.35	9.94 – 13.59	I_{soft}	55	9.94 – 11.35	9.94 – 11.90
		I_{int}	70	11.18 – 12.88	10.43 – 13.35
		I_{stiff}	85	12.40 – 13.59	11.72 – 13.59
2.00	9.96 – 14.16	I_{soft}	95	9.96 – 11.16	9.69 – 11.69
		I_{int}	135	11.64 – 13.51	10.77 – 13.99
		I_{stiff}	165	13.11 – 14.16	12.25 – 14.16
2.40	11.57 – 14.42	I_{soft}	–	–	–
		I_{int}	170	11.57 – 13.15	11.57 – 13.76
		I_{stiff}	220	13.30 – 14.42	12.35 – 14.42

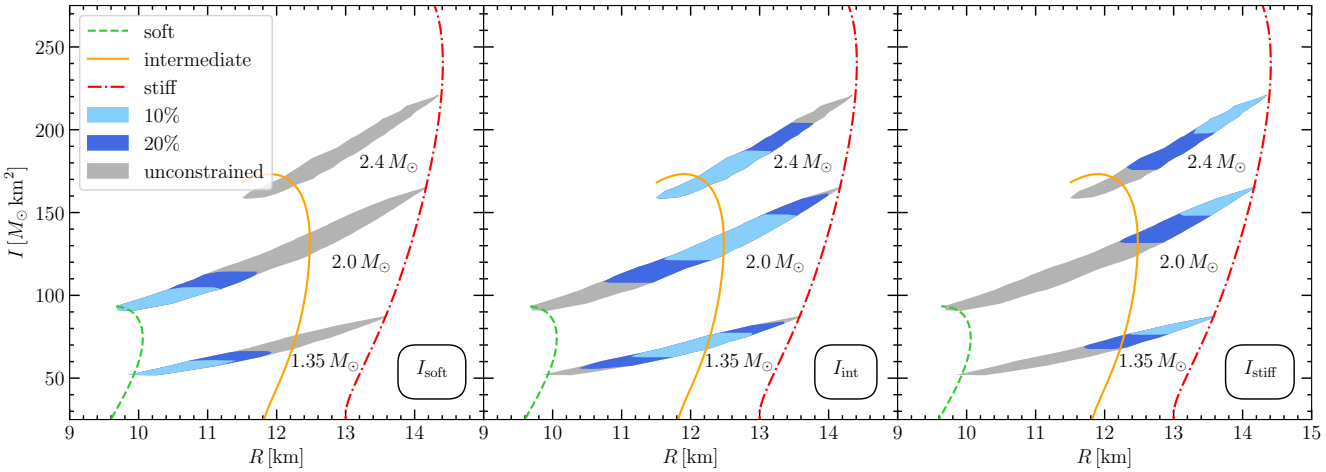

Figure 5.9.: Moment of inertia I as a function of radius R for the piecewise polytropic EOS model. The gray band gives the allowed I–R range resulting from the general EOS band as shown in Fig. 5.1. The dark gray, light blue, and dark blue areas show the allowed I–R values for the particular neutron star masses indicated, where the dark gray area includes all possible I–R pairs for each mass, and the light blue (dark blue) area corresponds to an assumed measurement of the moment of inertia with central value $I_{\rm c}$ given in Table 5.1 with a relative uncertainty of $\Delta I = \pm 10\%$ ($\pm 20\%$). The three panels assume central values $I_{\rm c}$ that approximately correspond to the soft (a), intermediate (b), and stiff (c) EOS (see Table 5.1). Note that for a $2.4\,M_\odot$ neutron star, the soft EOS is ruled out and thus no compatible $I_{\rm c}$ exists in this case.

Moreover, we show in Table 5.2 and Fig. 5.10 how these radius constraints change if one uses instead of the piecewise polytropic EOS model the speed of sound parametrization from our paper [118] to extrapolate to higher densities. The results show that the radius constraints are remarkable consistent, with the largest differences due to the underlying allowed ranges (see the gray regions versus the area within the three representative EOS in Fig. 5.10), which has the largest impact for heavy mass neutron stars and the stiff EOS scenario.

Figures 5.9 and 5.10 clearly show that a measurement of $I_{\rm c}$ with a relative uncertainty of $\Delta I = \pm 10\%$ ($\pm 20\%$) in (almost) all cases significantly improves the constraints on neutron star radii. For a $\pm 10\%$

Table 5.2.: Same as Table 5.1 but corresponding to Fig. 5.10 using the speed of sound parametrization from our paper, Ref. [118] to extrapolate to higher densities.

$M\,[M_\odot]$	$R\,[{\rm km}]$ (literature)	$I_{\rm c}\,[M_\odot\,{\rm km}^2]$		$R\,[{\rm km}]$	
				$\Delta I_{\rm c} = 10\%$	$\Delta I_{\rm c} = 20\%$
1.35	$10.03 - 13.26$	$I_{\rm soft}$	55	$10.03 - 11.40$	$10.03 - 11.93$
		$I_{\rm int}$	70	$11.27 - 12.83$	$10.54 - 13.26$
		$I_{\rm stiff}$	85	$12.46 - 13.26$	$11.72 - 13.26$
2.00	$9.46 - 13.59$	$I_{\rm soft}$	95	$9.46 - 11.05$	$9.46 - 11.66$
		$I_{\rm int}$	135	$11.66 - 13.38$	$10.82 - 13.59$
		$I_{\rm stiff}$	165	$13.16 - 13.59$	$12.27 - 13.59$
2.40	$11.14 - 13.46$	$I_{\rm soft}$	–	–	–
		$I_{\rm int}$	170	$11.26 - 12.99$	$11.14 - 13.46$
		$I_{\rm stiff}$	220	$13.29 - 13.46$	$12.29 - 13.46$

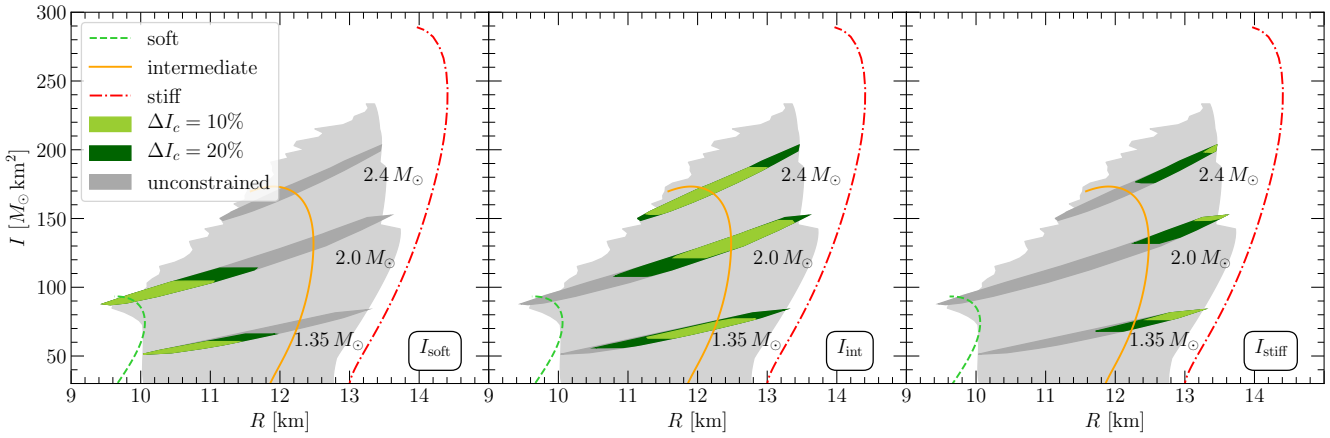

Figure 5.10.: Same as Fig. 5.9 but using the speed of sound parametrization from our paper [118] to extrapolate to higher densities.

measurement, if the measured value of I_c is located close to the center of the EOS band, the radius range decrease by a factor of ≈ 2, whereas the radius becomes even more narrowly predicted when I_c is located close to the soft or stiff EOS. In the latter cases, the radius spread in Table 5.1 is only $1.1-1.5\,\mathrm{km}$ for the piecewise polytropic EOS model and $0.2-1.5\,\mathrm{km}$ for the speed of sound parametrization.

The corresponding constraints for the EOS for the different cases of Fig. 5.9 are shown in Fig. 5.11. The gray region is again the general EOS band based on the piecewise polytropic EOS model of Ref. [137], whereas the different panels show the constraints for the assumed simultaneous measurements of the mass (different rows) and the moment of inertia (different columns). Naturally, we find that the constraints on the EOS are the strongest for those cases that also give the strongest radius constraints. In addition, small values of I tend to give stronger constraints on the EOS at higher densities, whereas large values for I provide stronger constraints at lower densities. Moreover, measurements of heavy neutron stars provide stronger constraints on the EOS than the scenarios for typical neutron stars. Finally, we show in Fig. 5.12 the EOS constraints corresponding to in Fig. 5.10 using the speed of sound parametrization from our paper [118] to extrapolate to higher densities.

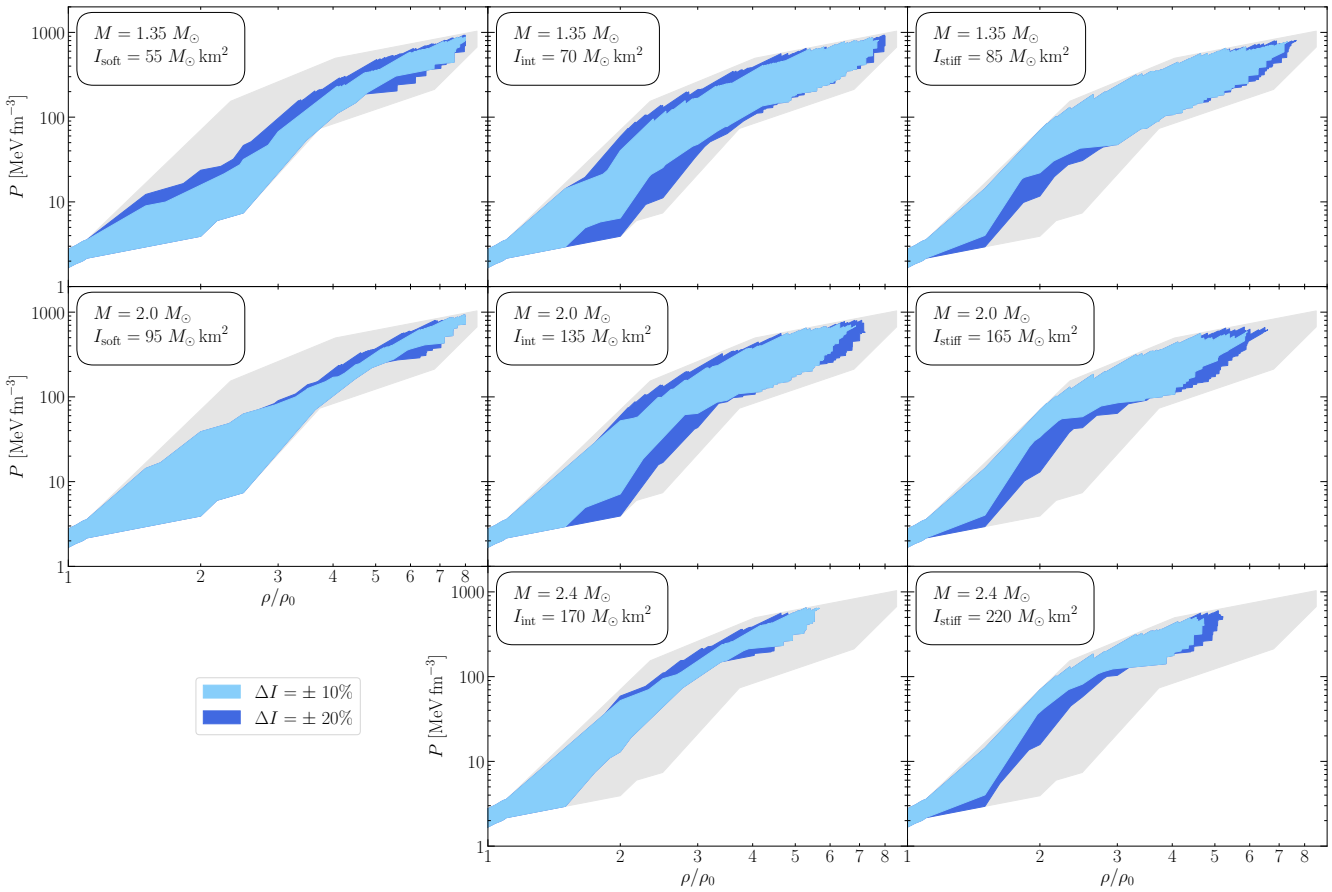

Figure 5.11.: Pressure P as a function of mass density ρ/ρ_0 in units of the saturation density. The gray region is the general EOS band based on the piecewise polytropic EOS model of Ref. [137]. The light and dark blue areas show the allowed EOS range for assumed simultaneous measurements of the mass (different rows) and the moment of inertia (different columns), as in Fig. 5.9 and Table 5.1, with a relative uncertainty of $\Delta I = \pm 10\%$ ($\pm 20\%$).

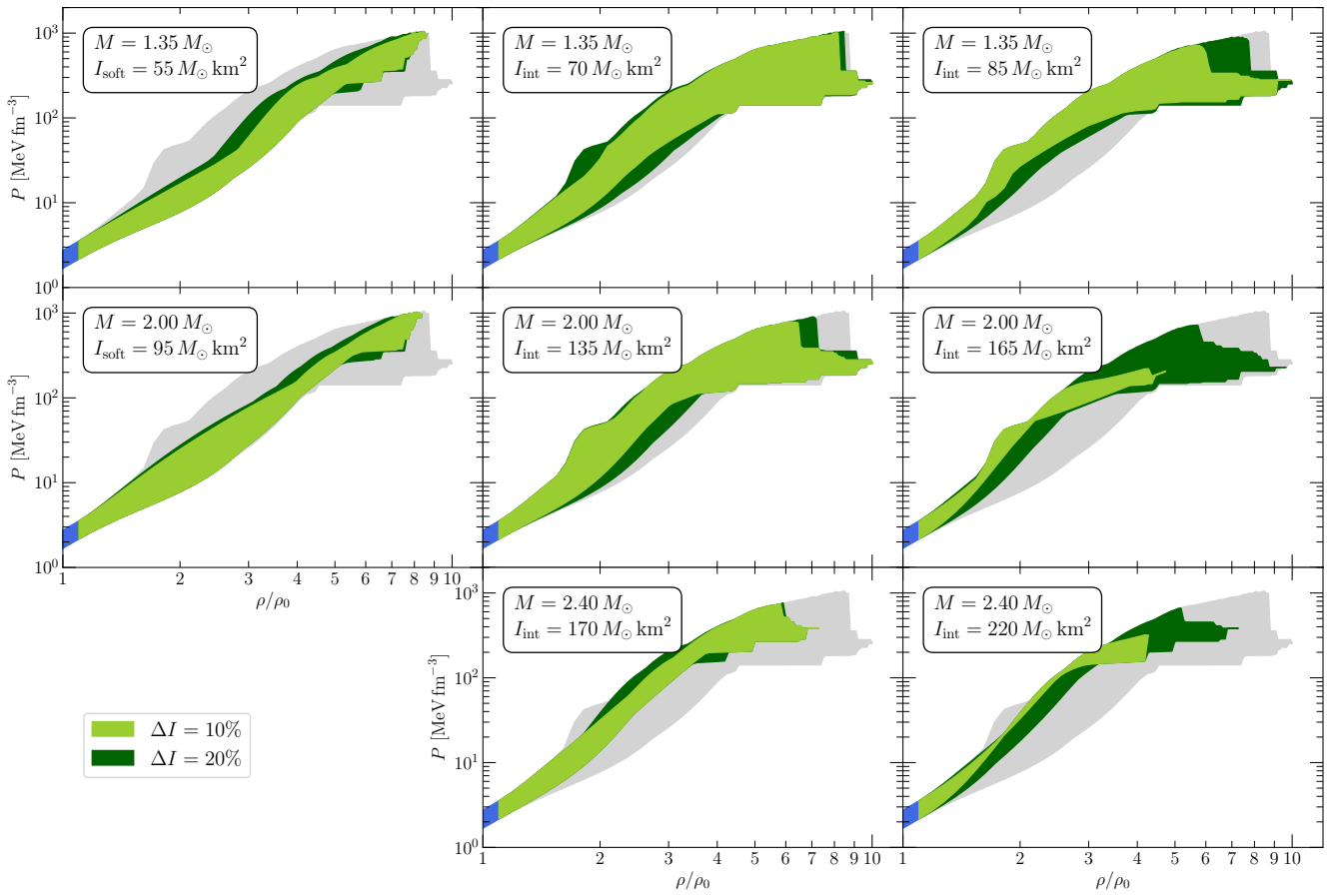

Figure 5.12.: Same as Fig. 5.11 but using the speed of sound parametrization from our paper [118] to extrapolate to higher densities.

6 Tidal interactions in neutron star binary systems

In the previous two chapters, we discussed isolated non-rotating as well as slowly rotating neutron stars. In this chapter, we extend our considerations by investigating binary neutron star systems. To this end, we treat the tidal interactions with the companion as a small perturbation as discussed in Chap. 3. We provide an overview on the dimensionless tidal deformability and give an estimate for typical neutron stars. The tidal deformability is a measure for the response of a neutron star to an external tidal field [298]. Moreover, we investigate the impact of a measurement of this observable on the radius of neutron stars. We then investigate properties of binary neutron star merger. The pioneering observation of the first detection of GW from a binary neutron star merger started a new and exciting era for nuclear physics and astrophysics. We confront both the piecewise polytropic EOS model and the speed of sound parametrization with the constraints imposed by the event GW170817 and infer constraints for the radius of neutron stars as well as the EOS.

Yagi and Yunes (2013) [297] found that EOS independent relations between the moment of inertia, the tidal deformability, and the quadrupole moment of neutron stars exist. The combination of these observables is referred to as the I-Love-Q trio. We investigate the properties of the I-Love-Q trio for the piecewise polytropic EOS model and explore the universal relations among the various combinations of the trio. With the I-Love-Q trio at hand, we revisit the correlations among EOS properties at nuclear densities and properties of typical neutron stars discussed in Chap. 4. We study similar universal correlations for the trio which opens up further possibilities in constraining the EOS in the future.

6.1 Impact of a tidal deformability measurement on the equation of state

First, we study the dimensionless tidal deformability $\bar{\lambda}$ for the piecewise polytropic EOS model (cf. Sec. 2.3.2) in general. The discretization of the EOS parameter space is the same as presented in Chap. 4. We calculate the dimensionless tidal deformability with the framework presented in Sec. 3.4 in conjunction of the numerical method presented in Sec. 3.6. In the left panel of Fig. 6.1, we provide an uncertainty band for the dimensionless tidal deformability. From our results, we infer a range of $\bar{\lambda}_{1.4M_\odot} = 118.9 - 928.3$ for a typical neutron star with a mass of $M = 1.4\,M_\odot$. The lower bound for $\bar{\lambda}_{1.4M_\odot}$ based on our analysis is consistent with the work of Annala *et al.* [15] in which the authors state that the lower bound is $\bar{\lambda}_{1.4M_\odot} = 120$. Another study by Lim and Holt [184] found the range to be $\bar{\lambda}_{1.4M_\odot} = 256 - 442$ for the 68% credibility interval and $\bar{\lambda}_{1.4M_\odot} = 136 - 519$ for the 95% credibility interval, respectively, which are significantly smaller compared to our result. Steiner *et al.* [249] found for the same mass at 95% credibility interval the range $\lambda_{1.4M_\odot} = 0.6 - 6 \times 10^{36}\,\mathrm{g\,cm^2\,s^2}$ which is equivalent to $\bar{\lambda}_{1.4M_\odot} = 106 - 1061$ which is consistent with our range. Moreover, the left panel of Fig. 6.1 shows that the three representative EOS, which represent the limits and central part of the radius uncertainty bands in Ref. [137] also define the corresponding regimes of the tidal deformability uncertainty band.

In the right panel of Fig. 6.1, we show the dimensionless tidal deformability $\bar{\lambda}$ as a function of the compactness parameter C. Generally, it is evident that the dimensionless tidal deformability decreases with increasing compactness. This can be easily understood: the more compact a neutron star is, the more difficult it is to deform the neutron star due to an external tidal field [298]. We also highlight the ranges of both quantities for a $M = 1.4\,M_\odot$ neutron stars based on the EOS uncertainty range of Ref. [137]. The figure shows a strong correlation between $\bar{\lambda}$ and the compactness C, which is consistent

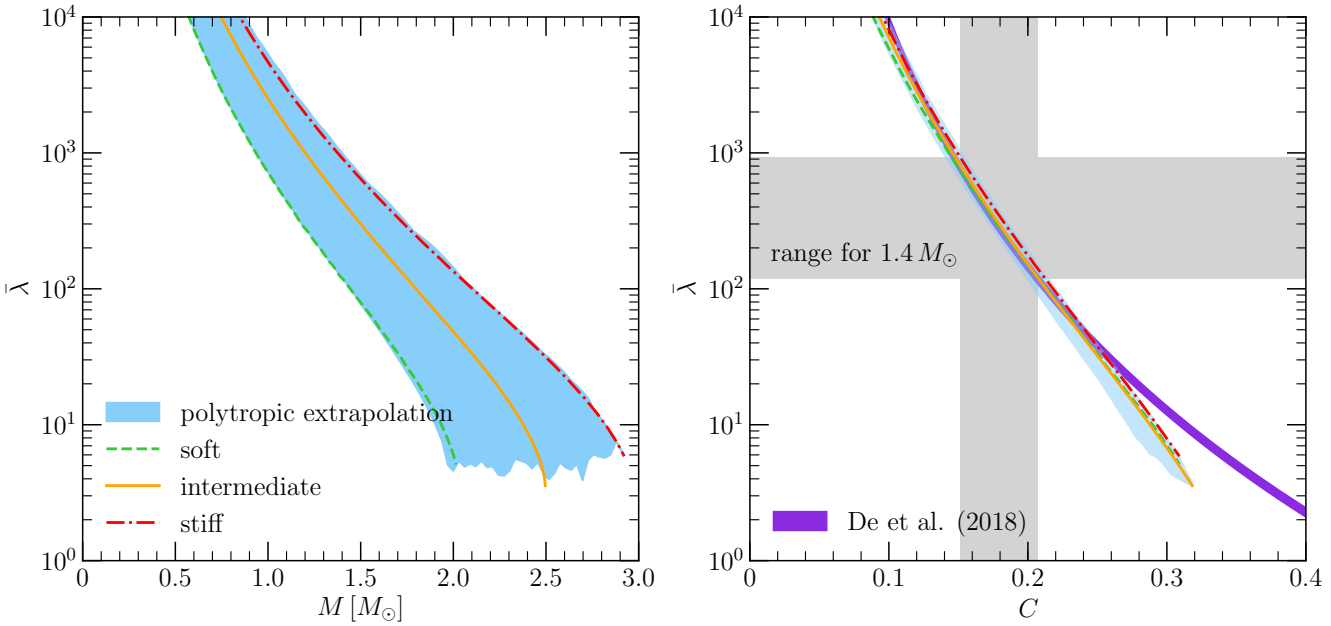

Figure 6.1.: *Left panel*: Dimensionless tidal deformability $\bar{\lambda}$ as a function of the mass M for the piecewise polytropic EOS model. Additionally, we present the individual results for the three representative EOS. *Right panel*: Dimensionless tidal deformability $\bar{\lambda}$ as a function of the compactness parameter C. The gray shaded area represents the ranges for $\bar{\lambda}_{1.4\,M_\odot}$ and $C_{1.4\,M_\odot}$ in the case of a typical neutron star with a mass of $1.4\,M_\odot$. The purple band shows the scaling law valid for the mass range $M = 1.1 - 1.6\,M_\odot$ found by De *et al.* [79]

with previous studies. In Ref. [79] it was found that $\bar{\lambda}$ approximately fulfills the following scaling relation:

$$\bar{\lambda} \approx aC^{-6}, \tag{6.1}$$

with $a = 0.0093 \pm 0.0007$ for masses in the range of $M = 1.1 - 1.6\,M_\odot$. The corresponding band is shown in the right panel of Fig. 6.1, which is in good agreement with our results.

The work of Maselli *et al.* [197] utilizes the relation between the dimensionless tidal deformability $\bar{\lambda}$ and the compactness $C = M/R$ to investigate the impact of a tidal deformability measurement on the compactness of neutron stars. Previous studies (cf. Refs. [197, 298]) argued that the tidal deformability can be obtained with an accuracy of 60% by GW observations. The authors deduced that a 60% measurement of the tidal deformability can potentially constrain the compactness to 10% [197]. We apply the uncertainty of 60% and determine the compactness parameter ranges that are compatible with the tidal deformability ranges. In Table 6.1 we summarize our results.

In the following, we investigate the connection between the dimensionless tidal deformability, the mass, and the radius. In Chap. 3, we presented a framework to access the dimensionless tidal deformability. To this end, we insert Eq. (3.46) into Eq. (3.28) and obtain [75, 101]

$$\bar{\lambda} = \frac{2}{3} k_2 \left(\frac{R}{M}\right)^5 . \tag{6.2}$$

Tews *et al.* [265] found that the Love number k_2 remains almost constant for neutron stars of different masses and radii. This implies that both quantities, mass and the radius, are connected by a linear correlation for a given constant tidal deformability. We investigate this linear scaling behavior for the piecewise polytropic EOS model. To this end, we study regions with constant values for the dimensionless

Table 6.1.: Hypothetical measurements of the dimensionless tidal deformability $\bar{\lambda}$ with an uncertainty of 60% and the resulting ranges for the compactness parameter in the case of the piecewise polytropic EOS model.

$\bar{\lambda}_i$	C
200 ± 120	$0.17 - 0.23$
400 ± 240	$0.15 - 0.20$
600 ± 360	$0.14 - 0.19$
800 ± 480	$0.13 - 0.18$

tidal deformability $\bar{\lambda}$ in the mass-radius uncertainty band. To be specific, we choose the values $\bar{\lambda}_1 = 200$, $\bar{\lambda}_2 = 400$, $\bar{\lambda}_3 = 600$, and $\bar{\lambda}_4 = 800$ (see left panel of Fig. 6.2). For the determination of the shown bands we sample over all EOS of the piecewise polytropic model and determine the masses and radii $M(\bar{\lambda}_i)$ and $R(\bar{\lambda}_i)$ for each EOS. Our results exhibit the expected approximate linear relation between the radius and the mass of neutron stars over the full range of values for the dimensionless tidal deformability. Moreover, the results show that a precise measurement of the dimensionless tidal deformability leads to tight neutron star radius constraints. This finding is consistent with the results of Ref. [265]. In the right panel of Fig. 6.2, we show the allowed values of $\bar{\lambda}_{1.4\,M_\odot}$ and $R_{1.4\,M_\odot}$ for a fixed neutron star mass $M = 1.4\,M_\odot$, where we also highlighted the corresponding results for the three representative EOS. The detailed ranges for the shown mass are given in Table 6.2 for some representative values for the dimensionless tidal deformability.

Table 6.2.: Radius constraints for a typical neutron star with a mass of $M = 1.4\,M_\odot$ under the assumption of a measurement of the dimensionless tidal deformability $\bar{\lambda}_i$ with vanishing uncertainty in the case of the piecewise polytropic EOS model.

$\bar{\lambda}_i$	$R_{1.4\,M_\odot}$ [km]
200	$10.6 - 11.2$
400	$11.9 - 12.4$
600	$12.7 - 13.0$
800	$13.3 - 13.4$

6.2 Properties of binary neutron star mergers

We explore the properties of binary neutron star merger predicted by the piecewise polytropic EOS model. In Chap. 1 we introduced the chirp mass $\mathscr{M}$ and the binary tidal deformability $\widetilde{\Lambda}$ (cf. Eqns. (1.7) and (1.9)) in the context of the first observation of a binary neutron star merger. Figure 6.3 shows the results for the tidal deformability, where the color coding of each sampling point indicates the radius of individual the neutron star configurations. Specifically, the left panel shows for reference the dimensionless tidal deformability $\bar{\lambda}$ of an individual neutron star (see left panel of Fig. 6.1), while the right panel shows the binary tidal deformability $\widetilde{\Lambda}$ of a system consisting of the neutron stars with masses M_1 and M_2, where we imposed the constraint $M_1, M_2 \geq 1.0\,M_\odot$ and choose $M_1 \geq M_2$ without loss of generality. In addition, we assume that both neutron stars obey the same single EOS. Sampling over all possible mass pairings M_1 and M_2 allows to determine the resulting chirp mass $\mathscr{M}$ for a given EOS as well as individual tidal deformabilities $\bar{\lambda}_1$ and $\bar{\lambda}_2$ and eventually the binary tidal deformability $\widetilde{\Lambda}$. The color coding in the right panel shows the radius of a neutron star with $M = 1.4\,M_\odot$ for the given EOS, while

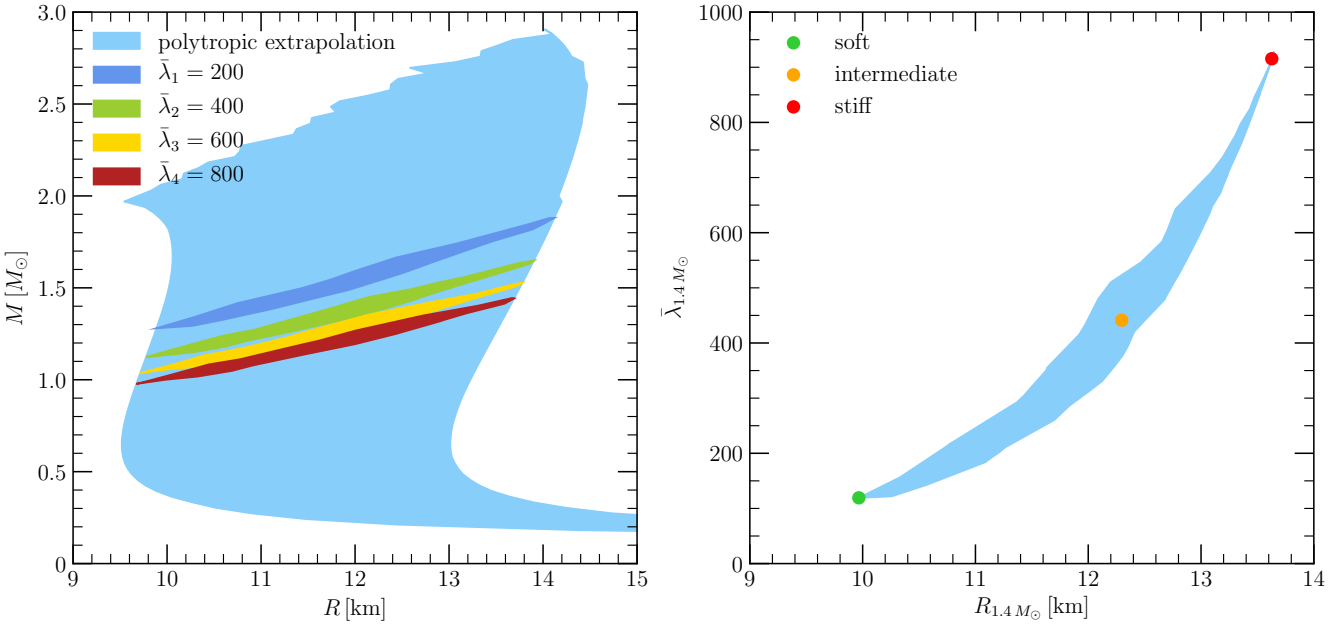

Figure 6.2.: *Left panel*: Mass-radius uncertainty band for the piecewise polytropic EOS model in light blue. Further, we show areas with constant $\bar{\lambda}$, i.e., $\bar{\lambda}_1 = 200$ (blue), $\bar{\lambda}_2 = 400$ (green), $\bar{\lambda}_3 = 600$ (yellow), and $\bar{\lambda}_4 = 800$ (red). Our results recover the expected linear relation between the neutron star mass and radius for fixed tidal deformability. *Right panel*: Dimensionless tidal deformability as a function of the radius for neutron stars with a mass of $M = 1.4\,M_\odot$. Additionally, we highlight the results for the three representative EOS.

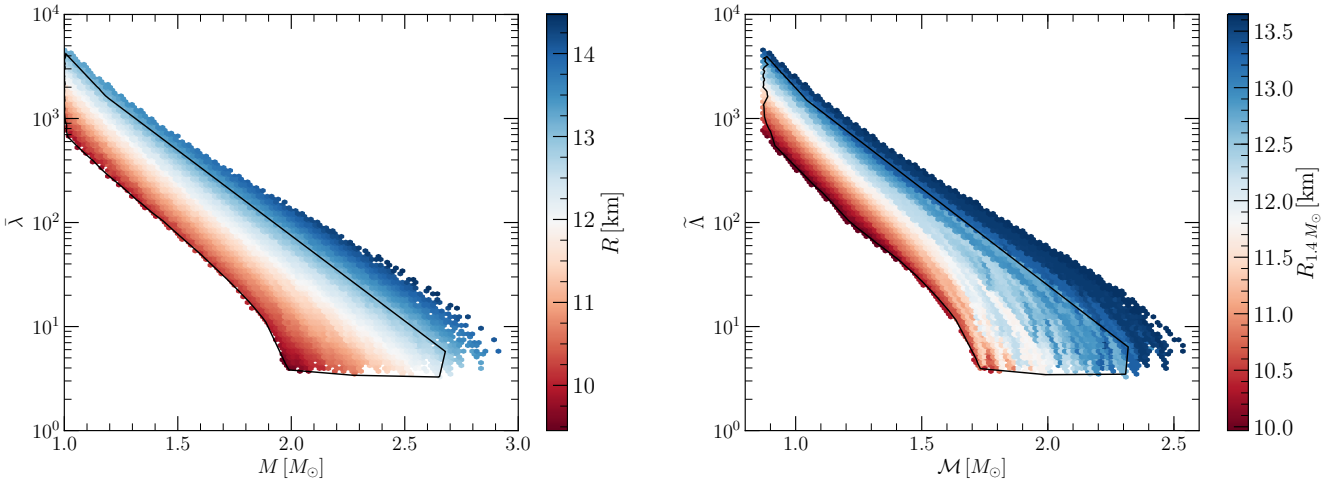

Figure 6.3.: *Left panel*: The dimensionless tidal deformability $\bar{\lambda}$ as a function of the mass M for the piecewise polytropic EOS model. The color coding indicates the radius of each configuration and demonstrates that there exists a correlation between all three shown observables. The black outline indicates the $\bar{\lambda}_{1.4\,M_\odot}$ constraint obtained from the analysis of Ref. [5, 6, 7]. *Right panel*: Binary tidal deformability $\tilde{\Lambda}$ as a function of the chirp mass $\mathscr{M}$, while the color denotes the radius $R_{1.4\,M_\odot}$ of a neutron star with mass $M = 1.4\,M_\odot$. The shown analysis is restricted to neutron stars with $M \geq 1.0\,M_\odot$. The black envelope contains all EOS that are compatible with the constraints for $\tilde{\Lambda}$ and $\mathscr{M}$ inferred from GW170817 [5, 6, 7].

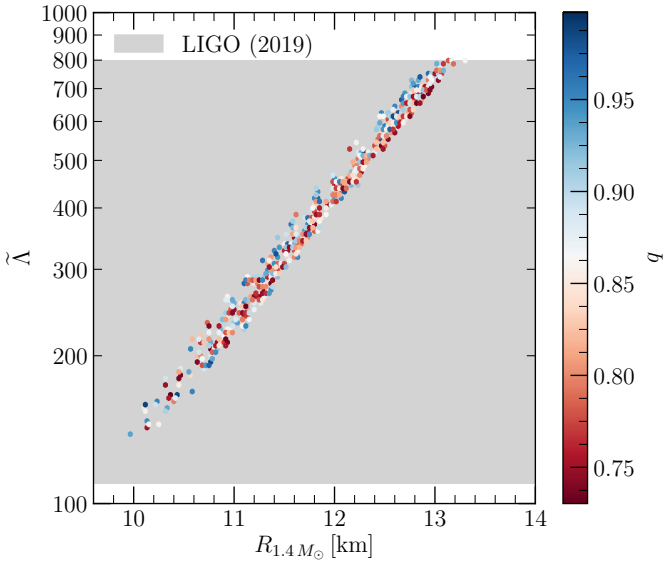

Figure 6.4.: Binary tidal deformability $\tilde{\Lambda}$ as a function of the radius of a neutron star with mass $M = 1.4\,M_\odot$ with a color coding for the mass ratio $q = M_2/M_1$ for the piecewise polytropic EOS model. We show only the results that are compatible with the LIGO constraints. The gray band indicates the $\tilde{\Lambda}$ range given in Refs. [6, 7].

the black envelope marks the regions that are consistent with the extracted constraints of Refs. [5, 6, 7] for M_1, M_2, $q = M_2/M_1$, $\bar{\lambda}_{1.4\,M_\odot}$, $\mathscr{M}$, and $\tilde{\Lambda}$. In both panels the black envelopes mark all cases that are consistent with the constraints imposed by the GW170817 signal [5, 6, 7].

In Fig. 6.4, we show the binary tidal deformability $\tilde{\Lambda}$ as a function of the radius of a neutron mass with mass $M = 1.4\,M_\odot$, while the color coding denotes the mass ratio $q = M_2/M_1$. In the plot we include only those configurations that are compatible with the constraints of Ref. [7]. Obviously, there is a strong correlation between the binary tidal deformability and the radius, while the mass ratio q exhibits no correlation to $\tilde{\Lambda}$ or $R_{1.4\,M_\odot}$. In Fig. 6.5 we show the constraints for the individual tidal deformabilities $\bar{\lambda}_1$ and $\bar{\lambda}_2$, extracted from the analysis of GW170817 [7] whereas the color coding indicates the radius of a $1.4\,M_\odot$ neutron star.

Above, we studied the scaling law given in Eq. (6.1) for the dimensionless tidal deformability. Zhao and Lattimer [305] suggest a similar scaling law for the binary tidal deformability, i.e.,

$$\tilde{\Lambda} \propto \left(\frac{\mathscr{M}}{R_{1.4\,M_\odot}} \right)^{-6}, \tag{6.3}$$

which can be motivated by comparing the left and right panel of Fig. 6.3, where one observes similarities that are consistent with the findings stated in Ref. [305]. In Fig. 6.6, we show the scaled binary tidal deformability as a function of the chirp mass based on the piecewise polytropic EOS model. In addition, the maximum mass $M_{\rm max}$ predicted by each individual EOS is depicted.

6.2.1 Constraints for the equation of state from GW170817

The extracted constraints for the different observables from GW170817 (cf. Table 1.1 and Refs. [5, 6, 7]) translate into constraints for the EOS and the mass-radius relations. In Fig. 6.7 we summarize these uncertainty bands using the piecewise polytropic EOS model (upper panel) and the speed of sound parametrization (lower panel). The gray bands in each panel shows the uncertainty bands just based

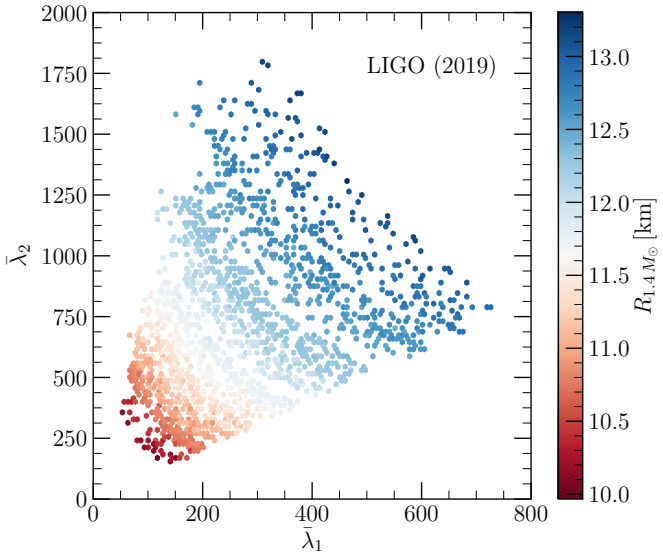

Figure 6.5.: Dimensionless tidal deformability $\bar{\lambda}_2$ as a function of dimensionless tidal deformability $\bar{\lambda}_1$ with a color coding for the radius of $1.4\,M_\odot$ neutron stars. We only present the results of EOS that are compatible with the properties of GW170817 given in Refs. [6, 7].

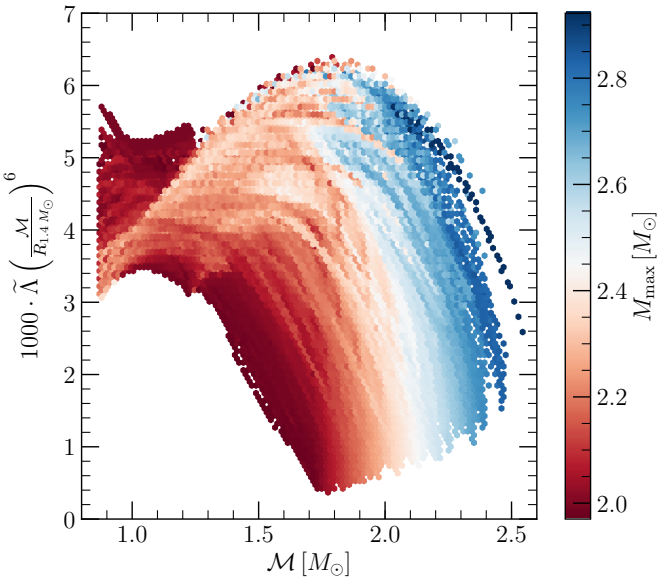

Figure 6.6.: Scaled binary tidal deformability as a function of the chirp mass. The maximum mass $M_{\max}$ is represented by a color coding for the piecewise polytropic EOS model.

on mass measurements and causality considerations (see Refs. [118, 137]). The blue and green bands indicate the new bands after incorporating the constraints from the GW170817 signal [6, 7]. It is manifest that the current constraints do not lead to a significant reduction of the uncertainties. For the radius uncertainty band, however, some of the stiff EOS are ruled out. Compared to the original radius uncertainty range $R_{1.4\,M_\odot} = 9.97-13.65\,\mathrm{km}$ the range gets reduced to $R_{1.4\,M_\odot} = 9.97-12.85\,\mathrm{km}$. Furthermore, the maximum mass M_{max} is decreased from $M_{\mathrm{max}} = 2.92\,M_\odot$ to $M_{\mathrm{max}} = 2.68\,M_\odot$. We find similar trends for the speed of sound parameterization as shown in the lower panel. Here we find a radius range of $R_{1.4\,M_\odot} = 10.11-12.85\,\mathrm{km}$ for a $1.4\,M_\odot$ neutron star.

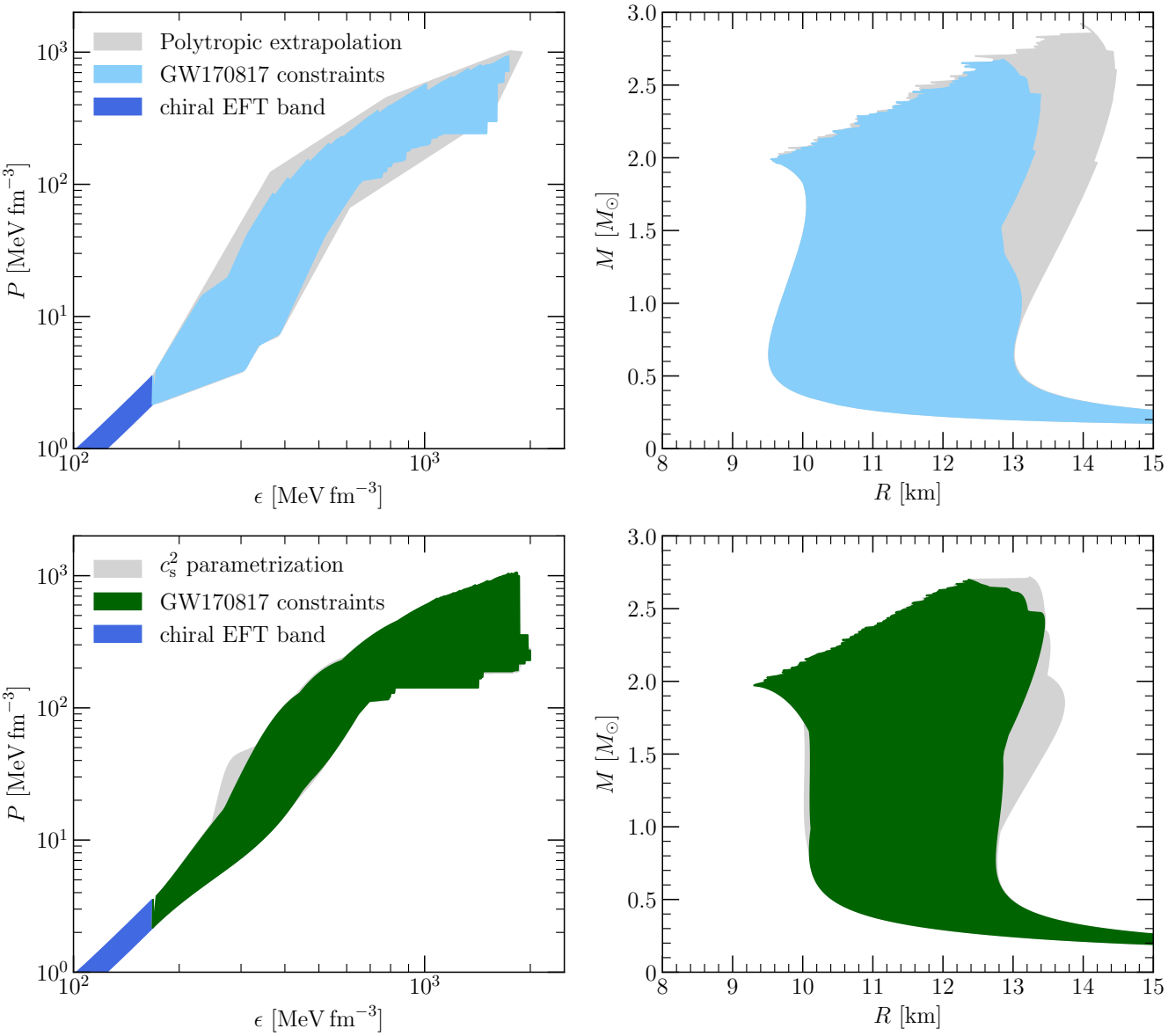

Figure 6.7.: *Upper panels*: We show the pressure P as a function of the energy density ϵ in the left panel. In the right panel the neutron star mass M as a function of the radius R is depicted. The gray band represent the general bands based on the piecewise polytropic EOS model. The EOS and mass-radius relations that agree with the constraints from the GW170817 signal are shown as light blue bands. *Lower panels*: Similar to the upper panels. Results for the speed of sound parametrization are shown in gray, whereas the constraints imposed by GW170817 are shown in green.

6.2.2 Constraints from simultaneous measurements of the moment of inertia and constraints from GW170817

We now study to what degree simultaneous measurements of moment of inertia and GW can help to improve the constraints on the EOS and the radius of neutron stars. For this we combine the constraints determined in the previous section with the approach presented in Sec. 5.3. In particular, we sample over all EOS based on the piecewise polytropic EOS model and assume three different representative values for the moment of inertia, $I_{\rm soft}$, $I_{\rm int}$, and $I_{\rm stiff}$ (see Table 6.3). These values span the allowed range of values for the moment of inertia that are compatible with current constraints from neutron star measurements. For each of the hypothetical moment of inertia measurements we assume an uncertainty of 10 or 20 %, respectively. In Fig. 6.8 we show the resulting radius uncertainty ranges. The blue band shows the radius band determined from the data of GW170817 for the piecewise polytropic EOS model (compare Fig. 6.7). The gray bands denote the allowed values for the moment of inertia for the three representative neutron star masses $M = 1.35\,M_\odot$, $M = 2.0\,M_\odot$ and $M = 2.4\,M_\odot$ (see Sec. 5.3), while the pink and purple bands take into account the constraints from the moment of inertia measurements with an uncertainty of 10 and 20%, respectively. We find that the scenarios $I_{\rm int}$ and $I_{\rm stiff}$ (central and right panel) are sensitive to the observational data of GW170817, while for the case $I_{\rm soft}$ the radius limits are purely determined by the moment of inertia constraints. The detailed uncertainty ranges as well as the explicit values for the moment of inertia are summarized in Table 6.3.

In Fig. 6.9, we show the constraints for the pressure as a function of energy density for different neutron star masses (rows) and moment of inertia values (columns). As in Fig. 6.8 the blue band shows the constraints only using information from GW170817 and observed neutron star masses (see Fig. 6.7), while the pink and purple bands take into account constraints from the indicated moment of inertia values with the given error bars. The figure shows that the measurements of small values for the moment of inertia (left column) impose significant additional constraints at higher densities, while large values (right column) in addition lead to strong constraints at intermediate densities.

Table 6.3.: Radius constraints resulting from simultaneous mass and moment of inertia measurements, assuming the mass uncertainty is negligible. The columns give the assumed values for M (in units of $M_\odot$), the radius based on the framework presented in Ref. [137] using the mass constraint $M_{\rm max} \geq 1.97\,M_\odot$ and causality constraint (in units of km), central value $I_{\rm c}$ of the moment of inertia (in units of $M_\odot\,{\rm km}^2$), as well as the resulting radius ranges from Fig. 6.8 (in units of km), assuming a relative uncertainty of $\Delta I = \pm 10\%$ and $\pm 20\%$, respectively. Additionally, we include the constraints imposed by the properties of GW170817 (cf. Refs. [5, 6, 7]). For each assumed mass, we consider three values of $I_{\rm c}$ that approximately correspond to the soft, intermediate (int), and stiff EOS of the three representative EOS.

$M\,[M_\odot]$	$R\,[{\rm km}]$ (literature)		$I_{\rm c}\,[M_\odot\,{\rm km}^2]$	$R\,[{\rm km}]$ $\Delta I_{\rm c} = 10\%$	$R\,[{\rm km}]$ $\Delta I_{\rm c} = 20\%$
1.35	$9.94 - 13.59$	$I_{\rm soft}$	55	$9.93 - 11.35$	$9.93 - 11.90$
		$I_{\rm int}$	70	$11.26 - 11.85$	$10.43 - 12.86$
		$I_{\rm stiff}$	85	$12.40 - 12.86$	$11.75 - 12.86$
2.00	$9.96 - 14.16$	$I_{\rm soft}$	95	$9.96 - 11.09$	$9.96 - 11.60$
		$I_{\rm int}$	135	$11.64 - 13.28$	$10.80 - 13.28$
		$I_{\rm stiff}$	165	$13.11 - 13.28$	$12.25 - 13.28$
2.40	$11.57 - 14.42$	$I_{\rm soft}$	–	–	–
		$I_{\rm int}$	170	$11.57 - 12.90$	$11.57 - 13.39$
		$I_{\rm stiff}$	220	$13.34 - 13.39$	$12.52 - 13.39$

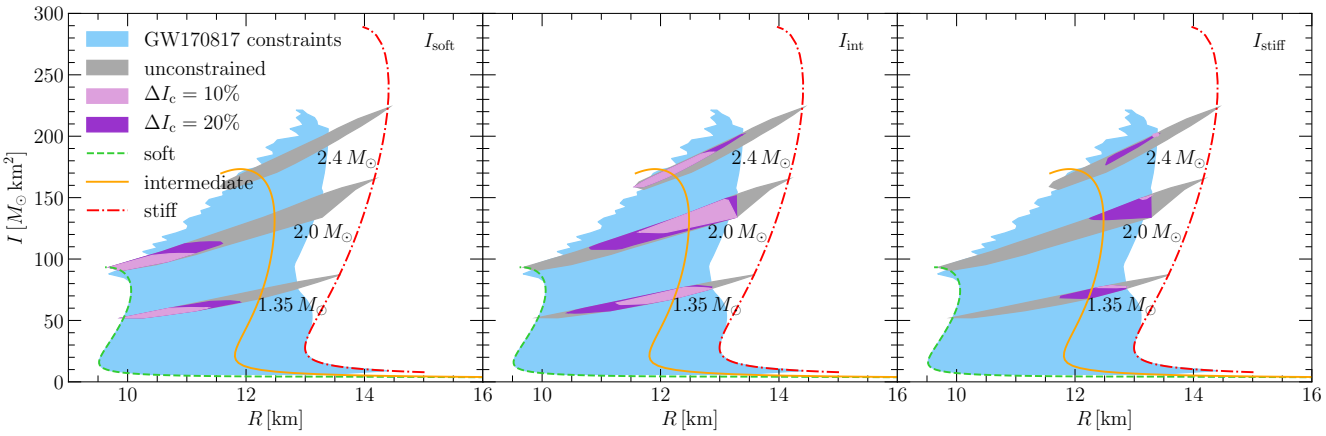

Figure 6.8.: Similar as Fig. 5.9. Radius uncertainty bands from combined constraints of neutron star masses, GW170817 and hypothetical moment of inertia measurements. The blue bands correspond to the range determined from GW170817 and neutron star masses alone (compare Fig. 6.7) in the case of the piecewise polytropic EOS model. The three panels show the results using different moment of inertia values, I_{soft}, I_{int}, and I_{stiff} (see Table 6.3 for details). The gray areas represent the regions compatible with the causality and mass constraints for three different neutron star masses, while the light purple and dark purple areas show the regions compatible with the corresponding moment of inertia values I_{c} and an assumed uncertainty ΔI_{c} of 10 and 20%, respectively. The green, yellow and red lines show the results for the three representative EOS of Ref. [137].

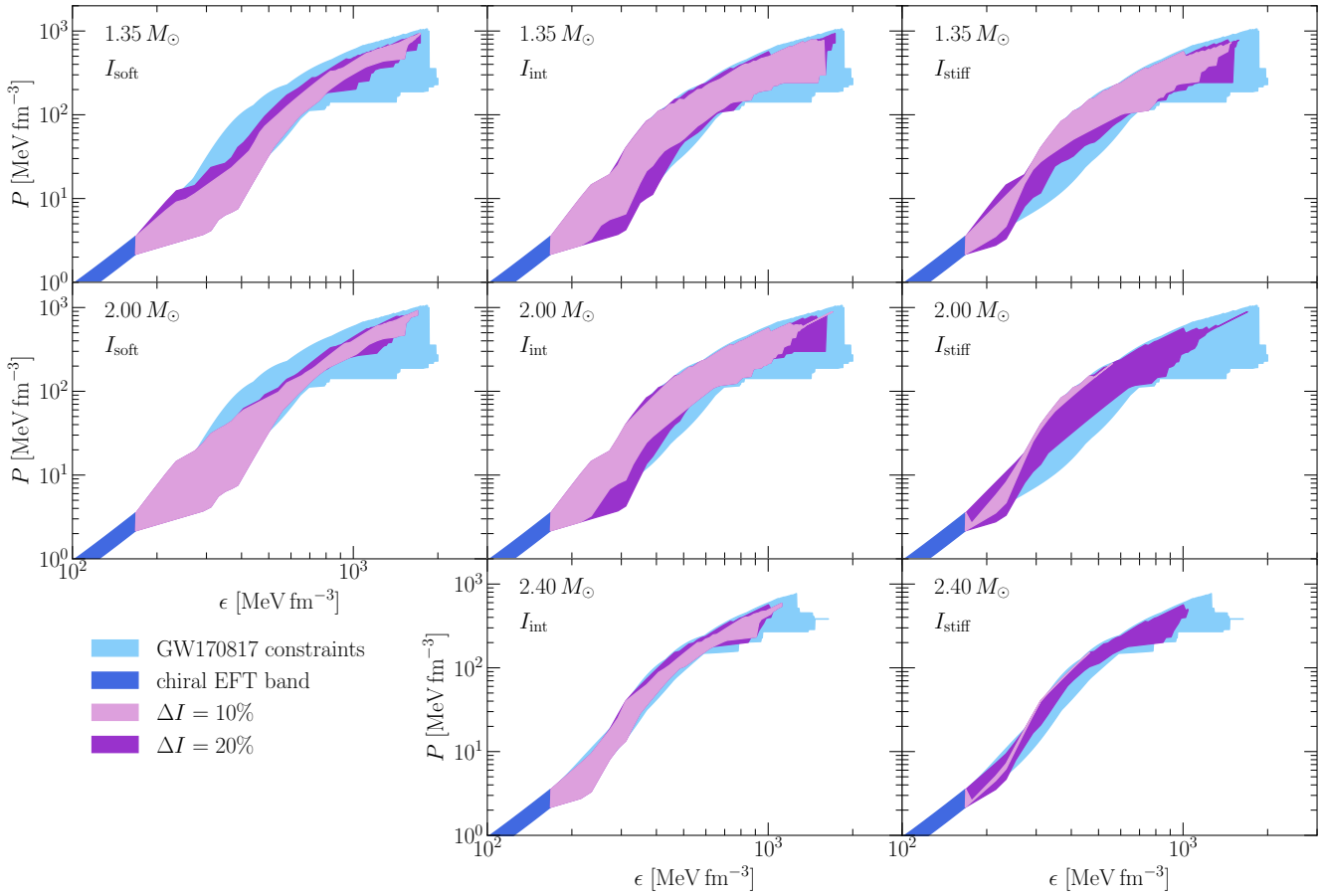

Figure 6.9.: Similar as Fig. 5.11. Uncertainty bands for the EOS from combined constraints of neutron star masses, GW170817 and a hypothetical moment of inertia measurement for different neutron star masses (rows) and hypothetical moment of inertia values (columns). We use the same color coding as in Fig. 6.8. For details see the text.

6.3 Moment of inertia, tidal deformability, and quadrupole moment

The moment of inertia, the tidal deformability, and the quadrupole moment of neutron stars have been the focus of many studies, see, e.g., Refs. [296, 297, 298, 299, 300]. Even though these observables are sensitive to the internal structure of the neutron star, the trio is connected by EOS independent relations [297]. Of special interest are the dimensionless quantities

$$\bar{I} \equiv \frac{I}{M^3}\,, \qquad \bar{\lambda} \equiv \frac{\lambda}{M^5}\,, \qquad \bar{Q} \equiv \frac{Q}{M^3\chi^2}\,,$$

with the dimensionless spin parameter

$$\chi = \frac{J}{M^2}\,.$$

Here, we note that our sign in the definition of $\bar{Q}$ is different to the definition given by Yagi and Yunes [297]. This is because of the definition for the quadrupole moment Q given in Eq. (3.62) that is based on the works of Hartle as well as Hartle and Thorne [130, 133], where the quadrupole moment of neutron stars is defined with the opposite sign.

We start by investigating the trio as functions of the mass M and the compactness parameter C. In Fig. 6.10, we present our results for the dimensionless observables $\bar{I}$, $\bar{\lambda}$, and $\bar{Q}$ for the piecewise polytropic EOS model and highlight additionally the results for the three representative EOS. We present the trio as a function of the mass M in the left panels. In the right panels, each member of the trio is shown as a function of the compactness C. The resulting bands are rather narrow and the relations approach each other with increasing compactness. Furthermore, we show the corresponding results for black holes in the right panels. The compactness parameter for black holes (BH) is given by $C_{\rm BH} = 0.5$ [298]. The corresponding dimensionless observables in the case of black holes are given by [45, 109, 128, 214, 269]

$$\bar{I}_{\rm BH} = 4\,, \qquad \bar{\lambda}_{\rm BH} = 0\,, \qquad \bar{Q}_{\rm BH} = 1\,.$$

Therefore, we highlight the black hole limit as stars in the case of the moment of inertia $\bar{I}$ and the quadrupole moment $\bar{Q}$ in the right panels in Fig. 6.10. In the case of the dimensionless tidal deformability $\bar{\lambda}$, we show an arrow that indicates the black hole limit as the actual point is at lower $\bar{\lambda}$ than shown in the figure. The uncertainty bands in the case of the piecewise polytropic EOS model approach indeed the black hole limits. Further, we observe that the resulting uncertainty bands are remarkably thin.

In Fig. 6.11, we extend our considerations to the speed of sound parametrization. The resulting bands are similar to the results of the piecewise polytropic EOS model. Moreover, the EOS based on the speed of sound parametrization approach also the black hole limit.

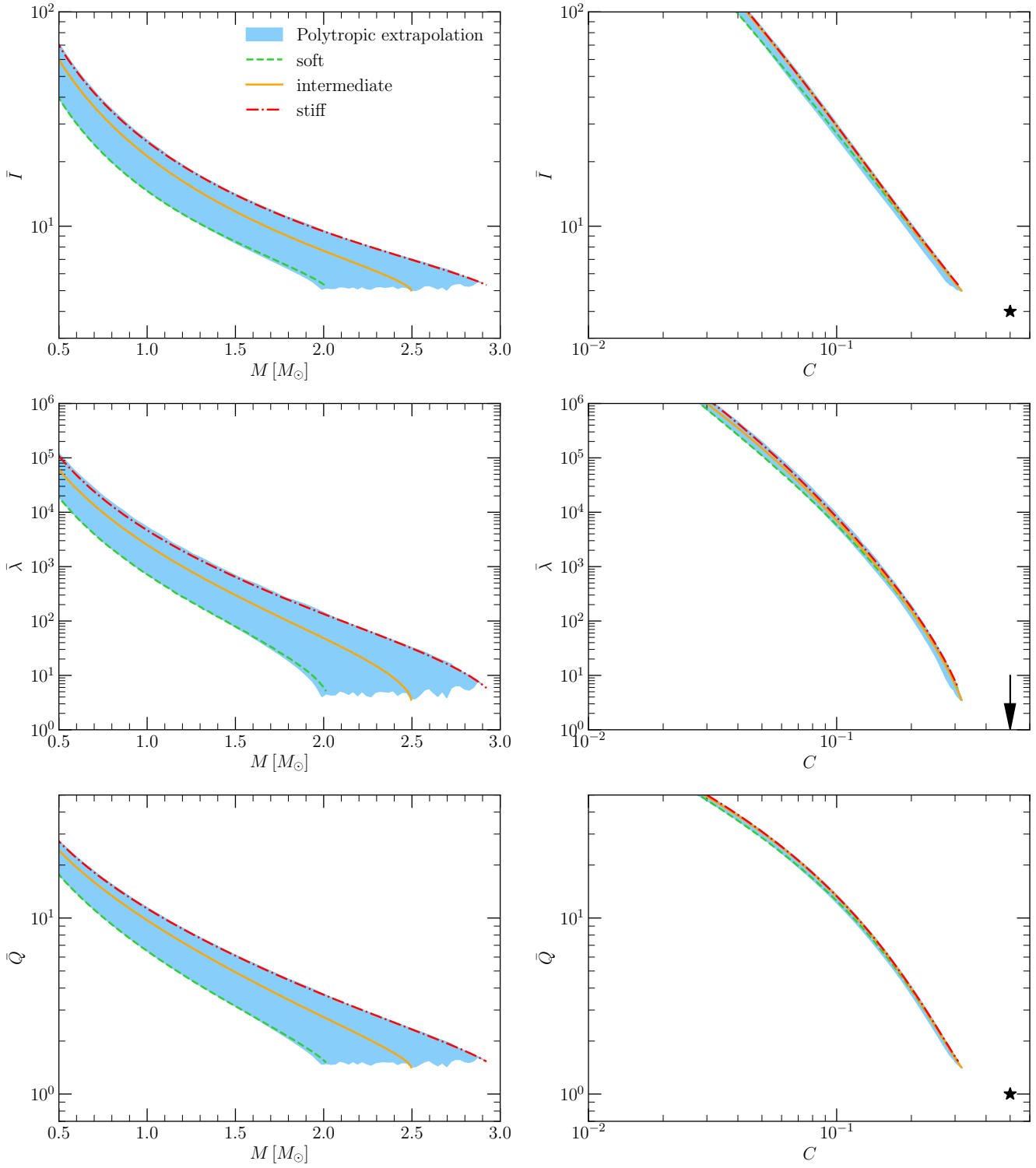

Figure 6.10.: In all panels, we present our results for the the piecewise polytropic EOS model and for the three representative EOS. The panels on the left side show each observable of the I-Love-Q trio as a function of the neutron star mass. The panels on the right side show each member of the trio as a function of the compactness. Additionally, we added stars to indicate the corresponding limits for black holes $\bar{I}_{\rm BH}$ and $\bar{Q}_{\rm BH}$ in the case of $\bar{I}(C)$ and $\bar{Q}(C)$. In the case of $\bar{\lambda}(C)$, we show an arrow that points to the black hole limit $\bar{\lambda}_{\rm BH}$. The piecewise polytropic EOS model exhibits a tight correlation for the I-Love-Q trio as a function of the compactness parameter.

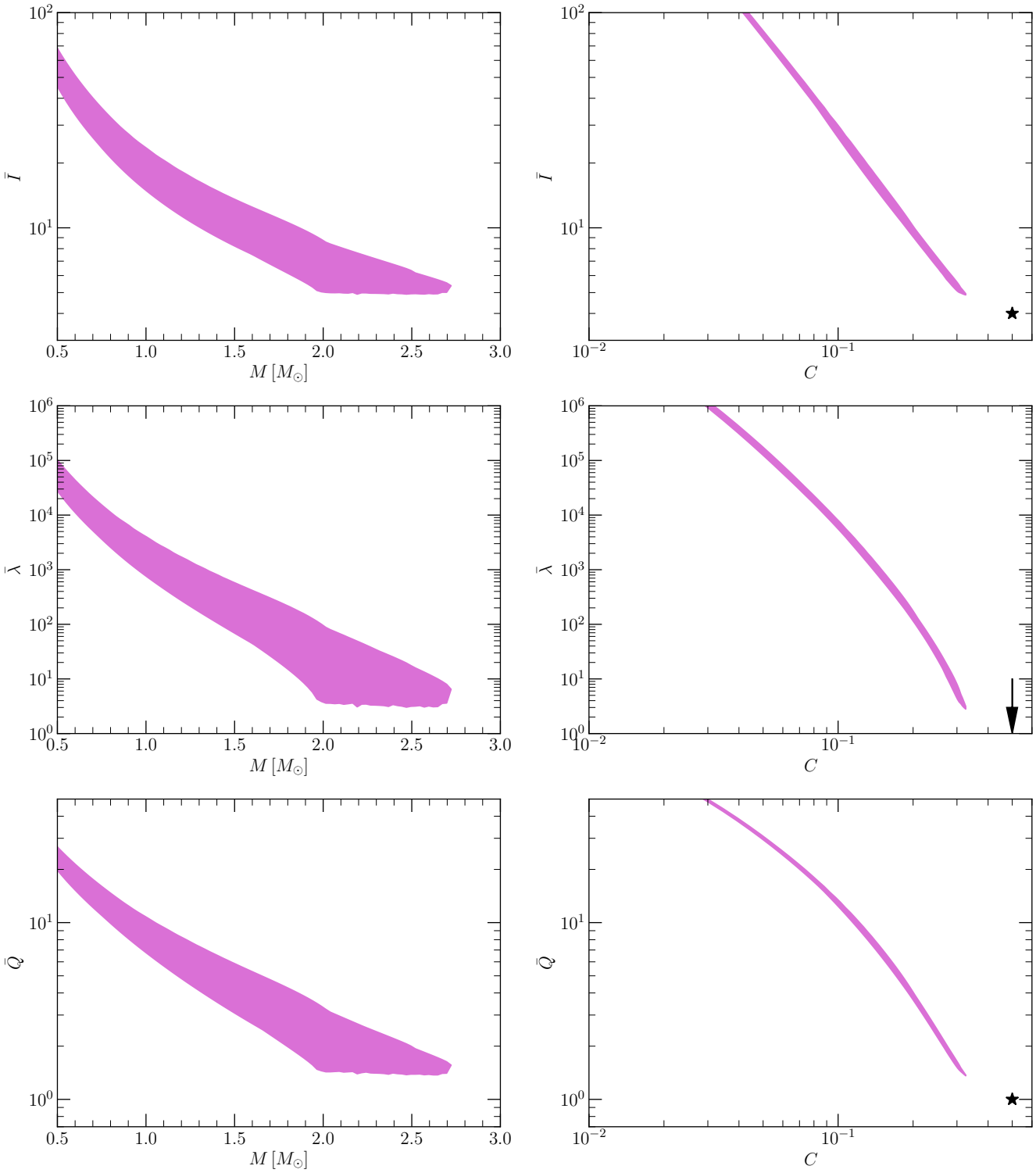

Figure 6.11.: Similar figure as Fig. 6.10. We present the results for the I-Love-Q trio in the case of the speed of sound parametrization in purple.

6.3.1 Revisiting correlations among neutron star properties

In Chap. 4, we studied a correlation between the radius of typical neutron stars with masses of $1\,M_\odot$ and $1.4\,M_\odot$, respectively, and the pressure of the EOS evaluated at twice saturation density. We now extend our considerations to the I-Love-Q- trio. Similar considerations were done in previous works: Lattimer and Schutz [182] found an approximate relation for the moment of inertia and the compactness parameter which the authors combined with the radius-pressure correlation introduced in Ref. [177]. For a fixed mass, the authors of Ref. [182] ascertain that the moment of inertia is correlated with the pressure in the vicinity of the saturation density. A similar correlation between the dimensionless tidal deformability and the pressure at twice saturation density was investigated in the studies presented in Refs. [184, 305].

We explore whether the suggested correlations emerge among the members of the I-Love-Q trio and the pressure at twice saturation density. Hereto, we consider the piecewise polytropic EOS model. We sample over all EOS inside the piecewise polytropic EOS uncertainty band and evaluate each member of the I-Love-Q trio at the masses $1\,M_\odot$ as well as $1.4\,M_\odot$ and the pressure at twice saturation density. In each case, we determine the envelope. We present our results in Fig. 6.12, where the upper row refers to the fixed neutron star mass $1\,M_\odot$ and the lower row to the fixed mass $1.4\,M_\odot$. The panels from left to right depict the dimensionless moment of inertia $\bar{I}$, the dimensionless tidal deformability $\bar{\lambda}$, and the dimensionless quadrupole moment $\bar{Q}$. We observe that the members of the I-Love-Q trio exhibit a weak a correlation with the pressure at twice saturation density.

6.3.2 I-Love-Q relations

In Sec. 5.2, we discussed universal relations and introduced such a relation between the compactness parameter C and the normalized moment of inertia $I/(MR^2)$. In the present chapter, we explored a similar relation between another dimensionless moment of inertia $\bar{I}$ and the compactness parameter C and similar relations between the dimensionless tidal deformability $\bar{\lambda}$ and the compactness parameter C as well as the dimensionless quadrupole moment $\bar{Q}$ and the compactness parameter C. We now investigate relations among the members of the three observables $\bar{I}$, $\bar{\lambda}$, and $\bar{Q}$.

Yagi and Yunes [297] discovered the I-Love-Q relations which appear to be EOS insensitive combinations of the moment of inertia, the tidal deformability, and the quadrupole moment. The authors of Ref. [298] give two possible explanations for the insensitivity of the I-Love-Q relations to details of the EOS: First, the authors suggest that $\bar{I}$, $\bar{\lambda}$, and $\bar{Q}$ are mostly sensitive to the low-density regime of the EOS. For densities as low as they appear in the outer crust of a neutron star, realistic EOS are well constrained and thus approach each other [298]. In a subsequent work [296], the authors argued that the sensitivity of the I-Love-Q trio to the low-density regime of the EOS is a misconception. Yagi and Yunes [296] found that the moment of inertia $\bar{I}$ and the quadrupole moment $\bar{Q}$ are mostly sensitive to contributions provided by the outer core. Second, for increasing compactness parameter, the I-Love-Q relations of neutron stars approach the black hole limit. A consequence of the *no-hair theorem* is that the I-Love-Q relations of black holes are insensitive to details of the "internal structure" [298] (see also references therein). The no-hair theorem[1] states that a black hole is characterized by only three parameters which are the mass, the electric charge, and the spin [67, 142]. However, the applicability of the black hole limit to neutron stars is not obvious [300].

In Refs. [297, 298], the authors present fit functions for the universal functions using several realistic EOS (cf. Refs. [297, 298] for details). The fit relation is given by

$$\ln y = a + b \ln x + c\,(\ln x)^2 + d\,(\ln x)^3 + e\,(\ln x)^4 \ , \tag{6.4}$$

[1] The no-hair theorem holds for stationary, isolated black holes. In reality, black holes are accreting mass and are surrounded by other objects [300].

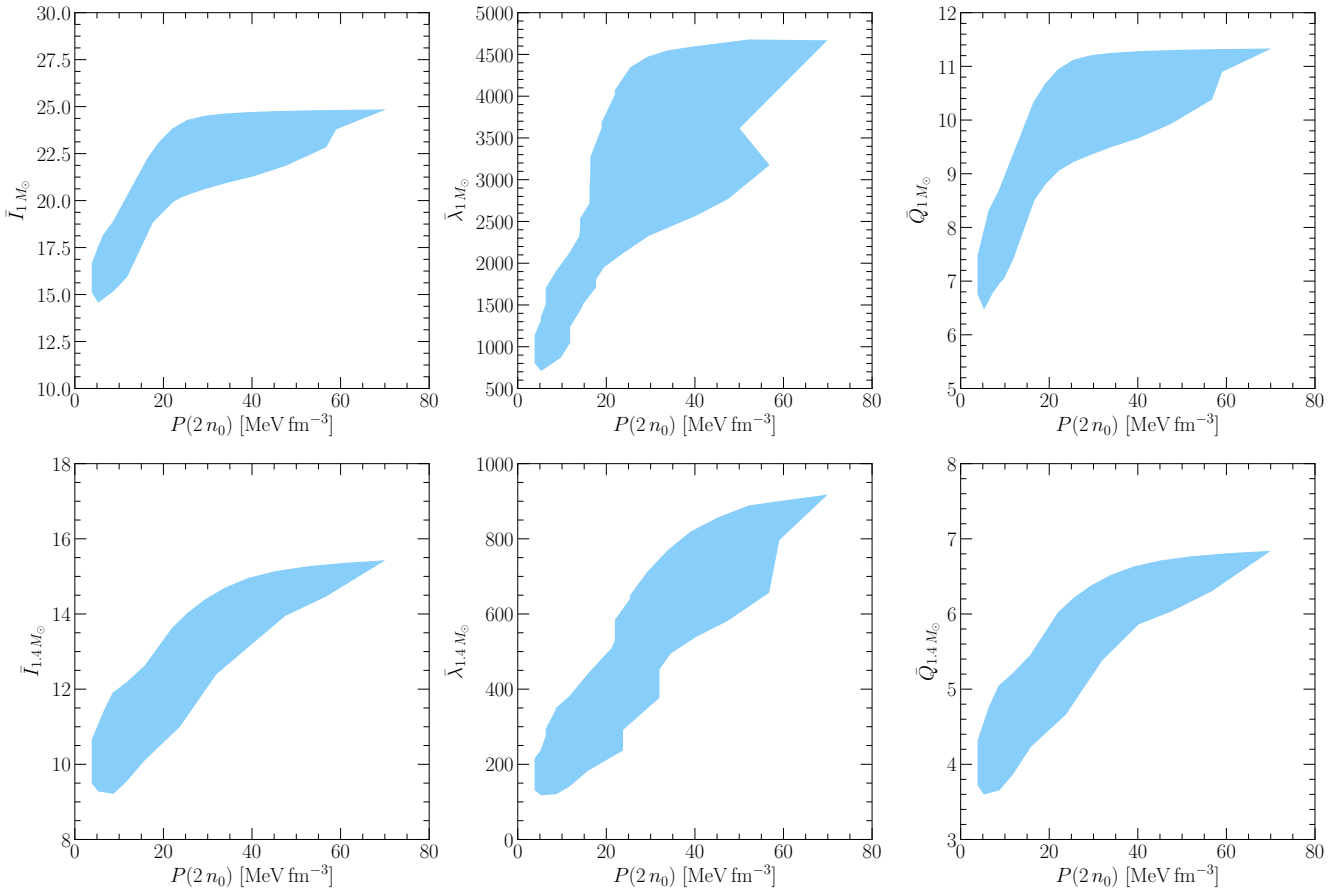

Figure 6.12.: The upper row refers to the fixed neutron star mass $1\,M_\odot$ and the lower row to $1.4\,M_\odot$. The three panels in each row show each one part of the I-Love-Q trio as a function of the pressure evaluated at twice saturation density. The results shown are based on the piecewise polytropic EOS model.

where x and y stand for the neutron star observables $\bar{I}$, $\bar{\lambda}$, and $\bar{Q}$ and the coefficients a, b, c, d, and e are the fit coefficients that are listed in Table 6.4. The coefficients were updated in a subsequent work by Yagi and Yunes [300] by taking more realistic EOS into account. Further works that investigate the I-Love-Q relations can be found in Refs. [27, 175, 197].

We investigate the relations among the members of the I-Love-Q trio for both the piecewise polytropic EOS model and the speed of sound parametrization. Therefore, we sample for both models individually over the whole uncertainty bands and determine the three relations among the moment of inertia, the tidal deformability, and the quadrupole moment, i.e., $\bar{I}(\bar{\lambda})$, $\bar{I}(\bar{Q})$, and $\bar{Q}(\bar{\lambda})$. For each of the three relations we determine the envelope. We show our results in Fig. 6.13. From left to right, we show the $\bar{I}-\bar{\lambda}$, the

Table 6.4.: Coefficients of the I-Love-Q relations given in Eq. (6.4). The fit function was introduced in Refs. [297, 298] and the coefficients were revisited in Ref. [300].

y	x	a	b	c	d	e
$\bar{I}$	$\bar{\lambda}$	1.496	0.05951	0.02238	-6.953×10^{-4}	8.345×10^{-6}
$\bar{I}$	$\bar{Q}$	1.393	0.5471	0.03028	0.01926	4.434×10^{-4}
$\bar{Q}$	$\bar{\lambda}$	0.1940	0.09163	0.04812	-4.283×10^{-3}	1.245×10^{-4}

$\bar{I}-\bar{Q}$, and the $\bar{Q}-\bar{\lambda}$ relations. In each panel, we present the corresponding fit functions given in Eq. (6.4) [297] with the revisited coefficients from Table 6.4 (cf. Ref. [300]). In the first row of panels, we show the results for the three representative EOS of the piecewise polytropic EOS model which are in good agreement with the fit functions by Refs. [297, 300]. In the seconds row of panels, we show the results for the entirety of the EOS uncertainty band in the case of the piecewise polytropic EOS model. Our results presented in Fig. 6.13 confirm that the I-Love-Q relations approximately hold for the piecewise polytropic EOS model discussed in this work. In the third row of panels, we present the results using the speed of sound parametrization.

The I-Love-Q relations provide applications in astrophysics. The measurement of one observable of the I-Love-Q trio provides access to the remaining members through the universal relations [298].

6.3.2.1 Revisiting constraints from moment of inertia measurements

Next, we can compare our results for the hypothetical moment of inertia measurements of PSR J0737−3039A with constraints from the GW signal of the neutron star merger GW170817 [5, 6, 7]. GW170817 provides constraints for the dimensionless tidal deformability $\bar{\lambda}_{1.4\,M_\odot}$ of a $1.4\,M_\odot$ neutron star, with $\bar{\lambda}_{1.4\,M_\odot} \leqslant 800$ from [5] and $70 \leqslant \bar{\lambda}_{1.4\,M_\odot} \leqslant 580$ from the more recent analysis [6]. We use the I-Love relation from Yagi and Yunes [297] to translate these into constraints for the moment of inertia $I_{1.4\,M_\odot}$ of $1.4\,M_\odot$ neutron stars, leading to the following ranges $I_{1.4\,M_\odot} \leqslant 88.6\,M_\odot\,\mathrm{km}^2$ and $48.7\,M_\odot\,\mathrm{km}^2 \leqslant I_{1.4\,M_\odot} \leqslant 81.2\,M_\odot\,\mathrm{km}^2$, respectively. We extrapolate these ranges from $1.4\,M_\odot$ to $1.338\,M_\odot$ by using the upper boundary of the uncertainty band from the left panel in Fig. 5.1. This leads to $I_{1.338\,M_\odot} \leqslant 82.0\,M_\odot\,\mathrm{km}^2$ and $44.6\,M_\odot\,\mathrm{km}^2 \leqslant I_{1.338\,M_\odot} \leqslant 74.6\,M_\odot\,\mathrm{km}^2$, respectively. These are shown in Fig. 6.14 as the orange and yellow regions, respectively, where we have adjusted the radius range of these regions to the maximal allowed radius from the general EOS correlation for the maximal I from the more conservative orange region. The comparison of the GW170817 constraints in Fig. 6.14 demonstrates the consistency with the general EOS band based on nuclear physics and the observation of a $2\,M_\odot$ neutron star. Finally, we have checked that the extracted moment of inertia is very similar, if one first scales the dimensionless tidal deformability to $1.338\,M_\odot$, and then uses the I-Love relation to translate this to constraints for I, which leads to $I_{1.338\,M_\odot} \leqslant 83.4\,M_\odot\,\mathrm{km}^2$ and $45.1\,M_\odot\,\mathrm{km}^2 \leqslant I_{1.338\,M_\odot} \leqslant 76.3\,M_\odot\,\mathrm{km}^2$, respectively.

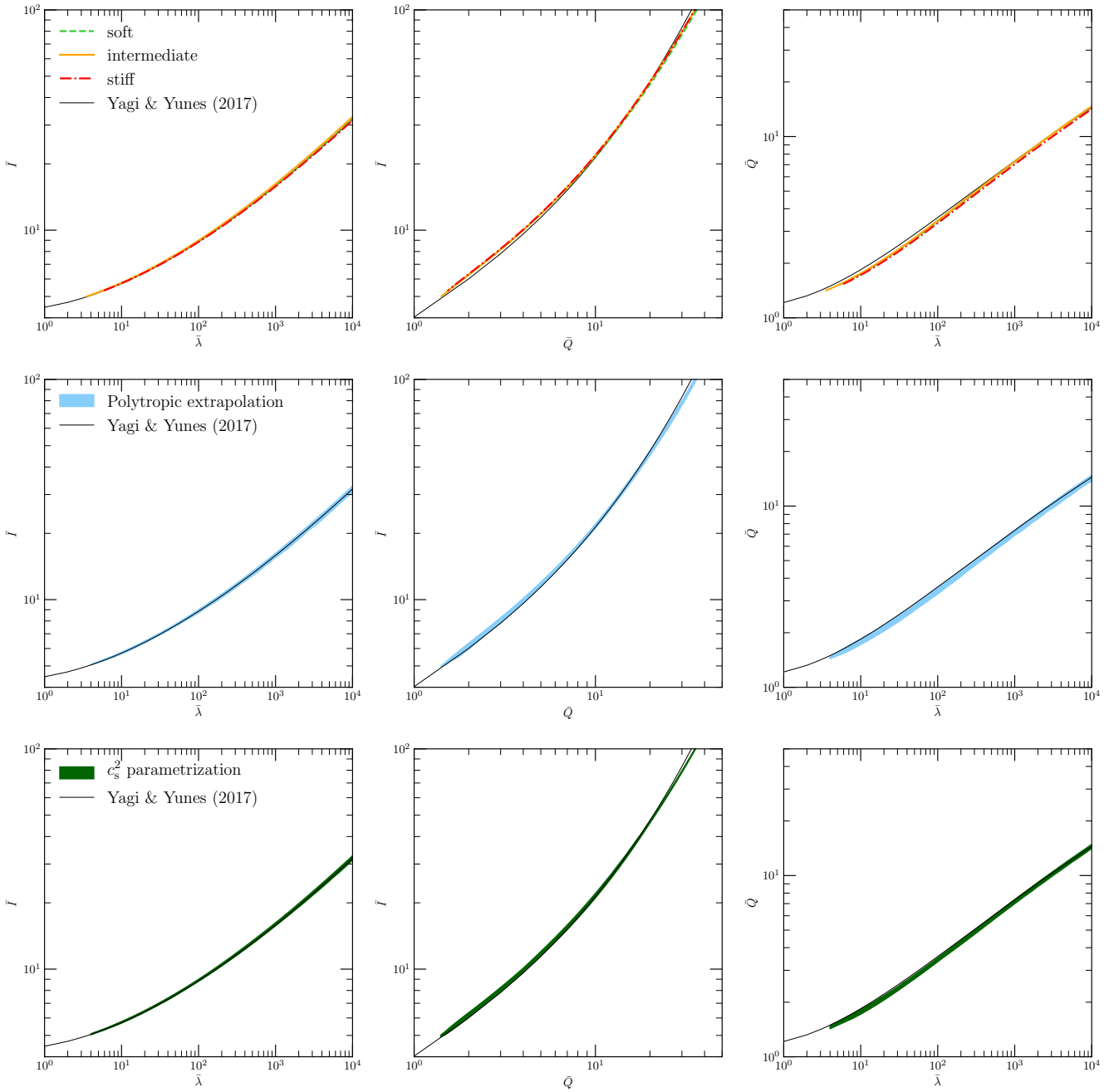

Figure 6.13.: From left to write the panels show the I-Love, I-Q, and Q-Love relations. Each panel features the according relation (solid black) introduced by Yagi and Yunes (2013) [297] with the revisited fit coefficients taken from a follow-up work by Yagi and Yunes (2017) [300]. *Top panels*: I-Love-Q relations for the three representative EOS of the piecewise polytropic EOS model. *Middle panels*: I-Love-Q relations for the piecewise polytropic EOS model. *Bottom panels*: I-Love-Q relations for the speed of sound parametrization.

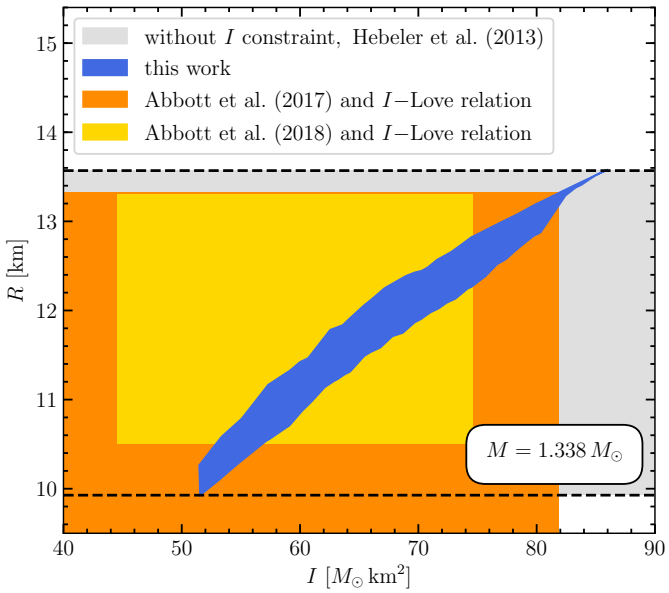

Figure 6.14.: Similar as Fig. 5.8. Radius of the neutron star PSR J0737 − 3039A with mass $1.338\,M_\odot$ as a function of the moment of inertia I. The gray band within the black dashed lines represents the full radius range based on Ref. [137]. The blue band shows the allowed moments of inertia I for this neutron star and how this correlates with the radius. In addition, we compare our results with the GW constraints from the neutron star merger GW170817 from Ref. [5] (orange region) and the more recent analysis Ref. [6] (yellow region), for details see text.

7 Summary and outlook

In this thesis, we have studied properties of neutron stars and the impact of astrophysical observations on the radius of neutron stars and the nuclear EOS. Hereto, we used results from state-of-the-art chiral EFT interactions that provide an uncertainty band for the EOS up to nuclear densities. For higher densities, we used two different extrapolation methods. First, we applied the established method of the piecewise polytropic expansion following Ref. [137]. Second, we parametrized the speed of sound in the interior of neutron stars calculated as in our paper, Ref. [118]. From the speed of sound parametrization we inferred the EOS using standard thermodynamic relations. Both approaches allow us to obtain a large number of EOS and to probe the EOS space in a systematic manner. Having the EOS at hand, we applied the EOS to determine neutron star observables. We used the Hartle-Thorne approximation for the metric of spacetime up to second order in the angular velocity of the neutron star. Using this approach, we determined properties of non-rotating neutron stars, slowly rotating neutron stars, and neutron stars in binary systems.

We started our considerations by investigating non-rotating neutron stars. We explored the EOS parameter space as well as the mass-radius uncertainty band for both the piecewise polytropic EOS model and the speed of sound parametrization. In the literature correlations between EOS parameters at nuclear densities and neutron star radii of typical neutron stars are discussed. We investigated whether such correlations emerge also in the EOS models presented in this work. Indeed, both models exhibit the correlation between the pressure at twice nuclear saturation density and the radius of typical neutron stars. Nevertheless, we identified deviations from results presented in the literature. Subsequently, we assumed hypothetical, simultaneous mass-radius measurements. The aim of this research was to obtain constraints for the EOS based on a sequence of mass-radius measurements. For our assumptions, we took the primary targets of the NICER mission into account. Hereto, we utilized two different approaches to infer the constraints for the radius and the EOS. First, we performed simple compatibility cuts. Second, we showed the results of using Bayesian statistics in a collaborative work (cf. Ref. [118]). We conclude that the parameterization of the EOS does indeed matter. Moreover, we observed that the obtained posterior distributions favor larger radii over smaller radii. We suggest that this result can be explained by the lack of freedom in the matching to the EOS inferred from chiral EFT interactions.

We then extended our considerations from non-rotating neutron stars to slowly rotating neutron stars. We presented an uncertainty band for the moment of inertia of neutron stars. The remarkable double neutron star system PSR J0737−3039 provides the prospect of a future moment of inertia measurement. The mass of the double pulsar is known and we therefore deduce from the piecewise polytropic EOS model a reasonable range for the moment of inertia of this particular mass star. Assuming hypothetical moment of inertia measurements and applying the possible achievable uncertainty, we derive constraints for the radius of neutron stars. We generalize our considerations to further masses and explored their radius constraints. Moreover, we provide EOS uncertainty bands for each considered scenario. We also applied the hypothetical moment of inertia scenarios to the speed of sound parametrization. The two EOS parametrizations exhibit no significant differences in the resulting radius constraints.

Ultimately, we considered neutron stars in binary systems which permits the investigation of tidal effects and quadrupole moments. We studied the dimensionless tidal deformability and investigate the impact of a measurement of this observable. We explored properties of binary neutron star systems and merger. The pioneering observation of GW from a binary neutron star merger in August 2017 opened up a new era of gravitational wave astronomy. We applied the results of this detection to both EOS models to study the impact on the radius of neutron stars and the EOS itself. We observed that the constraints imposed by GW170817 have no significant impact on the radius of neutron stars or the

EOS. Previous studies observed universal relations among neutron star observables that are remarkably insensitive to details of the underlying EOS. These universal relations connect the moment of inertia, the tidal deformability, and the quadrupole moment. Accordingly, these universal relations are named I-Love-Q relations. The I-Love-Q relations hold up very well for both the piecewise polytropic and speed of sound EOS models. This result is impressive since both models yield a large amount of EOS

In the future, improvements of the EOS parametrization can be included by considering a parametrization of the EOS in the density regime of the chiral EFT band. This will allow to probe the correlations between different neutron star observables and the pressure at lower densities than twice saturation density. Such a parametrization can then also be used to investigate if the mass-radius parameter space is more smoothly covered compared with the approach discussed in Refs. [118, 137]. Moreover, the extension of a chiral EFT band parametrization can be used in a future work to revisit the priors and the analysis presented in our work, Ref. [118]. Beside a new parametrization of the EOS inside the chiral EFT band, future developments on chiral interactions can provide improved nuclear forces which can in turn provide more constraints for the nuclear EOS and thus the radius of neutron stars. Future progress in pQCD can also yield additional information on the EOS in the high-density regime to which the EOS in the density regime relevant for neutron stars can be matched.

In addition, the NICER mission will yield simultaneous measurements of masses and radii of neutron stars. The protocol outlined and applied to hypothetical scenarios in Chap. 4 and our paper in Ref. [118] can then be applied to the actual NICER results once publicly available. The approach of Bayesian statistics can also be used to study the impact of multi-messenger astronomy by including GW observations.

A Details of the auxiliary function j for the rotational drag and the quadrupole moment

In Chap. 3, we introduced the slow-rotation approximation by Hartle and Thorne (cf. Refs. [130, 133]) to study neutron star observables. There, we provide details on the auxiliary function j (cf. Eq. (3.17)). In Section 3.6, we described how we solve the differential equations. We transform the second-order differential equation for $\bar{\omega}$ into a system of first order-differential equations. This system of differential equations features the function j that depends on the metric functions λ and ν. Moreover, the function j shows up as the factor

$$\frac{1}{j}\frac{\mathrm{d}j}{\mathrm{d}r}\,.$$

In the following, we show that the factor given above does not depend on the metric function ν:

$$\frac{1}{j}\frac{\mathrm{d}j}{\mathrm{d}r} = \mathrm{e}^{\frac{1}{2}(\nu+\lambda)}\cdot\frac{\mathrm{d}}{\mathrm{d}r}\left(\mathrm{e}^{-\frac{1}{2}(\nu+\lambda)}\right) = -\frac{1}{2}\left(\nu'+\lambda'\right). \tag{A.1}$$

The expression above shows that the combination of the function j and the radial logarithmic derivative solely depend on the radial derivative of the metric functions ν and λ. Using the differential equation of the metric function ν given in Eq. (3.6) and determining the derivative of Eq. (3.8) with respect to the radial coordinate yields:

$$\frac{1}{j}\frac{\mathrm{d}j}{\mathrm{d}r} = -\frac{4\pi r^3(P+\epsilon)}{r(r-2m)}\,. \tag{A.2}$$

We use the expression above to simplify the differential equation for the rotational drag.

We now discuss how the definition of the function j can be rewritten in terms of the enthalpy h. We solve the integral equation given in Eq. (3.79) using the boundary conditions,

$$\nu(R) = \ln\left(1-\frac{2M}{R}\right) \quad \text{and} \quad h(R) = 0\,,$$

at the surface of the neutron star,. This leads to

$$j(h) = \left(\frac{1-\frac{2m}{r}}{1-\frac{2M}{R}}\right)^{\frac{1}{2}}\cdot\mathrm{e}^{h}\,. \tag{A.3}$$

The expression above can then be used to determine j^2. Moreover, it is useful to determine an expression for the derivative

$$\frac{\mathrm{d}j^2}{\mathrm{d}r} = 2j\cdot\frac{\mathrm{d}j}{\mathrm{d}r} = -2j^2\frac{4\pi r^3(P+\epsilon)}{r(r-2m)}\,, \tag{A.4}$$

where we used the expression given in Eq. (A.2). We insert the expressions for j^2 and its derivative into the differential equations for h_2 and v_2 which are required for the calculation of the quadrupole moment of neutron stars (cf. Sec. 3.6).

B Numerical test cases

We present numerical test cases that we used to benchmark our implementation of the EOS models presented in Chap. 2 as well as the structure equations of neutron star observables presented in Chap. 3. We use a selection of references to benchmark our implementation and show qualitative as well as quantitative comparisons.

In Chap. 4, we discussed the representative EOS based on a piecewise polytropic EOS model introduced in Ref. [137], where the authors also provide numerical data for the EOS as well as the resulting mass-radius relations. In Fig. B.1, we show our results in comparison with the results given in Ref. [137]. The qualitative comparison shows that our results for the mass-radius relations are in very good agreement with the literature. Nonetheless, we note that the radii of light neutron stars ($M \lesssim 1\,M_\odot$) appear to be slightly smaller than the corresponding results in Ref. [137].

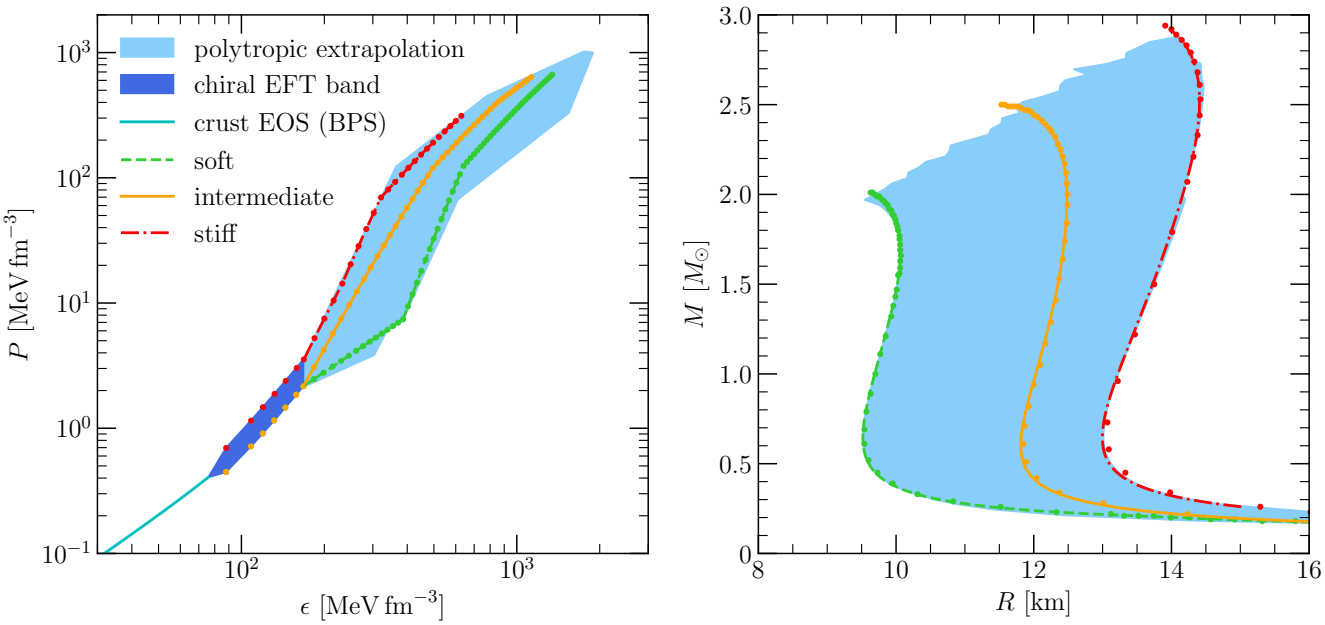

Figure B.1.: *Left panel*: Pressure P as a function of energy density ϵ. *Right panel*: Neutron star mass M as a function of the radius R. The dashed, solid, and dash-dotted lines present our results. The results from the work of Hebeler *et al.* [137] are shown as dots, where the data is taken from Ref. [137].

For a more quantitative discussion of the comparison, we use the numerical data for the three representative EOS given in Ref. [137]. The provided data includes among other quantities values for the central pressure and the corresponding radius and mass of the resulting neutron stars. We interpolate each the radius R and the mass M as a function of the central pressure P_c based on our results. We then determine the relative errors for the radius and the mass. As seen in Fig. B.1, the relative errors for both radii and masses are larger for light neutron stars than for heavy neutron stars. The observed relative errors are a few permille except for the light neutron stars. For light neutron stars the relative errors are at the percent level. We show the relative errors for the radii and masses in the case of the three representative EOS in Fig. B.2.

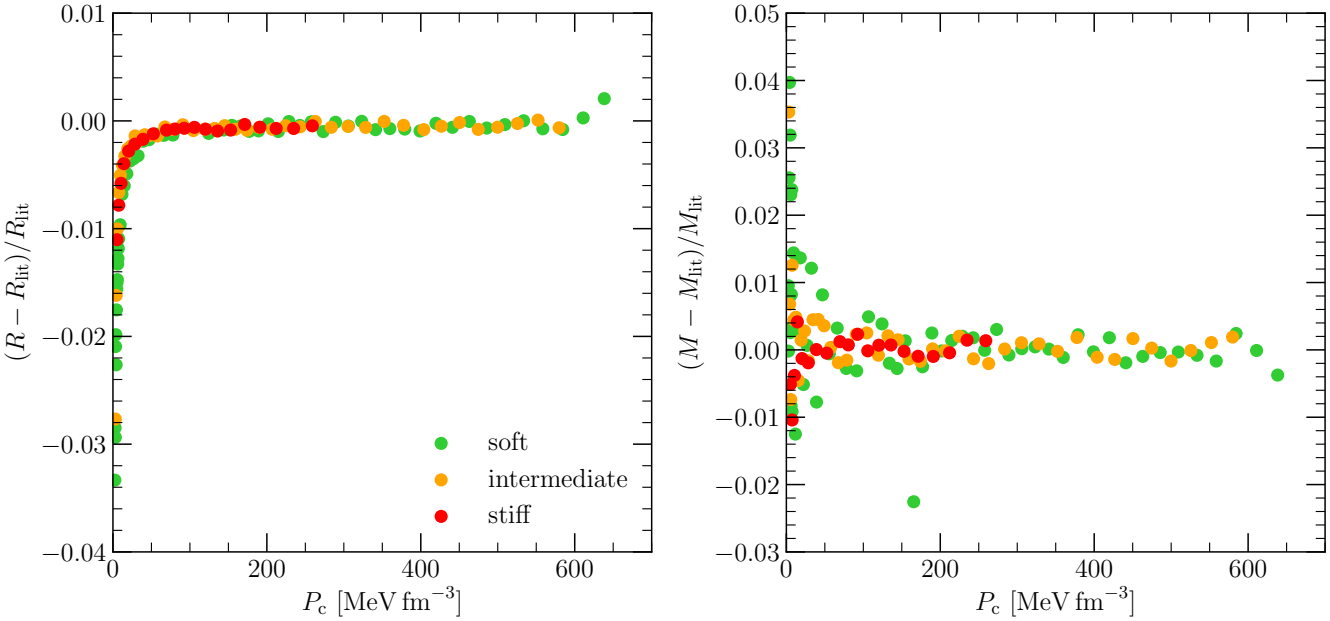

Figure B.2.: Relative errors for the radii (left panel) and the masses (right panel) for the three representative EOS introduced by Hebeler *et al.* [137]. We determined the radii and masses at the central pressures $P_{\rm c}$ as listed in Ref. [137].

In Sec. 2.3.3, we introduced a parametrization of the speed of sound inside neutron stars to generate the EOS. This model was set up in collaboration with G. Raaijmakers, K. Hebeler, A. Schwenk, and A. Watts and published in our paper, Ref. [118]. While setting up the model, we performed parallel benchmarks and therefore ensure that our independently obtained results agree.

Further, we benchmark the implementation of the binding energy. A list of realistic EOS including the underlying approach and considered composition is given in Ref. [177] (cf. also references therein for the individual EOS). Lattimer and Prakash [177] do not provide numerical values for the binding energy, however, we digitalize the figures to extract data that we then use for our benchmarks. Hereto, we choose BE$/M^2$ as a function of M (cf. Fig. 8 in Ref. [177]) instead of BE$/M$ as a function of C (cf. Fig. 9 in Ref. [177]) for our benchmark. We calculate the masses M and binding energies BE and determine via interpolation BE$/M^2(M)$. We evaluate the interpolation function at the masses M_i we chose for the comparison. We present the numerical comparison of the literature results with our calculations in Table B.1. The relative errors are in the order of a few percent, hence our results are in good agreement with the literature.

As a further benchmark, we use results shown in Ref. [182]. We digitized the data presented in Fig. 1 of Ref. [182], were the authors show the scaled moment of inertia $I/M^{3/2}$ as a function of the neutron star mass M for various EOS. We present the quantitative comparison in Table B.2. We find the relative errors to be less than one percent except for one value for the WFF3 EOS.

We benchmark our implementation of the calculation of the tidal deformability by comparing with the results of Hinderer *et al.* [147]. In Ref. [147], the results for the radius R, the compactness C, the Love number k_2, and the tidal deformability λ are given evaluated for neutron stars with a mass of $1.4\,M_\odot$ for several realistic EOS. We use Eq. (6.2) to determine k_2. In Table B.3, we present a quantitative comparison of our results for the EOS AP1 and AP3 with the results given in Ref. [147].

Postnikov *et al.* [218] studied tidal Love numbers and determined masses, radii, compactness parameters, tidal Love number, and tidal deformabilities for various EOS. We extracted the data from Figs. 6 – 10 from Ref. [218] and compare with our results obtained for the two EOS WFF1 and AP4. The numerical comparison is presented in Table B.4.

Table B.1.: Data taken from Ref. [177] (cf. Fig. 8 therein) and compared to our results. Δ is the relative difference in percent.

		literature	this work	
EOS	$M\ [M_\odot]$	$\mathrm{BE}/M^2\ [M_\odot^{-1}]$	$\mathrm{BE}/M^2\ [M_\odot^{-1}]$	$\Delta\,[\%]$
AP3	1.00	0.078	0.078	0
	1.25	0.080	0.080	0
	1.50	0.082	0.082	0
	1.75	0.085	0.085	0
	2.00	0.089	0.089	0
	2.25	0.094	0.094	0
AP4	1.00	0.082	0.081	−1.2
	1.25	0.084	0.084	0
	1.50	0.088	0.087	−1.1
	1.75	0.092	0.091	−1.1
	2.0	0.097	0.096	−1.0
WFF1	1.00	0.084	0.092	9.5
	1.25	0.088	0.095	8.0
	1.50	0.093	0.098	5.4
	1.75	0.099	0.103	4.0
WFF2	1.00	0.076	0.084	10.5
	1.25	0.080	0.087	8.7
	1.50	0.084	0.090	7.1
	1.75	0.089	0.094	5.6
WFF3	1.00	0.080	0.085	6.3
	1.25	0.083	0.088	6.0
	1.50	0.088	0.091	3.4
	1.75	0.094	0.097	3.2

Table B.2.: Data digitized from Ref. [182] (cf. Fig. 1 therein) and compared to our results. Δ is the relative difference in percent.

		literature	this work	
EOS	$M\ [M_\odot]$	$I/M^{3/2}\ [\mathrm{km}^2\, M_\odot^{-1/2}]$	$I/M^{3/2}\ [\mathrm{km}^2\, M_\odot^{-1/2}]$	$\Delta\,[\%]$
AP3	1.00	45.1	45.2	0.2
	1.25	44.7	44.8	0.2
	1.50	44.4	44.4	0
	1.75	44.0	44.0	0
	2.00	43.4	43.4	0
	2.25	42.0	42.1	0.2
AP4	1.00	41.2	41.2	0
	1.25	40.6	40.6	0
	1.50	40.0	40.0	0
	1.75	39.3	39.3	0
	2.00	38.2	38.3	0.3
WFF1	1.00	35.4	35.4	0
	1.25	35.2	35.3	0.3
	1.50	35.2	35.2	0
	1.75	35.0	35.0	0
WFF2	1.00	39.8	39.8	0
	1.25	39.2	39.3	0.3
	1.50	38.7	38.7	0
	1.75	38.0	38.1	0.3
WFF3	1.00	39.4	39.4	0
	1.25	38.1	38.2	0.3
	1.50	36.5	36.7	0.5
	1.75	33.7	32.5	−3.6

Table B.3.: Comparison with the results given in Ref. [147] (cf. Table 1 therein) for the radius R, the compactness C, the tidal Love number k_2, and the dimensionless tidal deformability $\bar{\lambda}$ of a $1.4\,M_\odot$ neutron star. Δ is the relative error in percent.

	AP1			AP3		
	literature	this work	$\Delta\,[\%]$	literature	this work	$\Delta\,[\%]$
$R\,[\mathrm{km}]$	9.36	9.37	0.1	12.09	11.77	−2.6
C	0.221	0.221	0	0.171	0.176	2.9
k_2	0.0512	0.0516	0.8	0.0858	0.1006	17.2
$\lambda\,[10^{36}\,\mathrm{g\,cm^2\,s^2}]$	0.368	0.372	1.1	2.22	2.27	2.3

Table B.4.: Comparison with the results given in Ref. [218] (cf. Figs. 6 – 10 therein) for the radius R, the compactness C, the tidal Love number k_2, and the dimensionless tidal deformability $\bar{\lambda}$ of $1\,M_\odot$ and $1.4\,M_\odot$ neutron stars. Δ is the relative error in percent.

		WFF3			AP4		
	$M\,[M_\odot]$	literature	this work	$\Delta\,[\%]$	literature	this work	$\Delta\,[\%]$
$R\,[\mathrm{km}]$	1.0	11.1	11.1	0	11.4	11.5	0.9
	1.4	10.9	10.9	0	11.4	11.4	0
C	1.0	0.13	0.13	0	0.13	0.13	0
	1.4	0.19	0.19	0	0.18	0.18	0
k_2	1.0	0.10	0.08	−20.0	0.10	0.10	0
	1.4	0.07	0.06	−14.3	0.08	0.08	0
$10^{-4}\,\lambda\,[\mathrm{km}^5]$	1.0	1.1	0.9	−18.2	1.3	1.3	0
	1.4	0.7	0.6	−14.3	1.0	1.0	0

Bibliography

[1] *"ATNF Pulsar Catalogue", web interface to database, Australia Telescope National Facility*. http://www.atnf.csiro.au/research/pulsar/psrcat. Last visited 2019-05-21.

[2] *LIGO and Virgo observatories detect neutron star smash-ups*. https://news.psu.edu/story/572677/2019/05/02/research/ligo-and-virgo-observatories-detect-neutron-star-smash-ups. Last visited 2019-05-24.

[3] B. P. Abbott, R. Abbott, T. D. Abbott, M. R. Abernathy, F. Acernese *et al.* (LIGO Scientific and Virgo collaborations). *GW151226: Observation of Gravitational Waves from a 22-Solar-Mass Binary Black Hole Coalescence*. Phys. Rev. Lett. **116**, 241103 (2016).

[4] B. P. Abbott, R. Abbott, T. D. Abbott, M. R. Abernathy, F. Acernese *et al.* (LIGO Scientific and Virgo collaborations). *Observation of Gravitational Waves from a Binary Black Hole Merger*. Phys. Rev. Lett. **116**, 061102 (2016).

[5] B. P. Abbott, R. Abbott, T. D. Abbott, F. Acernese, K. Ackley *et al.* (LIGO Scientific and Virgo collaborations). *GW170817: Observation of Gravitational Waves from a Binary Neutron Star Inspiral*. Phys. Rev. Lett. **119**, 161101 (2017).

[6] B. P. Abbott, R. Abbott, T. D. Abbott, F. Acernese, K. Ackley *et al.* (LIGO Scientific and Virgo collaborations). *GW170817: Measurements of neutron star radii and equation of state*. Phys. Rev. Lett. **121**, 161101 (2018).

[7] B. P. Abbott, R. Abbott, T. D. Abbott, F. Acernese, K. Ackley *et al.* (LIGO Scientific and Virgo collaborations). *Properties of the binary neutron star merger GW170817*. Phys. Rev. **X 9**, 011001 (2019).

[8] B. P. Abbott, R. Abbott, R. Adhikari, P. Ajith, B. Allen *et al.* (LIGO Scientific collaboration). *LIGO: The Laser interferometer gravitational-wave observatory*. Rept. Prog. Phys. **72**, 076901 (2009).

[9] A. Abramovici, W. E. Althouse, R. W. P. Drever, Y. Gürsel, S. Kawamura *et al.* *LIGO: The Laser interferometer gravitational wave observatory*. Science **256**, 325 (1992).

[10] M. Abramowitz and I. A. Stegun. *Handbook of Mathematical Functions with Formulas, Graphs, and Mathematical Tables*. Tenth edition, (U.S. Government Printing Office, Washington, DC, USA, 1972).

[11] F. Acernese, M. Agathos, K. Agatsuma, D. Aisa, N. Allemandou *et al.* (VIRGO collaboration). *Advanced Virgo: a second-generation interferometric gravitational wave detector*. Class. Quant. Grav. **32**, 024001 (2015).

[12] K. Akiyama, A. Alberdi, W. Alef, K. Asada, R. Azulay *et al.* (Event Horizon Telescope collaboration). *First M87 Event Horizon Telescope Results. I. The Shadow of the Supermassive Black Hole*. Astrophys. J. Lett. **875**, L1 (2019).

[13] V. A. Ambartsumyan and G. S. Saakyan. *The Degenerate Superdense Gas of Elementary Particles*. Sov. Astron. **4**, 187 (1960).

[14] N. Andersson, V. Ferrari, D. I. Jones, K. D. Kokkotas, B. Krishnan *et al.* *Gravitational waves from neutron stars: Promises and challenges*. Gen. Rel. Grav. **43**, 409 (2011).

[15] E. Annala, T. Gorda, A. Kurkela, and A. Vuorinen. *Gravitational-wave constraints on the neutron-star-matter Equation of State*. Phys. Rev. Lett. **120**, 172703 (2018).

[16] J. Antoniadis, P. C. C. Freire, N. Wex, T. M. Tauris, R. S. Lynch *et al. A Massive Pulsar in a Compact Relativistic Binary*. Science **340**, 6131 (2013).

[17] W. D. Arnett and R. L. Bowers. *A Microscopic Interpretation of Neutron Star Structure*. Astrophys. J. Suppl. **33**, 415 (1977).

[18] Z. Arzoumanian, K. C. Gendreau, C. L. Baker, T. Cazeau, P. Hestnes *et al. The neutron star interior composition explorer (NICER): mission definition*. In *Space Telescopes and Instrumentation* **9144**, 914420 (2014).

[19] Y. Aso, Y. Michimura, K. Somiya, M. Ando, O. Miyakawa *et al.* (KAGRA collaboration). *Interferometer design of the KAGRA gravitational wave detector*. Phys. Rev. **D 88**, 043007 (2013).

[20] W. Baade and F. Zwicky. *Cosmic Rays from Super-novae*. Proc. National Acad. Sci. **20**, 259 (1934).

[21] W. Baade and F. Zwicky. *On Super-novae*. Proc. National Acad. Sci. **20**, 254 (1934).

[22] W. Baade and F. Zwicky. *Remarks on Super-Novae and Cosmic Rays*. Phys. Rev. **46**, 76 (1934).

[23] G. Baardsen, A. Ekström, G. Hagen, and M. Hjorth-Jensen. *Coupled-cluster studies of infinite nuclear matter*. Phys. Rev. **C 88**, 054312 (2013).

[24] M. Baldo and G. F. Burgio. *Properties of the nuclear medium*. Rept. Prog. Phys. **75**, 026301 (2012).

[25] B. M. Barker and R. F. O'Connell. *Gravitational Two-Body Problem with Arbitrary Masses, Spins, and Quadrupole Moments*. Phys. Rev. **D 12**, 329 (1975).

[26] B. M. Barker and R. F. O'Connell. *Relativistic effects in the binary pulsar PSR* $1913+16$. Astrophys. J. Lett. **199**, L25 (1975).

[27] M. Bauböck, E. Berti, D. Psaltis, and F. Özel. *Relations Between Neutron-Star Parameters in the Hartle-Thorne Approximation*. Astrophys. J. **777**, 68 (2013).

[28] G. Baym. *The Golden Era of Neutron Stars: from Hadrons to Quarks*. In *8th International Conference on Quarks and Nuclear Physics (QNP2018) Tsukuba, Japan, November 13-17, 2018* (2019).

[29] G. Baym and C. J. Pethick. *Neutron Stars*. Ann. Rev. Nucl. Part. Sci. **25**, 27 (1975).

[30] G. Baym and C. J. Pethick. *Physics of Neutron Stars*. Ann. Rev. Astron. Astrophys. **17**, 415 (1979).

[31] G. Baym, C. J. Pethick, and P. Sutherland. *The Ground state of matter at high densities: Equation of state and stellar models*. Astrophys. J. **170**, 299 (1971).

[32] G. A. Baym and C. J. Pethick. *Landau Fermi liquid theory: concepts and applications*, (Wiley-VCH, New York, 1991).

[33] W. Becker (editor). *Neutron Stars and Pulsars*, (Springer, Berlin, Heidelberg, 2009).

[34] P. Bedaque and A. W. Steiner. *Sound velocity bound and neutron stars*. Phys. Rev. Lett. **114**, 031103 (2015).

[35] M. Bejger, T. Bulik, and P. Haensel. *Constraints on the dense matter equation of state from the measurements of PSR J*$0737-3039$*A moment of inertia and PSR J*$0751+1807$ *mass*. Mon. Not. Roy. Astron. Soc. **364**, 635 (2005).

[36] M. Bejger and P. Haensel. *Moments of inertia for neutron stars and strange stars: Limits derived for the Crab pulsar*. Astron. Astrophys. **396**, 917 (2002).

[37] M. Bejger and P. Haensel. *Accelerated expansion of the Crab nebula and evaluation of its neutron - star parameters*. Astron. Astrophys. **405**, 747 (2003).

[38] M. Bejger, P. Haensel, and J. L. Zdunik. *Mixed-phase induced core-quakes and the changes in neutron star parameters*. Mon. Not. Roy. Astron. Soc. **359**, 699 (2005).

[39] S. Bernuzzi, A. Nagar, M. Thierfelder, and B. Brügmann. *Tidal effects in binary neutron star coalescence*. Phys. Rev. **D 86**, 044030 (2012).

[40] E. Berti, F. White, A. Maniopoulou, and M. Bruni. *Rotating neutron stars: An invariant comparison of approximate and numerical spacetime models*. Mon. Not. Roy. Astron. Soc. **358**, 923 (2005).

[41] B. Bertotti, L. Iess, and P. Tortora. *A test of general relativity using radio links with the Cassini spacecraft*. Nature **425**, 374 (2003).

[42] H. A. Bethe. *Supernova mechanism*. Rev. Mod. Phys. **62**, 801 (1990).

[43] S. Bethke. *Experimental tests of asymptotic freedom*. Prog. Part. Nucl. Phys. **58**, 351 (2007).

[44] L. Bildsten, E. E. Salpeter, and I. Wasserman. *The fate of accreted CNO elements in neutron star atmospheres - X-ray bursts and gamma-ray lines*. Astrophys. J. **384**, 143 (1992).

[45] T. Binnington and E. Poisson. *Relativistic theory of tidal Love numbers*. Phys. Rev. **D 80**, 084018 (2009).

[46] L. Blanchet, T. Damour, B. R. Iyer, C. M. Will, and A. G. Wiseman. *Gravitational radiation damping of compact binary systems to second post-Newtonian order*. Phys. Rev. Lett. **74**, 3515 (1995).

[47] S. A. Bludman and M. A. Ruderman. *Possibility of the Speed of Sound Exceeding the Speed of Light in Ultradense Matter*. Phys. Rev. **170**, 1176 (1968).

[48] S. A. Bludman and M. A. Ruderman. *Noncausality and instability in ultradense matter*. Phys. Rev. **D 1**, 3243 (1970).

[49] C. Bradaschia. *The Virgo Project: A Wide Band Antenna for Gravitational Wave Detection*. Nucl. Instrum. Meth. **A 289**, 518 (1990).

[50] K. Brecher and G. Caporaso. *Obese 'neutron' stars*. Nature **259**, 377 (1976).

[51] R. P. Breton, V. M. Kaspi, M. Kramer, M. A. McLaughlin, M. Lyutikov *et al. Relativistic Spin Precession in the Double Pulsar*. Science **321**, 104 (2008).

[52] C. Breu and L. Rezzolla. *Maximum mass, moment of inertia and compactness of relativistic stars*. Mon. Not. Roy. Astron. Soc. **459**, 646 (2016).

[53] D. R. Brill and J. M. Cohen. *Rotating masses and their effect on inertial frames*. Phys. Rev. **143**, 1011 (1966).

[54] B. A. Brown. *Neutron radii in nuclei and the neutron equation of state*. Phys. Rev. Lett. **85**, 5296 (2000).

[55] J. Buchner, A. Georgakakis, K. Nandra, L. Hsu, C. Rangel *et al. X-ray spectral modelling of the AGN obscuring region in the CDFS: Bayesian model selection and catalogue*. Astron. Astrophys. **564**, A125 (2014).

[56] M. Burgay, N. D'Amico, A. Possenti, R. N. Manchester, A. G. Lyne *et al. An Increased estimate of the merger rate of double neutron stars from observations of a highly relativistic system*. Nature **426**, 531 (2003).

[57] A. Burrows and J. M. Lattimer. *The birth of neutron stars*. Astrophys. J. **307**, 178 (1986).

[58] M. Camenzind. *Compact Objects in Astrophysics: White Dwarfs, Neutron Stars, and Black Holes*, (Springer, Berlin, Heidelberg, 2007).

[59] A. G. W. Cameron. *Pycnonuclear Reactions and Nova Explosions.* Astrophys. J. **130**, 916 (1959).

[60] V. Canuto. *Equation of State at Ultrahigh Densities. 1.* Ann. Rev. Astron. Astrophys. **12**, 167 (1974).

[61] V. Canuto. *Equation of State at Ultrahigh Densities. 2.* Ann. Rev. Astron. Astrophys. **13**, 335 (1975).

[62] A. Carbone, A. Cipollone, C. Barbieri, A. Rios, and A. Polls. *Self-consistent Green's functions formalism with three-body interactions*. Phys. Rev. **C 88**, 054326 (2013).

[63] A. Carbone, A. Rios, and A. Polls. *Symmetric nuclear matter with chiral three-nucleon forces in the self-consistent Green's functions approach*. Phys. Rev. **C 88**, 044302 (2013).

[64] J. L. Cervantes-Cota, S. Galindo-Uribarri, and G.-F. Smoot. *A Brief History of Gravitational Waves*. Universe **2**, 22 (2016).

[65] J. Chadwick. *Possible Existence of a neutron*. Nature **129**, 312 (1932).

[66] N. Chamel and P. Haensel. *Physics of Neutron Star Crusts*. Living Rev. Rel. **11**, 10 (2008).

[67] P. T. Chruściel, J. Lopes Costa, and M. Heusler. *Stationary Black Holes: Uniqueness and Beyond*. Living Rev. Rel. **15**, 7 (2012).

[68] J. M. Comella, H. D. Craft, Jr., R. V. E. Lovelace, J. M. Sutton, and G. L. Tyler. *Crab Nebula Pulsar NP 0532*. Nature **221**, 453 (1969).

[69] H. T. Cromartie *et al. A very massive neutron star: relativistiv Shapiro delay measurements of PSR J*0740 + 6620 arXiv:1904.06759.

[70] C. Cutler, T. A. Apostolatos, L. Bildsten, L. S. Finn, E. E. Flanagan *et al. The Last three minutes: issues in gravitational wave measurements of coalescing compact binaries*. Phys. Rev. Lett. **70**, 2984 (1993).

[71] C. Cutler and E. E. Flanagan. *Gravitational waves from merging compact binaries: How accurately can one extract the binary's parameters from the inspiral wave form?* Phys. Rev. **D 49**, 2658 (1994).

[72] C. Cutler and K. S. Thorne. *An Overview of gravitational wave sources*. In *Proceedings, 16th International Conference on General Relativity and Gravitation: Durban, South Africa, July 15-21, 2001* 72 (2013).

[73] T. Damour and N. Deruelle. *General relativistic celestial mechanics of binary systems. I. The post-Newtonian motion*. Ann. Inst. Henri Poincaré **43**, 107 (1985).

[74] T. Damour and N. Deruelle. *General relativistic celestial mechanics of binary systems. II. The post-Newtonian timing formula*. Ann. Inst. Henri Poincaré **44**, 263 (1986).

[75] T. Damour and A. Nagar. *Relativistic tidal properties of neutron stars*. Phys. Rev. **D 80**, 084035 (2009).

[76] T. Damour and G. Schäfer. *Higher-order relativistic periastron advances and binary pulsars*. Nuovo Cimento **101**, 127 (1988).

[77] T. Damour and J. H. Taylor. *Strong field tests of relativistic gravity and binary pulsars*. Phys. Rev. **D 45**, 1840 (1992).

[78] P. Danielewicz, R. Lacey, and W. G. Lynch. *Determination of the equation of state of dense matter*. Science **298**, 1592 (2002).

[79] S. De, D. Finstad, J. M. Lattimer, D. A. Brown, E. Berger, and C. M. Biwer. *Tidal Deformabilities and Radii of Neutron Stars from the Observation of GW170817*. Phys. Rev. Lett. **121**, 091102 (2018). Erratum: Phys. Rev. Lett. **121**, 259902 (2018).

[80] P. Demorest, T. Pennucci, S. Ransom, M. Roberts, and J. Hessels. *Shapiro Delay Measurement of a Two Solar Mass Neutron Star*. Nature **467**, 1081 (2010).

[81] C. Drischler, A. Carbone, K. Hebeler, and A. Schwenk. *Neutron matter from chiral two- and three-nucleon calculations up to N^3LO*. Phys. Rev. **C 94**, 054307 (2016).

[82] C. Drischler, K. Hebeler, and A. Schwenk. *Chiral interactions up to next-to-next-to-next-to-leading order and nuclear saturation*. Phys. Rev. Lett. **122**, 042501 (2019).

[83] C. Drischler, V. Somà, and A. Schwenk. *Microscopic calculations and energy expansion for neutron-rich matter*. Phys. Rev. **C 89**, 025806 (2014).

[84] A. Einstein. *On the electrodynamics of moving bodies*. Annalen Phys. **17**, 891 (1905).

[85] A. Einstein. *The Field Equations of Gravitation*. Sitzungsber. Preuss. Akad. Wiss. Berlin (Math. Phys.) **1915**, 844 (1915).

[86] A. Einstein. *Approximative Integration of the Field Equations of Gravitation*. Sitzungsber. Preuss. Akad. Wiss. Berlin (Math. Phys.) **1916**, 688 (1916).

[87] A. Einstein. *Über Gravitationswellen*. Sitzungsber. Preuss. Akad. Wiss. Berlin (Math. Phys.) **1918**, 154 (1918).

[88] D. R. Entem and R. Machleidt. *Accurate charge dependent nucleon nucleon potential at fouth order of chiral perturbation theory*. Phys. Rev. **C 68**, 041001 (2003).

[89] E. Epelbaum. *Few-nucleon forces and systems in chiral effective field theory*. Prog. Part. Nucl. Phys. **57**, 654 (2006).

[90] E. Epelbaum. *Nuclear forces from chiral effective field theory*. Prog. Part. Nucl. Phys. **67**, 343 (2012).

[91] E. Epelbaum. *Nuclear Chiral EFT in the Precision Era*. In *Proceedings, 8th International Workshop on Chiral Dynamics (CD15): Pisas, Italy, June 29-July 3, 2015* **CD15**, 014 (2016).

[92] E. Epelbaum, W. Glockle, and U.-G. Meißner. *The Two-nucleon system at next-to-next-to-next-to-leading order*. Nucl. Phys. **A 747**, 362 (2005).

[93] E. Epelbaum, H.-W. Hammer, and U.-G. Meißner. *Modern Theory of Nuclear Forces*. Rev. Mod. Phys. **81**, 1773 (2009).

[94] E. Epelbaum, H. Krebs, and U.-G. Meißner. *Improved chiral nucleon-nucleon potential up to next-to-next-to-next-to-leading order*. Eur. Phys. J. **A 51**, 53 (2015).

[95] T. Ertl, H.-T. Janka, S. E. Woosley, T. Sukhbold, and M. Ugliano. *A two-parameter criterion for classifying the explodability of massive stars by the neutrino-driven mechanism*. Astrophys. J. **818**, 124 (2016).

[96] F. Feroz and M. P. Hobson. *Multimodal nested sampling: an efficient and robust alternative to MCMC methods for astronomical data analysis*. Mon. Not. Roy. Astron. Soc. **384**, 449 (2008).

[97] F. Feroz, M. P. Hobson, and M. Bridges. *MultiNest: an efficient and robust Bayesian inference tool for cosmology and particle physics*. Mon. Not. Roy. Astron. Soc. **398**, 1601 (2009).

[98] F. Feroz, M. P. Hobson, A. G. W. Cameron, and A. N. Pettitt. *Importance Nested Sampling and the MultiNest Algorithm* arXiv:1306.2144.

[99] A. L. Fetter and J. D. Walecka. *Quantum theory of many-particle systems*, (McGraw-Hill, New York, 1971).

[100] L. S. Finn and D. F. Chernoff. *Observing binary inspiral in gravitational radiation: One interferometer*. Phys. Rev. **D 47**, 2198 (1993).

[101] E. E. Flanagan and T. Hinderer. *Constraining neutron star tidal Love numbers with gravitational wave detectors*. Phys. Rev. **D 77**, 021502 (2008).

[102] E. Fonseca, T. T. Pennucci, J. A. Ellis, I. H. Stairs, D. J. Nice *et al. The NANOGrav Nine-year Data Set: Mass and Geometric Measurements of Binary Millisecond Pulsars*. Astrophys. J. **832**, 167 (2016).

[103] E. S. Fraga, A. Kurkela, and A. Vuorinen. *Interacting quark matter equation of state for compact stars*. Astrophys. J. Lett. **781**, L25 (2014).

[104] E. S. Fraga, A. Kurkela, and A. Vuorinen. *Neutron star structure from QCD*. Eur. Phys. J. **A 52**, 49 (2016).

[105] C. L. Fryer, W. Benz, M. Herant, and S. A. Colgate. *What can the accretion-induced collapse of white dwarfs really explain?* Astrophys. J. **516**, 892 (1999).

[106] S. Gandolfi, J. Carlson, and S. Reddy. *The maximum mass and radius of neutron stars and the nuclear symmetry energy*. Phys. Rev. **C 85**, 032801 (2012).

[107] S. Gandolfi, A. Lovato, J. Carlson, and K. E. Schmidt. *From the lightest nuclei to the equation of state of asymmetric nuclear matter with realistic nuclear interactions*. Phys. Rev. **C 90**, 061306 (2014).

[108] K. C. Gendreau, Z. Arzoumanian, and T. Okajima. *The Neutron star Interior Composition ExploreR (NICER): an Explorer mission of opportunity for soft x-ray timing spectroscopy*. In *Space Telescopes and Instrumentation* **8443**, 844313 (2012).

[109] R. P. Geroch. *Multipole moments. II. Curved space*. J. Math. Phys. **11**, 2580 (1970).

[110] A. Gezerlis, I. Tews, E. Epelbaum, M. Freunek, S. Gandolfi *et al. Local chiral effective field theory interactions and quantum Monte Carlo applications*. Phys. Rev. **C 90**, 054323 (2014).

[111] A. Gezerlis, I. Tews, E. Epelbaum, S. Gandolfi, K. Hebeler, A. Nogga, and A. Schwenk. *Quantum Monte Carlo Calculations with Chiral Effective Field Theory Interactions*. Phys. Rev. Lett. **111**, 032501 (2013).

[112] N. K. Glendenning. *Compact stars: nuclear physics, particle physics, and general relativity*. Second edition, (Springer, New York, NY, 2000).

[113] N. K. Glendenning. *Special and General Relativity: With Applications to White Dwarfs, Neutron Stars and Black Holes*, (Springer, New York, NY, 2007).

[114] T. Gold. *Rotating neutron stars as the origin of the pulsating radio sources*. Nature **218**, 731 (1968).

[115] J. Goldstone. *Field Theories with Superconductor Solutions*. Nuovo Cimento **19**, 154 (1961).

[116] J. Goldstone, A. Salam, and S. Weinberg. *Broken Symmetries*. Phys. Rev. **127**, 965 (1962).

[117] T. Gorda. *Global properties of rotating neutron stars with QCD equations of state*. Astron. Astrophys. **832**, 28 (2016).

[118] S. K. Greif, G. Raaijmakers, K. Hebeler, A. Schwenk, and A. L. Watts. *Equation of state sensitivities when inferring neutron star and dense matter properties*. Mon. Not. Roy. Astron. Soc. **485**, 5363 (2019).

[119] D. J. Gross and F. Wilczek. *Ultraviolet Behavior of Nonabelian Gauge Theories*. Phys. Rev. Lett. **30**, 1343 (1973).

[120] P. Haensel and M. Fortin. *Equation of state for neutron stars. Some recent developments*. J. Phys. Conf. Ser. **932**, 012034 (2017).

[121] P. Haensel, M. Kutschera, and M. Prószyński. *Uncertainty in the Saturation Density of Nuclear Matter and Neutron Star Models*. Astron. Astrophys. **102**, 299 (1981).

[122] P. Haensel and A. Y. Potekhin. *Analytical representations of unified equations of state of neutron-star matter*. Astron. Astrophys. **428**, 191 (2004).

[123] P. Haensel, A. Y. Potekhin, and D. G. Yakovlev. *Neutron stars 1: Equation of state and structure*, (Springer, New York, 2006).

[124] G. Hagen, T. Papenbrock, A. Ekström, K. A. Wendt, G. Baardsen *et al. Coupled-cluster calculations of nucleonic matter*. Phys. Rev. **C 89**, 014319 (2014).

[125] G. Hagen, T. Papenbrock, M. Hjorth-Jensen, and D. J. Dean. *Coupled-cluster computations of atomic nuclei*. Rept. Prog. Phys. **77**, 096302 (2014).

[126] T. Hamada and E. E. Salpeter. *Models for Zero-Temperature Stars.* Astrophys. J. **134**, 683 (1961).

[127] H.-W. Hammer, A. Nogga, and A. Schwenk. *Three-body forces: From cold atoms to nuclei*. Rev. Mod. Phys. **85**, 197 (2013).

[128] R. O. Hansen. *Multipole moments of stationary space-times*. J. Math. Phys. **15**, 46 (1974).

[129] G. M. Harry (LIGO Scientific collaboration). *Advanced LIGO: The next generation of gravitational wave detectors*. Class. Quant. Grav. **27**, 084006 (2010).

[130] J. B. Hartle. *Slowly rotating relativistic stars. 1. Equations of structure*. Astrophys. J. **150**, 1005 (1967).

[131] J. B. Hartle. *Bounds on the Mass and Moment of Inertia of Non-Rotating Neutron Stars*. Phys. Rep. **46**, 201 (1978).

[132] J. B. Hartle and D. H. Sharp. *Variational Principle for the Equilibrium of a Relativistic, Rotating Star*. Astrophys. J. **147**, 317 (1967).

[133] J. B. Hartle and K. S. Thorne. *Slowly Rotating Relativistic Stars. II. Models for Neutron Stars and Supermassive Stars*. Astrophys. J. **153**, 807 (1968).

[134] M. Hashimoto, H. Seki, and M. Yamada. *Shape of Nuclei in the Crust of Neutron Star*. Prog. Theor. Phys. **71**, 320 (1984).

[135] K. Hebeler, J. D. Holt, J. Menéndez, and A. Schwenk. *Nuclear forces and their impact on neutron-rich nuclei and neutron-rich matter*. Ann. Rev. Nucl. Part. Sci. **65**, 457 (2015).

[136] K. Hebeler, J. M. Lattimer, C. J. Pethick, and A. Schwenk. *Constraints on neutron star radii based on chiral effective field theory interactions*. Phys. Rev. Lett. **105**, 161102 (2010).

[137] K. Hebeler, J. M. Lattimer, C. J. Pethick, and A. Schwenk. *Equation of state and neutron star properties constrained by nuclear physics and observation*. Astrophys. J. **773**, 11 (2013).

[138] K. Hebeler and A. Schwenk. *Chiral three-nucleon forces and neutron matter*. Phys. Rev. **C 82**, 014314 (2010).

[139] D. J. Hegyi. *The upper mass limit for neutron stars including differential rotation*. Astrophys. J. **217**, 244 (1977).

[140] H. Heiselberg and V. R. Pandharipande. *Recent progress in neutron star theory*. Ann. Rev. Nucl. Part. Sci. **50**, 481 (2000).

[141] J. W. T. Hessels, S. M. Ransom, I. H. Stairs, P. C. C. Freire, V. M. Kaspi, and F. Camila. *A radio pulsar spinning at* 716 Hz. Science **311**, 1901 (2006).

[142] M. Heusler. *No hair theorems and black holes with hair*. In *Journees relativistes 96. Proceedings, Conference, Ascona, Switzerland, May 26-30, 1996* **69**, 501 (1996).

[143] A. Hewish, S. J. Bell, J. D. Pilkington, P. F. Scott, and R. A. Collins. *Observation of a rapidly pulsating radio source*. Nature **217**, 709 (1968).

[144] A. Hewish and S. E. Okoye. *Evidence for an Unusual Source of High Radio Brightness Temperature in the Crab Nebula*. Nature **207**, 59 (1965).

[145] I. Hinchliffe and A. V. Manohar. *The QCD coupling constant*. Ann. Rev. Nucl. Part. Sci. **50**, 643 (2000).

[146] T. Hinderer. *Tidal Love numbers of neutron stars*. Astrophys. J. **677**, 1216 (2008). Erratum: Astrophys. J. **697**, 964 (2009).

[147] T. Hinderer, B. D. Lackey, R. N. Lang, and J. S. Read. *Tidal deformability of neutron stars with realistic equations of state and their gavitational wave signatures*. Phys. Rev. **D 81**, 123016 (2010).

[148] C. J. Horowitz and J. Piekarewicz. *Neutron star structure and the neutron radius of Pb-208*. Phys. Rev. Lett. **86**, 5647 (2001).

[149] C. J. Horowitz, S. J. Pollock, P. A. Souder, and R. Michaels. *Parity violating measurements of neutron densities*. Phys. Rev. **C 63**, 025501 (2001).

[150] F. Hoyle, J. V. Narlikar, and J. A. Wheeler. *Electromagnetic Waves from Very Dense Stars*. Nature **203**, 914 (1964).

[151] R. A. Hulse. *The discovery of the binary pulsar*. Rev. Mod. Phys. **66**, 699 (1994).

[152] R. A. Hulse and J. H. Taylor. *Discovery of a pulsar in a binary system*. Astrophys. J. Lett. **195**, L51 (1975).

[153] H.-T. Janka. *Explosion Mechanisms of Core-Collapse Supernavae*. Ann. Rev. Nucl. Part. Sci. **62**, 407 (2012).

[154] H.-T. Janka, K. Langanke, A. Marek, G. Martínez-Pinedo, and B. Müller. *Theory of Core-Collapse Supernovae*. Phys. Rept. **442**, 38 (2007).

[155] N. Kalantar-Nayestanaki, E. Epelbaum, J. G. Messchendorp, and A. Nogga. *Signatures of three-nucleon interactions in few-nucleon systems*. Rept. Prog. Phys. **75**, 016301 (2012).

[156] R. Kippenhahn, A. Weigert, and A. Weiss. *Stellar Structure and Evolution*. Second edition, (Springer, Heidelberg, New York, Dordrecht, London, 2012).

[157] P. Klüpfel, P.-G. Reinhard, T. J. Bürvenich, and J. A. Maruhn. *Variations on a theme by Skyrme: A systematic study of adjustments of model parameters*. Phys. Rev. **C 79**, 034310 (2009).

[158] M. Kortelainen, T. Lesinski, J. Moré, W. Nazarewicz, J. Sarich *et al. Nuclear Energy Density Optimization*. Phys. Rev. **C 82**, 024313 (2010).

[159] M. Kortelainen, J. McDonnell, W. Nazarewicz, E. Olsen, P.-G. Reinhard *et al. Nuclear energy density optimization: Shell structure*. Phys. Rev. **C 89**, 054314 (2014).

[160] U. Kraemmer and A. Rebhan. *Advances in perturbative thermal field theory*. Rept. Prog. Phys. **351**, 351 (2004).

[161] M. Kramer, I. H. Stairs, R. N. Manchester, M. A. McLaughlin, A. G. Lyne *et al. Tests of general relativity from timing the double pulsar*. Science **314**, 97 (2006).

[162] M. Kramer and N. Wex. *The double pulsar system: A unique laboratory for gravity*. Class. Quant. Grav. **26**, 073001 (2009).

[163] T. Krüger, I. Tews, K. Hebeler, and A. Schwenk. *Neutron matter from chiral effective field theory interations*. Phys. Rev. **C 88**, 025802 (2013).

[164] A. Kurkela, E. S. Fraga, J. Schaffner-Bielich, and A. Vuorinen. *Constraining neutron star matter with Quantum Chromodynamics*. Astrophys. J. **789**, 127 (2014).

[165] A. Kurkela, P. Romatschke, and A. Vuorinen. *Cold Quark Matter*. Phys. Rev. **D 81**, 105021 (2010).

[166] A. Kurkela, P. Romatschke, A. Vuorinen, and B. Wu. *Looking inside neutron stars: Microscopic calculations confront observations* arXiv:1006.4062.

[167] B. D. Lackey, K. Kyutoku, M. Shibata, P. R. Brady, and J. L. Friedman. *Extracting equation of state parameters from black hole-neutron star mergers. I. Nonspinning black holes*. Phys. Rev. **D 85**, 044061 (2012).

[168] B. D. Lackey, K. Kyutoku, M. Shibata, P. R. Brady, and J. L. Friedman. *Extracting equation of state parameters from black hole-neutron star mergers: aligned-spin black holes and a preliminary waveform model*. Phys. Rev. **D 89**, 043009 (2014).

[169] L. D. Landau. *On the theory of stars*. Phys. Z. Sowjetunion **1**, 285 (1932).

[170] L. D. Landau and E. M. Lifshitz. *Fluid Mechanics*. Second edition, (Pergamon Press, Oxford, England, 1987).

[171] J. M. Lattimer. *Observed Neutron Star Masses*. http://www.stellarcollapse.org/nsmasses. Last visited 2019-05-31.

[172] J. M. Lattimer. *The nuclear equation of state and neutron star masses*. Ann. Rev. Nucl. Part. Sci. **62**, 485 (2012).

[173] J. M. Lattimer. *Symmetry energy in nuclei and neutron stars*. Nucl. Phys. **A 928**, 276 (2014).

[174] J. M. Lattimer. *Introduction to neutron stars*. AIP Conf. Proc. **1645**, 61 (2015).

[175] J. M. Lattimer and Y. Lim. *Constraining the Symmetry Parameters of the Nuclear interaction*. Astrophys. J. **771**, 51 (2013).

[176] J. M. Lattimer and M. Prakash. *Nuclear matter and its role in supernovae, neutron stars and compact object binary mergers*. Phys. Rept. **333**, 121 (2000).

[177] J. M. Lattimer and M. Prakash. *Neutron star structure and the equation of state*. Astrophys. J. **550**, 426 (2001).

[178] J. M. Lattimer and M. Prakash. *The physics of neutron stars*. Science **304**, 536 (2004).

[179] J. M. Lattimer and M. Prakash. *The Ultimate energy density of observable cold matter*. Phys. Rev. Lett. **94**, 111101 (2005).

[180] J. M. Lattimer and M. Prakash. *Neutron Star Observations: Prognosis for Equation of State Constraints*. Phys. Rept. **442**, 109 (2007).

[181] J. M. Lattimer and M. Prakash. *The Equation of State of Hot, Dense Matter and Neutron Stars*. Phys. Rept. **621**, 127 (2016).

[182] J. M. Lattimer and B. F. Schutz. *Constraining the equation of state with moment of inertia measurements*. Astrophys. J. **629**, 979 (2005).

[183] J. M. Lattimer and A. W. Steiner. *Constraints on the symmetry energy using the mass-radius relation of neutron stars*. Eur. Phys. J. **A 50**, 40 (2014).

[184] Y. Lim and J. W. Holt. *Neutron star tidal deformabilities constrained by nuclear theory and experiment*. Phys. Rev. Lett. **121**, 062701 (2018).

[185] L. Lindblom. *Determining the nuclear equation of state from neutron-star masses and radii*. Astrophys. J. **398**, 569 (1992).

[186] L. Lindblom. *Spectral Representations of Neutron-Star Equations of State*. Phys. Rev. **D 82**, 103011 (2010).

[187] L. Lindblom and N. M. Indik. *A Spectral Appoach to the Relativistic Inverse Stellar Structure Problem*. Phys. Rev. **D 86**, 084003 (2012).

[188] L. Lindblom and N. M. Indik. *Spectral Approach to the Relativistic Inverse Stellar Structure Problem II*. Phys. Rev. **D 89**, 064003 (2014). Erratum: Phys. Rev. **D 93**, 129903 (2016).

[189] D. R. Lorimer and M. Kramer. *Handbook of Pulsar Astronomy*, (Cambridge University Press, 2005).

[190] A. E. H. Love. *The Yielding of the Earth to Disturbing Forces*. Proc. R. Soc. A **82**, 73 (1909).

[191] A. G. Lyne, M. Burgay, M. Kramer, A. Possenti, R. N. Manchester *et al. A Double - pulsar system - A Rare laboratory for relativistic gravity and plasma physics*. Science **303**, 1153 (2004).

[192] J. E. Lynn, I. Tews, J. Carlson, S. Gandolfi, A. Gezerlis, K. E. Schmidt, and A. Schwenk. *Chiral Three-Nucleon Interactions in Light Nuclei, Neutron-α Scattering, and Neutron Matter*. Phys. Rev. Lett. **116**, 062501 (2016).

[193] M. Machleidt and D. R. Entem. *Chiral effective field theory and nuclear forces*. Phys. Rep. **503**, 1 (2011).

[194] R. Machleidt. *Chiral Symmetry and the Nucleon-Nucleon Interaction*. Symmetry **8**, 26 (2016).

[195] R. N. Manchester, G. B. Hobbs, A. Teoh, and M. Hobbs. *The Australia Telescope National Facility pulsar catalogue*. Astron. J. **129**, 1993 (2005).

[196] R. N. Manchester and J. H. Taylor. *Pulsars*, (W. H. Freeman and Company, 1977).

[197] A. Maselli, V. Cardoso, V. Ferrari, L. Gualtieri, and P. Pani. *Equation-of-state-independent relations in neutron stars*. Phys. Rev. **D 88**, 023007 (2013).

[198] M. C. Miller and F. K. Lamb. *Determining Neutron Star Properties by Fitting Oblate-star Waveform Models to X-ray Burst Oscillations*. Astrophys. J. **808**, 31 (2015).

[199] M. C. Miller and N. Yunes. *The new frontier of gravitational waves*. Nature **568**, 469 (2019).

[200] C. W. Misner, K. S. Thorne, and J. A. Wheeler. *Gravitation*, (W. H. Freeman, San Francisco, 1973).

[201] I. A. Morrison, T. W. Baumgarte, S. L. Shapiro, and V. R. Pandharipande. *The Moment of inertia of the binary pulsar J*0737−3039*A: Constraining the nuclear equation of state*. Astrophys. J. Lett. **617**, L135 (2004).

[202] M. Nauenberg and G. Chapline, Jr. *Determination of Properties of Cold Stars in General Relativity by a Variational Method*. Astrophys. J. **179**, 277 (1973).

[203] J. W. Negele and D. Vautherin. *Neutron star matter at subnuclear densities*. Nucl. Phys. **A 207**, 298 (1973).

[204] T. Nikšić, N. Paar, P.-G. Reinhard, and D. Vretenar. *Optimizing relativistic energy density functionals: covariance analysis*. J. Phys. **G 42**, 034008 (2015).

[205] J. R. Oppenheimer and G. M. Volkoff. *On Massive neutron cores*. Phys. Rev. **55**, 374 (1939).

[206] K. Oyamatsu, M. Hashimoto, and M. Yamada. *Further Study of the Nuclear Shape in High-Density Matter*. Prog. Theor. Phys. **72**, 373 (1984).

[207] F. Özel and D. Psaltis. *Reconstructing the Neutron-Star Equation of State from Astrophysical Measurements*. Phys. Rev. **D 80**, 103003 (2009).

[208] F. Özel, D. Psaltis, Z. Arzoumanian, S. Morsink, and M. Bauböck. *Measuring Neutron Star Radii via Pulse Profile Modeling with NICER*. Astrophys. J. **832**, 92 (2016).

[209] F. Özel, D. Psaltis, T. Güver, G. Baym, C. Heinke, and S. Guillot. *The Dense Matter Equation of State from Neutron Star Radius and Mass Measurements*. Astrophys. J. **820**, 28 (2016).

[210] P. Pani, L. Gualtieri, A. Maselli, and V. Ferrari. *Tidal Love numbers of a spinning compact object*. Phys. Rev. **D 92**, 024010 (2015).

[211] P. C. Peters and J. Mathews. *Gravitational radiation from point masses in a Keplerian orbit*. Phys. Rev. **131**, 435 (1963).

[212] C. J. Pethick, A. Akmal, V. R. Pandharipande, and D. G. Ravenhall. *Neutron star structure*. Nucl. Phys. Proc. Suppl. **80**, 1114 (2000).

[213] J. Piekarewicz, B. K. Agrawal, G. Colò, W. Nazarewicz, N. Paar *et al. Electric dipole polarizability and the neutron skin*. Phys. Rev. **C 85**, 041302 (2012).

[214] E. Poisson. *Gravitational waves from inspiraling compact binaries: The Quadruple moment term*. Phys. Rev. **D 57**, 5287 (1998).

[215] E. Poisson and C. M. Will. *Gravitational waves from inspiraling compact binaries: Parameter estimation using second post-Newtonian wave forms*. Phys. Rev. **D 52**, 848 (1995).

[216] H. D. Politzer. *Reliable Perturbative Results for Strong Interactions*. Phys. Rev. Lett. **30**, 1346 (1973).

[217] J. A. Pons, F. M. Walter, J. M. Lattimer, M. Prakash, R. Neuhäuser, and P. An. *Towards a mass and radius determination of the nearby isolated neutron star RX J*185635 − 3754. Astrophys. J. **564**, 981 (2002).

[218] S. Postnikov, M. Prakash, and J. M. Lattimer. *Tidal Love Number of Neutron and Self-Bound Quark Stars*. Phys. Rev. **D 82**, 024016 (2010).

[219] A. Y. Potekhin. *The physics of neutron stars*. Phys. Usp. **53**, 1235 (2010).

[220] C. A. Raithel, F. Özel, and D. Psaltis. *Model-Independent Inference of Neutron Star Radii from Moment of Inertia Measurements*. Phys. Rev. **C 93**, 032801 (2016). Addendum: Phys. Rev. **C 93**, 049905 (2016).

[221] C. A. Raithel, F. Özel, and D. Psaltis. *From Neutron Star Observables to the Equation of State. II. Bayesian Inference of Equation of State Pressures*. Astrophys. J. **844**, 156 (2017).

[222] D. G. Ravenhall and C. J. Pethick. *Neutron star moments of inertia*. Astrophys. J. **424**, 846 (1994).

[223] D. G. Ravenhall, C. J. Pethick, and J. R. Wilson. *Structure of matter below nuclear saturation density*. Phys. Rev. Lett. **50**, 2066 (1983).

[224] J. S. Read, L. Baiotti, J. D. E. Creighton, J. L. Friedman, B. Giacomazzo *et al. Matter effects on binary neutron star waveforms*. Phys. Rev. **D 88**, 044042 (2013).

[225] J. S. Read, B. D. Lackey, B. J. Owen, and J. L. Friedman. *Constraints on a phenomenologically parameterized neutron-star equation of state*. Phys. Rev. **D 79**, 124032 (2009).

[226] D. J. Reardin, G. Hobbs, W. Coles, Y. Levin, M. J. Keith *et al. Timing analysis for 20 millisecond pulsars in the Parkes Pulsar Timing Array*. Mon. Not. Roy. Astron. Soc. **455**, 1751 (2016).

[227] T. Regge and J. A. Wheeler. *Stability of a Schwarzschild singularity*. Phys. Rev. **108**, 1063 (1957).

[228] L. Rezzolla, P. Pizzochero, D. I. Jones, N. Rea, and I. Vidaña (editors). *The Physics and Astrophysics of Neutron Stars*, (Springer, Switzerland, 2018).

[229] C. E. Rhoades, Jr. and R. Ruffini. *Maximum mass of a neutron star*. Phys. Rev. Lett. **32**, 324 (1974).

[230] T. E. Riley, G. Raaijmakers, and A. L. Watts. *On parametrized cold dense matter equation-of-state inference*. Mon. Not. Roy. Astron. Soc. **478**, 1093 (2018).

[231] A. Rios, A. Polls, and I. Vidaña. *Hot neutron matter from a Self-Consistent Green's Functions approach*. Phys. Rev. **C 79**, 025802 (2009).

[232] X. Roca-Maza, M. Centelles, X. Viñas, and M. Warda. *Neutron skin of* ^{208}Pb*, nuclear symmetry energy, and the parity radius experiment*. Phys. Rev. Lett. **106**, 252501 (2011).

[233] R. W. Romani. *Model atmospheres for cooling neutron stars*. Astrophys. J. **313**, 718 (1987).

[234] M. A. Ruderman. *Causes of Sound Faster than Light in Classical Models of Ultradense Matter*. Phys. Rev. **172**, 1286 (1968).

[235] E. E. Salpeter. *Matter at high densities*. Ann. Phys. **11**, 393 (1960).

[236] E. E. Salpeter. *Energy and Pressure of a Zero-Temperature Plasma*. Astrophys. J. **134**, 669 (1961).

[237] B. S. Sathaprakash and B. F. Schutz. *Physics, Astrophysics and Cosmology with Gravitational Waves*. Living Rev. Rel. **12**, 2 (2009).

[238] B. F. Schutz. *Determining the Hubble Constant from Gravitational Wave Observations*. Nature **323**, 310 (1986).

[239] B. F. Schutz. *Gravitational Wave Sources and Their Detectability*. Class. Quant. Grav. **6**, 1761 (1989).

[240] A. Schwenk and B. Friman. *Polarization contribution to the spin dependence of the effective interaction in neutron matter*. Phys. Rev. Lett. **92**, 082501 (2004).

[241] A. Schwenk, B. Friman, and G. E. Brown. *Renormalization group approach to neutron matter: Quasiparticle interactions, superfluid gaps and the equation of state*. Nucl. Phys. **A 713**, 191 (2003).

[242] D. W. Scott. *Multivariate density estimation: theory, practice, and visualization*. Wiley series in probability and mathematical statistics. Applied probability and statistics, (A Wiley-interscience publication, New York, NY, 1992).

[243] S. L. Shapiro and S. A. Teukolsky. *Black holes, white dwarfs, and neutron stars: The physics of compact objects*, (Wiley-VCH, Weinheim, 1983).

[244] M. Shibata, K. Taniguchi, and K. Uryu. *Merger of binary neutron stars with realistic equations of state in full general relativity*. Phys. Rev. **D 71**, 084021 (2005).

[245] J. Skilling. *Nested Sampling*. In *AIP Conference Proceedings* **735**, 395 (2004).

[246] T. Skyrme. *The effective nucler potential*. Nucl. Phys. **9**, 615 (1959).

[247] K. Somiya (KAGRA collaboration). *Detector configuration of KAGRA: The Japanese cryogenic gravitational-wave detector*. Class. Quant. Grav. **29**, 124007 (2012).

[248] I. H. Stairs. *Testing general relativity with pulsar timing*. Living Rev. Rel. **6**, 5 (2003).

[249] A. W. Steiner, S. Gandolfi, F. J. Fattoyev, and W. G. Newton. *Using Neutron Star Observations to Determine Crust Thicknesses, Moments of Inertia, and Tidal Deformabilities*. Phys. Rev. **C 91**, 015804 (2015).

[250] A. W. Steiner, J. M. Lattimer, and E. F. Brown. *The Equation of State from Observed Masses and Radii of Neutron Stars*. Astrophys. J. **722**, 33 (2010).

[251] A. W. Steiner, J. M. Lattimer, and E. F. Brown. *The Neutron Star Mass-Radius Relation and the Equation of State of Dense Matter*. Astrophys. J. Lett. **765**, L5 (2013).

[252] A. W. Steiner, J. M. Lattimer, and E. F. Brown. *Neutron Star Radii, Universal Relations, and the Role of Prior Distributions*. Eur. Phys. J. **A 52**, 18 (2016).

[253] A. W. Steiner, M. Prakash, J. M. Lattimer, and P. J. Ellis. *Isospin asymmetry in nuclei and neutron stars*. Phys. Rept. **411**, 325 (2005).

[254] G. Sterman, J. Smith, J. C. Collins, J. Whitmore, R. Brock *et al. Handbook of perturbative QCD: Version 1.0*. Rev. Mod. Phys. **67**, 157 (1995).

[255] N. Straumann. *General Relativity*. Second edition, (Springer, Dordrecht, Heidelberg, New Work, London, 2013).

[256] A. Tamii, I. Poltoratska, P. von Neumann-Cosel, Y. Fujita, T. Adachi *et al.* *Complete electric dipole response and the neutron skin in 208Pb*. Phys. Rev. Lett. **107**, 062502 (2011).

[257] M. Tanabashi, K. Hagiwara, K. Hikasa, K. Nakamura, Y. Sumino *et al.* (Particle Data Group). *Review of Particle Physics*. Phys. Rev. **D 98**, 030001 (2018).

[258] T. M. Tauris, M. Kramer, P. C. C. Freire, N. Wex, H.-T. Janka *et al.* *Formation of Double Neutron Star Systems*. Astrophys. J. **846**, 170 (2017).

[259] J. H. Taylor. *Binary pulsars and relativistic gravity*. Rev. Mod. Phys. **66**, 711 (1994).

[260] J. H. Taylor and J. M. Weisberg. *Further experimental tests of relativistic gravity using the binary pulsar PSR* $1913+16$. Astrophys. J. **345**, 434 (1989).

[261] I. Tews. *Quantum Monte Carlo calculations with chiral effective field theory interactions*. Ph.D. thesis, Technische Universität Darmstadt (2015).

[262] I. Tews, J. Carlson, S. Gandolfi, and S. Reddy. *Constraining the speed of sound inside neutron stars with chiral effective field theory interactions and observations*. Astrophys. J. **860**, 149 (2018).

[263] I. Tews, S. Gandolfi, A. Gezerlis, and A. Schwenk. *Quantum Monte Carlo calculations of neutron matter with chiral three-body forces*. Phys. Rev. **C 93**, 024305 (2016).

[264] I. Tews, T. Krüger, K. Hebeler, and A. Schwenk. *Neutron matter at next-to-next-to-next-to-leading order in chiral effective field theory*. Phys. Rev. Lett. **110**, 032504 (2013).

[265] I. Tews, J. Margueron, and S. Reddy. *Confronting gravitational-wave observations with modern nuclear physics*. Eur. Phys. J. **A 55**, 97 (2019).

[266] H. Thirring. *Über die Wirkung ferner Massen in der Einsteinschen Gravitationstheorie.* Phys. Zs. **19**, 33 (1918).

[267] K. S. Thorne. *Tidal stabilization of rigidly rotating, fully relativistic neutron stars*. Phys. Rev. **D 58**, 124031 (1998).

[268] K. S. Thorne and A. Campolattaro. *Non-Radial Pulsation of General-Relativistic Stellar Models. I. Analytic Analysis for* $l \geq 2$. Astrophys. J. **149**, 591 (1967).

[269] K. S. Thorne, R. H. Price, and D. A. MacDonald. *Black Holes: The Membrane Paradigm*, (Yale University Press, New Haven, 1986).

[270] R. C. Tolman. *Static solutions of Einstein's field equations for spheres of fluid*. Phys. Rev. **55**, 364 (1939).

[271] L. Trippa, G. Colò, and E. Vigezzi. *The Giant Dipole Resonance as a quantitative constraint on the symmetry energy*. Phys. Rev. **C 77**, 061304 (2008).

[272] R. Trotta. *Bayes in the sky: Bayesian inference and model selection in cosmology*. Contemp. Phys. **49**, 71 (2008).

[273] S. Typel and B. A. Brown. *Neutron radii and the neutron equation of state in relativistic models*. Phys. Rev. **C 64**, 027302 (2001).

[274] M. Ugliano, H.-T. Janka, A. Marek, and A. Arcones. *Progenitor-Explosion Connection and Remnant Birth Masses for Neutrino-Driven Supernovae of Iron-Core Progenitors*. Astrophys. J. **757**, 69 (2012). Erratum: T. Ertl, M. Ugliano, H.-T. Janka, A. Marek, and A. Arcones, Astrophys. J. **821**, 69 (2016).

[275] C. S. Unnikrishnan. *IndIGO and LIGO-India: Scope and plans for gravitational wave research and precision metrology in India*. Int. J. Mod. Phys. **D 22**, 1341010 (2013).

[276] M. Urbanec, J. C. Miller, and Z. Stuchlík. *Quadrupole moments of rotating neutron stars and strange stars*. Mon. Not. Roy. Astron. Soc. **433**, 1903 (2013).

[277] I. Vidaña. *A short walk through the physics of neutron stars*. Eur. Phys. J. Plus **133**, 445 (2018).

[278] C. Vuille and J. Ipser. *On the maximum mass of neutron stars*. AIP Conf. Proc. **493**, 60 (1999).

[279] A. Vuorinen. *Quark Matter Equation of State from Perturbative QCD*. In *Proceedings, 12th Conference on Quark Confinement and the Hadron Spectrum (Confinement XII): Thessaloniki, Greece* **137**, 09011 (2017).

[280] F. M. Walter, S. J. Wolk, and R. Neuhäuser. *Discovery of a nearby isolated neutron star*. Nature **379**, 233 (1996).

[281] G. Watanabe, K. Iida, and K. Sato. *Thermodynamic properties of nuclear 'pasta' in neutron star crusts*. Nucl. Phys. **A 676**, 455 (2000). Erratum: Nucl. Phys. **A 726**, 357 (2003).

[282] A. L. Watts, N. Andersson, D. Chakrabarty, M. Feroci, K. Hebeler *et al. Colloquium: Measuring the neutron star equation of state using x-ray timing*. Rev. Mod. Phys. **88**, 021001 (2016).

[283] J. Weber. *Evidence for discovery of gravitational radiation*. Phys. Rev. Lett. **22**, 1320 (1969).

[284] S. Weinberg. *Approximate Symmetries and Pseudo-Goldstone Bosons*. Phys. Rev. Lett. **29**, 1698 (1972).

[285] S. Weinberg. *Gravitation and Cosmology*, (John Wiley and Sons, New York, 1972).

[286] S. Weinberg. *Phenomenological Lagrangians*. Physica **A 96**, 327 (1979).

[287] S. Weinberg. *Nuclear forces from chiral Lagrangians*. Phys. Lett. **B 251**, 288 (1990).

[288] S. Weinberg. *Effective chiral Lagrangians for nucleon-pion interactions and nuclear forces*. Nucl. Phys. **B 363**, 3 (1991).

[289] S. Weinberg. *Three body interactions among nucleons and pions*. Phys. Lett. **B 295**, 114 (1992).

[290] N. Wex. *The second post-Newtonian motion of compact binary-star systems with spin*. Class. Quant. Grav. **12**, 983 (1995).

[291] F. Wilczek. *Quantum Chromodynamics (QCD): The Modern Theory of the Strong Interaction*. Ann. Rev. Nucl. Part. Sci. **32**, 177 (1982).

[292] C. M. Will. *The binary pulsar, gravitational waves, and the Nobel prize*. Phys. Usp. **37**, 697 (1994).

[293] C. M. Will. *The Confrontation between General Relativity and Experiment*. Living Rev. Rel. **17**, 4 (2014).

[294] J. G. Williams, S. G. Turyshev, and D. H. Boggs. *Progress in lunar laser ranging tests of relativistic gravity*. Phys. Rev. Lett. **93**, 261101 (2004).

[295] B. Willke, P. Aufmuth, C. Aulbert, S. Babak, R. Balasubramanian *et al. The GEO 600 gravitational wave detector*. Class. Quant. Grav. **19**, 1377 (2002).

[296] K. Yagi, L. C. Stein, G. Pappas, N. Yunes, and T. A. Apostolatos. *Why I-Love-Q: Explaining why universality emerges in compact objects*. Phys. Rev. **D 90**, 063010 (2014).

[297] K. Yagi and N. Yunes. *I-Love-Q*. Science **341**, 365 (2013).

[298] K. Yagi and N. Yunes. *I-Love-Q relations in neutron stars and their applications to astrophysics, gravitational waves, and fundamental physics*. Phys. Rev. **D 88**, 023009 (2013).

[299] K. Yagi and N. Yunes. *I-Love-Q Relations: From Compact Stars to Black Holes*. Class. Quant. Grav. **33**, 095005 (2016).

[300] K. Yagi and N. Yunes. *Approximate Universal Relations for Neutron Stars and Quark Stars*. Phys. Rept. **681**, 1 (2017).

[301] D. G. Yakovlev, P. Haensel, G. Baym, and C. J. Pethick. *Lev Landau and the concept of neutron stars*. Phys. Usp. **56**, 289 (2013).

[302] K. L. S. Yip and P. T. Leung. *Tidal Love numbers and moment-Love relations of polytropic stars*. Mon. Not. Roy. Astron. Soc. **472**, 4981 (2017).

[303] V. E. Zavlin and G. G. Pavlov. *Modeling neutron star atmospheres*. In *Neutron stars, pulsars and supernova remnants. Proceedings, 270th WE-Heraeus Seminar, Bad Honnef, Germany, January 21-25, 2002* 262 (2002).

[304] J. L. Zdunik, M. Bejger, P. Haensel, and E. Gourgoulhon. *Phase transitions in rotating neutron stars cores: back bending, stability, corequakes and pulsar timing*. Astron. Astrophys. **450**, 747 (2006).

[305] T. Zhao and J. M. Lattimer. *Tidal Deformabilities and Neutron Star Mergers*. Phys. Rev. **D 98**, 063020 (2018).

Acknowledgements

Throughout my research project and during the preparation of this manuscript, I received a tremendous amount of support and assistance. And I can truthfully state that my doctoral research time has been a life-changing experience for me. I therefore want to thank all those people that in one way or another contributed to the success of this thesis.

First and foremost, I would like to express my deep gratitude to Achim Schwenk for letting me join his group and for introducing me to the exciting topic of neutron stars. I have profoundly benefited from his expertise over the last years. I appreciate his effort in encouraging me to pursue personal growth. He taught me a great deal about scientific research and life in general.

I would also like to thank Kai Hebeler. He was always willing to help and had good ideas when I was stuck. He always gave me constructive comments and warm encouragement.

I would also like to extend my sincere thanks to Anna Watts who provided me the opportunity to visit her group in Amsterdam for a research internship and I genuinely felt welcome. Moreover, I thank her for agreeing to be the second reviewer of my thesis.

I am also grateful to Geert Raaijmakers for the pleasant and fruitful collaboration. The numerous discussions in both Amsterdam and Darmstadt as well as via email were crucial to refine our speed of sound parametrization and to put our implementations to the test.

Particularly, I would like to thank all those who have proofread the present manuscript: Kai Hebeler, Thomas Jahn, Mirko Plößer, Achim Schwenk, and Corbinian Wellenhofer. Otherwise this thesis would have been about *rotting neutron stars* at some point.

I would like to acknowledge all the other members of the *strongint* group: Catharina Brase, Matthias Heinz, Jan Hoppe, Jonas Keller, Sebastian König, Yeunhwan Lim, Sabrina Schäfer, Timon Seibel, Rodric Seutin, and Lars Zurek and also the former members I was fortunate to meet: Alexander Bartl, Steven Bilaj, Arianna Carbone, Toño Coello Pérez, Sebastian Dietz, Christian Drischler, Victoria Durant, Martin Hoferichter, Lukas Huth, Maximilian Jacobi, Philipp Klos, Dmitry Kobyakov, Thomas Krüger, Joel Lynn, Marc Schönborn, Johannes Simonis, Ingo Tews, Sulamith Weber, and Kyle Wendt. Whether physics related topics or not, our discussions about many facets of life over lunchtime and especially during our coffee breaks were always enlightening, fruitful, and pleasant.

I really appreciated my time as a doctoral student at the *theory center*. The people provided always a stimulating and fun environment. I thank my fellow doctoral students for helpful feedback and scientific discussions.

I gratefully acknowledge the funding I received from the Deutsche Forschungsgemeinschaft through grant Sonderforschungsbereich 1245 which enabled me to conduct my research. The support also encompassed my participation at various interesting conferences which allowed me to foster international contacts as well as my research internship at the University of Amsterdam.

Moreover, I thank the Wilhelm und Else Heraeus-Stiftung which supported my participation at several spring meetings of the Deutsche Physikalische Gesellschaft.

Last but not the least, I would like to express my heartfelt thanks to Thomas for supporting me emotionally throughout writing my thesis and my life in general. You are the apple of my eye.

Curriculum Vitae

Name	Svenja Kim Greif
Date of Birth	October 07, 1990
Place of Birth	Groß-Gerau, Germany
Citizenship	German

Employment

since 2016 — research associate at Technische Universität Darmstadt

Education

since 2016 — Ph.D. research in physics at Technische Universität Darmstadt
Supervisor: Achim Schwenk

2014 – 2016 — Master's studies in physics at Technische Universität Darmstadt
Master's degree (final mark: 1.36)
Thesis: *Constraining the radius of neutron stars through the moment of inertia*
Supervisor: Achim Schwenk

2010 – 2014 — Bachelor's studies in physics at Technische Universität Darmstadt
Bachelor's degree (final mark: 2.71)
Thesis: *γ-γ-Koinzidenz Spektroskopie nach Neutroneneinfang an* ^{155}Gd
Supervisor: Norbert Pietralla

2001 – 2010 — Carl-Schurz-Schule, Frankfurt am Main
Abitur (final mark: 2.2)

Collaboration Visits

May 01 – 31, 2017 — Research Internship with Anna Watts
Anton Pannekoek Institute, University of Amsterdam, Amsterdam
supported by the DFG – SFB 1245

Memberships

since 2017 — Member of the *Deutsche Physikalische Gesellschaft*

Miscellaneous

since 2017 — Member of the *Gender equality and family friendliness team* of the *DFG – SFB 1245*

2017 - 2019 — Equal opportunities officer of the department of physics of the Technische Universität Darmstadt

Erklärung zur Dissertation

Hiermit versichere ich, dass ich die vorliegende Dissertation selbstständig angefertigt und keine anderen als die angegebenen Quellen und Hilfsmittel verwendet habe. Alle wörtlichen und paraphrasierten Zitate wurden angemessen kenntlich gemacht. Die Arbeit hat bisher noch nicht zu Prüfungszwecken gedient.

Darmstadt, den 28. November 2019

_____

(Svenja Greif)